

## **Irradiating, hydrating and densifying glasses to control their properties**

Ren, Xiangting

*DOI (link to publication from Publisher):*  
[10.54337/aau494413506](https://doi.org/10.54337/aau494413506)

*Publication date:*  
2022

*Document Version*  
Publisher's PDF, also known as Version of record

[Link to publication from Aalborg University](#)

*Citation for published version (APA):*  
Ren, X. (2022). *Irradiating, hydrating and densifying glasses to control their properties*. Aalborg Universitetsforlag. <https://doi.org/10.54337/aau494413506>

### **General rights**

Copyright and moral rights for the publications made accessible in the public portal are retained by the authors and/or other copyright owners and it is a condition of accessing publications that users recognise and abide by the legal requirements associated with these rights.

- Users may download and print one copy of any publication from the public portal for the purpose of private study or research.
- You may not further distribute the material or use it for any profit-making activity or commercial gain
- You may freely distribute the URL identifying the publication in the public portal -

### **Take down policy**

If you believe that this document breaches copyright please contact us at [vbn@aub.aau.dk](mailto:vbn@aub.aau.dk) providing details, and we will remove access to the work immediately and investigate your claim.



# **IRRADIATING, HYDRATING AND DENSIFYING GLASSES TO CONTROL THEIR PROPERTIES**

**BY  
XIANGTING REN**

**DISSERTATION SUBMITTED 2022**



**AALBORG UNIVERSITY**  
DENMARK





# **IRRADIATING, HYDRATING AND DENSIFYING GLASSES TO CONTROL THEIR PROPERTIES**

by

Xiangting Ren



**AALBORG UNIVERSITY**  
DENMARK

Dissertation submitted 2022

Dissertation submitted: July 2022

PhD supervisor: Prof. Morten M. Smedskjær,  
Aalborg University

PhD committee: Associate Professor Vittorio Boffa (chair)  
Aalborg University, Denmark

Associate Professor Sharafat Ali  
Linnæus University, Sweden

Professor Ondrej Gedeon  
University of Chemistry and Technology, The Czech Republic

PhD Series: Faculty of Engineering and Science, Aalborg University

Department: Department of Chemistry and Bioscience

ISSN (online): 2446-1636  
ISBN (online): 978-87-7573-874-8

Published by:  
Aalborg University Press  
Kroghstræde 3  
DK – 9220 Aalborg Ø  
Phone: +45 99407140  
aauf@forlag.aau.dk  
forlag.aau.dk

© Copyright: Xiangting Ren

Printed in Denmark by Stibo Complete, 2022



## CV

Ms. Xiangting Ren was born in Tengzhou, Shandong, P. R. China in June 1993. She got her Master's degree in the department of Chemistry, School of Science, Tianjin University, P. R. China in 2019, she got the China Scholarship Council (CSC) scholarship in June 2019, and then started her PhD study at the Department of Chemistry and Bioscience in Aalborg University in September 2019. Her research has been focused on irradiation, hydrating and densifying glasses to control their properties during the three-year PhD study at AAU.



## ENGLISH SUMMARY

Due to their numerous excellent properties such as high hardness, transparency, and chemical durability, oxide glasses play an important role for innovation in a variety of industries, including information technology and energy, communications, medical, and consumer electronics. The practical strength of glasses is substantially lower than the theoretical value due to surface imperfections and flaws.

Furthermore, impact or scratching events may cause cracks on the glass surface, magnifying local tensile strains and resulting in catastrophic failures. As a result, the future application of oxide glasses in various industries has been severely limited. Glass scientists have thus been interested in researching and designing tougher glass. Furthermore, different intrinsic and extrinsic post-treatment approaches have been tested to allow the design of stronger and more damage-resistant oxide glasses. Our research mainly focuses on post-treatment processing of oxide glasses, specifically, we plan to focus on hot compression, irradiation, and hydration treatments of glasses.

Firstly, we investigated the mechanical properties of various calcium aluminoborate glasses (CABS) with different compositions after hot compression. We found that the density, elastic modulus and hardness of the glass after isostatic pressing increased. The increase in network connectivity and bonding density was also attributed to the increase in hardness. The crack initiation resistance, on the other hand, decreased because the residual stress driving indentation cracking was larger in the hot compressed glass than in the as-made glass. We also studied the effect of different pressures, temperatures, and time routes on the densification behavior of oxide glass by performing hot-compression treatments on SNAB (sodium aluminoborosilicate) and NAB (sodium aluminoborate) glasses under various conditions. The impact of densification under different routes on NAB glass is more pronounced than that on SNAB glass. The study also discovered that the impact of densification along various paths on the structure and mechanical properties of these two glasses is similar. The increase in the coordination number of B and Al after densification is the fundamental structural alteration. In terms of mechanical properties, it has been discovered that after densification, hardness increases and crack resistance decreases. Additionally, the effects and changes are related to the treatment conditions (pressure, temperature, time).

Secondly, we have also evaluated the relationship between structure and mechanical properties in CABS glasses exposed to irradiation using both experimental data and MD simulations. Irradiation-induced structure changes in CABS glasses are shown to be mostly caused by boron speciation shifts from  $^{[4]}\text{B}$  to  $^{[3]}\text{B}$ , which results in a more open structure with increased disorder at the medium-range length scale.

The modulus and hardness of the glass surface layers decrease after irradiation, whereas crack resistance increases dramatically. Finally, we also demonstrated how a cobalt-based hybrid coordination network crystal is an excellent glass former and that its melting point and glass transition temperature can be greatly decreased by adding water. This mechanism is similar to the impact of water on other network "modifiers" in the field of oxide glasses, where such structural alteration is a common scientific and practical application.

# DANSK RESUME

På grund af deres mange fremragende egenskaber såsom høj hårdhed, gennemsigtighed, og kemisk bestandighed, spiller oxidglas en afgørende rolle for innovation i en række forskellige industrier, herunder inden for informationsteknologi, energi, kommunikation, medicin og forbrugerelektronik. Dog er den praktiske brudstyrke af glas væsentligt lavere end den teoretiske værdi på grund af overfladedefekter og fejl.

Ydermere kan stød eller ridser forårsage revner på glasoverfladen, forstørre lokale trækspændinger og resultere i katastrofale fejl. Som følge heraf er anvendelserne af oxidglas i forskellige industrier blevet stærkt begrænset. Glasforskere har været interesseret i at undersøge og konstruere hårdere glas for at imødekomme det øgede behov for glas i fremtidige applikationer. For at muliggøre designet af stærkere og mere bestandige oxidglas er forskellige efterbehandlingsmetoder blevet afprøvet. Vores forskning fokuserer hovedsageligt på efterbehandling af oxidglas, og heraf specifikt på højtemperaturs trykbehandlinger, bestråling og fugtighedsbehandlinger af glas.

Som det første undersøgte vi de mekaniske egenskaber af forskellige calciumaluminoboratglas (CABS) med forskellige sammensætningsforhold efter højtemperaturs trykbehandling. Vi fandt ud af, at tætheden, elasticitetsmodul og hårdheden af glasset efter behandlingen steg. Stigningen i hårdhed blev tilskrevet stigningen i netværkskrydsbinding og bindingstæthed. På den anden side faldt modstanden mod revneinitiering, fordi den resterende spændingsdrivende forbygningsrevnedannelse var større i det højtryksbehandlede glas end i det ubehandlede glas. Vi undersøgte også effekten af forskellige tryk, temperaturer og tidsruiter for densifikationsadfærden af oxidglas ved at udføre højtryksbehandlinger ved høj temperatur på SNAB- og NAB-glas under forskellige forhold. Indvirkningen af densifikation fra tryk og temperaturhistorien af NAB-glas er mere markant end for SNAB-glas. Undersøgelsen fandt, at indvirkningen af densifikationshistorien på strukturen og de mekaniske egenskaber af disse to glas er konstant. For begge glas er stigningen i koordinationstallet for B og Al efter densifikation den primære strukturelle ændring. Med hensyn til mekaniske egenskaber er det blevet opdaget, at hårdheden øges og revnemodstanden falder efter densifikation. Desuden er ændringerne relateret til betingelserne for behandlingerne (tryk, temperatur, tid).

For det andet har vi i denne afhandling også brugt både eksperimentelle målinger og MD-simuleringer til at evaluere sammenhængen mellem struktur og mekaniske

egenskaber i CABS-glas udsat for bestråling. Det blev fundet, hvordan bors koordinationsstal skifter fra  $^{[4]}\text{B}$  til  $^{[3]}\text{B}$ , hvilket fører til en mere åben struktur med øget uorden på mellemlang længdeskala, hvilket tilskrives som den primære årsag til bestrålingsinducerede strukturændringer i CABS-glas. Det er desuden fundet, hvordan modulus og hårdhed af glasoverfladen falder efter bestråling, hvorimod revnemodstanden øges dramatisk.

Endelig har vi også vist, hvordan et kobolt-baseret hybrid koordinationsnetværk er en fremragende glassdanner, og hvordan dets smeltepunkt og glasovergangstemperatur kan reduceres kraftigt ved at tilsætte vand. Denne mekanisme ligner virkningen af vand og andre netværks-"nedbrydere" inden for oxidglas, hvor en sådan strukturel ændring er velkendt og har stor praktisk anvendelse



# ACKNOWLEDGEMENTS

I would like to thank many people who helped me during my Ph.D. Without them, it would be hard for me to imagine that I would be able to successfully complete my PhD studies. First of all, I would like to thank my supervisor, Professor Morten Mattrup Smedskjær. In 2019, I met him for the first time through a Skype meeting. With his enthusiastic help, I successfully won the CSC scholarship, which allowed me to come to Aalborg University in Denmark to study for my doctorate. After that, his research attitude and research methods have greatly helped and inspired my study and research during my doctoral period. With his help, I was able to carry out my research and experiments smoothly. I am very grateful to him for his with guidance, I can complete my research project independently. During these three years, I also learned from communicating with him how to better design experiments, write high-level scientific papers, and overcome research challenges. These are huge benefits and help in my life and I really appreciate his help.

I would like to thank all my collaborators who have greatly helped my experiments and article with their excellent expertise and experience. I would like to thank Associate Professor Lars R. Jensen of the Materials department for his consistent help with Raman spectroscopy and infrared testing. This helped me a lot in the completion of the article. In addition, he participated in the revision of the manuscript. Our collaborators at Corning: Dr. Randall E. Youngman. Dr. Randall provides specific help and guidance on the tricky technique of solid-state NMR spectroscopy. In addition, he participated in the revision of the manuscript. In addition, I would like to thank our collaborator at UCLA: Prof. Mathieu Bauchy. He often gives me some scientific discussions and constructive critiques in our weekly group meetings. At the same time, he also provides great help for simulation. I would like to thank our collaborators Haibo Peng in Lanzhou University for the irradiation treatment, thanks for collaborators in Warsaw, Poland: Profs. Sylwester Rzoska, Boleslaw Lucznik and Michal Bockowski. Thanks for their great help with the hot compression experiments and for participating in scientific discussions and manuscript reviews. I would like to thank our collaborators Thomas Sørensen Quaade and Katharina Xenia Kaiser in Materials department for the guidance and assistance with DSC testing, and also thanks to Christophe A. N. Biscio and Lisbeth Fajstrup in department of mathematical sciences, Aalborg University, and many thanks to Professor John Wang at the National University of Singapore for his great help and guidance during my study abroad in Singapore, and Dr Shibo Xi for his help with XAFS testing and analysis. It was also an unforgettable experience to work with all my colleagues in the chemical department. They helped me a lot with lab discussions, reviewing papers, and other leisure activities.

I would like to thank everyone to express my gratitude: Prof. Yuanzheng Yue, Assoc. Prof. Donghong Yu, Assoc. Prof. Morten Christensen, Assoc. Prof. Vittorio Boffa,

Assoc. Prof. Thorbjørn Nielsen, Assoc. Prof. Mads Jørgensen, Assoc. Prof. Cejna Quist-Jensen, Dr. Ang Qiao, Dr. Tobias Bechgaard, Dr. Martin Østergaard, Dr. Rasmus Peterson, Dr. Usuma Naknikham, Dr. Katie Kedwell, Dr. Kacper Januchta, Dr. Malwina Stepniewska, Dr. Theany To, Dr. Anil Kumar Suri, Dr. Qi Zhang, Dr. Tao Du, Wei Fan, Wei Xu, Pengfei Liu, Mikkel Bødker, Katarzyna Janowska, Rasmus Madsen, Søren Sørensen, Anne Sophie Jødal, Johan Christensen, Rasmus Christensen, Chengwei Gao, Zhencai Li, Xianzheng Ma, Jiajia Yan, Xinxin Chen, Zhimin Chen, Daming Sun, Jingnan Wu, Jing Gao, Annemarie Davidsen, Anne Flensburg, Lisbeth Wybrandt, Timo Kirwa.

In addition, I would like to personally express my heartfelt thanks to my lovely friends: xi zhou, qian Liu, Jin man, Zhi dan, min, yun yu, Luo na, Bin qian. Finally, I am very grateful to all my family members. With their endless love, encouragement and support, I was able to continue my studies for a PhD and go abroad. During my doctoral study, they also gave me a lot of care and warmth in usual life. Most of all, I would like to thanks my parents, mainly for their unconditional support and selfless love and concern for me, which is also the driving force for me to keep on progressing and learning, I will always love you all! And express my most sincere thanks to you all!

# CONTENTS

<b>Chapter 1. Introduction .....</b>	<b>11</b>
1.1. Background and challenges.....	11
1.2. Objectives.....	13
1.3. Thesis content .....	13
<b>Chapter 2. Indentation of glasses .....</b>	<b>15</b>
2.1 Deformation mechanism .....	15
2.2. Indentation cracking.....	20
2.3 Summary .....	23
<b>Chapter 3. Densification of glasses through hot-compression .....</b>	<b>24</b>
3.1 hot-compression .....	24
3.2 Structure of Glasses.....	25
3.3 Densification effect on structure.....	30
3.4 Densification effect on mechanical property .....	31
3.4.1. Density .....	31
3.4.2. Hardness.....	32
3.4.3. Crack resistance .....	34
3.4.4. The Recovery of the Indentation Side Length ( $L_{SR}$ ).....	36
3.5 Summary .....	37
<b>Chapter 4. Glass irradiation.....</b>	<b>39</b>
4.1 Irradiation Post-treatment.....	39
4.2 Irrataiton effect on structure.....	40
4.3 Experimental mechanical properties .....	50
4.4 Summary .....	50
<b>Chapter 5. Glass hydration by water addition.....</b>	<b>52</b>
5.1 Invetigated glass systems .....	52
5.2 Hydration of glass .....	54
5.3 Structure changes for glass.....	55
5.4 Water effect the properties for glass .....	59
5.5 Summary .....	60

<b>Chapter 6. conclusion and Perspectives .....</b>	<b>62</b>
6.1. Conclusion .....	62
6.2. Perspective .....	63
<b>Biography.....</b>	<b>65</b>
<b>List of publications.....</b>	<b>76</b>

# CHAPTER 1. INTRODUCTION

## 1.1. BACKGROUND AND CHALLENGES

Oxide glasses play a critical role for innovation in a variety of industries, including information technology and energy, communications, medical, consumer electronics, and so on. This is mainly due to their many excellent properties such as high hardness, transparency, and chemical durability. However, design of new oxide glasses is challenged by the fact that around 3/5 of the atoms in these materials are oxygens, and as such, the possibilities for property tuning are thus relatively limited by composition variation alone (1). The number of potential oxide glass compositions is enormous (2) and much above what could be examined experimentally, at least using existing composition-structure-property approaches. This is due to their non-crystalline (atomic positions are not precisely known) (2), non-equilibrium state (additional order parameters are required to capture the effects of process-related factors), and non-ergodic state (due to long time scales involved with the relaxation process). In turn, this makes it impossible to use standard equilibrium approaches to capture the nature of the glassy state. Their mechanical qualities, in particular, have received a lot of attention. Due to the low practical strength and fracture toughness, current and prospective future uses are limited. The low strength arises due to surface flaws, causing stress to concentrate and potentially cause catastrophic damage (1), and the glasses also lack a stable shearing mechanism.

The practical application strength of glasses is substantially lower than the theoretical value due to surface imperfections and faults. Furthermore, impact or scratching events may cause cracks on the glass surface, magnifying local tensile strains and resulting in catastrophic failures. As a result, the future application of oxide glasses in various industries has been severely limited. Glass scientists have been interested in researching and constructing tougher glass in order to meet the increased needs for glasses in future applications.

Various intrinsic (3) and extrinsic post-treatment approaches have been tried to enable the construction of stronger and more damage-resistant oxide glasses, including the production of a surface layer with high compressive stress to restrict the formation and propagation of strength-limiting cracks. Indentation testing can be used to imitate real-life damage events under controlled settings to a certain extent and for specific applications. This will be achieved by developing and adopting new thermomechanical treatment protocols for modifying and tuning the structure and properties of oxide glasses. Our research mainly focuses on post-treatment processing of glasses, specifically, we plan to focus on hot compression, irradiation, and hydration treatments of glasses.

Firstly, hot compression is an interesting method for changing the structure and properties of oxide glass. It is a high-pressure treatment performed at or around the glass transition temperature ( $T_g$ ) (4). Research has found that hot compression of bulk oxide glasses at pressures up to 1 GPa around  $T_g$  could help to increase density, hardness, elastic moduli, and fracture toughness, whereas crack initiation resistance decreases (5-7).

High compression tests can lead to a knowledge of the indentation deformation mechanism due to the high stress that can be created in glasses under sharp contact loading, in addition to being an important tool for tuning characteristics, and this method also has recently been applied to describe the indentation deformation mechanism of oxide glasses (8-10). In addition, it is possible to address some of the unanswered questions regarding the nature of the glassy state through temperature-pressure studies of glassy systems. This is because exploring the temperature-pressure plane gives one additional degree of freedom compared to varying temperature alone (11). For the research in the thesis, we also explored hot compression post-treatment under different conditions for oxide glasses.

Secondly, it is well known that irradiation alters the surface structure and properties of glasses. In recent years, sodium borosilicate glasses (NBS) have been explored in particular because of its applications in the nuclear industry for the immobilization of high-level nuclear waste (12). Since these glasses are exposed to irradiation, it's critical to track how their mechanical properties, such as hardness, density, etc. For example, it has reported that hardness decreases upon irradiation by different ions, but the structural origin of the change remains unclear (13-15). After the process of irradiation, the internal structure of the glass has been found to change in a way that is not observed in standard melt-quenched glasses. By using irradiation treatment, the relationship between the mechanical properties and structural changes could also be further understood.

Thirdly, the post-treatment method of hydration will be explored. Some research suggests that only an adaptive network combined with few non-bridging oxygen and susceptible to surface hydration could produce micro-ductile deformation behavior. Therefore, certain improvements and adjustments of glass composition are needed (16,17). For our research, hydration treatment and research were carried out for a metal-organic framework (MOF) glass.

This thesis therefore mainly focuses on understanding the structural origins and underlying material features of indentation deformation and cracking behavior, through the study of the composition of the material and the explore of the corresponding post-treatment of oxide glasses, and also including the studies on the structure and hydration of MOF glass, further studies on water as a modifier to adjust

glass properties. Carrying out in-depth research on structural changes and properties for glasses, which is beneficial to explore and improve the properties of glasses.

## 1.2. OBJECTIVES

The overall goal of the Ph.D. project is mainly to improve our existing understanding of composition-structure-mechanical property relationships in glasses. Our research will also focus on the relationship between crack resistance and chemical composition, structural features, deformation mechanism, indentation recovery, and other physical and chemical properties. At the same time, we also have carried out research including the hydration influence on MOF glass, and further researched on water as a modifier to adjust the properties of glass. Furthermore, this alters both the physical and chemical properties of the resulting glass and draws strong parallels to the “modifier” concept in oxide glass chemistry where additives are commonly used to tune properties. More specifically, the proposed project focuses on post-treatment processing (hot compression, irradiation, hydration) of glasses. In this research, we will explore the effect of processing on glasses with different components, we will perform characterization tests and explore the correlation between variations in different properties. The following specific objectives will be achieved:

1. Indentation of glasses
2. Densification of glasses through hot-compression.
3. Glass irradiation.
4. Glass hydration by water addition.

## 1.3. THESIS CONTENT

The main experiments of the thesis are carried out at Aalborg University. This thesis consists of five papers, of which three have been published in peer-reviewed journals, and two in preparation. These papers constitute the main body of the thesis, and will be cited by their roman numerals throughout the thesis:

I. Chen L. T., **Ren X. T.**, Mao J. J., Mao Y. N., Zhang X. Y., Wang T. T., Sun M. L., Wang T. S., Smedskjaer M. M., Peng H. B\*. Radiation effects on structure and mechanical properties of borosilicate glasses. *Journal of Nuclear Materials* 552, 153025 (2021)

II. **Ren X. T.**, Liu P., Rzoska S. J., Lucznik B., Bockowski M., Smedskjaer M. M\*. Indentation response of calcium aluminoborosilicate glasses subjected to humid aging and hot compression. *Materials* 14, 3450 (2021).

III. **Ren X. T.**, Du T., Peng H., Jensen L. R., Biscio C. A. N., Fajstrup L., Bauchy M., Smedskjaer M. M\*. Irradiation-Induced Toughening of Calcium Aluminoborosilicate Glasses. *Materials Today Communications* 31, 103649 (2022).

IV. Søren S. Sørensen<sup>1</sup>, **Ren X. T.**<sup>1</sup>, Tao Du<sup>1</sup>, Shibo Xi, Lars R. Jensen, John Wang, Morten M. Smedskjaer\*, Water as a modifier in a hybrid coordination network glass. (First co-author, to be submitted).



# CHAPTER 2. INDENTATION OF GLASSES

Oxide glass materials can be used in a variety of applications (18) in daily life. In particular, their mechanical properties have received extensive attention. However, current and future uses are limited due to poor practical strength and fracture toughness, stress concentration due to surface defects and potentially catastrophic failure (19).

Early indentation investigations revealed that oxide glasses, unlike metals and ceramics, have a strong tendency to densify under compressive load. After decades of research, some research have discovered that the extent of densification is greatly influenced by the chemical composition of the glass, as well as its atomic packing density and Poisson's ratio. In order to improve the indentation response of oxide glasses, relationships between glass composition, indentation deformation mechanism, and the resulting indentation response is crucial to be established. The understanding of such correlations will aid in the development of tailored oxide glasses, with the goal of moving away from trial-and-error to model-based glass design. Therefore, to better understand the deformation and cracking mechanism of oxide glass, this chapter focuses on the deformation and cracking behavior caused by the sharp contact load, which is also of great help in improving the mechanical properties of oxide glass and making stronger glass.

## 2.1 DEFORMATION MECHANISM

Although composition-mechanical property relationships have been established for fundamental model systems, altering the chemical composition of oxide glasses to improve fracture resistance remains a tough challenge. Instrumented indentation is a typical method for examining the mechanical properties of glass. It is a quick and convenient method that simulates real-life damage for some applications, though interpretation can be difficult due to the complex stress fields that form under the indenter. Scientists have discovered that the extent of densification is highly controlled by the chemical composition of the glass, as well as its atomic packing density and Poisson's ratio, after decades of research.

After decades of research, scientists have discovered that the extent of densification is greatly influenced by the glass' chemical composition and, as a result, its atomic packing density and Poisson's ratio. The mechanism of densification has been shown using spectroscopic techniques, which include changes in bond angle distributions

and an increase in the coordination number of network-forming cations. Indentation is a popular technique since it requires a small sample area, is simple to prepare, and takes a short amount of time to complete. Indentation also offers information about the material's hardness, and elasticity data can be retrieved from the load-displacement curve when paired with depth-sensing apparatus (20).

Taylor (21) proposed that the indentation-induced deformation in glass was caused by shear flow (the term 'plastic flow' is also widely used in the literature for the same phenomenon), which is similar to that seen in ductile materials. Douglas (22) has highlighted the possibility of triggering cold viscous flow at sufficiently strong shear stresses, such as those experienced locally during sharp-contact loading. Marsh (23), who used quick indentation as well as indentation in liquid nitrogen to assess the hardness of various oxide glasses, backed up the claim of shear flow. Due to hardness varies with time and temperature, our findings strongly suggested that shear flow is at least partly to blame for indentation deformation. The glass surface is deformed due to densification, according to Peter (24) and later Evers (25), as demonstrated in Bridgman and Simon's high pressure studies (26,27).

Ernsberger (28) discovered a considerable increase in the refractive index of the glass in the zone beneath the depression imprint, indicating that densification occurs during contact loading, according to the evidence. Densification is a process in which the atomic network achieves a more densely packed arrangement, as demonstrated by infrared spectroscopy (29), although the bonds involved are not necessarily broken, in contrast to Marsh and others' volume-conservative shear flow (21). The hypothesis that indentation is linked to densification in oxide glasses is consistent with Neely and Mackenzie's later work (30), which demonstrated that some of the deformed zone can be restored after thermal annealing using amorphous silica as an example. Peter (31) demonstrated that the response of oxide glasses to indentation in general comprises both densification and shear flow by analyzing different glass compositions. Peter was able to visualize both deformation mechanisms using scanning electron microscopy (SEM) images of the indentation areas. Inspection of a sharp indentation imprint in the alkali silicate surface, on the other hand, reveals that during indentation, some of the material was displaced due to shear flow. The cross-section alimage of a ball indented alkali silicate glass (Figure 2-1) shows a substantial contrast between the bulk glass and a hemispherical deformation zone under the indent site, implying densification. A sharp indentation imprint in the alkali silicate surface, on the other hand, suggests that some of the material was displaced due to shear flow during indentation. As the material is built up around the imprint of the indentation on the glass (Figure 2-2). Besides the pile-up, the presence of shear bands (also known as slip lines) indicates that glasses are sheared during indentation (32-34). Shear bands (Figure 2-3) are flow-like material deformation observable as parallel lines or waves travelling outwards from the point of contact (34).

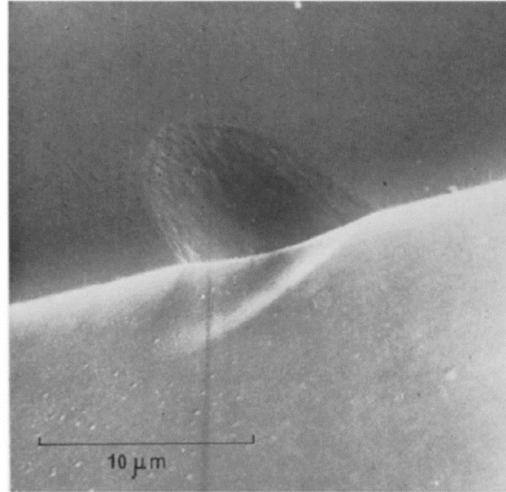


*Figure 2-1. A ball indentation impression in the surface of an alkali silicate glass, as well as a cross-section view of the deformation zone beneath the indentation cavity, as seen using a scanning electron microscope. The clear contrast line beneath the surface indicates the size of the densified zone. Figure reproduced from Peter (31) with permission of Elsevier.*

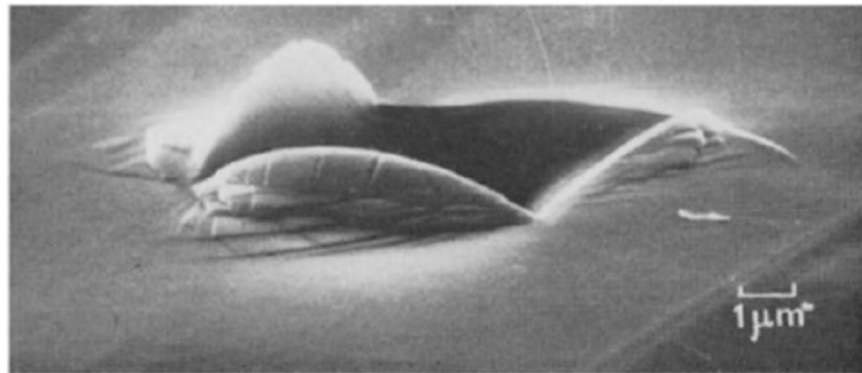


*Figure 2-2. Scanning electron microscopy image of an indent impression in an alkali silicate glass formed by a 70° pyramidal indenter. Figure from Peter (31) has been reproduced with permission of Elsevier.*

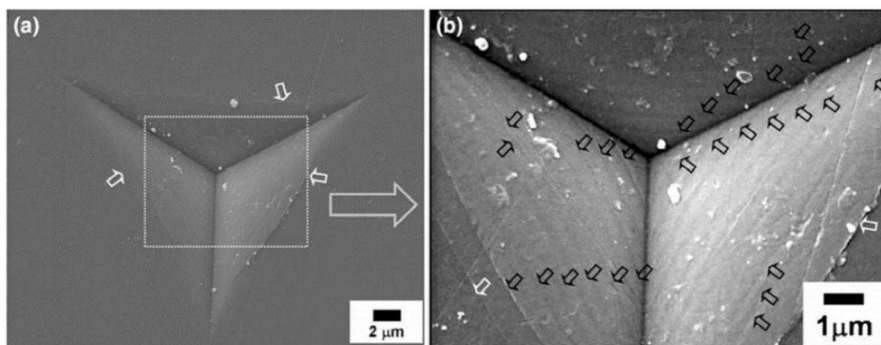


Figure 2-3. Berkovich indent impression with highlighted shear bands in a soda-lime silica glass. The shear bands represent plastic flow and are responsible for serration of the load-displacement curve obtained during the indentation. Figure reprinted from Chakraborty et al. (34) with permission of Springer Nature.

Optical microscopy is the easiest method for studying indentation-induced deformation in micro-indentation because crucial information may be derived from a qualitative assessment of the indentation imprint. The presence of shear faulting lines, for example, has been discovered. The indentation is frequently taken with the camera parallel to the glass surface (from above or below), allowing for quick examination after the indentation. In order to gain a better understanding of the subsurface damage, cross-section views of the indent sites could be investigated. This is done by shattering the glass sample diagonally across the indent, following radial cracks emanating from the indents' corners. In other words, a straight line of indents is formed to guide the fracture line, or an indent is placed adjacent to the tip of an existing scratch or arrested crack, and the specimen is then fractured, for example, by bending.

As mentioned in Ref. (35), atomic force microscopy (AFM) is commonly used for quantifying the deformation mechanism. This method involves taking topographic photographs of the indent location before and after a  $0.9T_g$  thermal treatment (Figure 2-4) to determine how much the indent cavity shrinks during annealing. However, annealing at  $0.9T_g$  has no effect on the volume displaced by shear flow because the viscosity is too high for any noticeable viscous flow to occur during the time scale of the experiment (2h) (36). We should point out that the annealing temperature of  $0.9T_g$  was determined based on data from only a few glass compositions, predominantly silicate glasses (37).

Indeed, the composition's liquid fragility should be considered while determining the annealing temperature and duration to ensure complete relaxation of the densified volume while avoiding viscous shear flow. The densification volume ( $V_d$ ) can be calculated by comparing the volumes below and above the surface plane before and after annealing:

$$V_d = (V_i^- - V_a^-) + (V_a^+ - V_i^+)$$

The volume recovery ratio ( $V_R$ ):

$$V_R = \frac{V_d}{V_i^-}$$

Sellappan et al. (38) also recommended distinguishing between the fraction of plastic flow that results in the so-called pile-up along indent edges (as shown in Figure 2-4) and the remainder volume that is moved downwards or radially away from the indent hole. This distinction is important because it has been proposed that pile-up dissipates the mechanical effort supplied during contact loading, whereas the remaining volume causes residual stress, which leads to indentation cracking (34). The extent of the densification zone formed during indentation has also been studied using a method based on dissolution and AFM measurements (39).

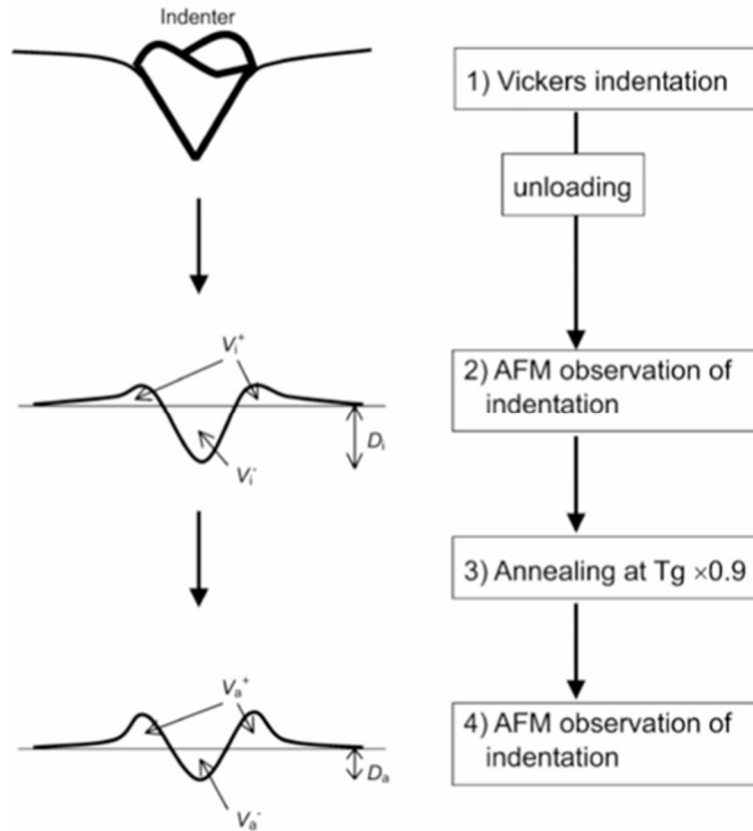


Figure 2-4. Schematic representation of the method for quantifying the densification contribution to the total indentation volume. With permission from Cambridge University Press, figure reproduced from Yoshida et al. (31).

## 2.2. INDENTATION CRACKING

The indentation reaction is classified as "normal," "anomalous," or "intermediate" depending on the deformation process and cracking response of the glass. The typical normal glass, such as soda-lime silicate, deforms to a large extent when indented with a Vickers tip due to a shearing process and generates median/radial and lateral cracks. A typical anomalous glass deforms primarily by densification and has a high tendency for ring/cone cracks, as well as median/radial and lateral cracks.

Furthermore, intermediate glass types exhibit both normal and abnormal behavior. These intermediate glasses deform with enhanced densification and less shear than

normal glasses. They do not, however, develop the ring/cone cracks that are typical in anomalous glasses. High stresses are required to initiate crack networks originating in the subsurface in glasses with this intermediate feature. As a result, the intermediate glasses remove the stress that cause ring and median cracks. Recently, it was discovered that some calcium aluminoborosilicate (CABS) glasses belong to the intermediate glass group (40), which are also mentioned in our research in Chapters 3 and 4. The deformation and indentation response of glasses is shown to be influenced by both contact geometry and glass structure. Indentation has been used to assess the damage resistance of different glasses since it not only simulates real-life damage for particular applications, but it is also a quick analysis procedure that needs little sample preparation. The approach proposed by Wada et al. (41) for corner cracking in glasses is the most frequent, in which a Vickers indenter is used to generate a series of imprints at varied loads. After unloading, each impression is assessed in terms of the amount of radial cracks coming from its corners. Divide the average value of cracks per indent by four to calculate the crack initiation probability at a given load (i.e., the number of corners per indent and hence the maximum number of radial cracks). This is done at various loads, ranging from low loads that cause no radial cracking (i.e., a 0% probability of crack initiation) to high loads that cause extensive cracking (i.e., 100% crack probability). After that, a suitable mathematical function is used to fit the data. As shown in Figure 2-5(a), indentation cracking resistance, or simply crack resistance, is defined as the load that corresponds to a 50% crack likelihood (CR).

We should indicate that CR does not describe resistance to the initiation of other types of fractures, such as lateral cracks, during abrupt contact loading. As a result, the "critical load for radial crack initiation" is a more precise term. It's also worth noting that CR takes into account not just the glass properties but also the test conditions. External parameters impacting the proneness of the tested glass to crack include loading rate, duration between unloading and recording the cracks, bluntness of the tip, and ambient conditions, relative humidity, in particular, plays a key role when analyzing CR (42).

For example, Kacper et al. (43) in our research group obtained bulk oxide glass with record high crack resistance by surface aging cesium aluminoborate glass under humid conditions, enabling it to withstand a load of about 500 N after humid aging, withstands sharp contact deformations without forming any strength-limiting cracks. The observed ultra-high crack resistance of this glass suggests the potential to use rational compositional design to improve the glass's damage resistance. Therefore, in this paper, we also prepared glasses with different compositions for some post-process (chapter 3,4). Besides, some calcium aluminosilicate glasses, were studied in ambient (50% RH) and inert N<sub>2</sub> conditions (44). At the load of 19.6 N, the researchers discovered an intrinsic compositional trend in the crack initiation probability when tested under N<sub>2</sub> atmosphere. Because all glasses have a 100% crack probability, it is not noticeable when tested in air (Figure 2-5(b)). When the bonds are pre-stressed, as during the indentation process, the effect of atmospheric moisture on crack initiation

is related to the hydrolysis of the oxide network. Which emphasizes the importance of comparing crack initiation statistics from different research with caution. Several studies (45,46) have sought to link the tendency to densify with the indentation cracking resistance in oxide glasses. Densification is thought to dissipate the energy given to the material during indentation. As a result of the lower residual stress after unloading (45), there is a lesser pushing force for fracture initiation. However, while the equations can forecast the typical cracking pattern, they can't anticipate the cracking pattern itself. There is no model of CR that is composition or property dependent. The weak of association between CR and  $V_R$  could be due to the fact that the deformation mechanism at the atomic scale, rather than the macroscopic volume change, should be taken into account, as different structural reorganizations may result in varying degrees of energy dissipation. In other words, two glasses with the same set of attributes ( $E$ ,  $H$ ,  $\nu$ , etc.) and the same tendency to densify (i.e., similar  $V_R$  values) must have the same CR value. If the toughness (i.e., resistance to crack propagation) of the two glasses differs sufficiently, the proneness of crack formation should also change. This is consistent with MD simulations on Na-K aluminosilicate glasses (47), which reveal that resistance to indentation-induced fracture is governed by two factors: i) The local fracture criterion is an inherent material feature that is heavily influenced by chemical composition, and ii) the evolution of stress during indentation as a function of indenter shape and other extrinsic characteristics.

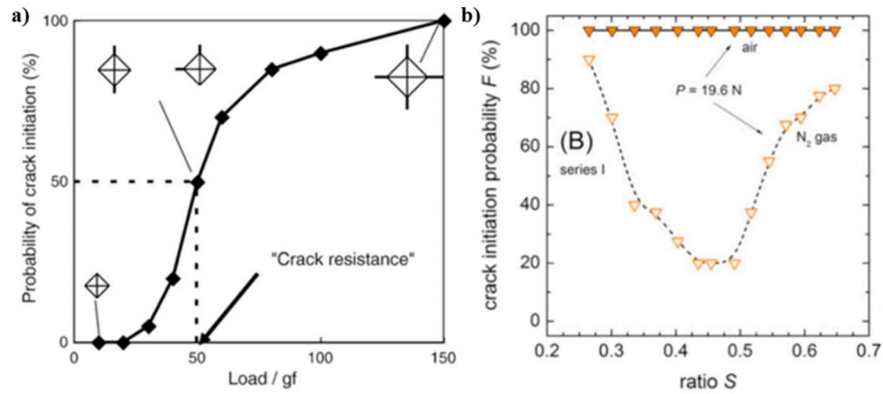


Figure 2-5. (a) Schematic representation of crack resistance determination. Figure reproduced from Kato et al. (44) with permission of Elsevier. (b) Crack initiation probability as a function of ratio  $S$  ( $Al/(Al+Si)$ ) in calcium aluminosilicate glasses measured in air with ~50% relative humidity (closed symbols) and in  $N_2$  gas (open symbols). Figure reproduced from Pönitzsch et al. (43) under the Attribution-Non-Commercial-No Derivatives 4.0 International license (CCBY-NC-ND4.0).



## 2.3 SUMMARY

In this chapter, we mainly introduces the deformation mechanism and cracking behavior of glass under contact load. From this chapter we could learn that understanding the critical load for cracking (crack initiation capability) is also an important component in the design of ultra-strong glass. Indentation was used to measure the damage resistance of various glasses because it simulates real damage in some applications and is a fast analytical technique that requires little sample preparation. The most popular method for glass with corner cracks is that proposed by Wada et al., where a Vickers indenter was used to induce a series of imprints under different loads. An appropriate mathematical function is then fitted to the data, then calculate the indentation cracking resistance. In addition, the crack initiation ability depends to a large extent on the composition of the glass, as well as some post-processing including hot compression, chemical surface enhancement, hydration, etc. However, to further understand how these factors relate to glass cracking, we must learn more about the glass network structure, the effect of composition, and the effect on the indentation response of the glass after post-treatment, these aspects are also investigated in the following sections, which will help in designing more damage-resistant glasses.

## CHAPTER 3. DENSIFICATION OF GLASSES THROUGH HOT-COMPRESSION

As we know, heat treatment and chemical composition changes are well-known methods for adjusting the structure and properties of glasses, but glass densification under high pressure offers a novel alternative, as pressure can precisely adjust the distance between atoms in the material and the bonding mode. Understanding the mechanism of densification under high pressure is also important for developing novel damage-resistant glasses. The degree of volume densification and the concomitant structural changes in the short- and medium-range length scales also contribute to the changes in glass characteristics under applied pressure. Many research have been conducted in recent years to better understand the impact of pressure. However, more research is needed to better understand and investigate the effect for oxide glass performance under high temperature and high pressure. What is more, it is also vital to investigate the effect of varied densification circumstances during the hot-compression treatment, i.e., different densification routes, to better understand the densification-structure-property relationships of glasses. Therefore, this chapter mainly introduces the glass densification through hot-compression, and also explore the structure and performance changes after densification.

### 3.1 HOT-COMPRESSION

Chemical composition changes and heat treatment are well-known methods for adjusting the structure and properties of glasses, but glass densification under high pressure (48,49) presents a novel option, as pressure can accurately adjust the distance between atoms in the material as well as the bonding mode. Understanding the mechanism of high-pressure densification is also crucial for developing novel damage-resistant glasses (50). The degree of volume densification and the resulting structural changes in the short- and medium-range length scales are related to changes of glass characteristics under applied pressure (51).

First, hot compression (heating the glass to a temperature near the glass transition temperature ( $T_g$ ) under high pressure) while under high pressure) can be used to permanently modify the structure and properties of oxide glasses (52). It has been found that hot compression around  $T_g$  at pressures of 1-2 GPa improves hardness, density, and elastic moduli while decreasing fracture initiation resistance (53). Compression experiments could provide insights into the deformation mechanism for indentation due to the high stress that can be created in glasses under acute contact loading (54), in addition to being a useful approach for tuning characteristics.

Various processes, such as sub- $T_g$  annealing, hot compression and cold compression, can be used to densify glass. The indentation procedure can also be used to create local densification of the glass. Furthermore, when the pressure is below 5-10 GPa, most of the pressure-induced glass structural changes are still reversible upon decompression in cold compression studies (55). This is not conducive to studying the effect of densification on glass structure and properties. As a result, glass densification by hot compression experiment provides numerous advantages, particularly near the glass transition temperature ( $T_g$ ): i) Thermocompression experiments allow for the fabrication of large samples ( $\text{cm}^2$  scale), which allows for more structural characterisation and mechanical testing. ii) Hot compression (at  $T_g$ ) has less structural relaxation issues due to the brief pressure drop during cooling. iii) The glass density grows linearly with pressure (below 1 GPa) during thermal compression at  $T_g$  (56, 57). As a result, the hot compression studies of glass at ambient pressure (1-2 GPa) and different temperature are the main emphasis of this research ( $T_g$ ). The glasses were isostatically compressed at their respective temperature values in a 1.0-2.0 GPa  $\text{N}_2$  environment for the hot compression procedure. The pressure and high temperature were maintained for different time, and afterwards the samples were cooled to room temperature at a cooling rate of 60 K/min to produce permanent compression of the glass samples. After that, the pressure chamber was decompressed at 30 MPa/min.

### 3.2 STRUCTURE OF GLASSES

Aluminoborosilicate glasses are used in a variety of applications that need mechanical durability, such as resistance to surface damage. In terms of their response to sharp contact loading, calcium aluminoborosilicate (CABS) glasses have recently been discovered to exhibit so-called intermediate behavior. The intermediate CABS glasses' net-work connectivity is lower than that of anomalous glasses, resulting in a higher degree of shear deformation and relief from the stresses that cause ring and median cracks (58). This results in a high resistance to crack initiation during indentation, which in turn is associated with the high shear band density in some CABS glasses. However, the relative amounts of shear and densification deformation were constant in the investigated CABS glass series with different  $\text{SiO}_2/\text{B}_2\text{O}_3$  ratios, but the load leading to indentation cracking varied according to the chemical composition. Therefore, the goal of this study was to learn and explore more about the structure and composition dependence of the indentation response of CABS glasses.

$\text{SiO}_2$  and  $\text{B}_2\text{O}_3$  are the primary network formers in CABS glasses due to their small cation size and high bond strength. Boron is found in a three- or four-fold coordinated state with oxygen in a random pattern (59). Calcium cations, or the creation of five- or six-fold coordinated aluminum or oxygen triclusters, are required to stabilize four-fold coordinated boron and aluminum. The boron speciation changes when alumina is added to borate glass (60). The previous study (2) employed the  $15\text{CaO}-15\text{Al}_2\text{O}_3-$

25B<sub>2</sub>O<sub>3</sub>-45SiO<sub>2</sub> (called CABS-ref) glass as the reference composition in this study. CABS-SiB (Si/B increase), CABS-CaB (Ca/B increase), CABS-BAl (B/Al increase), CABS-CaSi (Ca/Si increase), and CABS-CaAl (Ca/Al increase) were the five systematic composition modifications tested, as shown in Table 3-1.

*Table 3-1. Nominal chemical compositions of the CABS glasses and their measured glass transition temperature ( $T_g$ ). Table adapted from Paper II.*

Glass ID	SiO <sub>2</sub> (mol%)	Al <sub>2</sub> O <sub>3</sub> (mol%)	B <sub>2</sub> O <sub>3</sub> (mol%)	CaO (mol%)	Note	$T_g$ (°C)
CABS-ref	45	15	25	15	Reference glass	677
CABS-SiB	50	15	20	15	Si/B increase	652
CABS-CaB	45	15	20	20	Ca/B increase	683
CABS-BAl	45	10	30	15	B/Al increase	636
CABS-CaSi	40	15	25	20	Ca/Si increase	668
CABS-CaAl	45	10	25	20	Ca/Al increase	665

Some Refs (61-63) have previously explored the structure of alkali aluminoborate glasses. Both of the network-forming tetrahedral species tend to compete for the charge-balancing Na-cations, according to magic angle spinning (MAS) NMR investigations on <sup>11</sup>B and <sup>27</sup>Al nuclei. Rather than boron tetrahedra, charge-balancing aluminum tetrahedra (Al<sup>IV</sup>) are preferred (B<sup>IV</sup>). As a result, as Na-cations are re-associated to supply the insufficient positive charge to Al<sup>IV</sup> units, the proportion of four-fold coordinated boron species (N<sub>4</sub>) decreases when Al<sub>2</sub>O<sub>3</sub> is substituted for B<sub>2</sub>O<sub>3</sub>. Although prior research had not explored the relationship between aluminoborate structure and mechanical properties, low NBO and N<sub>4</sub> concentrations have been shown to enhance densification during indentation, which should lead to high CR values (45,46). As a result, sodium aluminoborate glasses are an excellent model system for determining the structural sources of strong crack resistance in oxide glasses. Borosilicate glass, on the other hand, has been routinely used for over a century. However, there is still a lack of knowledge about the structural response to densification. This is crucial for the development of novel glass products with enhanced characteristics and mechanical properties. The conversion of trigonal boron (<sup>3</sup>B) to tetrahedral boron (<sup>4</sup>B) in borosilicate glasses, which may be detected in composition (64), temperature (65), and pressure (66), has a substantial impact on the structure and properties of borosilicate glasses (67,68).

The effect of adding SiO<sub>2</sub> to lithium aluminoborate glasses on structural and mechanical properties was explored in a recent study (69). The addition of silica boosts average network stiffness, but its open tetrahedral structure reduces atomic packing density and makes the network structurally less responsive to applied stress. The analyzed chemical compositions of the glasses also could find in Table 3-2.

Table 3-2. The analyzed chemical compositions of the glasses as well as their measured glass transition temperature ( $T_g$ ). The error in  $T_g$  is within  $\pm 2^\circ\text{C}$ . Table adapted from Paper in preparation.

Glass ID	Na <sub>2</sub> O (mol%)	Al <sub>2</sub> O <sub>3</sub> (mol%)	B <sub>2</sub> O <sub>3</sub> (mol%)	SiO <sub>2</sub> (mol%)	$T_g$ ( $^\circ\text{C}$ )
NAB	20	22	58	-	453
SNAB	18	20	20	42	530

### 3.3 DENSIFICATION EFFECT ON STRUCTURE

The local and medium-range structure, vibrational density of states, and physical properties of glasses all vary considerably when high pressure is applied (70,71). Considering the structural changes, an increased pre-network coordination number (CN) is usually detected upon densification, such as B and Al (72,73). According to some investigations, increasing the pressure causes the glass to contain more tetrahedral boron ( $\text{B}^{\text{IV}}$ ), and this local structural alteration is irreversible after subsequent annealing at  $0.9T_g$  ambient pressure. Whereas property changes caused by pressure relax (74). This observation suggests that pressure-induced property changes are caused by more than just an increase in tetrahedral boron concentration (i.e., local structural coordination changes), but also by other types of structural alterations in the glass network. In our research, the structure of the densified glass was analyzed by Raman and solid-state nuclear magnetic resonance (NMR) spectroscopy, which can help to better analyze the structural changes after densification.

Based on our research, we will introduce the effect of compression on the structure of glass in detail, which is mainly reflected in the change of the network modifier environment and the coordination number of the network former. After the hot-compression treatment, for CABS glasses, the coordination number of boron and aluminum increases, resulting in more network bonds per atom. For hot compression, there are obvious changes in structure. What is more, we also used NMR spectroscopic measurements on  $^{27}\text{Al}$ ,  $^{11}\text{B}$ , and  $^{23}\text{Na}$  to better understand the effect of distinct hot compression routes on the short-range structure of the examined SNAB and NAB glasses. Using DMFit to deconvolve the spectra, the spectral deconvolution and corresponding spectral data of  $^{11}\text{B}$ ,  $^{27}\text{Al}$ ,  $^{23}\text{Na}$  were obtained, according to which the corresponding coordination number changes after densification were also analyzed. After hot compression, the  $\text{Al}^{\text{IV}}$  is mainly converted into  $\text{Al}^{\text{V}}$  and  $\text{Al}^{\text{VI}}$  units, the proportion of five-coordinated and six-coordinated aluminum has increased. And the changes of the coordination number of Al units under different hot-compression

paths are different. It also indicates that the degree of densification and the change of this coordination number are also related to the conditions of densification. Figure 3-1 and Figure 3-2 shows that the structure changes in Al units and B units of the NAB and SNAB glass after densification.

The  $^{27}\text{Al}$  MAS NMR spectra of SNAB and NAB glasses following densification under different pathways are shown in Figure 3-1. Three peaks at 60, 30 and 1 ppm in SNAB glass and three peaks around 60, 30 and 5 ppm in NAB glass may be clearly assigned to  $\text{Al}^{\text{IV}}$ ,  $\text{Al}^{\text{V}}$ , and  $\text{Al}^{\text{VI}}$ , respectively, in the glasses' spectrums (75). We detected considerable changes in aluminum despite relatively low pressures, which is consistent with earlier research (76). According to previous research (77), hot compression increases the areas of the  $\text{Al}^{\text{V}}$  and  $\text{Al}^{\text{VI}}$  peaks, which also correlates to the conversion of  $\text{Al}^{\text{IV}}$  to  $\text{Al}^{\text{V}}$  and  $\text{Al}^{\text{VI}}$  units. As a result, aluminum's CN increased.

The  $^{11}\text{B}$  MAS NMR spectra of SNAB and NAB glasses following densification under various hot compression techniques are shown in Figure 3-2. Both the glassy networks and the spectrums of the glasses contain  $\text{B}^{\text{III}}$  (about 5 to 20 ppm) and  $\text{B}^{\text{IV}}$  units (around -2.5 to 5 ppm). Indeed, the average CN of boron increases with hot compression, according to  $^{11}\text{B}$  MAS NMR spectra. NAB glass has a stronger densification effect than SNAB glass. As a result, temperature, pressure, and time all affect the degree of structural change caused by densification in SNAB and NAB glasses. According to the research, the average CN for B and Al increases after densification, and has a nearly perfect positive connection with the atom packing density ( $C_g$ ), indicating that the increase in  $C_g$  after densification is primarily attributable to the increase in CN for Al and B in structure. Figure 3-3 further indicates that when the atomic packing density increases after densification, the average Na-O distance decreases, indicating a distinct change in the sodium environment. This is further supported by research into sodium environments in glasses squeezed at higher pressures (78). The frequency shifts to higher frequencies when compressed at 2 GPa, which is consistent with prior findings on hot-compressed glass (79,80). Moreover, the impact on NAB is bigger than on SNAB. Previously, it was considered that variations in  $^{23}\text{Na}$  MAS NMR shifts reported for compressed glasses represented changes in Na-O bond lengths (80). The results in Figure 3-3 reveal a drop in the average Na-O bond length following densification based on this relationship. The average Na-O distance reduces with pressure (Figure 3-4), as does the partial molar volume of  $\text{Na}_2\text{O}$ , although the sodium coordination number may not change. Figure 3-4 further demonstrates that as the atomic packing density increases after densification, the average Na-O distance also decreases.

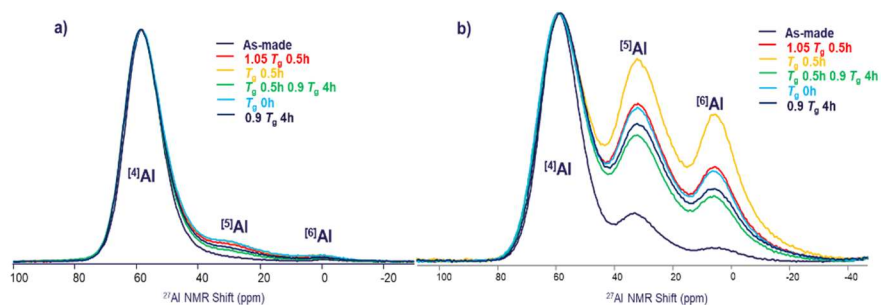


**Figure 3-1.**  $^{27}\text{Al}$  NMR spectra for the sodium aluminoborosilicate (SNAB) glasses (a) and the sodium aluminoborate (NAB) glasses (b) compressed at 2 GPa. Figure reproduced from Paper in preparation.

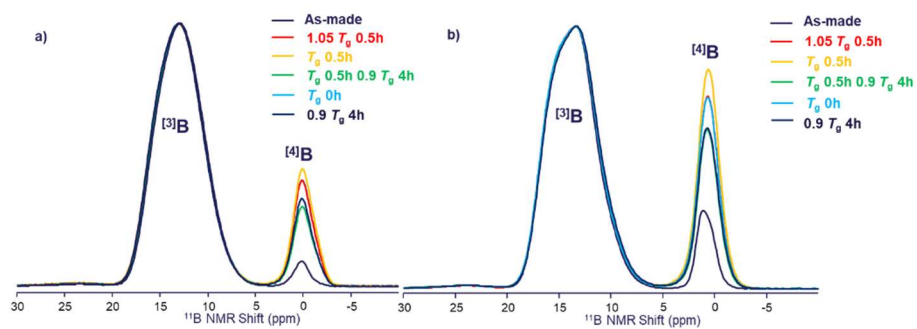


**Figure 3-2.**  $^{11}\text{B}$  NMR spectra for the sodium aluminoborosilicate (SNAB) glasses (a) and the sodium aluminoborate (NAB) glasses (b) compressed at 2 GPa. Figure reproduced from Paper in preparation.

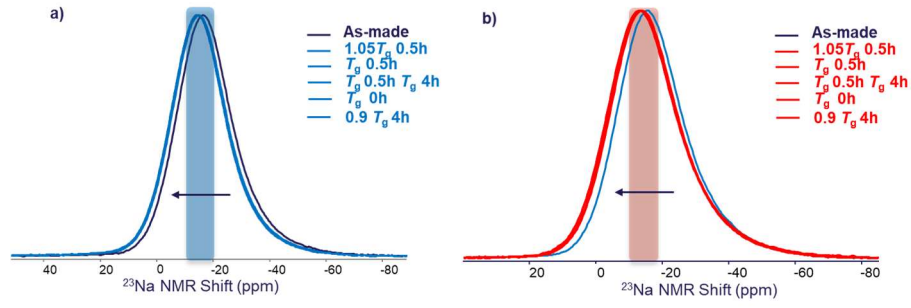


**Figure 3-3.**  $^{23}\text{Na}$  NMR spectra for the sodium aluminoborosilicate (SNAB) glasses (a) and the sodium aluminoborate (NAB) glasses (b) compressed at 2 GPa. Figure reproduced from Paper in preparation.

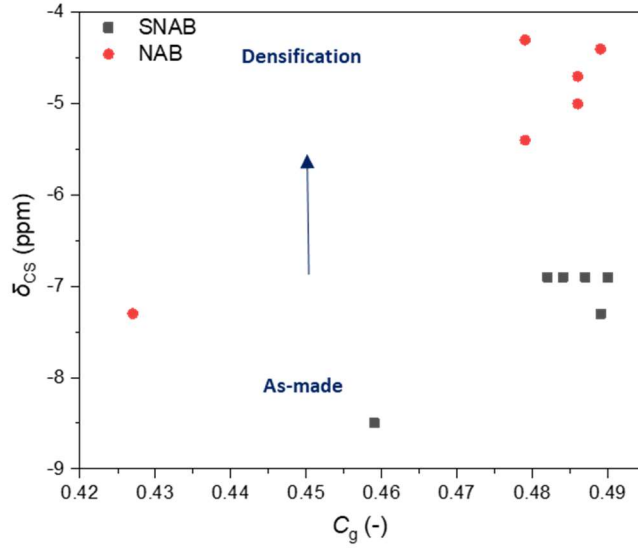


**Figure 3-4.** Atom packing density ( $C_g$ ) dependence of the  $^{23}\text{Na}$  NMR spectra ( $\delta_{cs}$  (ppm)) for the sodium aluminoborosilicate (SNAB) glasses and the sodium aluminoborate (NAB) glasses. Figure reproduced from Paper in preparation.



### 3.4 DENSIFICATION EFFECT ON MECHANICAL PROPERTY

Improving the mechanical qualities of glass, particularly its inherent brittleness, is a major technique for expanding future applications. On the other hand, the understanding for the structural origins of mechanical qualities like hardness and crack resistance, is still limited. Although it is generally known that the compression process can modify the mechanical characteristics of glass, the structural cause of this change is unknown. As a result, a thorough understanding of the mechanical characteristics of glass following compression is required.

#### 3.4.1. DENSITY

Numerous research (81) have demonstrated that free volume parameters (particularly atomic packing density) have a significant impact on hardness, elastic modulus, and other properties. As a result, investigating the effect of hot compression on density and atomic packing density can be helpful in comprehending the changes in relevant mechanical properties caused by densification. The research indicates that the density increased for CABS glasses, SNAB and NAB glasses (Table 3-3) after hot compression relative to the as-made sample, and that different hot compression conditions have distinct impacts on density. The atomic packing density ( $C_g$ ) is also calculated, which displays the condition dependency of atomic packing density ( $C_g$ ).  $C_g$  is the ratio of the molar volume of the glass to the lowest theoretical value of the volume filled by the constituent atoms. We discovered that  $C_g$  rises following hot compression, indicating that the network tightens as a result of the pressurized treatment. Hot compression has an obvious effect on the  $C_g$  of NAB glass than it does on SNAB glass.

Table 3-3. Density ( $\rho$ ) for SNAB and NAB glass for hot compression under different treatment condition. Table adapted from Paper in preparation.

Treatment condition (1GPa)	$\rho$ (g/cm <sup>3</sup> ) SNAB	$\rho$ (g/cm <sup>3</sup> ) NAB
As-made	2.376	2.229
1.05 $T_g$ 0.5h	2.444	2.402
$T_g$ 0.5h	2.441	2.368
$T_g$ 0.5h 0.9 $T_g$ 4h	2.444	2.373
$T_g$ 0h	2.411	2.313
0.9 $T_g$ 4h	2.411	2.306

Treatment condition (2GPa)	$\rho$ (g/cm <sup>3</sup> ) SNAB	$\rho$ (g/cm <sup>3</sup> ) NAB
As-made	2.376	2.229
1.05 $T_g$ 0.5h	2.556	2.548
$T_g$ 0.5h	2.516	2.535
$T_g$ 0.5h 0.9 $T_g$ 4h	2.530	2.534
$T_g$ 0h	2.479	2.497
0.9 $T_g$ 4h	2.473	2.507

### 3.4.2. HARDNESS

Hardness is sensitive to the constituent atoms' local bonding and atomic stacking behavior, as well as the presence of NBOs (82). As shown in Table 3-4 and Figure 3-4, the hardness for CABS glasses, NAB and SNAB glasses also increase, following heat compression for the sake of assessing changes in hardness, and the changes in different conditions are different. The rise in pressure is proportional to the increase in hardness.

Due to the bulk density of the glass increases after densification, the number of atomic bond restrictions per unit volume likewise increases during hot compression, resulting in a rise in Vickers hardness once more. Indeed, compression raises the CN of the boron and aluminum cations in the network, resulting in more bond restrictions per atom and contributing to the rise in Vickers hardness. The average number of rigid bond stretching and bond bending limitations are used to control the hardness of the glass.

Due to a rise in the coordination number in front of the network, pressure treatment will affect the amount of constraints, resulting in additional constraints per unit volume. In general, glasses with more plastic compressibility, or the capacity to densify more easily, have a higher pressure-induced rise in hardness. By converting B<sup>III</sup> to B<sup>IV</sup> during compression, a higher degree of densification is achieved, resulting in increased hardness. The importance of NBO in glass for pressure-induced hardness change was described in a recent study (82), and the pressure-induced hardness change and the NBO/T ratio had a positive association. This also shows that the increase in stiffness is due to overall network densification. As a result, the influence of different densification paths on glass hardness is dependent on the pressure, temperature, and time of compression. More broadly, this research demonstrates how pressure treatments might help improve the mechanical properties of industrial glasses. This means that parameters that must be relevant to a glass made at ambient pressure can be regulated as well. This opens up new avenues for industrial glass rational design.

Table 3-4. Vickers hardness ( $H_V$ ) for the as-made and hot-compressed CABS glasses. Table adapted from Paper II.

Glass ID	$H_V$ as-made (GPa)	$H_V$ hot (GPa)
CABS-ref	5.82	6.96
CABS-SiB	5.54	7.31
CABS-CaB	5.62	7.39
CABS-BAl	5.58	6.72
CABS-CaSi	5.81	7.14
CABS-CaAl	6.11	7.28

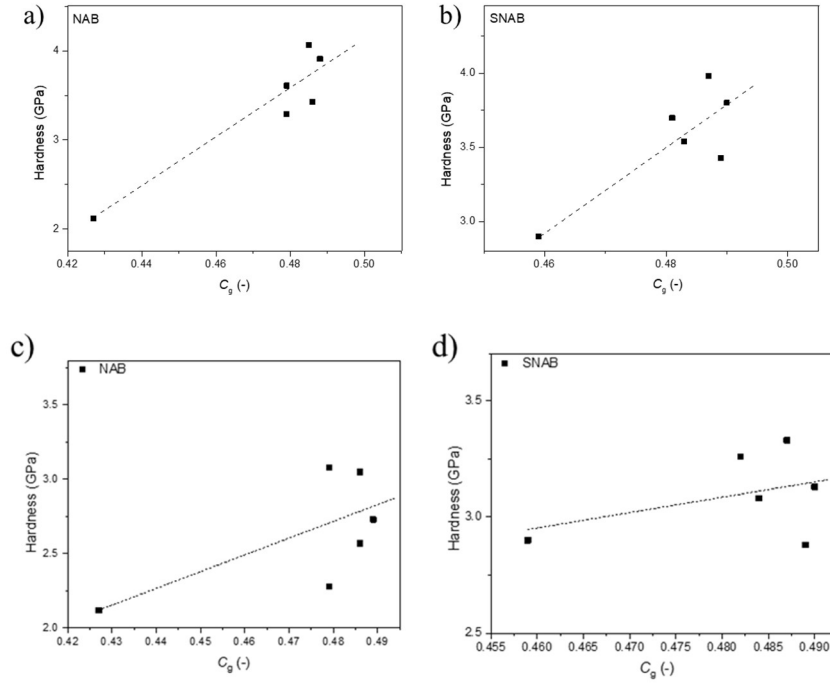


Figure 3-4. The relation between Vickers hardness and atomic packing density for SNAB and NAB glass. Figure adapted from Paper in preparation.

### 3.4.3. CRACK RESISTANCE

Due to a mismatch between the surrounding elastically deformed material and the degree of plastic deformation, indentation-induced crack initiation occurs under a sufficiently high stress. The crack resistance (CR), which is defined as the load that induces two corner cracks per indent for the four-sided pyramid indenter, was calculated using the indentation data generated at various loads. Corner cracks were the most common type of crack in the glass studied. The CR value will be affected significantly by different experimental settings and composition modifications. The residual stress that promotes indentation cracking is higher than that of the as-made glass when the glasses are compressed in various routes, which causes more noticeable cracking. As a result, the material is unable to release mechanical energy via densification, resulting in lower CR values.

For CABS glass, there are same conclusions, the residual stress driving indentation cracking is higher than that of completed glass when compressed at  $T_g$  and 1 GPa. Therefore, the material could not dissipate mechanical energy by densification, causing lower CR values. (Table 3-5)

The crack resistance of glasses after densification under various pathways is shown in Table 3-6. After densification, the CR of both glasses decrease, with the decrease in CR for NAB glass being larger than that for SNAB. The effects of hot-compressing densification on CR are also positively associated with pressure for SNAB and NAB glasses, with the change under 2GPa being higher than that under 1GPa. As a result, the influence of temperature under  $T_g$  is the most noticeable, and it is also favorably connected to processing time. This tendency coincides with the hardness and structural changes in glasses.

The increase in the coordination number is also the most obvious at  $T_g$ , for 0.5h, and the smallest in the paths of  $T_g$ , for 0.5h, and continuous at  $0.9T_g$ , for 4h, according to the examination of the NMR spectra of B and Al. As the coordination number of B and Al increases, the degree of densification during the indentation process decreases, the shear flow increases, and the CR decreases. Radial cracks are driven by residual stress, according to studies (83,84). Densification deformation produces less subsurface damage and less residual stress, therefore fracture resistance improves as densification contributes to the indenter. Due to the bulk density of the glass increases after densification, the number of atomic bond restrictions per unit volume increases as well during hot compression, making additional densification during indentation less likely.

*Table 3-5. Crack resistance (CR) for Vickers indentation of the as-made and hot-compressed CABS glasses. The error in CR was less than 15%. Table adapted from Paper II.*

<b>Glass ID</b>	<b><math>CR_{as-made}</math> (N)</b>	<b><math>CR_{hot}</math> (N)</b>
CABS-ref	13.0	5.6
CABS-SiB	13.6	7.8
CABS-CaB	5.6	3.8
CABS-BAl	18.9	8.0
CABS-CaSi	14.5	8.4
CABS-CaAl	8.2	6.9

*Table 3-6. Crack resistance (CR) for SNAB and NAB glass for hot compression under different treatment condition. Table adapted from Paper in preparation.*

<b>Treatment condition (1GPa)</b>	<b><math>CR_{SNAB}</math> (N)</b>	<b><math>CR_{NAB}</math> (N)</b>
As-made	13.6	7.5
$1.05 T_g$ 0.5h	5.0	4.5
$T_g$ 0.5h	4.1	4.3
$T_g$ 0.5h $0.9T_g$ 4h	7.6	5.7
$T_g$ 0h	6.8	4.4
$0.9T_g$ 4h	8.6	4.5

### 3.4.4. THE RECOVERY OF THE INDENTATION SIDE LENGTH ( $L_{SR}$ )

The composition dependency of indentation side recovery ( $L_{SR}$ ) for as-made CABS glasses is shown in Table 3-7.  $L_{SR}$  is the measure of the degree of shrinkage generated by a hot treatment below  $T_g$  on a Vickers indent, and prior research has demonstrated that  $L_{SR}$  can be used to assess the densification contribution to indentation deformation. After annealing, the depression had partially restored its shape, as shown in Figure 3-5. In comparison to the  $L_{SR}$  value of CABS-ref, CABS-BAl had the highest  $L_{SR}$  value (37.3%), while CABS-CaB had the lowest  $L_{SR}$  value (29.7%). The larger proportion of  $B_2O_3$  and hence concentration of three-fold coordinated B atoms in the CABS-BAl glass may explain this. The glass was able to densify more easily throughout the indentation process due to the open planar structure, resulting in a higher  $L_{SR}$ . In general, CABS glasses with a lower CaO content (15%) had a better indentation side recovery ( $L_{SR}$ ) value. This is similarly comparable to CR variation. Figure 3-6 depicts the relationship between CR and the degree of recovery, and hence the level of densification.

Table 3-7. Indentation side recovery ( $L_{SR}$ ) for the as-made calcium aluminoborosilicate glasses. The reported  $L_{SR}$  value and corresponding error are based on results from ten independent indentations. Table adapted from Paper II.

Glass ID	CABS-Ref	CABS-SiB	CABS-CaB	CABS-BAl	CABS-CaSi	CABS-CaAl
$L_{SR}$ (%)	35.9	33.7	29.7	37.3	34.3	30.9
Error	1.8	1.9	1.8	1.2	2.0	1.8

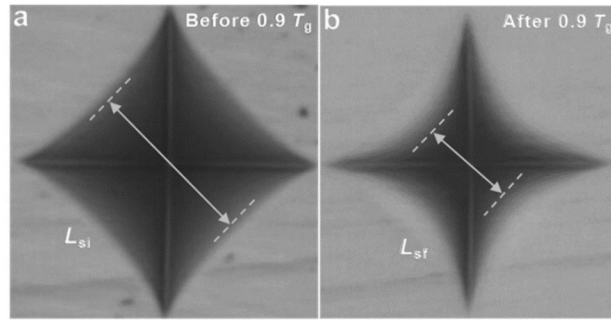


Figure 3-5. Optical micrographs of indents on the surface of the CABS glass created at 4.9 N before and after re-annealing at 0.9 $T_g$  for 2 h. Figure adapted from Paper II.

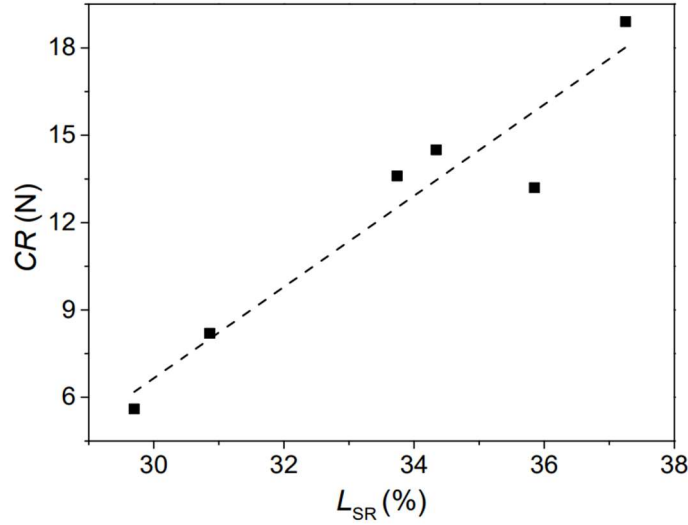


Figure 3-6. Relationship between crack resistance for Vickers indentation (CR) and indentation side recovery ( $L_{SR}$ ) of the as-made CABS glasses. Figure adapted from Paper II.

### 3.5 SUMMARY

In this chapter, we have explored the pressure-induced structural changes, and investigated the mechanical properties of a variety of calcium aluminoborate glasses (CABS) with various component ratios after hot compression. The density, elastic moduli, and hardness of the glasses treated with isostatic compression increased. The increase in network connection and binding density was also attributed to an increase in hardness. On the other hand, the crack initiation resistance decreased because the residual stress driving indentation cracking in the hot compressed glass was larger than in the as-made glass. We also studied the effect of different pressures, temperatures, and time routes on the densification behavior of oxide glass by performing hot-compression treatments on SNAB and NAB glasses under various conditions. The impact of densification under different routes on NAB glass is more visible than that on SNAB glass. Based on the structural study of Raman and NMR spectra, which may be related to the presence of silicon in SNAB glass. The rise in the coordination number of B and Al after densification is the fundamental structural alteration. For the influence of different conditions on its densification, it has been discovered that the degree of densification and pressure are positively correlated. The research also provides a foundation and important reference for the study and analysis of densification behavior in oxide glasses under different routes.





## CHAPTER 4. GLASS IRRADIATION

The effect of high-energy irradiation on glass mechanical characteristics and structure has recently been investigated, including our work on heavy ion irradiation treatment of sodium borosilicate (NBS) glasses for immobilization of high-level nuclear waste (85). When NBS glasses are irradiated, their indentation hardness decreases at first, then stabilizes when the irradiation dose is increased (86). The difference in irradiation impact between NBS and quartz glasses suggests that the hardness reduction in NBS glasses is attributed not only to silicate network transformation, but also to borate network transformation (87). Irradiated NBS glasses have also been studied using MD simulations, which reveal a decrease in hardness, which is consistent with experimental evidence (88). Irradiation reduces the elastic modulus of NBS glasses, also find the crack resistance also increases after irradiation, according to studies, although the structural alterations that cause these changes in mechanical characteristics are unknown (89). Based on this research, we started to explore the effect of irradiation for CABS glasses on the mechanical properties of CABS glasses is interesting because of their remarkable crack resistance. We recently also discovered that CABS glasses' chemical composition influences indentation deformation and cracking behavior (89). As a result, in this research, we use three different CABS glass compositions to execute irradiation treatment. The goal is to figure out what causes the differences in surface mechanical characteristics that result after irradiation.

### 4.1 IRRADIATION POST-TREATMENT

In this thesis, the first project is a study of borosilicate glass (NBS) irradiation treatment, which is also a collaboration with the Lanzhou University laboratory. Borosilicate glass could be used to treat high-level radioactive waste (HLW). Glass is subjected to irradiation during HLW disposal, particularly heavy ion irradiation associated with alpha decay, which is likely to have a long-term impact on glass performance. As a result, it's critical to comprehend borosilicate glass's irradiation stability.

We irradiated a range of sodium borosilicate glasses, as well as International Simple Glass (ISG), with 5 MeV Xe ions in this study. The irradiation effects on glass involve changes in macroscopic characteristics such as hardness, modulus, and crack initiation resistance (CR). We discovered that after irradiation, the glass's hardness and modulus decreased, whereas the CR of the glass increased dramatically. This also serves as a reference for the radiation treatment of CABS glass in the future. Our findings indicate that the boron structure is crucial in regulating the macroscopic radiation effect. The CABS system was then irradiated based on the result of this research.

The melt-quenching approach was used to make the three CABS glasses (Tables 4-1). The basic materials utilized were  $\text{CaCO}_3$  (99.5%, ChemSolute),  $\text{H}_3\text{BO}_3$  (99.5%, Honeywell International),  $\text{Al}_2\text{O}_3$  (99.5%, Sigma-Aldrich), and  $\text{SiO}_2$  (99.5%, 0.2-0.8 mm, Merck KGaA). We cut the glasses into the desired sizes after annealing for irradiation and characterisation. The glass samples ( $1.7 \times 1.2 \times 0.1 \text{ cm}^3$ ) were bombarded with Xe ions at room temperature at the Chinese Academy of Sciences' Institute of Modern Physics (IMP) (see Table 4-2). The xenon ions were created, chosen, and then propelled with a 5 MeV energy toward the sample. The sample in the target chamber was bombarded by a uniform ion beam generated by a pair of grating magnets. The target chamber had a pressure of  $7 \times 10^{-6} \text{ Pa}$ . The beam spot size was  $20 \times 20 \text{ mm}^2$  and the typical ion current was  $2 \text{ }\mu\text{A}$ . The samples were given two distinct doses of  $2.0 \times 10^{13} \text{ ions/cm}^2$  and  $2.0 \times 10^{14} \text{ ions/cm}^2$ , respectively.

Table 4-1. Nominal chemical compositions and their measured glass transition temperature ( $T_g$ ) of the CABS glasses. The glass ID is determined by the  $\text{Al}_2\text{O}_3$  to  $\text{B}_2\text{O}_3$  ratio. The error in  $T_g$  is within  $\pm 2^\circ\text{C}$ . Table adapted from Paper III.

Glass ID	$\text{SiO}_2$ (mol%)	$\text{Al}_2\text{O}_3$ (mol%)	$\text{B}_2\text{O}_3$ (mol%)	$\text{CaO}$ (mol%)	$T_g$ ( $^\circ\text{C}$ )
CABS-0.4	45	10	25	20	665
CABS-0.6	40	15	25	20	668
CABS-0.75	45	15	20	20	683

Table 4-2. Nominal chemical compositions and their measured glass transition temperature ( $T_g$ ) of the CABS glasses. The glass ID is determined by the  $\text{Al}_2\text{O}_3$  to  $\text{B}_2\text{O}_3$  ratio. The error in  $T_g$  is within  $\pm 2^\circ\text{C}$ . Table adapted from Paper III.

Glass ID	Ion Energy (MeV)	dE/dX Nuclear (MeV/(mg/cm <sup>2</sup> ))	Projected Range ( $\mu\text{m}$ )	Longitudinal Straggling ( $\text{\AA}$ )	Lateral Straggling ( $\text{\AA}$ )
CABS-0.4	5.00	9.151	1.73	1772	1839
CABS-0.6	5.00	9.132	1.73	1773	1842
CABS-0.75	5.00	9.080	1.71	1770	1835

## 4.2 IRRADIATION EFFECT ON STRUCTURE

In this research, we try to explore the structure changes by the Raman spectrum, and dividing the Raman spectra into four main bands and detail the predicted assignments in the following. The micro-Raman spectrum of the as-made and irradiated CABS-0.6 glass is shown in Figure 4-1a. Band region I ( $250$  to  $625 \text{ cm}^{-1}$ ) is anticipated to

contain contributions from the B-O-B, Al-O-Al, and B-O-Al stretching bands. Vibrations caused by superstructural units like pentaborates may also occur in this area.

In addition, Si-O-Si network units may be found in this area (90). Because peaks in this frequency range are often allocated to borate superstructures, band region II (625 to 860  $\text{cm}^{-1}$ ) is characteristic of  $\text{B}_2\text{O}_3$ -rich glasses (90). An aluminate network and B-O-Al stretching may also be present in this location. Triborates ( $\sim 770 \text{ cm}^{-1}$ ) and ditriborates ( $\sim 755 \text{ cm}^{-1}$ ) may be discovered in this region even the high intensity in this range of wavenumbers and the fact that they contain both  $^{10}\text{B}$  and  $^{11}\text{B}$  units. Given the high intensity in this range of wavenumbers and the fact that they contain both  $^{10}\text{B}$  and  $^{11}\text{B}$  units, triborates ( $\sim 770 \text{ cm}^{-1}$ ) and ditriborates ( $\sim 755 \text{ cm}^{-1}$ ) may also be detected in this region. The vibration of Si-O stretching also helps (800  $\text{cm}^{-1}$ ). Band area III (860-1200  $\text{cm}^{-1}$ ) is likely to feature contributions from  $\text{Q}^n$  species, with bands at 1000  $\text{cm}^{-1}$  attributable to  $\text{Q}^2$  species' stretching Si-O vibration (91). Finally, signal contributions from  $^{10}\text{B}$  units are often attributed to band region IV (1200 to 1600  $\text{cm}^{-1}$ ). In comparison to the as-made CABS glasses, the areas of bands II and IV increase following irradiation, as seen in Figures 4-1(a-b). This demonstrates that the irradiation treatment had the largest impact on the structure around the B units in the CABS glass structure, which is also consistent with previous findings (92).

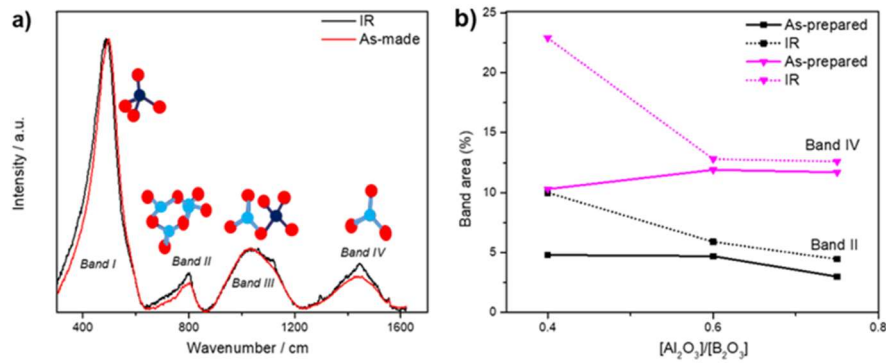


Figure 4-1. (a) Micro-Raman spectra of the as-made and irradiated CABS-0.6 glass and irradiated. The four band regions' assignments are detailed in the text. (b) Relative area fractions of the two main Raman bands (bands II and IV) for as-made and irradiated CABS glasses. Figure adapted from Paper III.

Figure 4-2a demonstrates that the average CN of B drops monotonically and eventually approaches a constant value in all glasses as the deposited energy increases. In other words, irradiation causes a partial conversion of  $^{10}\text{B}$  to  $^{11}\text{B}$ . These findings support the experimental Raman results, which reveal  $^{10}\text{B}$  to  $^{11}\text{B}$  conversion caused by irradiation (Figure 4-1a).

As the deposited energy increases, the average CN of B decreases monotonically and eventually approaches a constant value in all glasses, as shown in Figure 4-2a. Irradiation, in other words, causes a partial conversion of  $^{[4]}\text{B}$  to  $^{[3]}\text{B}$ . These findings support the experimental Raman results, which show that  $^{[4]}\text{B}$  to  $^{[3]}\text{B}$  conversion caused by irradiation (Figure 4-1a).

Interestingly, as the irradiation energy saturates, the final CN of B in the three glasses reaches a value of roughly 3.3, despite the variances in the beginning CN of B. On the other hand, no noticeable changes in the CN of Al and Si atoms after irradiation have been observed (Figure 4-2b, Figure 4-2c). Figure 4-3a also demonstrates that when the CABS glasses are irradiated, their densities fall and then plateau, which is consistent with the literature (93). As shown in Figure 4-3b, after irradiation, the enthalpy becomes less negative and eventually saturates.

Because short-range structure dominates enthalpy, the increase in enthalpy is primarily due to the creation of  $^{[3]}\text{B}$  species, which is favored at higher temperatures produced by irradiation events.

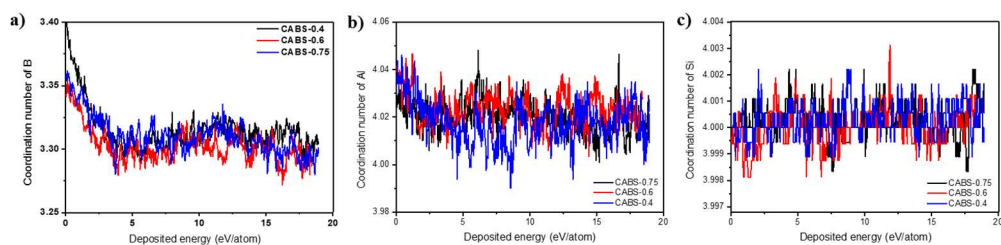


Figure 4-2. a) The simulated average of the coordination number for B, b) Al and c) Si of CABS glasses as function of the deposited energy during the process of irradiation. Figure reproduced from Paper III.

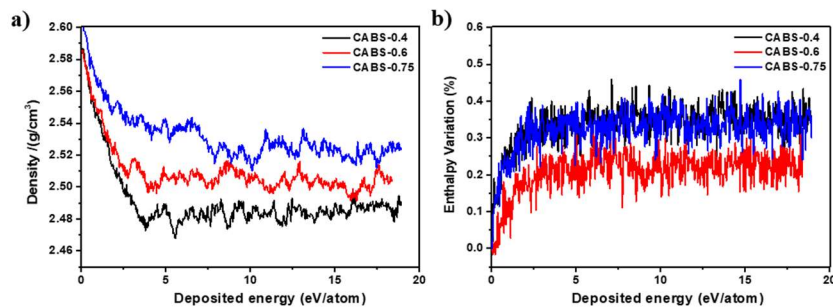


Figure 4-3. During the simulated irradiation process, the evolution of (a) density and (b) normalized enthalpy changes of CABS glasses as a function of deposited energy. Figure reproduced from Paper III.

The distribution for O-B-O bond angle moves towards a higher angle after irradiation, as illustrated in Figure 4-4a for the CABS-0.4 glass, which expresses itself as an increase in the intensity of the  $120^\circ$  angle at the expense of the  $109^\circ$  angle. Next, we explore the irradiation affects for ring formations. The ring size distribution for the CABS-0.4 glass coarsens after irradiation, as shown in Figure 4-4b, the fractions of some small rings (i.e., three- and four-membered) and large rings (i.e., seven-membered and greater) are increasing at the expense of intermediate-sized rings (i.e., five-membered), which is consistent with the behavior of other irradiated silicate glasses (94). Figure 4-4c shows that the simulated neutron structure factors for various irradiation states are often similar, with minor differences for the first strong diffraction peak (FSDP). Specifically, when the deposited energy increases, the FSDP shifts slightly towards a lower Q value, while its intensity drops, indicating greater disorder in the medium-range structure and swelling of CABS glasses. We analyze irradiation-induced structural modifications at medium-range length scales using persistent homology analysis of simulated glass structures. Figure 4-4d-f illustrates that following irradiation, the distribution of distinctive regions in the persistence diagrams tends to diffuse to the high-death regions, notably in the low-birth region, implying that loop sizes increase. Figures 4-4b and 4-4c show that irradiation changes the medium-range order structure of CABS glasses. These findings support the irradiation-induced expansion and loss of connectivity of the CABS glass structure. Overall, we conclude that irradiation affects both the short- (for example,  $^{14}\text{B}$  to  $^{13}\text{B}$  conversion) and medium-range structure (e.g., loop sizes increasing with reduced loop numbers).

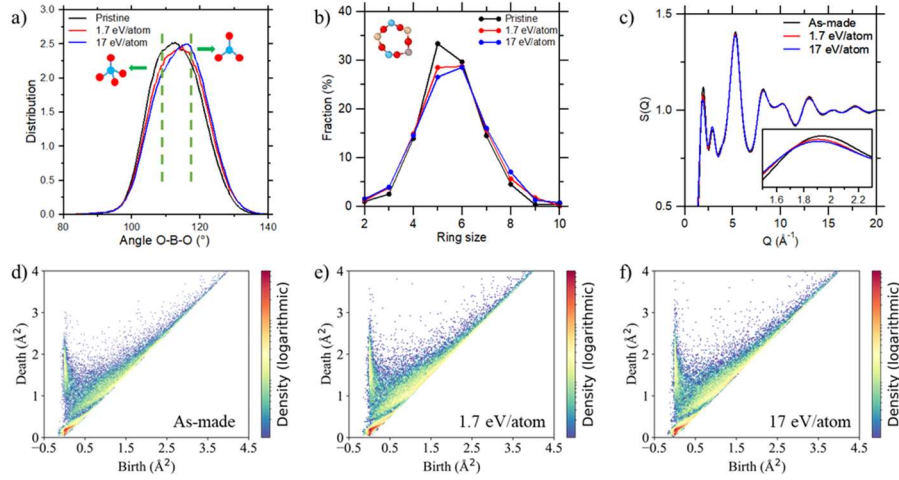


Figure 4-4. (a) Simulated O-B-O bond angle distribution, (b) ring size distribution, and (c) simulated neutron structure factor of CABS-0.4 glasses exposed to various amounts of irradiation energies, namely 0, 1.7, and 17 eV/atom. (d-f) Persistence diagrams for CABS-0.4 glass structure in (d) as-made condition and (e) 1.7 eV/atom, and (f) 17 eV/atom irradiation. Figure reproduced from Paper III.

### 4.3 EXPERIMENTAL MECHANICAL PROPERTIES

The first study is the irradiation treatment of borosilicate glass, mainly focus on the indentation test of the irradiated NBS glass, including the study of hardness and crack resistance. The study found that the hardness of the NBS glass system after irradiation decreased (Figure 4-5), and the crack resistance increased dramatically (Figure 4-6). Then followed by a related study on the irradiation post-treatment of CABS glasses. Figure 4-5 demonstrates the hardness of NBS glasses under various irradiation doses. The hardness of borosilicate glass decreases as the dose increases, with saturation at around 5.2 GPa for all borosilicate glasses. The dose required to achieve this apparent saturation is around 0.1 dpa.

Figure 4-7a shows a schematic representation of the micro-indentation technique for determining micromechanical characteristics. The hardness ( $H_v$ ), crack resistance (CR), and indentation fracture toughness ( $K_{IFT}$ ) of CABS glasses were investigated using an experimental indentation test before and after irradiation. Here, CR stands for fracture initiation resistance, and  $K_{IFT}$  stands for crack propagation resistance. Figure 4-8a shows the Young's modulus data for the as-made and irradiated CABS

glasses. The modulus of the as-made glasses was measured using ultrasonic echography, but the values were also calculated using force-depth curves based on the indentation test, because the irradiation procedure only affects the surface region ( $\sim 1.7 \mu\text{m}$ ). Although the absolute values differ between the two tests, as they mentioned for other glasses (95), the compositional trend is constant. The modulus values of the irradiated CABS glasses created by indentation reduced when compared to the as-made glasses, with a larger decrease for a higher irradiation dose. The decrease in modulus could be explained by density and structural changes. The less stiff and open structure of  $^{13}\text{B}$  could likely explain the decrease in modulus upon irradiation (96), as modulus is primarily regulated by bond strengths and the number of bonds per volume (97). Furthermore, Kieu et al. discovered that the increase of  $^{13}\text{B}$  atoms in the glass network is related to the decrease in modulus (98). As the transition from  $^{14}\text{B}$  to  $^{13}\text{B}$  occurs, more non-bridging oxygens are formed. That is, the  $\text{Ca}^{2+}$  ions that originally charged the  $[\text{BO}_4]$  groups can be converted into a network modifier that is attached to the  $\text{SiO}_4$  unit. Furthermore, based on medium-range structural changes, the creation of larger loops reduces bond density, resulting in lower modulus after irradiation (see Figure 4-8c-f).

The hardness statistics for the as-made and irradiated CABS glasses are shown in Figure 4-8b. Irradiation reduces hardness, which is consistent with prior findings for several borosilicate glasses irradiated with various ions (99). Structure investigation using Raman and MD simulations after irradiation reveals that some of the four-coordinated B atoms transition to three-coordinated B atoms.  $^{13}\text{B}$  has a more open structure, due to it doesn't require charge compensation, and it's also planar, making it easier to densify and increase its coordination number via indentation (100). According to studies, the larger the proportion of three-coordinated B, the lower the hardness (101). Plastic deformation will be accelerated as a result of the accumulation of free volume and reduction of boron coordination in tandem with the creation of non-bridging oxygen, resulting in a decrease in hardness (102).

The load dependence of hardness for the CABS-0.4 glass is shown in Figure 4-8c, with an initial reduction in hardness as the applied load increases for the as-made sample before reaching a nearly constant value. When the applied stress is increased, the irradiation sample's hardness decreases at first, then gradually increases until it achieves a constant value. Based on optical pictures of indents, we observed that the crack resistance of the irradiation glasses is larger than the as-made glasses (Figure 4-7b). In other words, the optical images for indentation under 15 N for the three irradiated CABS glasses show no breaks when compared to the as-made glasses.

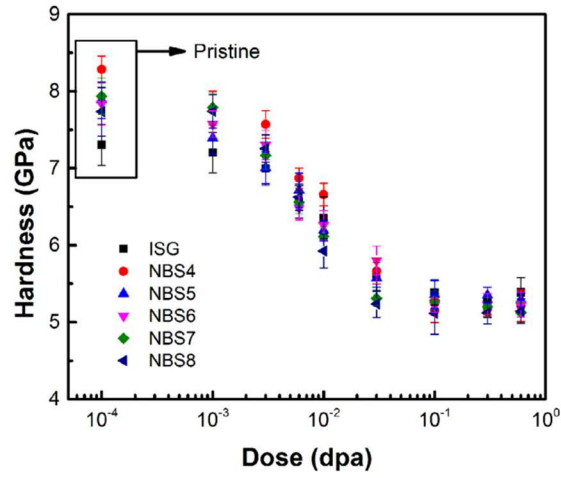


Figure 4-5: Hardness of borosilicate and ISG glasses as a function of irradiation dose. Figure adapted from Paper I.

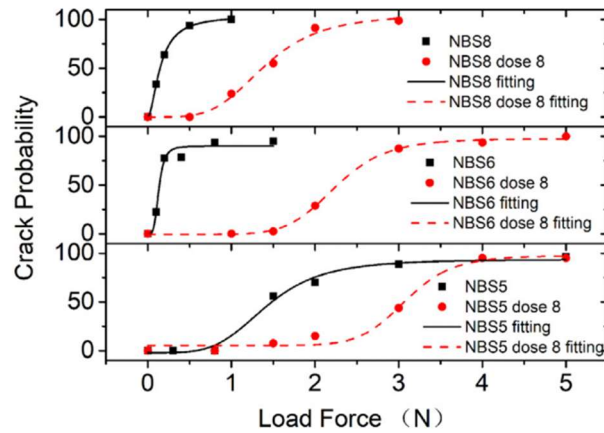


Figure 4-6: Hardness of borosilicate and ISG glasses as a function of irradiation dose. Figure adapted from Paper I.



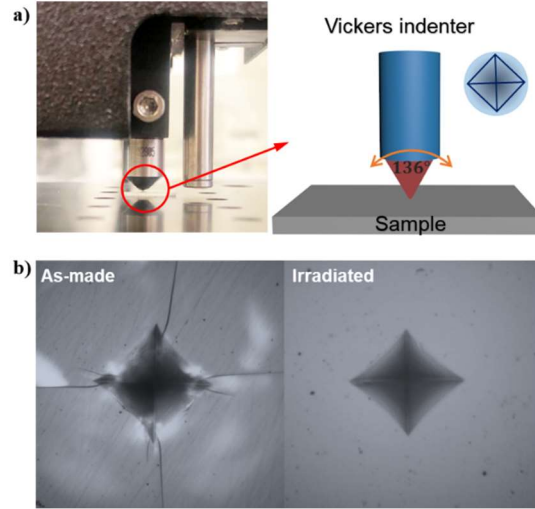


Figure 4-7. (a) Example of Vickers indentation for the CABS-0.4 glass. (b) Optical images of indents formed at 15 N on the surface of the as-made (left) and the irradiated (right) CABS-0.4 glasses, respectively. Figure reproduced from Paper III.

The crack resistance increased dramatically (Figure 4-6) for NBS glasses, the crack resistance of each type of borosilicate glass was tested at two distinct doses: pristine and 0.6 dpa. The fitting lines for the as-made and irradiated samples are solid and dashed lines, respectively. After ion irradiation, the crack resistance increases significantly, which is accompanied by a decrease in hardness. Figure 4-5d shows the fracture resistance of the as-made and irradiated CABS glasses; CR increases with irradiation. Crack resistance increased by more than 400% (from 5.6 N to 28 N) when irradiated CABS-0.75 glass was compared to as-made glass. According to the MD simulation results (Figure 4-2a), the initial CN of B in CABS-0.4 and CABS-0.75 is larger than that in CABS-0.6 before irradiation, and finally approaches a constant value in all glasses as the deposited energy increases. This indicates that the transition from  $^{[4]}B$  to  $^{[3]}B$  is more pronounced for CABS-0.4 and CABS-0.75 glasses, which is consistent with the CR change trend seen in the experiment. The radial crack's driving factor has been proven to be residual stress (103). The threshold load required to generate fractures rises as a result of the densification deformation causing less residual stress and subsurface damage.

In other words, as the amount of densification under the indenter increases, crack resistance normally increases. The significant shear deformation tendency of boron

atoms and the ease of boron coordination transition under stress, according to studies, improve crack resistance (104). The initial threefold boron content in the glass, not simply the boron content, is important for these mechanisms to work. As a result, as the four-coordinated B is changed into the three-coordinated B following irradiation, the "reversible" coordination shift of CABS under indentation serves to strengthen its crack resistance by releasing energy and reducing stress accumulation (104). In glass fracture mechanics, fracture toughness is used to quantify the stress and defect size required for fracture. As seen in Figure 4-8e, irradiation therapy raises  $K_{IFT}$ , with a larger increase for a higher irradiation dose. The fracture reaction of CBAS glasses is more ductile after irradiation, as shown in Figure 4-9a, and the stress-strain curves of three CABS glasses at uniaxial fracture are shown in Figures 4-9b–d, indicating that the nano-ductility of the irradiated materials was improved by a slower stress decrease following fracture onset. We also noted that following irradiation, the slope of the stress-strain curve in the elastic area (strain  $\epsilon < 0.05$ ) dropped, indicating that irradiation reduced stiffness. The fracture energy has also been calculated ( $G_c$ ). The  $G_c$  of CABS glass increases following irradiation, as seen in Figure 4-8f. Surprisingly, the CABS-0.4 glass exhibits the most toughening and the most evident  $^{[4]}\text{B}$  to  $^{[3]}\text{B}$  conversion after irradiation. The  $G_c$  values of all CABS glasses increase after irradiation, with the CABS-0.4 sample increasing the most from the lowest  $G_c$  value. The  $^{[4]}\text{B}$  to  $^{[3]}\text{B}$  conversion is the most substantial after irradiation in the CABS-0.4 sample, showing that the  $^{[4]}\text{B}$  to  $^{[3]}\text{B}$  conversion is responsible for the irradiation-induced nanoductility.

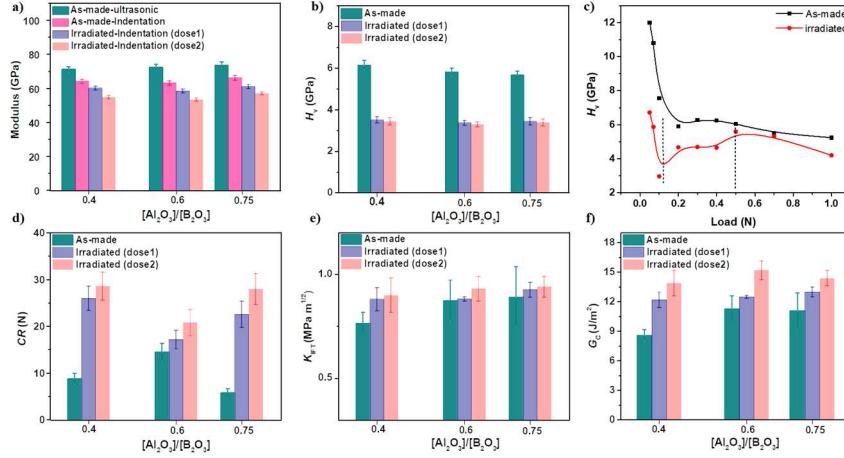


Figure 4-8. (a) Young's modulus ( $E$ ) for the as-made and irradiated CABS glasses as evaluated by ultrasonic echography or the load-depth indentation curve. Dose 1 and Dose 2 represent irradiation doses of  $2.0 \cdot 10^{13}$  ions/cm<sup>2</sup> and  $2.0 \cdot 10^{14}$  ions/cm<sup>2</sup>, respectively. (b) Vickers hardness ( $H_V$ ) for the as-made glass and irradiated glasses. (c) Hardness of the CABS-0.4 glass as a function of load. (d) Vickers indentation crack resistance (CR) of as-made and irradiated CABS glasses. (e) The indentation fracture toughness ( $K_{IFT}$ ) of the as-made and irradiated CABS glasses was evaluated using a sharp  $100^\circ$  tip. (f) Calculated fracture energy ( $G_c$ ) for the as-made and irradiated CABS glasses using  $K_{IFT}$  data. Figure reproduced from Paper III.

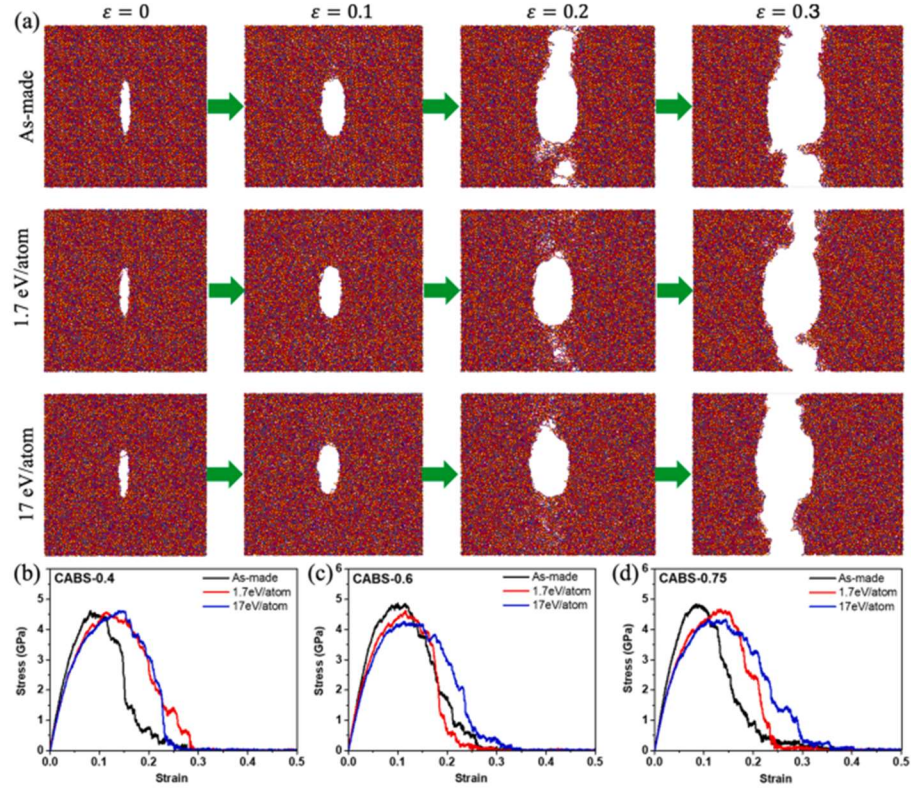


Figure 4-9. (a) Fracture evolution in pre-cracked CABS-0.4 glass at 0, 0.1, 0.2, and 0.3 tensile strains. (b-d) Stress-strain curves of CABS-0.4, CABS-0.6, and CABS-0.75 glasses exposed to various irradiation energies (0, 1.7, and 17 eV/atom). Figure reproduced from Paper III.

#### 4.4 SUMMARY

In this research, we used both experimental measurements and MD simulations to evaluate the relationship between structure and mechanical properties in CABS glasses exposed to irradiation in this study. The boron speciation shifts from  $^{[4]}\text{B}$  to  $^{[3]}\text{B}$ , which leads to a more open structure with enhanced disorder at the medium-range length scale, are found to be the principal cause of irradiation-induced structure alterations in CABS glasses. We evaluated the relationship between structure and mechanical properties in CABS glasses exposed to irradiation in this research using both experimental measurements and MD simulations. Irradiation-induced structure changes in CABS glasses are shown to be mostly caused by boron speciation shifts from  $^{[4]}\text{B}$  to  $^{[3]}\text{B}$ , which results in a more open structure with enhanced disorder at the medium-range length scale. CABS glasses having a higher initial fraction of

tetrahedral boron units are thus more vulnerable to irradiation-induced structural changes. After irradiation, the modulus and hardness of the glass surface layers decrease, while crack resistance increases dramatically. When irradiation CABS-0.75 glass was compared to as-made glass, crack resistance rose by more than 400%. Furthermore, as the applied stress was raised during indentation, the hardness of the specimen first declined, then increased somewhat, and ultimately reached a constant value. This could possibly be due to the decreased hardness of the irradiated layer. Furthermore, both experimental and modeling results show that irradiation increases fracture energy, which leads to increased nanoductility in irradiated structures. Irradiation-induced nanoductility is connected to changes in medium-range structure, which makes it easier for Al and B atoms to flip bonds. Surprisingly, the CABS glass composition with the greatest increase in CR and  $K_{IFT}$  had the most  $^{[4]}B$ -rich structure, making it more vulnerable to structural reorganization following irradiation.

## CHAPTER 5. GLASS HYDRATION BY WATER ADDITION

In this research, chemical diversity in hybrid organic-inorganic glasses is still a challenge and new hybrid glasses are often modifications of similar structures, which limits their usefulness.

The inclusion of so-called modifiers (e.g. alkali oxides) breaks the continuous network structure of the pure network-forming oxide, resulting in non-bridging oxygens, i.e. oxygens that will only covalently connect to one metal node. This is an often exploited fact concerning oxide glasses. This will usually result in considerable changes in thermal and mechanical properties, such as decreased melting temperatures and glass transition temperatures. This diversity, which is a result of the modifiers, is one of the main reasons for the wide range of uses of oxide glasses. Such modifiers have never been seen before in any hybrid glasses. However, in this work we present the first evidence of modifier behaviour using water in a cobalt-based bis-acetamide hybrid coordination network glass (HCNG) of composition  $\text{Co}(\text{hmba})_3[\text{CoBr}_4]$  where hmba: N,N'-1,6 hexamethylenebis(acetamide). We chose this system due to its large water sensitivity. Specifically, while this glass is fully water soluble, careful water addition results in significant alteration of physical properties including the melting and glass transition temperatures. In this study, we also illustrate how water may be used to exploit labile metal-ligand connections in a cobalt-based coordination network to produce a succession of non-stoichiometric glasses. We explain how water added to a cobalt-based hybrid coordination network enhances breaking of cobalt-oxygen bonds and depolymerizes the resulting glass network by using calorimetric, spectroscopical, and simulation results, as evidenced by significant decreases in melting and glass transition temperatures. Furthermore, the physical and chemical properties of the resulting glass are changed, drawing parallels with the "modifier" in oxide glass chemistry, where additives are frequently used to adjust properties.

### 5.1 INVESTIGATED GLASS SYSTEMS

Based on the previous study, we selected the  $15\text{CaO}-15\text{Al}_2\text{O}_3-25\text{B}_2\text{O}_3-45\text{SiO}_2$  (called CABS-ref) glass (66) as the reference composition for research on humid treatment because it had the best crack initiation resistance and it was interesting to see if it could be improved further. CABS-SiB (Si/B increase), CABS-CaB (Ca/B increase), CABS-BAl (B/Al increase), CABS-CaSi (Ca/Si increase), and CABS-CaAl (Ca/Al increase) were the five systematic composition modifications tested, as shown and mentioned in Table 3-1. The mechanical properties of the six glasses were assessed

after they were subjected to humid aging, which is the research that water as “modifier” affects the properties of oxide glass.

Based on previous research, In this work, we illustrate how water addition can be used to exploit labile metal-ligand linkages in a cobalt-based coordination network to produce a series of non-stoichiometric glasses. Although distinct from the other glass families, the hybrid glasses have structural similarities to network glasses, such as oxides, due to the way metallic nodes (typically Si, Ge, and P for oxides; transition metals for hybrids) are bridged in the oxide and hybrid cases, respectively, by single oxygens and large organic linkers. For the metal-organic network, we offer the first evidence of water as a modifier in a cobalt-based bis-acetamide hybrid coordination network glass (HCNG) with the composition  $\text{Co}(\text{hmba})_3[\text{CoBr}_4]$ , where hmba is N,N'-1,6 hexamethylenebis-acetate (acetamide) (105). This system is made up of octahedral  $\text{Co}^{2+}$  nodes coupled by weak coordination bonding through uncharged hmba structures in a 2D layer-like structure, with non-interconnected charge compensating  $\text{Co}[\text{Br}_4]^{2-}$  units between network layers. Due to its large water sensitivity we also select this system. The unit cell structure of  $\text{Co}(\text{hmba})_3[\text{CoBr}_4]$  is shown in Figure 5-1a, and different highlights have been given to the unit cell in Figure 5-1b, namely: 1) the layer-like percolating network of Co and hmba-linkers, and 2) the interpenetrating  $[\text{CoBr}_4]^{2-}$  tetrahedra are found in the multilayer network's voids. After producing crystals, the crystals were filtered, washed with anhydrous diethyl ether, and then dried on the filter by allowing more  $\text{N}_2$  suction (see Figure 5-2a).

While the melt formation and subsequent quenching into a glassy state for  $\text{Co}(\text{hmba})_3[\text{CoBr}_4]$  (see example picture of molten  $\text{Co}(\text{hmba})_3[\text{CoBr}_4]$  in Figure 5-2) and other bis-acetamide-containing HCNGs have been described previously, we have discovered that the system's properties are highly sensitive to the water content.

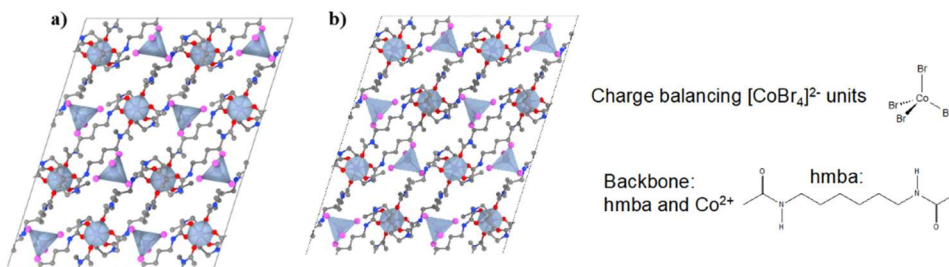


Figure 5-1 (a) Unit cell of crystalline  $\text{Co}(\text{hmba})_3[\text{CoBr}_4]$  with highlights of Co-tetra- and octahedra, which are shaded in grey, while atomic colors represent nitrogen (blue), carbon (grey), oxygen (red), and bromine (pink). Hydrogens are omitted for clarity. (b) The  $\text{Co}(\text{hmba})_3[\text{CoBr}_4]$  structure overlaid with highlights showing how  $\text{Co}^{2+}$  and hmba serve as the network part of the structure while  $[\text{CoBr}_4]^{2-}$ -tetrahedra are positioned between the layers within the network. Figure reproduced from Paper IV.

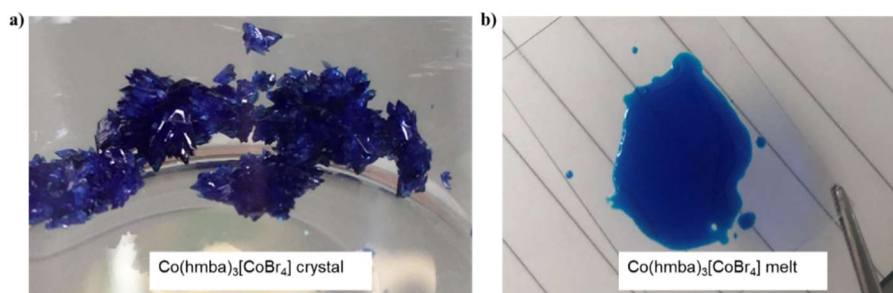


Figure 5-2. (a) crystal sample after 1-2 weeks of drying, forming  $\text{Co}(\text{hmba})_3[\text{CoBr}_4]$ . (b) A transparent microscope glass slide with molten  $\text{Co}(\text{hmba})_3[\text{CoBr}_4]$ . The distance between the lines is 9 mm. Figure reproduced from Paper IV.

## 5.2 HYDRATION OF GLASS

In the thesis,  $\text{Co}(\text{hmba})_3[\text{CoBr}_4]2\text{EtOH}$  crystals were synthesized using the technique described in Refs. (106) The crystals were filtered, then washed in anhydrous diethyl ether before being dried on the filter by sucking in more  $\text{N}_2$ . These crystals are structurally identical to the  $\text{Co}(\text{hmba})_3[\text{CoBr}_4]2\text{EtOH}$  crystals produced by previous researchers. The  $\text{Co}(\text{hmba})_3[\text{CoBr}_4]2\text{EtOH}$  structure was observed to spontaneously release the bound EtOH molecules during storage at just above room temperature and high vacuum, similar to prior studies (see Figure 5-2a). X-ray diffraction investigation (Figure 5-3) confirmed both crystalline structures, but a glassy sample of the



unhydrated glass was found to be amorphous (Figure 5-3). All crystals were kept in a desiccator or at slightly higher temperatures (40 °C) and vacuum (<10 mbar). Thermal analysis was carried out utilizing hermetically sealed Al pans and a TA Q2000 differential scanning calorimeter (DSC). Each scan employed around 5 mg of  $\text{Co}(\text{hmba})_3[\text{CoBr}_4]$  with different volumes of water (ranging from 0-0.8  $\mu\text{L}$  of deionized water). Based on this, we could perform DSC testing during glass formation with different water contents and explored the effect of hydration on glass formation, including glass transition temperature ( $T_g$ ) and melting point.

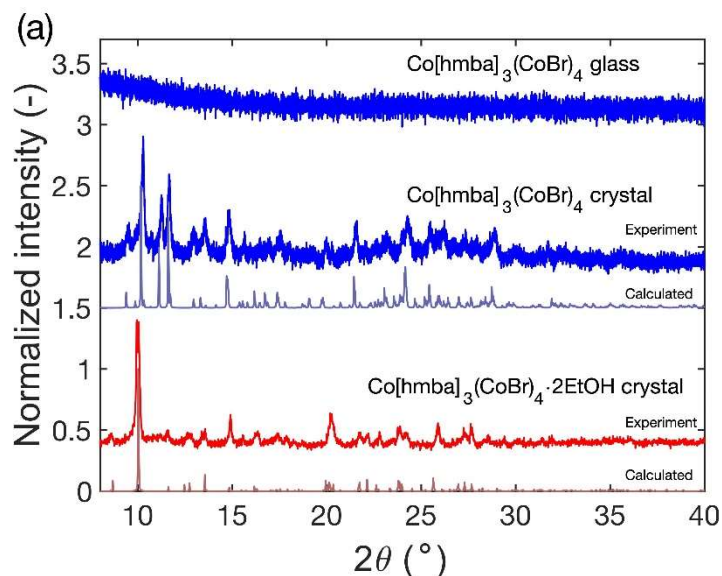


Figure 5-3. X-ray diffraction patterns of synthesized ethanol-containing crystals and subsequent dried crystals of compositions  $\text{Co}(\text{hmba})_3[\text{CoBr}_4] \cdot 2\text{EtOH}$ ,  $\text{Co}(\text{hmba})_3[\text{CoBr}_4]$ , as well as glassy  $\text{Co}(\text{hmba})_3[\text{CoBr}_4]$ . Figure reproduced from Paper IV.

### 5.3 STRUCTURE CHANGES FOR GLASS

For the  $\text{Co}(\text{hmba})_3[\text{CoBr}_4]$ , following thermal characterization, we used a range of spectroscopic approaches to analyze the pure and water-containing HCNGs. We probed the UV-visible absorption spectra of the pristine and hydrated glasses and display normalized spectra of these in Figure 5-4a. A broad band at 6-700 nm exists for all samples in the visible absorption spectrum shown in Figure 5-4a. We believe that the crystal field splitting in  $[\text{CoBr}_4]^{2-}$ , where  $\text{Br}^-$  ligands are tetrahedrally coupled

to Co-centres, is the source of this absorption band because: 1)  $\text{Br}^-$  is in the lowest splitting region of the spectrochemical series, and 2) lower coordination is known to promote lower splitting. Due to its projected larger splitting and higher coordination state, the octahedral Co surrounded by carbonyls would be expected to have absorption at lower wavelengths (i.e., higher energies). According to the preceding theories, only the Co-hmba network is reorganized during melt quenching, whereas the charge compensating  $[\text{CoBr}_4]^{2-}$  remains stable in both pristine and hydrated glasses.

We used finite temperature *ab initio* molecular dynamics of the  $\text{Co}(\text{hmba})_3[\text{CoBr}_4]$  system as well as  $\text{Co}(\text{hmba})_3[\text{CoBr}_4]\cdot n\text{Water}$  to answer these and other key concerns about the melting mechanism of the examined HCNGs. To compute the mean square displacement (MSD, see Figure 5-4b of the Co MSD as a function of temperature) as a measure of the system's solid-like behavior, we first initiated dynamics of the pristine structure as acquired from its CIF file at temperatures of 500, 1000, and 1500 K. The Lindemann ratio of the Co-O bonds (107) (i.e., the ratio of the calculated amplitude of the atomic vibrations divided by the bond length) [29,30], as shown in the inset of Figure 5-4b, shows an increasing trend from 0.10 to 0.18 when the temperature is increased from 500 to 1500 K.

Next, using the coordination numbers (CNs) of the two separate Co-centres, we would like to learn more about the melting transition in HCNGs (i.e., the Co-O and Co-Br CNs). We do so by running new 1000 K simulations, but instead of just using anhydrous glass, now adding one, two, or three water molecules to the unit cell before starting the dynamics. We discover that the Co-O and Co-Br correlations' coordination number changes are significantly different (Figures 5-4c and 5-5, respectively).

Within the first 10 ps, the CN of the Co-O centres (i.e., the network percolating species) drops dramatically from 6 to 4. (Figure 5-4c). Furthermore, the presence of water appears to accelerate this fall in CN, as evidenced by the rapid initial decrease in CN in the first picosecond of the simulations with the most water. Simultaneously, the Co-Br centers see only modest deviations from the ideal four-coordinated state due to the high temperature, but deviations rapidly develop as time passes to re-establish the tetrahedral state, regardless of water concentration (Figure 5-5).

When one water molecule moves inside the structure during the heating process at 1000 K (Figure 5-4d), it appears to search multiple parts of the structural space, approaching both the Co-O octahedra and the Co-Br tetrahedra, but not fully approaching either Co-centres or actually replacing the bromide ions or the oxygens in hmba. We may provide a sketch of a potential HCNG melting mechanism using the approaches outlined, as shown in Figure 5-6. First, for the heating process of an anhydrous  $\text{Co}(\text{hmba})_3[\text{CoBr}_4]$  system, the labile bonds between Co and hmba (i.e., the Co-O bonds) tend to break, increasing the total connectedness of the system and eventually causing it to melt. This will be accompanied by certain tetrahedral Co-Br

structures within the network splitting. Water will often speed up this process and result in a more depolymerized network. More specifically, our findings imply that water can efficiently rearrange and replace the oxygens in hmba to form dangling organic motifs, lowering the glass transition temperature from 16 °C to -15 °C for fully polymerized and fully depolymerized glass structures, respectively.

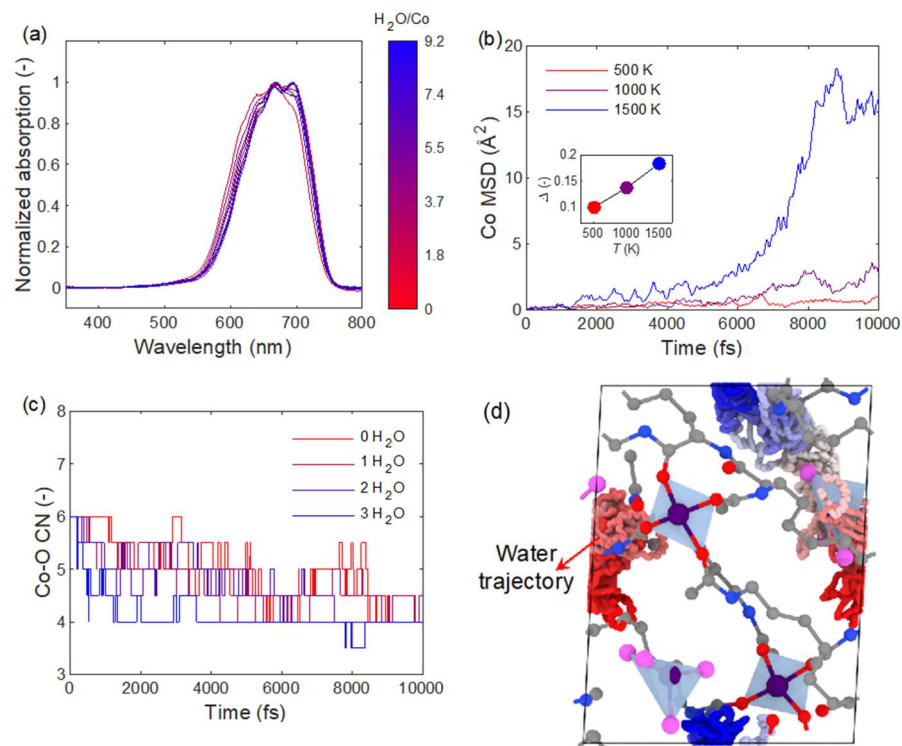


Figure 5-4. (a) Normalized visible absorption spectra of HCNGs with varying water content as indicated by the colorbar. (b) Mean square displacement (MSD) of Co atoms in the simulations of the Co(hmba)<sub>3</sub>[CoBr<sub>4</sub>] system at 500, 1000, and 1500 K. The inset shows the Lindemann ratio of the Co-O bonds ( $\Delta$ ) at the three studied temperatures. (c) Average coordination numbers (CN) of the Co-O correlation in structures containing 0, 1, 2, or 3 water molecules. (d) Trace of one water molecule's trajectory over 10 ps of simulation time at 1000 K with blue being the starting point and red being the ending point. The final picture depicts the remaining part of the structure. Figure reproduced from Paper IV.

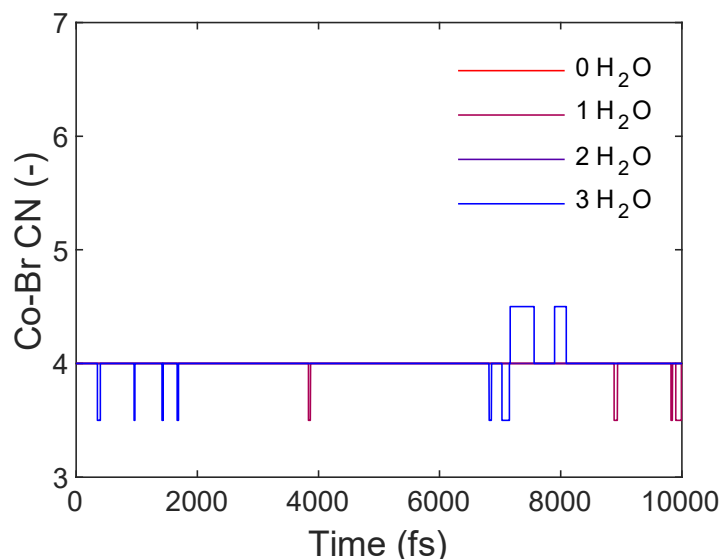


Figure 5-5. Co-Br coordination numbers of Co atoms initially surrounded by Br atoms during the simulated time range as well as for simulations of 0, 1, 2, and 3 water molecules at 1000 K. Figure reproduced from Paper IV.

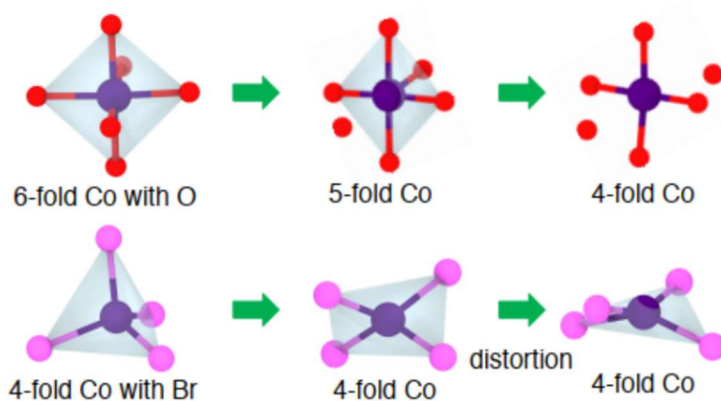


Figure 5-6. Sketch of the suggested melting and glass-forming mechanism. Figure reproduced from Paper IV.

## 5.4 WATER EFFECT THE PROPERTIES FOR GLASS

In this thesis, we explored the effect of hydration on glass properties. Figure 5-7a shows how the melting transition broadens and ends at much lower temperatures when water is added (right of Figure 5-7a), while the glass transition temperature decreases significantly (left portion of Figure 5-7a). Figure 5-7b shows a plot of the melting and glass transition temperatures ( $T_m$  and  $T_g$ , respectively) as a function of water content. At a water concentration of ~15 wt%, the melting temperature drops from over 110 °C to a stable value of ~70 °C as the water concentration increases. This effect is performed in such a way that both transition temperatures decrease dramatically after the first addition of water, then level out. For the maximum water content, a decline from a pristine value of 16 °C to -15 °C is found for the glass transition temperatures (i.e., 9 water molecules for per bridging-Co). There is a large initial decrease followed by stabilization for both  $T_m$  and  $T_g$ . The  $T_m$  and  $T_g$  levels off at 3-4 water molecules for per bridging-Co, according to the results. This is significant because it is equal to the bridging-Co to hmbsa ratio in the system, implying that there is one water molecule for per hmbsa linker. Given the chemical environment of the percolating network, which consists of Co-nodes connected by bidentate hmbsa-linkers via Co-O coordination bonds, monodentate water appears to be a viable replacement for the bridging carbonyl oxygens around the Co-centers. The  $[\text{CoBr}_4]^{2-}$  tetrahedra will remain intact, and a fully depolymerized network of Co will be surrounded by a dispersion of hmbsa-linkers and water molecules. This would eventually approximate a water modifier behavior in an HCNG-something that has yet to be explained for hybrid glasses but is quite frequent in the oxide glass family.

While a decrease in  $T_g$  (and  $T_m$ ) is to be expected with the addition of water (and subsequent depolymerization), the magnitude of the decrease is of particular importance. The lowered glass transition temperature is a way to compare the drop in  $T_g$  after adding water in this case. Figure 5-7c shows a plot of  $T_g^*$  as a function of water content for the examined HCNGs as well as a variety of silicates, organic sugars, and polymers (108). We could find that water addition has a substantial effect on inorganic silicates and certain polymers, which can reduce their  $T_g$  by approximately 50% when adding 10-15wt% of water. This is in contrast to the majority of sugars and polymers, as well as the examined HCNGs, which only experience moderate (~10-15%) reductions in  $T_g$  in the same water concentration range. However, when water is added, HCNGs appear to have a more converging  $T_g$  than other systems, which is likely related to the fact that water greatly outnumbered bridging Co atoms at low water concentrations (5-10 wt%). Eventually, a glassy system emerges that is controlled by weak long-range cohesive forces rather than the Co-hmbsa network.

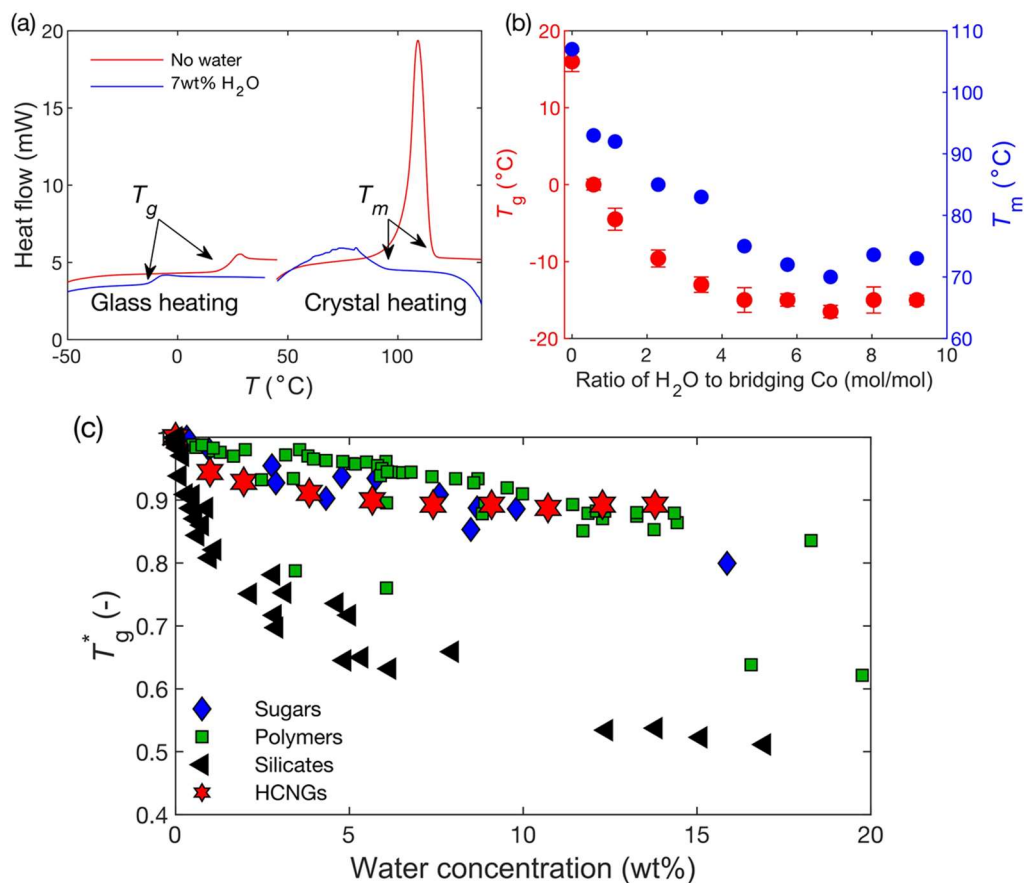


Figure 5-7. (a) Differential scanning calorimetry upscans of crystalline (right) and glassy (left)  $\text{Co}(\text{hmba})_3[\text{CoBr}_4]$  with and without added water. (b) Melting and glass transition temperatures ( $T_m$  and  $T_g$ , respectively) of the  $\text{Co}(\text{hmba})_3[\text{CoBr}_4]$  as a function of the  $\text{H}_2\text{O}$  to bridging Co (i.e., Co atoms bonding to hmba linkers) ratio. (c) Reduced glass transition temperature of the  $\text{Co}(\text{hmba})_3[\text{CoBr}_4] \cdot \text{water}$  glasses at various water concentrations as well as for a variety of sugars, organic polymers, and silicate glasses as obtained from Refs.<sup>112,113</sup>. Figure adapted from Paper IV.

## 5.5 SUMMARY

In this chapter, we demonstrated how a cobalt-based hybrid coordination network crystal is an excellent glass forming that can be greatly decreased in melting point and

glass transition temperature by adding water. We demonstrated how water promotes the disintegration of the internal network of  $\text{Co}^{2+}$  ions and bis-acetamide organic linkers whereas  $\text{Co}[\text{Br}_4]^{2-}$  centers stay relatively intact using calorimetric, spectroscopic, and computational methods. The former is most likely achieved by substituting the organic ligand's labile Co-O bonds with coordination to water molecules. This mechanism is similar to the impact of water and other network "modifiers" in the field of oxide glasses, where such structural alteration is a common scientific and practical application. As a result, our findings could pave the way for a major expansion of glass-forming hybrid systems, as well as significant chemical non-stoichiometric diversification, besides, this also provides a reference and approach for the improvement of the properties of glasses.

## CHAPTER 6. CONCLUSION AND PERSPECTIVES

We will briefly review the main findings and their potential implications, as well as explore viewpoints and proposals for future research in this chapter.

### 6.1. CONCLUSION

In this thesis, we explore the mechanical properties of a variety of glasses with various compositions and subject them to various post-treatments, such as hot compression, irradiation, and hydration. We also explored the structure and properties of MOF glass, as well as the use of water as a modifier to modify the glass's properties. Furthermore, this alters the physical and chemical properties of the resulting glass, and thus bears a strong resemblance to the idea of "modifiers" in oxide glass chemistry. This approach will eventually enable the diversification of hybrid glass chemistry, fine-tuning of physical and chemical properties, and significantly extend the number of glass-forming hybrid systems.

Changes in chemical composition and post-treatments are well-known methods for fine-tuning glass structure and properties of glass. In this study, we designed glass with different compositions to study the effect of composition on its structure and mechanical properties, and also performed a series of post-treatments to explore its indentation response and changes in mechanical properties. The application of pressure allows precise tuning of interatomic distances and bonding patterns in a material, which makes glass densification under high pressure (109) a new alternative. More importantly, to better understand the densification-structure-property relationship of glass, the effect of diverse densification environments (i.e., different densification routes) during autoclaving is investigated. Therefore, in this study, the hot compression of SNAB and NAB glasses under different conditions was mainly introduced, and the effects of different pressure, temperature and time routes on the densification behavior of oxide glasses were investigated. According to the investigation and test of its structure and mechanical properties, we found that the influence after hot compression is also related to the composition. The study also discovered that the impact of densification along various paths on the structure and mechanical properties of these two glasses is constant. The rise in the coordination number of B and Al after densification is the fundamental structural alteration. In terms of mechanical properties, it has been discovered that after densification, hardness increases and crack resistance decreases; additionally, the effects and changes are related to the conditions (pressure, temperature, time); it has been discovered that the degree of densification and pressure are positively correlated. Our investigation of the effect of different routes on densification provides a foundation



and important reference for the study and analysis of densification behavior under different routes.

What is more, in this research, we also used both experimental measurements and MD simulations to evaluate the relationship between structure and mechanical properties in CABS glasses exposed to irradiation. Irradiation-induced structure changes in CABS glasses are shown to be mostly caused by boron speciation shifts from  $^{[4]}\text{B}$  to  $^{[3]}\text{B}$ , which results in a more open structure with increased disorder at the medium-range length scale. Furthermore, both experimental and modeling results reveal that irradiation enhances fracture energy, resulting in increased nanoductility in the irradiated structures. Nanoductility caused by irradiation is connected to alterations in medium-range structure, which makes it easier for Al and B atoms to flip bonds.

Finally, in this chapter, we explored the structure and properties of MOF glass, as well as the explore of water as a modifier to modify the glass's properties, we also show that how cobalt-based hybrid coordination network crystals can be an excellent glass-forming material, the melting point and glass transition temperature can be considerably lowered by adding water, and the influence of water on its structure and properties has also been explored. Experiments and simulations suggest that water facilitates the breaking of network-forming Co-O bonds, allowing for the tuning of glass properties within this glass family and, eventually, the tuning of melting temperatures of other hybrid crystals, allowing for a dramatic increase in the number of meltable, and thus glass-forming, hybrid systems. Therefore, our findings could pave the way for a major expansion of glass-forming hybrid systems and significant stoichiometric diversification. Furthermore, this alters the physical and chemical properties of the resulting glass, this approach will eventually enable the diversification of hybrid glass chemistry, fine-tuning of physical and chemical properties, moreover, provide references and methods for improving the mechanical properties of oxide glasses, and also significantly extend the number of glass-forming hybrid systems.

## 6.2. PERSPECTIVE

Improving the fracture toughness and strength of glass materials is increasingly relevant for a range of applications where brittleness and surface defect propensity are still limiting factors. Here, we describe how a combination of custom chemistry and irradiation post-treatment improved the mechanical properties of glass. In this thesis, we have understood the structural origin and related properties of glass deformation behavior and cracking behavior through compositional design and post-processing methods such as densification, irradiation and hydration, and also explore the improvement of mechanical properties of glass by post-treatment, but the following research topics still require further research. Densification and structural changes (rearrangement of the short- and medium-range structure, which can dissipate the energy of the applied load) are known to occur during the deformation process under

acute contact loading. In this research, we study the glass deformation and cracking behavior, as well as how post-treatment affects the glass structure and mechanical properties.

At the same time, we also find that the influencing factors of mid-range structural rearrangements is needed to gain a better understanding of changes in structure, not just coordination number. As a result, the glass cracking behavior can be predicted more extensively and precisely. We also show how cobalt-based hybrid coordination network crystals can be excellent glass-forming materials, and also investigate the effect of water on their structure and properties, which can greatly reduce the melting point and glass transition temperature.

Based on the above research and results, for future work, the influence of different components on glass properties will be further explored. Based on the research on MOF glass in this paper, composite materials of MOF glass with different compositions can be prepared, such as MOF glass-crystal composites. Different types and contents of crystals will be selected to prepare Co-MOF glass-crystal composites. The main purpose is to study the impact of these different crystals on the material structure and properties. We will also explore the impact of water on glass formation and structure-properties, explore new hybrid glass systems, and provide more references for extending hybrid glass systems. Secondly, we also can try to improve the mechanical properties of the oxide glass by post-treatment, such as post-treatment of the glass by combining irradiation and hot compression to explore the changes of its mechanical properties. This can provide a great reference for improving the properties of glass.

## BIOGRAPHY

1. L. Wondraczek, J.C. Mauro, J. Eckert, U. Kühn, J. Horbach, J. Deubener, T. Rouxel, Towards ultrastrong glasses, *Adv. Mater.* 2011;23:4578.
2. E. D. Zanotto, F. A. B. J. Coutinho, How many non-crystalline solids can be made from all the elements of the periodic table? *Non-Cryst. Solids.* 2004; 347:285.
3. Mauro, J.C., Tandia, A., Vargheese, K.D., Mauro, Y.Z., Smedskjaer, M.M. Accelerating the design of functional glasses through modeling. *Chem. Mater.* 2016;28:4267-4277.
4. Tatumisago, M., Morimoto, H., Yamashita, H., Minami, T. Preparation of amorphous solid electrolytes in the system  $\text{Li}_2\text{S}-\text{SiS}_2-\text{Li}_4\text{SiO}_4$  by mechanical milling. *Solid State Ion.* 2000;136-137:483-488.
5. Guerette, M., Ackerson, M.R., Thomas, J., Yuan, F., Watson, E.B., Walker, D., Huang, L. Structure and properties of silica glass densified in cold compression and hot compression. *Sci. Rep.* 2015; 5:15343.
6. Svenson, M.N., Bechgaard, T.K., Fuglsang, S.D., Pedersen, R.H., Tjell, A.Ø., Østergaard, M.B., Youngman, R.E., Mauro, J.C., Rzoska, S.J., Bockowski, M. Composition-Structure-Property Relations of Compressed Borosilicate Glasses. *Phys. Rev. Appl.* 2014;2:024006.
7. Striepe, S., Smedskjaer, M.M., Deubener, J., Bauer, U., Behrens, H., Potuzak, M., Youngman, R.E., Mauro, J.C., Yue, Y. Elastic and micromechanical properties of isostatically compressed soda-lime-borate glasses. *J. Non-Cryst. Solids* 2013;364:44-52.
8. Koch, C.C. Amorphization of single composition powders by mechanical milling. *Scr. Mater.* 1996;34:21-27.
9. Fukunaga, T., Kajikawa, S., Hokari, Y., Mizutani, U. The structure of amorphous Se-S prepared by mechanical alloying. *J. Non-Cryst. Solids* 1998;232-234:465-469.

10. Esaka, T., Takai, S., Nishimura, N., Kagaku, D. Preparation of the Bi<sub>2</sub>O<sub>3</sub>-based Fluorite-type solid solutions by mechanical alloying. *Denki Kagaku* 1996;64:1021.
11. M. M. Smedskjaer, S. J. Rzoska, M. Bockowski, J. C. Mauro, Mixed alkaline earth effect in the compressibility of aluminosilicate glasses, *J. Chem. Phys.* 2014;140:054511.
12. C.M. Jantzen, D.I. Kaplan, N.E. Bibler, D.K. Peeler, M. JohnPlodinec, Performance of a buried radioactive high level waste (HLW) glass after 24 years, *J. Nucl. Mater.* 2008;378:244.
13. L. Chen, W. Yuan, S. Nan, X. Du, D. F. Zhang, P. Lv, H. B. Peng, T. S. Wang, Study of modifications in the mechanical properties of sodium aluminoborosilicate glass induced by heavy ions and electrons, *Methods Phys. Res., Sect. B* 2016;370:42.
14. S. Peugeot, P. Y. Noël, J. L. Loubet, S. Pavan, P. Nivet, A. Chenet, Effects of deposited nuclear and electronic energy on the hardness of R7T7-type containment glass, *Methods Phys. Res., Sect. B* 2006;246:379.
15. J. de Bonfils, S. Peugeot, G. Panczer, D. d. Ligny, S. Henry, P. Y. Noël, A. Chenet, B. Champagnon, Effect of chemical composition on borosilicate glass behavior under irradiation, *J. Non-Cryst. Solids* 2010;356:388.
16. Madsen, R. S. K.; Qiao, A.; Sen, J.; Hung, I.; Chen, K.; Gan, Z.; Sen, S.; Yue, Y. Ultrahigh-Field <sup>67</sup>Zn NMR Reveals Short-Range Disorder in Zeolitic Imidazolate Framework Glasses. *Science*. 2020;367 (6485):1473-1476.
17. Liu, M.; McGillicuddy, R. D.; Vuong, H.; Tao, S.; Slavney, A. H.; Gonzalez, M. I.; Billinge, S. J. L.; Mason, J. A. Network-Forming Liquids from Metal-Bis(Acetamide) Frameworks with Low Melting Temperatures. *J. Am. Chem. Soc.* 2021.
18. Rosales-Sosa, G.A.; Masuno, A.; Higo, Y.J.; Inoue, H. Crack-resistant Al<sub>2</sub>O<sub>3</sub>-SiO<sub>2</sub> glasses. *Sci. Rep.* 2016;6:23620.
19. Januchta, K.; Youngman, R.E.; Goel, A.; Bauchy, M.; Logunov, S.L.; Rzoska, S.J.; Bockowski, M.; Jensen, L.R.; Smedskjaer, M.M. Discovery of ultra-crack-resistant oxide glasses with adaptive networks. *Chem. Mater.* 2017; 29:5865-5876.

20. W.C. Oliver, G.M. Pharr, An improved technique for determining hardness and elastic modulus using load and displacement sensing indentation experiments, *J. Mater. Res.* 1992;7:1564-1583.
21. E.W. Taylor, Plastic deformation of optical glass, *Nature* 1949; 163:323.
22. R.W. Douglas, Some comments on indentation tests on glass, *J. Soc. Glas. Technol.* 1958;42:145-157.
23. D.M. Marsh, Plastic flowing lass, *Proc. R. Soc. A Math. Phys. Eng. Sci.* 1964;279:420-435.
24. K. Peter, Brittle fracture and microplasticity of glass in indentation experiments, *Glastech. Ber.* 1964;37:333-345.
25. M. Evers, Plastic deformation of glass with diamond indenters, *Glastech. Ber.* 1967;40:41-43.
26. P.W. Bridgman, I. Simon, Effects of very high pressures on glass, *J.Appl.Phys.* 1953;24:405-413.
27. P.W. Bridgman, The effect of pressure on the tensile properties of several metals and other materials, *J. Appl. Phys.* 1953;24: 560-570.
28. F.M. Ernsberger, Role of densification in deformation of glasses under point loading, *J. Am. Ceram. Soc.* 1968;51:545-547.
29. J. D. Mackenzie, High-pressure effects on oxide glasses: II, subsequent heat treatment, *J. Am. Ceram. Soc.* 1963;46:470-476.
30. J. E. Neely, J. D. Mackenzie, Hardness and low-temperature deformation of silica glass, *J. Mater. Sci.* 1968;3:603-609.
31. K. W. Peter, Densification and flow phenomena of glass in indentation experiments, *J. Non-Cryst. Solids* 1970;5:103-115.
32. A. Arora, D. B. Marshall, B. R. Lawn, M. V. Swain, Indentation deformation/fracture of normal and anomalous glasses, *J. Non-Cryst. Solids* 1979;31:415-428.
33. J. T. Hagan, Shear deformation under pyramidal indentations in soda-lime glass, *J. Mater.Sci.* 1980;15:1417-1424.

34. R. Chakraborty, A. Dey, A. K. Mukhopadhyay, Loading rate effect on nanohardness of soda-lime-silicaglass, *Metall. Mater. Trans. A* 2010;41:1301-1312.
35. S.Yoshida,J.-C.Sangleboeuf, T.Rouxel, Quantitativeevaluationofindentation-induceddensificationin glass, *J.Mater.Res.* 2005;20:3404-3412.
36. T.Rouxel, J.-C.Sangleboeuf, C.Moysan,B.Truffin,Indentationtopometryin glassesbyatomicforcemicroscopy, *J.Non-Cryst.Solids* 2004;344:26-36.
37. C.A.Angell, Formationofglassesfromliquidsandbiopolymers, *SourceSci. New Ser.* 1995;267:924-1935. Accessed date:26 July 2017.
38. P. Sellappan, T. Rouxel, F. Celarie, E. Becker, P. Houizot, R. Conradt, Composition dependence of indentation deformation and indentation cracking in glass, *Acta Mater.* 2013;61:5949-5965.
39. Y.-F. Niu, K. Han, J.-P. Guin, Locally enhanced dissolution rate as a probe for nanocontact-induced densification in oxide glasses, *Langmuir* 2012;28:10733-10740.
40. T.M. Gross, J. Wu, D.E. Baker, J.J. Price, R. Yongsunthon, *J. Non-Cryst. Solids* 2018;494:13-20.
41. D.A. Kilymis, J. -M. Delaye, *J. Non-Cryst. Solids* 2014;401:147-153.
42. T.K. Bechgaard, J.C. Mauro, M.M. Smedskjaer, Time and humidity dependence of indentation cracking in aluminosilicate glasses, *J. Non-Cryst. Solids* 2018;491:64-70.
43. Kacper Januchta, Malwina Stepniewska, Lars R. Jensen, Yang Zhang, Marcel A. J. Somers, Mathieu Bauchy, Yuanzheng Yue, Morten M. Smedskjaer, Breaking the limit of micro-ductility in oxide glasses, *Adv. Sci.* 2019;6: 1901281.
44. A. Pönitzsch, M. Nofz, L. Wondraczek, J. Deubener, Bulk elastic properties, hardness and fatigue of calcium aluminosilicate glasses in the intermediate-silica range, *J. Non-Cryst. Solids* 2016;434:1-12.
45. Y. Kato, H. Yamazaki, S. Yoshida, J. Matsuoka, Effect of densification on crack initiation under Vickers indentation test, *J. Non-Cryst. Solids* 2010;356:768-1773.

46. Y. Kato, H. Yamazaki, Y. Kubo, S. Yoshida, J. Matsuoka, T. Akai, Effect of  $B_2O_3$  content on crack initiation under Vickers indentation test, *J. Ceram. Soc. Jpn.* 2010;118:792-798.
47. J. Luo, K.D. Vargheese, A. Tandia, G. Hu, J.C. Mauro, Crack nucleation criterion and its application to impact indentation in glasses, *Sci.Rep.* 2016;6:23720.
48. Wondraczek, L., and Mauro, J. C. Advancing glasses through fundamental research. *J. Eur. Ceram. Soc.* 2009;29:1227-1234.
49. Mauro, J. C., and Zanotto, E. D. Two centuries of glass research: historical trends, current status, and grand challenges for the future. *Int. J. Appl. Glass Sci.* 2014;5:313-327.
50. Mauro JC, Tandia A, Vargheese KD, Mauro YZ, Smedskjaer MM. Accelerating the design of functional glasses through modeling. *Chem Mater.* 2016; 28(12):4267-77.
51. Kapoor S, Wondraczek L, Smedskjaer MM. Pressure-Induced densification of oxide glasses at the glass transition. *Front Mater.* 2017;(4):1-20.
52. Tatumisago, M.; Morimoto, H.; Yamashita, H.; Minami, T. Preparation of amorphous solid electrolytes in the system  $Li_2S-SiS_2-Li_4SiO_4$  by mechanical milling. *Solid State Ion.* 2000;136-137:483-488.
53. Guerette, M.; Ackerson, M.R.; Thomas, J.; Yuan, F.; Watson, E.B.; Walker, D.; Huang, L. Structure and properties of silica glass densified in cold compression and hot compression. *Sci. Rep.* 2015;5:15343.
54. Koch, C.C. Amorphization of single composition powders by mechanical milling. *Scr. Mater.* 1996;34:21-27.
55. Salmon PS, Zeidler A. Networks under pressure: the development of in situ high-pressure neutron diffraction for glassy and liquid materials. *J Phys Condens Matter.* 2015;27(13):133201.
56. Smedskjaer MM, Youngman RE, Striepe S, Potuzak M, Bauer U, Deubener J, et al. Irreversibility of Pressure Induced Boron Speciation Change in Glass. *Sci Rep.* 2015;4(1):3770.
57. Striepe S, Smedskjaer MM, Deubener J, Bauer U, Behrens H, Potuzak M, et

- al. Elastic and micromechanical properties of isostatically compressed soda-lime-borate glasses. *J Non Cryst Solids*. 2013;364(1):44-5.
58. Yoffe, E.H. Elastic stress fields caused by indenting brittle materials. *Philos. Mag. A* 1982;46:617.
  59. Motke, S.G.; Yawale, S.P.; Yawale, S.S. Infrared spectra of zinc doped lead borate glasses. *Bull. Mater. Sci.* 2002;25:75-78.
  60. Januchta, K.; Youngman, R.E.; Goel, A.; Bauchy, M.; Rzoska, S.J.; Bockowski, M.; Smedskjaer, M.M. Structural origin of high crack resistance in sodium aluminoborate glasses. *J. Non-Cryst. Solids* 2017;460: 54-65.
  61. R. Gresch, W. Müller-Warmuth, H. Dutz,  $^{11}\text{B}$  and  $^{27}\text{Al}$  NMR studies of glasses in the system  $\text{Na}_2\text{O}-\text{B}_2\text{O}_3-\text{Al}_2\text{O}_3$  ("NABAL"), *J. Non-Cryst. Solids* 1976;21:31-40.
  62. L. Züchner, J.C.C. Chan, W. Müller-Warmuth, H. Eckert, Short-range order and site connectivities in sodium aluminoborate glasses: I. Quantification of local environments by high-resolution  $^{11}\text{B}$ ,  $^{23}\text{Na}$ , and  $^{27}\text{Al}$  solid-state NMR, *J. Phys. Chem. B* 1998;102: 4495–4506.
  63. J.C.C. Chan, M. Bertmer, H. Eckert, Site connectivities in amorphous materials studied by double-resonance NMR of quadrupolar nuclei: high resolution  $^{11}\text{B} \leftrightarrow ^{27}\text{Al}$  spectroscopy of aluminoborate glasses, *J. Am. Chem. Soc.* 1999;121:5238–5248.
  64. Du L-S, Stebbins JF. Nature of silicon–boron mixing in sodium borosilicate glasses: a high-resolution  $^{11}\text{B}$  and  $^{17}\text{O}$  NMR study. *J. Phys Chem B*. 2003;107:10063-76.
  65. Sen S, Topping T, Yu P, Youngman R. Atomic-scale understanding of structural relaxation in simple and complex borosilicate glasses. *Physical Review B*. 2007;75:094203.
  66. Edwards T, Endo T, Walton JH, Sen S. Observation of the transition state for pressure-induced  $\text{BO}_3 \rightarrow \text{BO}_4$  conversion in glass. *Science*. 2014;345:1027 – 9.
  67. Wu J, Gross TM, Huang L, Jaccani SP, Youngman RE, Rzoska SJ, et al. Composition and pressure effects on the structure, elastic properties and hardness of aluminoborosilicate glass. *J Non-Cryst Solids*. 2020;530:119797.



68. Wu J, Gross TM. Structural changes in calcium aluminoborosilicate glasses recovered from pressures of 1.5 to 3GPa: interactions of two network species with coordination number increases. *J Non-Cryst Solids*. 2017;478:50-7.
69. Liu P, Januchta K, Jensen LR, Bauchy M, Smedskjaer MM. Competitive effects of free volume, rigidity, and self-adaptivity on indentation response of silicoaluminoborate glasses. *J Am Ceram Soc*. 2020;103 (2):944-54.
70. Kapoor S, Wondraczek L, Smedskjaer MM. Pressure-Induced densification of oxide glasses at the glass transition. *Front Mater*. 2017;(4):1-20.
71. Peter KW. Densification and flow phenomena of glass in indentation experiments. *J Non Cryst Solids*. 1970;5(2):103-15.
72. Lee SK, Mun KY, Kim Y, Lhee J, Okuchi T, Lin J. Degree of permanent densification in oxide glasses upon extreme compression up to 24 gpa at room temperature. *J Phys Chem Lett*. 2020;11(8):2917-24.
73. Januchta K, Youngman RE, Goel A, Bauchy M, Logunov SL, Rzoska SJ, et al. Discovery of ultra-crack-resistant oxide glasses with adaptive networks. *Chem Mater*. 2017;29(14):5865-76.
74. Martin B. Østergaard, Randall E. Youngman, Mouritz N. Svenson, Sylwester J. Rzoska, Michal Bockowski, Lars R. Jensen, Morten M. Smedskjaer. Temperature-Dependent Densification of Sodium Borosilicate Glass. *RSC Adv.*, 2015;5:78845-78851.
75. Saurabh Kapoor, Xiaoju Guo, Randall E. Youngman, Carrie L. Hogue, John C. Mauro, Sylwester J. Rzoska, Michal Bockowski, Lars R. Jensen, Morten M. Smedskjaer. Network Glasses under pressure: permanent densification in modifier-free  $\text{Al}_2\text{O}_3\text{-B}_2\text{O}_3\text{-P}_2\text{O}_5\text{-SiO}_2$  systems. *Physical review applied* 2017; 7:054011.
76. Januchta K, Youngman RE, Goel A, Bauchy M, Logunov SL, Rzoska SJ, et al. Discovery of ultra-crack-resistant oxide glasses with adaptive networks. *Chem Mater*. 2017;29(14):5865-76.
77. Svenson MN, Bechgaard TK, Fuglsang SD, Pedersen RH, Tjell AØ, Østergaard MB, et al. Composition-Structure-Property relations of compressed borosilicate glasses. *Phys Rev Appl*. 2014;2(2):024006.
78. Lee, S. K. Effect of pressure on structure of oxide glasses at high pressure: insights from solid-state NMR of quadrupolar nuclides. *Solid State Nucl. Magn. Reson*. 2010;38:45-57.

79. M. M. Smedskjaer, R. E. Youngman, S. Striepe, M. Potuazak, U. Bauer, J. Deubender, H. Behrens, J. Mauro and Y. Yue, *Sci. Rep.*, 2014;4:1-5.
80. J. Wu, J. Deubener, J. F. Stebbins, L. Grygarova, H. Behrens, L. Wondraczek and Y. Z. Yue, *J. Phys. Chem.*, 2009;131:104504.
81. Sellappan P, Rouxel T, Celarie F, Becker E, Houizot P, Conradt R. Composition dependence of indentation deformation and indentation cracking in glass. *Acta Mater.* 2013;61(16):5949-65.
82. Bechgaard, T. K., Goel, A., Youngman, R. E., Mauro, J. C., Rzoska, S. J., Bockowski, M., et al. Structure and mechanical properties of compressed sodium aluminosilicate glasses: role of non-bridging oxygens. *J. Non Cryst. Solids* 2016;441:49-57.
83. R.F. Cook, G.M. Pharr, Direct Observation and Analysis of Indentation Cracking in Glasses and Ceramics, *J. Am. Ceram. Soc.* 1990;73:787-817.
84. S.S. Chiang, D.B. Marshall, A.G. Evans, The response of solids to elastic/plastic indentation. I. Stresses and residual stresses, *J. Appl. Phys.* 1982;53:298-311.
85. C.M. Jantzen, D.I. Kaplan, N.E. Bibler, D.K. Peeler, M. John Plodinec, J. Nucl. Mater. 2008;378:244–256.
86. W. Yuan, H. Peng, M. Sun, X. Du, P. Lv, Y. Zhao, F. Liu, B. Zhang, X. Zhang, L. Chen, T. Wang, *J. Chem. Phys.* 2017;147:234502.
87. M. Guan, X.Y. Zhang, K.J. Yang, T.T. Wang, F.F. Liu, M.L. Sun, X. Du, T.S. Wang, H.B. Peng, *J. Non-Cryst. Solids* 2019;518:118–122.
88. D.A. Kilymis, J.M. Delaye, *J. Non-Cryst. Solids* 2013;382:87–94.
89. X. Ren, P. Liu, S.J. Rzoska, B. Lucznik, M. Bockowski, M.M. Smedskjaer, *Materials* 2021;14:3450.
90. H. Li, Y. Su, L. Li, D.M. Strachan, *J. Non-Cryst. Solids* 2001;292:167–176.
91. N. Ollier, T. Charpentier, B. Boizot, G. Wallez, D. Ghaleb, *J. Non-Cryst. Solids* 2004;341:26–34.
92. W. Yuan, H. Peng, M. Sun, X. Du, P. Lv, Y. Zhao, F. Liu, B. Zhang, X. Zhang,

- L. Chen, T. Wang, *J. Chem. Phys.* 2017;147:234502.
93. J.-M. Delaye, S. Peugnet, G. Bureau, G. Calas, *J. Non-Cryst. Solids* 2011;357:2763–2768.
  94. N.M.A. Krishnan, B. Wang, Y. Yu, Y. Le Pape, G. Sant, M. Bauchy, *Phys. Rev.* 2017;7:031019.
  95. S.M. Garner, *Flexible Glass: Enabling Thin, Lightweight, and Flexible Electronics*, John Wiley & Sons, 2017.
  96. L. Chen, W. Yuan, S. Nan, X. Du, D.F. Zhang, P. Lv, H.B. Peng, T.S. Wang, *Nucl. Instrum. Methods Phys. Res. Sect. B Beam Interact. Mater. At.* 2016;370:42–48.
  97. K. Januchta, M. Bauchy, R.E. Youngman, S.J. Rzoska, M. Bockowski, M.M. Smedskjaer, *Phys. Rev. Mater.* 2017;1:063603.
  98. L.-H. Kieu, J.-M. Delaye, C. Stolz, *J. Non-Cryst. Solids* 2012;358:3268–3279.
  99. L.T. Chen, X.T. Ren, Y.N. Mao, J.J. Mao, X.Y. Zhang, T.T. Wang, M.L. Sun, T.S. Wang, M.M. Smedskjaer, H.B. Peng, *J. Nucl. Mater.* 2021;552:153025.
  100. H.B. Peng, M.L. Sun, K.J. Yang, H. Chen, D. Yang, W. Yuan, L. Chen, B.H. Duan, T.S. Wang, *J. Non-Cryst. Solids* 2016;443:143–147.
  101. J. de Bonfils, S. Peugnet, G. Panczer, D. de Ligny, S. Henry, P.-Y. Noël, A. Chenet, B. Champagnon, *J. Non-Cryst. Solids* 2010;356:388–393.
  102. L.-H. Kieu, D. Kilymis, J.-M. Delaye, S. Peugnet, *Procedia Mater. Sci.* 2014;7:262–271.
  103. B. Lawn, *Fracture of Brittle Solids*, 2nd ed., Cambridge University Press, Cambridge, 1993.
  104. H. Liu, B. Deng, S. Sundararaman, Y. Shi, L. Huang, *J. Appl. Phys.* 2020;128:035106.
  105. Liu, M.; McGillicuddy, R. D.; Vuong, H.; Tao, S.; Slavney, A. H.; Gonzalez, M. I.; Billinge, S. J. L.; Mason, J. A. Network-Forming Liquids from Metal-Bis(Acetamide) Frameworks with Low Melting Temperatures. *J. Am. Chem. Soc.* 2021;143,7:2801–2811.

106. Goodgame, D. M. L.; Grachvogel, D. A.; Hussain, I.; White, A. J. P.; Williams, D. J. Formation of Polymeric Network Arrays by Complexes of Manganese(II) or Cobalt(II) with Alkane Chain Linked Bis(Amide) Ligands of Biological Relevance. *Inorg. Chem.* 1999;38(9):2057–2063.
107. Gaillac, R.; Pullumbi, P.; Beyer, K. A.; Chapman, K. W.; Keen, D. A.; Bennett, T. D.; Coudert, F. X. Liquid Metal–Organic Frameworks. *Nat. Mater.* 2017;16:1149–1155.
108. Cummins, H. Z.; Zhang, H.; Oh, J.; Seo, J. A.; Kim, H. K.; Hwang, Y. H.; Yang, Y. S.; Yu, Y. S.; Inn, Y. The Liquid-Glass Transition in Sugars: Relaxation Dynamics in Trehalose. *J. Non. Cryst. Solids* 2006;352:(42-49 SPEC. ISS.), 4464–4474.
109. Wondraczek, L., and Mauro, J. C. Advancing glasses through fundamental research. *J. Eur. Ceram. Soc.* 2009;(29):1227-123.



# LIST OF PUBLICATIONS

## PUBLICATIONS IN PEER-REVIEW JOURNALS

*Contributed as first author or main co-author:*

Chen L. T., **Ren X. T.**, Mao J. J., Mao Y. N., Zhang X. Y., Wang T. T., Sun M. L., Wang T. S., Smedskjaer M. M., Peng H. B. Radiation effects on structure and mechanical properties of borosilicate glasses. *Journal of Nuclear Materials* 552, 153025 (2021).

**Ren X.T.**, Liu P., Rzoska S. J., Lucznik B., Bockowski M., Smedskjaer M. M. Indentation response of calcium aluminoborosilicate glasses subjected to humid aging and hot compression. *Materials* 14, 3450 (2021).

**Ren X.T.**, Du T., Peng H., Jensen L. R., Biscio C. A. N., Fajstrup L., Bauchy M., Smedskjaer M. M. Irradiation-Induced Toughening of Calcium Aluminoborosilicate Glasses. *Materials Today Communications* 31, 103649 (2022).

Søren S. Sørensen<sup>1</sup>, **Xiangting Ren<sup>1</sup>**, Tao Du<sup>1</sup>, Shibo Xi, Lars R. Jensen, John Wang, Morten M. Smedskjaer, Water as a modifier in a hybrid coordination network glass. (First co-author, to be submitted).

## ORAL AND POSTER PRESENTATIONS AT CONFERENCES

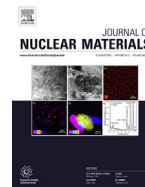
**Xiangting Ren**, Tao Du, Haibo Peng, Lars R. Jensen, Mathieu Bauchy, Morten M. Smedskjaer. “Effect of ion irradiation on the indentation response of oxide glasses”. Oral presentation: PACRIM 14/GOMD '21 International Conference, 2021.

**Xiangting Ren**, Michal Bockowski, Randall E. Youngman, Lars R. Jensen, Morten M. Smedskjaer. “Densification of oxide glasses at different time-temperature-pressure routes”. Poster presentation: PACRIM 14/GOMD '21 International Conference, 2021.



# Paper I





# Radiation effects on structure and mechanical properties of borosilicate glasses

L.T. Chen<sup>a,b</sup>, X.T. Ren<sup>c</sup>, Y.N. Mao<sup>a,b</sup>, J.J. Mao<sup>a,b</sup>, X.Y. Zhang<sup>a,b</sup>, T.T. Wang<sup>a,b</sup>, M.L. Sun<sup>a,b</sup>, T.S. Wang<sup>a,b</sup>, M.M. Smedskjaer<sup>c</sup>, H.B. Peng<sup>a,b,\*</sup>

<sup>a</sup> School of Nuclear Science and Technology, Lanzhou University, Lanzhou, 730000, China

<sup>b</sup> Key Laboratory of Special Function Materials and Structure Design Ministry of Education, Lanzhou University, Lanzhou, 730000, China

<sup>c</sup> Department of Chemistry and Bioscience, Aalborg University, 9220 Aalborg, Denmark

## ARTICLE INFO

### Article history:

Received 18 January 2021

Revised 28 March 2021

Accepted 15 April 2021

Available online 23 April 2021

### Keywords:

borosilicate glass

nano-hardness

modulus

crack resistance

irradiation

## ABSTRACT

Borosilicate glass is a candidate material for solidification of high-level radioactive waste (HLW). During disposal of HLW, the glass will be subjected to irradiation, especially the heavy ion irradiation related to alpha decay is expected to affect the properties of the glasses over billions of years. Therefore, it is important to understand the stability of borosilicate glasses upon irradiation. In this work, we study a series of sodium borosilicate glasses as well as the International Simple Glass (ISG) and subject them to irradiation with 5 MeV Xe ions. The radiation effects on the glasses include variations of macroscopic characteristics such as nano-hardness, modulus, volume change and crack initiation resistance (CR). We found that hardness, modulus, and volume changes of the glasses saturate at a certain irradiation dose, above which no further change is observed. The saturated values of hardness and modulus are found to be the same for glasses with different composition, while the saturated volume change depends on the glass composition. In addition, CR of the glasses increases dramatically upon irradiation. Meanwhile, we also studied the structure changes upon irradiation for both borosilicate and ISG glasses using Raman and infrared spectroscopies, showing an apparent transformation of  $\text{BO}_4$  to  $\text{BO}_3$  groups in borosilicate glasses irradiated with heavy ions. We thus this structural change in relation to the changes of mechanical/elastic properties. Our findings suggest that boron structures play an important role in controlling the macroscopic radiation effects.

© 2021 Elsevier B.V. All rights reserved.

## 1. Introduction

Borosilicate glasses are widely used in different fields, because of their characteristics such as relatively high thermal conductivity, chemical stability and thermal shock resistance. Consequently, borosilicate glasses are chosen as host materials to solidify high level radioactive waste (HLW) in many countries. This vitrification of the HLW is done to keep the biosphere safe [1,2]. During disposal of HLW, the vitrified materials suffer from radiation from the HLW [3]. Various questions thus arise, such as whether the vitrified materials are stable and when the vitrifications lose their ability to solidify the HLW. Therefore, the radiation effects on the glass structure and properties have been studied extensively [4–9].

Ions, gamma rays, neutron and beta have been irradiated on different glasses to simulate radiation effects in the vitrifications [10–14]. Oxygen are formed in glasses with irradiation of ion, gamma

and beta [10,11,13,15]. The defects have been identified in different glasses upon irradiation of gamma and beta. However, compared with a dramatic change in hardness and modulus induced by ions and alpha decays, hardness variation induced by electron in borosilicate glass is only around 4%, which is much less than the hardness variation induced by He ions [16]. Upon irradiation of ions or alpha decays, the hardness and modulus of borosilicate glasses drop by 30% and 15%, respectively [17,18].

Weber *et al.* have proposed that the fracture properties are important for HLW disposal because fracture increases the surface area, which leads to higher leaching tendency [19]. Ewing and Weber have summarized the radiation effects in vitrifications [20], while Weber and Peugeot have demonstrated that hardness of vitrifications with alpha decay drop greatly [3,18]. Furthermore, Peugeot has proposed that the changes in hardness and modulus of vitrifications can be assigned to nuclear energy deposition [18], laying an experimental foundation for radiation effects in vitrifications induced by alpha decay with simulation of irradiation of ions. Moreover, Mir and Peugeot have proposed results of glasses irradi-

\* Corresponding author.

E-mail address: [penghb@lzu.edu.cn](mailto:penghb@lzu.edu.cn) (H.B. Peng).

**Table 1**  
Compositions and properties of borosilicate glasses.

Mol%	NBS2	NBS4	NBS5	NBS6	NBS7	NBS8	ISG
Na <sub>2</sub> O	16.0	20.0	14.2	15.3	16.7	17.9	12.6
SiO <sub>2</sub>	67.3	64.0	67.3	64.5	61.4	58.7	60.2
B <sub>2</sub> O <sub>3</sub>	16.7	16.0	18.6	20.2	21.9	23.4	16.0
Al <sub>2</sub> O <sub>3</sub>	0	0	0	0	0	0	3.8
CaO	0	0	0	0	0	0	5.7
ZrO <sub>2</sub>	0	0	0	0	0	0	1.7
R=Na <sub>2</sub> O/B <sub>2</sub> O <sub>3</sub>	0.96	1.25	0.76	0.76	0.76	0.76	0.79
K=SiO <sub>2</sub> /B <sub>2</sub> O <sub>3</sub>	4.02	4.00	3.62	3.20	2.80	2.50	3.76
Density(g/cm <sup>3</sup> )	2.36	2.50	2.44	2.46	2.45	2.49	2.50
Hardness(GPa)	7.2±0.3	8.3±0.2	7.9±0.3	7.8±0.3	7.9±0.3	7.7±0.3	7.3±0.3
Modulus(GPa)	86.6±1.2	94.3±1.2	84.8±1.3	87.0±1.8	85.0±2.0	86.1±2.7	79.4±1.3

ated with dual beam and suggested that irradiation of helium ions could recover the properties of glasses [8,21].

Wang and Peng have studied radiation effects in borosilicate glasses and compared with results of fused silica [22–26]. From their experimental results, radiation effects in borosilicate glasses are found not to be the same as those in fused silica [27]. Therefore, it is interesting to study which structural features dominate the changes in borosilicate glasses upon ion irradiation. Besides experimental studies, simulations of radiation effects in borosilicate glasses were also carried to answer this question. With molecular dynamics simulation method, Kieu and Yuan suggested that partial transformation of [BO<sub>4</sub>] to [BO<sub>3</sub>] leads to a change in hardness of borosilicate glass after the irradiation of ions [25,28]. As such, there is a need to investigate in more details how the composition of borosilicate glasses influence the radiation effects on mechanical properties.

## 2. Material and methods

The borosilicate glasses with different compositions were prepared by melt-quenching. Melting and stirring were done at a temperature of 1300 °C for 4 hours and subsequently the quenched glasses were naturally cooled down to room temperature. The cooling rate was less than 5 °C/min. Afterwards, the glasses were re-heated to a temperature of 500 °C for 48 hours to remove the residual stress. After that, the glasses were cut into prisms with the dimension of 10×10×1 mm<sup>3</sup>, which were optically polished on both sides. Compositions of the borosilicate glasses are listed in Table 1.

Table 1 presents compositions and properties of the pristine borosilicate glasses. The NBS series glasses are ternary glasses, which are made from sodium oxide, silica and boric oxide. The glass named ISG is the International Simple Glass [5]. The *R* value of NBS5 to NBS8, which is defined as molar ratio of sodium oxide to boric oxide, is kept constant, while it varies for the other NBS glasses.

## 3. Experimental

The NBS and ISG glasses were irradiated with Xe ions to study radiation effects on mechanical properties. The radiation experiment was carry out at Institute of Modern Physics (IMP) of Chinese Academy of Sciences. The different glasses were irradiated with 5 MeV Xe ions at room temperature. Xe ions were produced, selected and then accelerated to energy of 5 MeV. A pair of rastering magnets was used to produce uniform ion beam. Then ion beam bombarded on samples in a target chamber. Pressure in the target chamber was  $7.6 \times 10^{-5}$  Pa. The typical ion current was 2 μA and the size of a beam spot was 20×20 mm<sup>2</sup>. Each specific glass sample was separated into two series and irradiated with two different methods, separately. First, a series of samples, which were

half covered with aluminum foil, that were irradiated with different doses to form an edge between the irradiated and unirradiated regions. Second, a series of samples that were irradiated evenly on surface to study macroscopic and microscopic changes.

After irradiation, the volume changes of the borosilicate glasses were measured with an atomic force microscopy (AFM) under ambient conditions. The typical ion penetration range in the glasses was about 2 μm. The volume change in ion-irradiated glasses could be expressed as:

$$\frac{\Delta V}{V} = \frac{h}{R_p}, \quad (1)$$

where *V* is volume of the damaged region induced by ions in the glass, Δ*V* is change in the volume, *R<sub>p</sub>* is range of the ions in the glass, and *h* is the height of the step between the edge.

The hardness and modulus of the glasses were measured by MTS G200 nanoindenter device with a Berkovich diamond indenter. A continuous stiffness mode was selected. The maximum load was 500 mN and the penetration depth was 2 μm. During the measurement, the temperature was kept at 21°C±3°C, and relative humidity was 40% RH. The hardness could be expressed as:

$$H = \frac{P}{A}, \quad (2)$$

where *H* is nanohardness of glass, *P* is load applied on the tip, and *A* is the projected area after unloading. The Young's modulus could be obtained as:

$$\frac{1}{E_r} = \frac{1 - \nu^2}{E} + \frac{1 - \nu_i^2}{E_i}, \quad (3)$$

where *E<sub>r</sub>* is reduced modulus, *E*, *ν* and *E<sub>i</sub>*, *ν<sub>i</sub>* are moduli and Poisson ratio of samples and diamond indenter, respectively. The Poisson ratios of samples are set 0.22 and that of diamond indenter is 0.07.

Micro-indentation testing using a Nanovea CB500 hardness tester was used to evaluate the crack initiation resistance (CR). Following previous methods [29], CR was evaluated from the resistance of the glass to the initiation of corner cracks upon indentation. That is, we applied increasing loads (from 0.1 to 5 N) using a Vickers tip. After the test, the numbers of corner cracks caused by the residual indentation were counted. The probability of crack occurrence (PCI) was derived as the ratio between the number of corners, where a corner crack was formed and the total number of corners on all indents. CR is defined as a load that generates two cracks (PCI = 50%) on average. On each sample, at least 20 indents were engraved with loading duration of 15 seconds and dwell time of 10 seconds. The cracks were counted 2 hours after unloading. The measurements were conducted under laboratory conditions (room temperature, relative humidity 40–45%).

The Raman spectra of pristine and irradiated NBS glasses were measured with an iHR550 device (Horiba Co.). The 1200 line/mm grating was selected and the resolution of Raman spectroscopy is

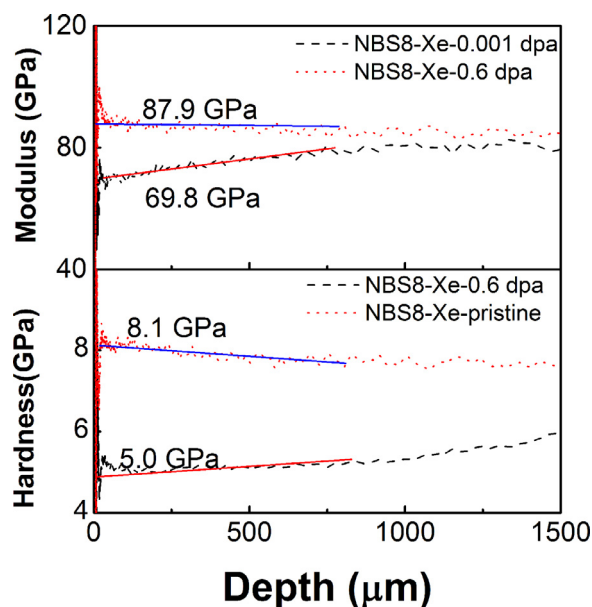


Fig. 1. Hardness and moduli depth curves of the NBS8 glass. The solid lines are fitting lines that can obtain the hardness and moduli of glass at depth of zero. The typical measurement curves with different doses were presented.

$0.75 \text{ cm}^{-1}$ . A 532 nm semiconductor laser was used as the excitation source. The infrared spectroscopy measurements of different NBS glasses were taken with an attenuated total reflectance Spectrum Two (Perkin Elmer). The typical range of infrared spectra was from 400 to  $4000 \text{ cm}^{-1}$ , with a resolution of  $2 \text{ cm}^{-1}$ .

#### 4. Results

Fig. 1 presents examples of measured hardness and modulus depth curves for NBS8 glass. The extrapolation method is suggested in this work for analyzing hardness of the non-crystalline glass material while the hardness of crystalline materials could be obtained via other method [30,31]. More details about this extrapolation method is given in previous work [26]. With extrapolation analysis method, the measured curves of elastic properties (hardness and modulus) with depth range from 300 nm to 800 nm were fitted with a linear function and then hardness and modulus were deduced at the zero depth.

The damage profile (the solid line) in NBS4 glass with irradiation of single energy Xe ion is shown in Fig. 2, revealing a roughly uniform damaged region in the glass surface [32]. The damage profile was simulated by SRIM program [32]. The full-cascade method was suggested by Weber and the displacement energy was set to 40 eV [33,34]. With irradiation of single energy ion, the roughly uniform damage layer is formed, and the dash line presents the mean damage in the layer. The radiation dose is obtained from the mean damage.

Fig. 3 presents the Raman spectra of the pristine glasses, showing four main peaks. A peak at  $500 \text{ cm}^{-1}$  was attributed by combination of Si-O-Si bending vibration and breath mode of four-membered ring [10,35]. The peak of  $630 \text{ cm}^{-1}$  is due to vibration of danburite-like structure [36,37]. A region from the 900 to  $1300 \text{ cm}^{-1}$  is due to a series Si-O<sup>-</sup> stretching vibrations from Q<sup>n</sup> structures, i.e., silicon atom connects with oxygen atoms and *n* (0,1,2,3,4) presents the number of bridging oxygen atoms. The peaks of  $1078 \text{ cm}^{-1}$  was assigned to Q<sup>3</sup>, and that of  $986 \text{ cm}^{-1}$  was assigned to Q<sup>2</sup> [11,36]. The Raman spectra of NBS4 and NBS2 glasses are different from Raman spectra of NBS5, NBS6, NBS7, and NBS8 glasses. Indeed, the *R* values of NBS4 and NBS2 glasses

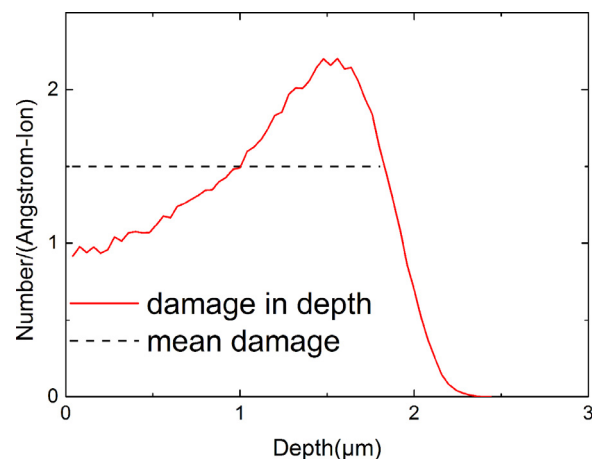


Fig. 2. The damage profile in NBS4 glass irradiated with Xe ions. The solid line presents damage profile in NBS4 glass and the dash line presents mean damage in NBS4 glass.

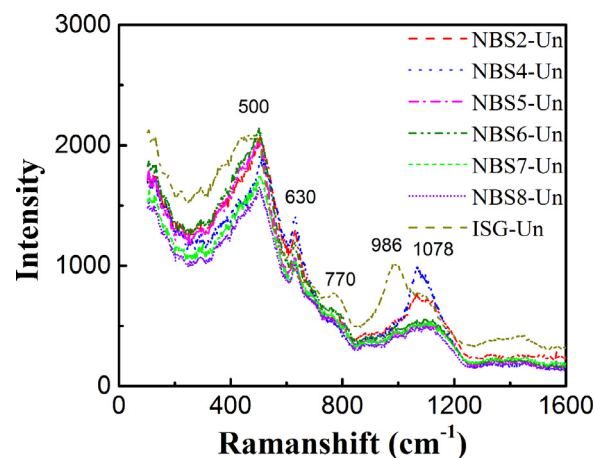


Fig. 3. Raman spectra of pristine NBS glasses.

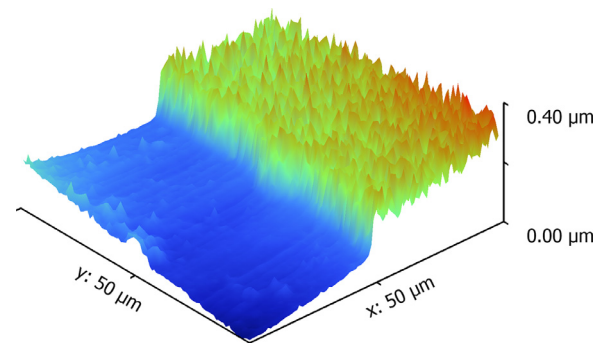


Fig. 4. The typical AFM plot of NBS4 glass irradiated with 0.1 dpa Xe ions.

are 1.25 and 0.96, respectively, while it is 0.75 for the other NBS glasses. Compared with the Raman spectrum of NBS2 glass, the Raman spectrum of NBS4 has lower intensity of  $500 \text{ cm}^{-1}$  peak and higher intensities of  $630$  and  $1078 \text{ cm}^{-1}$  peaks. This indicates that there are more Q<sup>3</sup> structures and combinations between BO<sub>4</sub> and SiO<sub>4</sub> in NBS4 compared to NBS2 glass. The broad band between  $1250$  and  $1500 \text{ cm}^{-1}$  can be assigned to B-O elongations in BO<sub>3</sub> groups.

A 3D view of the surface topography of the NBS4 glass is depicted in Fig. 4. With irradiation dose of 0.1 dpa, a step with height of 30 nm is formed on the surface of NBS4. The ion-irradiated re-

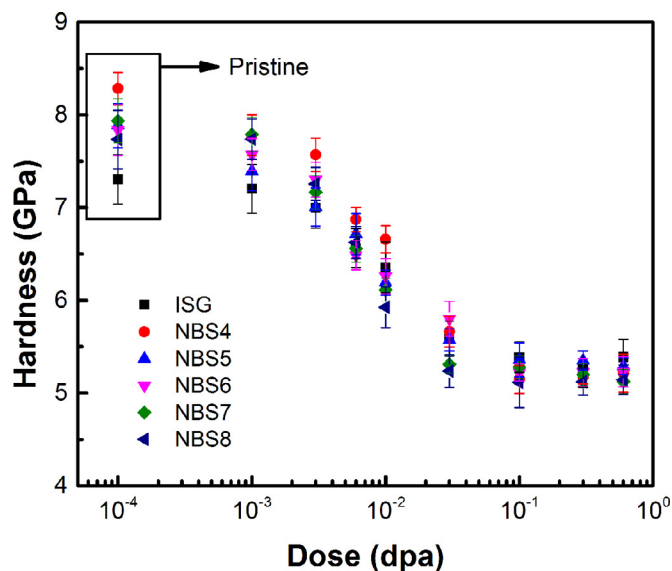


Fig. 5. Dependence of hardness of borosilicate glasses and ISG glass on irradiation dose.

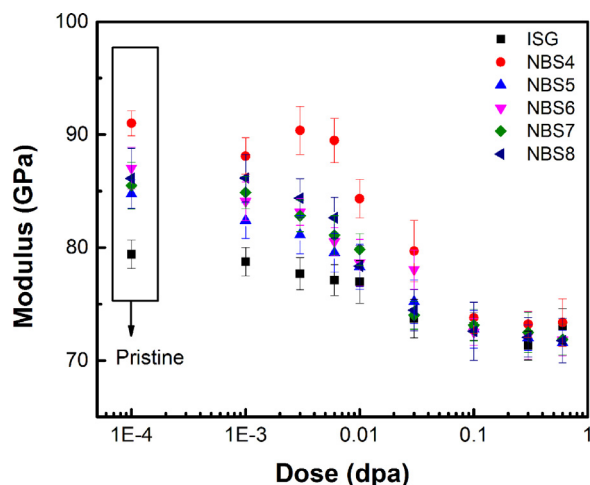


Fig. 6. Dependence of modulus of borosilicate glasses and ISG glass on irradiation dose.

gion is higher than unirradiated region, which indicates swelling in NBS4 glass. With irradiation dose 0.006 dpa, the step is hardly found on the glasses. Therefore, the volume change of the glasses at low dose was set 0%. For all the glass, the step is easily measured after irradiation dose of 0.1 dpa.

Fig. 5 shows the hardness of NBS glasses with different irradiation dose. With increase of the dose, the hardness of the borosilicate glass decreases, with a saturation at about 5.2 GPa for all the borosilicate glasses. The dose leading to this apparent saturation is around 0.1 dpa. On the other hand, the hardness of the pristine glasses with different compositions is different. With irradiation dose of 0.1 dpa, the difference in hardness of borosilicate glasses becomes less than 0.3 GPa. The evolution of the moduli of the borosilicate and ISG glasses with dose is depicted in Fig. 6. As the irradiation dose increases, the modulus decreases and then saturates at dose of 0.1 dpa. Independent of composition, the saturated moduli of borosilicate glasses are about  $72 \pm 1.5$  GPa.

Fig. 7 presents infrared spectra of pristine and ion-irradiated NBS glasses. All the spectra have been normalized at the maximum intensity. For all the NBS glasses, an increase in the regions around  $680 \text{ cm}^{-1}$  and  $1200$  to  $1500 \text{ cm}^{-1}$  is observed upon in-

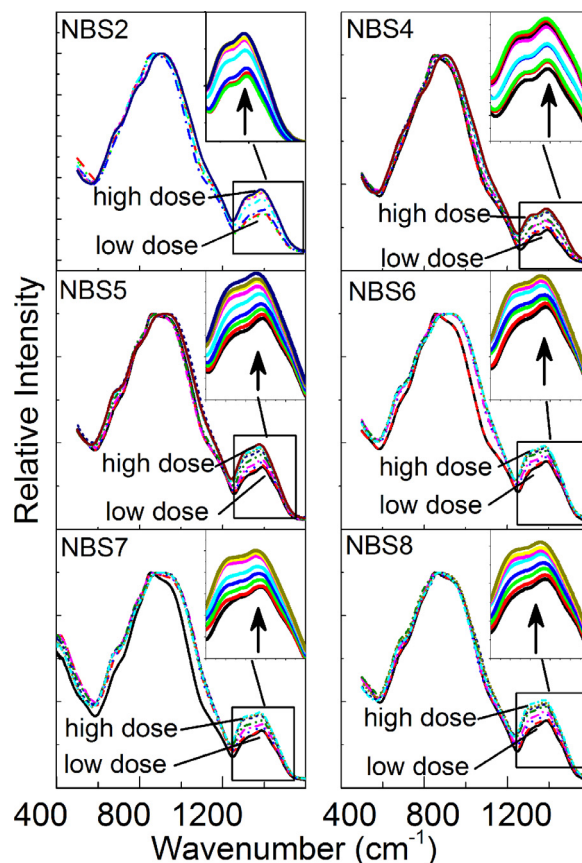


Fig. 7. Infrared spectra of NBS glasses with different irradiation doses.

creasing irradiation dose. Both regions are assigned to vibrations from  $\text{BO}_3$  structures. The  $680 \text{ cm}^{-1}$  region is due to bending vibration of B-O-B bond [38,39]. The stretching vibration of trigonal  $\text{BO}_3$  leads to the peaks from  $1200$  to  $1500 \text{ cm}^{-1}$  [38,40,41]. The insets in Fig. 7 present intensities of the vibration corresponding to trigonal  $\text{BO}_3$  structural units in the region of  $1200$ – $1500 \text{ cm}^{-1}$  and the direction of arrows illustrate the increasing trend of irradiation dose. Moreover, there is increase in the peak of  $950 \text{ cm}^{-1}$  for NBS glasses, except for NBS8 glass. The peak at  $950 \text{ cm}^{-1}$  is associated to  $Q^3$  units [42]. The region from  $1200$  to  $1500 \text{ cm}^{-1}$  is hardly affected by any overlapping absorbance from neighboring peaks, and therefore, its intensity is a good index to confirm the increase in the fraction of  $\text{BO}_3$  units.

We have then fitted the infrared absorbance region from  $1200$  to  $1500 \text{ cm}^{-1}$  with three Gaussian peaks at  $1310$ ,  $1390$  and  $1470 \text{ cm}^{-1}$ . The typical fitting results are presented in Fig. 8. The experimental curve of NBS8 is obtained from original spectrum by subtracting an oblique baseline, so as the experimental curves of other NBS glasses in this work. The  $1310 \text{ cm}^{-1}$  peak is attributed to 'loose'  $\text{BO}_3$  units, the  $1390 \text{ cm}^{-1}$  peak is assigned to  $\text{BO}_3$  units connected with  $\text{BO}_4$  units, and the  $1470 \text{ cm}^{-1}$  peak is corresponded to  $\text{BO}_3$  units bonding with  $\text{BO}_3$  units [36]. The regions of  $1200$  to  $1500 \text{ cm}^{-1}$  are majorly contributed by peaks of  $1310$  and  $1390 \text{ cm}^{-1}$ , both the intensities of the peaks increase with dose. Fig. 9 depicts the fitting intensity of  $1310 \text{ cm}^{-1}$  peak evolving with the irradiation dose. Here the error bars are smaller than the dimension of symbols. For all the NBS glasses, the intensity increases with the irradiation dose, indicating that the fraction of  $\text{BO}_3$  units in the NBS glasses increases with the irradiation dose.

Fig. 10 presents a plot of hardness versus the moduli for the borosilicate glasses with different composition. For the pristine borosilicate glasses, the values of hardness and moduli spread



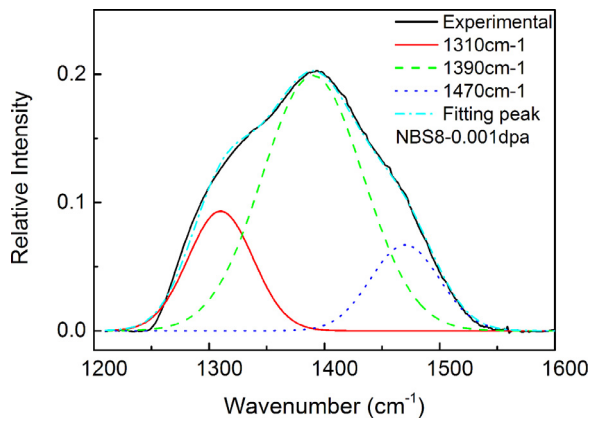


Fig. 8. The typical Gaussian fitting result of infrared spectra of NBS8.

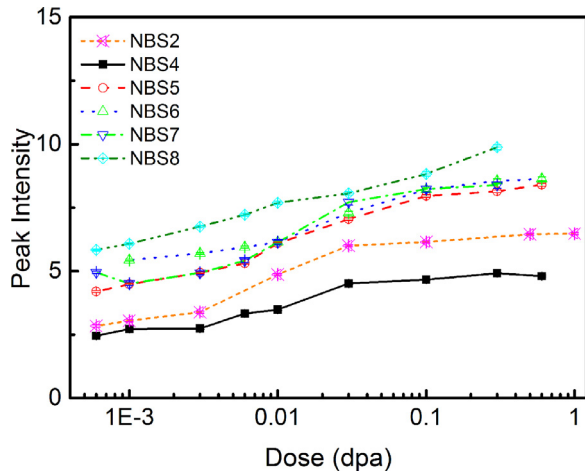


Fig. 9. The relation between the intensities of the  $1310\text{ cm}^{-1}$  on infrared spectra and the irradiation dose.

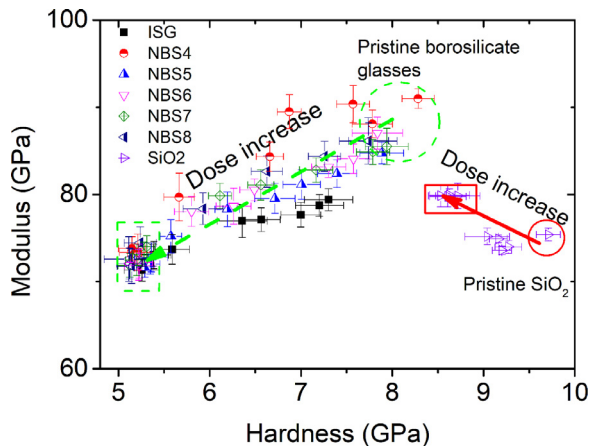


Fig. 10. As dose increased, the moduli of glasses changed with hardness. As the dose increased the arrow with dashed line illustrates properties' evolitional trend of borosilicate glasses, and the arrow with solid line illustrates that of fused silica.

in a large range as shown in the dashed circle. The arrow with dashed line in Fig. 10 shows the increasing direction of irradiation dose for borosilicate glasses, which indicates that both hardness and moduli of borosilicate glasses decrease with irradiation dose. On the other hand, all of the saturated hardness and moduli values of the borosilicate glasses can be found in a relatively small dashed rectangle region. Besides, we are also interested in the modulus-hardness relationship of other glass materials. The

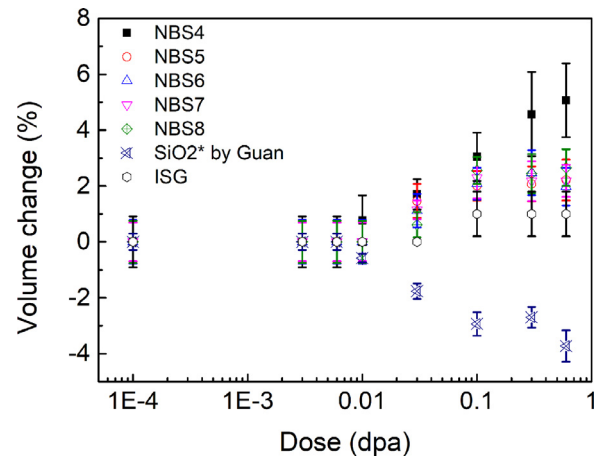


Fig. 11. Volume change of glasses as a function of the irradiation dose. The symbol of \* presents data of  $\text{SiO}_2$  from Ref. [27].

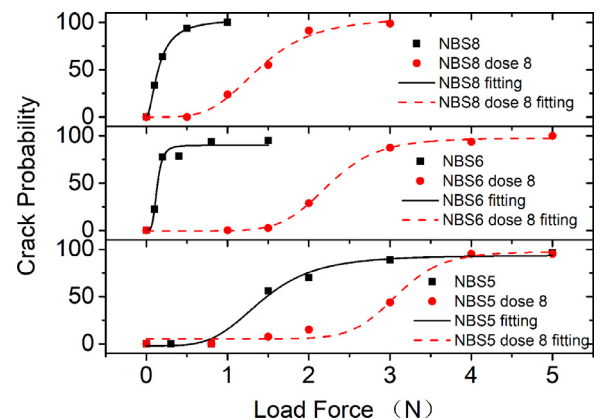


Fig. 12. Crack initiation probability as a function of applied indentation load for both pristine and ion-irradiated borosilicate glasses. Results are shown for three selected glass compositions.

modulus-hardness results of fused silica irradiated with Xe ions reported recently in Ref. [27] are also included here. The arrow with solid line in Fig. 10 illustrates evolution of hardness and moduli of the fused silica when the dose increases. For fused silica, it's clear that the hardness decreases while the modulus increases with irradiation doses. In general, either the hardness of borosilicate glass or that of fused silica decrease with irradiation dose. However, the evolitional trend of modulus-hardness relationship of fused silica, presented as the arrow with solid line, is quite different from that of borosilicate glasses, presented as the arrow with dashed line. As such, the influence of radiation on the hardness and modulus of borosilicate glass is different from that of fused silica.

The irradiation-induced volume changes of different glasses are presented in Fig. 11. All the borosilicate glasses expand with increasing dose, while the opposite is observed for fused silica. Similar to hardness and modulus results, there is an apparent saturation of the volume at high irradiation dose. The saturated change in the volume of NBS4 is about  $4 \pm 1.2\%$ , while that of NBS5, NBS6, NBS7, and NBS8 is about  $2.2 \pm 0.8\%$ . For the ISG glass, the saturated change in the volume is about  $1 \pm 0.8\%$ . With irradiation of Xe ions, the volume of the fused silica changed by  $-3.7 \pm 0.6\%$ .

The crack initiation probability as a function of the Vickers indentation load of three selected borosilicate glasses is shown in Fig. 12. For each kind of borosilicate glass, the crack resistance was determined for two different doses, the pristine and dose of 0.6 dpa. The solid and dashed lines are the fitting lines for the pristine and irradiated samples, respectively. The CR values (determined as

**Table 2**

The crack resistances of the borosilicate glasses, the unit is N.

	NBS2	NBS4	NBS5	NBS6	NBS7	NBS8
Pristine	0.2	0.1	1.2	0.1	0.2	0.2
Irradiated	2.7	2.0	3.1	2.3	2.0	1.4

the load for 50% crack probability) are listed in Table 2. After irradiation of ions, the crack resistance increases dramatically, which is matched with the decrease in hardness.

In summary, for all the borosilicate glasses, the saturated hardness and modulus are about 5.1 GPa and 75 GPa, respectively. Comparing with the changes in the hardness, modulus, volume and crack resistance, we conclude that saturated values of hardness and modulus are independent on the glass composition, while the changes in crack resistance and volume depend on the glass composition.

## 5. Discussion

We have found that hardness and moduli of borosilicate glasses with different compositions are approximately the same when they have the same  $R$  values. The borosilicate glasses with different  $R$  values have different hardness and moduli. Considering the Raman structural data, the intensity of the  $1076\text{ cm}^{-1}$  peak is related to the  $Q^3$  structures. The  $Q^3$  region of NBS5,6,7,8 glasses in the Raman spectra is approximately the same, while it differs from that of NBS2 and NBS4 glasses. This indicates that microstructure of the pristine borosilicate glasses depend strongly on the  $R$  value. As for the ISG, the doping of calcium oxide and aluminum oxide alters its microstructure and consequently its properties and Raman spectrum are different from those of the NBS glasses. For the present glasses, the  $R$  value is higher than 0.5, and according to Manara *et al.*, both danburite units ( $\text{Na}_2\text{O} \cdot \text{B}_2\text{O}_3 \cdot 2\text{SiO}_2$ ) and reedmergnerite units ( $\text{Na}_2\text{O} \cdot \text{B}_2\text{O}_3 \cdot 8\text{SiO}_2$ ) should be presented [37].

Upon ion irradiation, the different trends in the variations of hardness-modulus relationship, for borosilicate glasses and fused silica (as seen arrows with solid and dashed lines in Fig. 10), suggest that different changes in microstructure are produced by impact of ions in different glass materials. The basic structure of silica is the network of silica tetrahedron. As for borosilicate glass, there are at least four structures: silica tetrahedron, the danburite units, the reedmergnerite units and trigonal  $\text{BO}_3$  unit. In addition, in units of danburite and reedmergnerite, boron atoms exist as borate tetrahedra. Upon ion irradiation, for the fused silica, the network of silica tetrahedron would be broken, and then the hardness and modulus of the silica varied. But the microscopic structural origin of the hardness or modulus variations is different in the case of borosilicate glasses. As mentioned above, the number of  $\text{BO}_3$  structures is proportional to the intensity of the peak at  $1310\text{ cm}^{-1}$  in infrared spectra. Upon ion irradiation, for all the borosilicate glasses with different compositions, a rough linear relationship between the hardness and intensity of  $1310\text{ cm}^{-1}$  peak was observed in Fig. 13. This presents the existence of a strong dependence of hardness on the structures of boron atoms. The changes in hardness and moduli of borosilicate glasses should be assigned to changes in boron related structures.

Our results from infrared spectra (Fig. 7, Fig. 9 and Fig. 13) suggest an increase in the fraction of  $\text{BO}_3$  units in the NBS glasses with radiation dose. Kieu and Yuan's simulations suggest that, after irradiation, boron tetrahedron would turn into  $\text{BO}_3$  [28,43]. This infers that, with irradiation, both the danburite units and the reedmergnerite units would be broken because of the transformation of boron tetrahedron to the trigonal boron. This could explain the

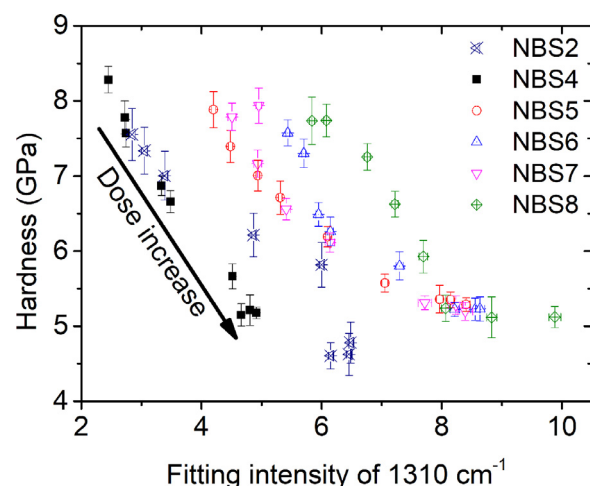


**Fig. 13.** The relation between the hardness and intensities of  $1310\text{ cm}^{-1}$ . The arrow with solid line exhibits variation of hardness and number of  $\text{BO}_3$  with the increase of dose.

decrease in the hardness and moduli of the borosilicate glasses changed with the irradiation of ions, as both hardness and elastic modulus [44] are controlled by the network rigidity, which decreases upon  $\text{BO}_4$  to  $\text{BO}_3$  conversion. It would also explain the increase in CR upon ion irradiation.  $\text{BO}_3$  has an open and planar structure, which makes it prone to undergo densification during indentation. Glasses which are more prone to densification and undergo structural changes during indentation generally exhibit higher crack resistance [45].

After irradiation of ions, the changes in volume of borosilicate glasses might be affected by three reasons. The first is the transformation of  $\text{BO}_4$  to  $\text{BO}_3$  that induces the volume increase or the density decrease. Density increase in the borosilicate glasses, produced by transformation of  $\text{BO}_3$  to  $\text{BO}_4$ , has been shown by Lee *et al.* [46]. This infers a linkage between the volume changes and transformation of  $\text{BO}_4$  to  $\text{BO}_3$  in borosilicate glasses. Therefore, the transformation of  $\text{BO}_4$  to  $\text{BO}_3$  could result in a density increase or swelling effect. The second reason is the change in silicate structures that might lead to a decrease in volume. This could be implied by the shrinkage in the fused silica irradiated by ions [27]. The third reason is the existence of doped ions in the glass could increase the disorder degree of the network in the borosilicate glasses. Except  $\text{BO}_4$  and  $\text{BO}_3$ , the doped ions, for instance Al atoms, could also form other network structures in borosilicate glass. This makes structures of ISG glass much more complex than that of the ternary borosilicate glasses. Similarly, the disorder degree of ISG glass will increase as well, as a result of the increasing amount of network structures formed by doped ions. However, the  $\text{B}_2\text{O}_3$  content of ISG is less than that of all of the NBS glasses in this work. With this reason alone, we have been able to conclude that the  $\text{BO}_4$  structure in the ISG glass is less than that in the ternary borosilicate glasses. Based on the reasons above, the  $\text{BO}_4$  structure in the ISG glass is less than that in the ternary borosilicate glasses. Moreover, the transformation of  $\text{BO}_4$  to  $\text{BO}_3$  in the irradiated ISG glass, which could induce swelling effect, is not so much as that in the ternary borosilicate glasses. Therefore, upon ion irradiation, the volume change in the ISG glass is much less than that of the borosilicate glasses.

In general, the boron atoms affect the network of pristine borosilicate glass. With irradiation of ions, the basic units of the network, the boron tetrahedron, would change, which, in turn, appears to cause the changes in the network of borosilicate glasses and macroscopic properties.

## 6. Conclusions

Borosilicate glasses with different compositions have been fabricated and analyzed with Raman and infrared spectroscopy and nano- and micro-indentation. The  $R$  value appears to play a key role in both microstructure and mechanical performance. Radiation effects in borosilicate glasses and fused silica have also been studied by measuring hardness, modulus, volume change and crack resistance. The hardness and modulus of borosilicate glasses shared similar saturated trends, i.e., they decrease with the dose and then saturate. For both the hardness and volume changes, their saturated values are the same for different borosilicate glasses, independent on the glass composition. The volume changes are saturated with the dose, but the saturated volume changes depend on the glass composition. The infrared spectra of NBS glasses suggest that, with irradiation of ions, the  $\text{BO}_3$  units in all the borosilicate glasses increase with irradiation dose. Both characteristics of the pristine glasses and ion-irradiated glasses indicate that the boron atoms play an important role. After irradiation, the crack resistance of the borosilicate glasses increases substantially.

## Declaration of Competing Interest

The authors declare that they have no known competing financial interests or personal relationships that could have appeared to influence the work reported in this paper.

## CRediT authorship contribution statement

**L.T. Chen:** Writing - original draft, Resources. **X.T. Ren:** Investigation, Writing - review & editing. **Y.N. Mao:** Resources, Formal analysis. **J.J. Mao:** Writing - original draft, Data curation. **X.Y. Zhang:** Investigation. **T.T. Wang:** Investigation, Writing - review & editing. **M.L. Sun:** Writing - review & editing. **T.S. Wang:** Funding acquisition. **M.M. Smedskjaer:** Writing - review & editing. **H.B. Peng:** Supervision, Funding acquisition, Writing - review & editing.

## Acknowledgments

This work was supported by National Natural Science Foundation of China (Grant No. U1867207) and DSTI Foundation of Gansu (Grant No. 2018ZX-07). H.B. Peng is supported by INWARD coordinated research project (Ion Beam Irradiation for High Level Nuclear Waste Form Development, F11022) from IAEA. The technical supports from the 320 kV ECR HCLs platform at IMP (Lanzhou) and Suzhou Institute of Nano-tech and Nano-bionics are greatly appreciated. X.T. Ren and M.M. Smedskjaer acknowledge support from the China Scholarship Council (CSC No. 201906250152).

## Supplementary materials

Supplementary material associated with this article can be found, in the online version, at doi:[10.1016/j.jnucmat.2021.153025](https://doi.org/10.1016/j.jnucmat.2021.153025).

## References

- [1] L.L. Hench, D.E. Clark, J. Campbell, High level waste immobilisation forms, *Nuclear Chem. Waste Manage.* 5 (1984) 149–173.
- [2] D.H. Day, A.E. Hughes, J.W. Leake, J.A.C. Marples, G.P. Marsh, J. Rae, B.O. Wade, The management of radioactive waste, *Rep. Prog. Phys.* 48 (1985) 101–169.
- [3] W.J. Weber, Radiation effect in nuclear waste glasses, *Nucl. Instr. Meth. B.* 32 (1988) 471–479.
- [4] N.E. Bibler, Effects of alpha, gamma, and alpha recoil radiation on borosilicate glass containing Savannah River Plant defense high level waste, *Mater. Res. Soc. Symp. Proc.* 6 (1982) 681–687.
- [5] S. Gin, A. Abdelouas, L.J. Criscenti, W.L. Ebert, K. Ferrand, T. Geisler, M.T. Harrison, Y. Inagaki, S. Mitsui, K.T. Mueller, J.C. Marra, C.G. Pantano, E.M. Pierce, J.V. Ryan, J.M. Schofield, C.I. Steefel, D. Vienna, An international initiative on long-term behavior of high-level nuclear waste glass, *Mater. Today* 16 (2013) 243–248.
- [6] S. Peugeot, C. Mendoza, E.A. Maugeri, J.M. Delaye, R. Caraballo, T. Charpentier, M. Tribet, O. Bouty, C. Jégou, Alpha Decays Impact Nuclear Glass Struct. *Procedia Mater. Sci.* 7 (2014) 252–261.
- [7] A.H. Mir, S. Peugeot, Using external ion irradiations for simulating self-irradiation damage in nuclear waste glasses: State of the art, recommendations and prospects, *J. Nucl. Mater.* 539 (2020) 152246.
- [8] A.H. Mir, S. Peugeot, M. Toulemonde, P. Bulot, C. Jégou, S. Miro, S. Bouffard, Defect recovery and damage reduction in borosilicate glasses under double ion beam irradiation, *EPL (Europhysics Letters)* 112 (2015) 36002.
- [9] A.H. Mir, B. Boizot, T. Charpentier, M. Gennissou, M. Odorico, R. Podor, C. Jégou, S. Bouffard, S. Peugeot, Surface and bulk electron irradiation effects in simple and complex glasses, *J. Non Cryst. Solids* 453 (2016) 141–149.
- [10] N. Ollier, B. Boizot, B. Reynard, D. Ghaleb, G. Petite,  $\beta$  irradiation in borosilicate glasses: the role of the mixed alkali effect, *Nucl. Instr. and Meth. B.* 218 (2004) 176–182.
- [11] B. Boizot, N. Ollier, F. Olivier, G. Petite, D. Ghaleb, E. Malchukova, Irradiation effects in simplified nuclear waste glasses, *Nucl. Instr. Meth. B.* 240 (2005) 146–151.
- [12] D.L. Griscom, C.I. Merzbacher, R.A. Weeks, R.A. Zuh, Electron spin resonance studies of defect centers induced in a high-level nuclear waste glass simulated by gamma-irradiation and ion-implantation, *J. Non Cryst. Solids* 258 (1999) 34–37.
- [13] M. Mohapatra, R.M. Kadam, R.K. Mishra, C.P. Kaushik, B.S. Tomar, S.V. Godbole, Gamma radiation induced changes in nuclear waste glass containing Eu, *Physica B: Condens. Matter.* 406 (2011) 3980–3984.
- [14] S. Peugeot, T. Fares, E.A. Maugeri, R. Caraballo, T. Charpentier, L. Martel, J. Somers, A. Janssen, T. Wiss, F. Rozenblum, M. Magnin, X. Deschanel, C. Jégou, Effect of  $10\text{B}(\text{n}, \alpha)^7\text{Li}$  irradiation on the structure of a sodium borosilicate glass, *Nucl. Instr. Meth. B.* 327 (2014) 22–28.
- [15] M. Mohapatra, V.K. Manchanda, Characterization of borosilicate glass as host matrix for high level waste, *IOP Conference Series: Materials Science and Engineering*, 2, 2009.
- [16] K.J. Yang, T.S. Wang, G.F. Zhang, H.B. Peng, L. Chen, L.M. Zhang, C.X. Li, F. Tian, W. Yuan, Study of irradiation damage in borosilicate glass induced by He ions and electrons, *Nucl. Instr. Meth. B.* 307 (2013) 541–544.
- [17] S. Peugeot, J.N. Cachia, C. Jégou, X. Deschanel, D. Roudil, V. Broudic, J.M. Delaye, J.M. Bart, Irradiation stability of R7T7-type borosilicate glass, *J. Nucl. Mater.* 354 (2006) 1–13.
- [18] S. Peugeot, P.Y. Noël, J.L. Loubet, S. Pavan, P. Nivet, A. Chenet, Effects of deposited nuclear and electronic energy on the hardness of R7T7-type containment glass, *Nucl. Instr. Meth. B.* 246 (2006) 379–386.
- [19] W.J. Weber, H. Matzke, J.L. Routort, Indentation testing of nuclear-waste glasses, *J. Mater. Sci.* 19 (1984) 2533–2545.
- [20] R.C. Ewing, W.J. Weber, F.W.C. Jr, Radiation effects in nuclear waste forms for high-level radioactive waste, *Prog. Nucl. Energy* 29 (1995) 63–127.
- [21] A.H. Mir, I. Monnet, M. Toulemonde, S. Bouffard, C. Jégou, S. Peugeot, Mono and sequential ion irradiation induced damage formation and damage recovery in oxide glasses: Stopping power dependence of the mechanical properties, *J. Nucl. Mater.* 469 (2016) 244–250.
- [22] L. Chen, T.S. Wang, K.J. Yang, H.B. Peng, G.F. Zhang, L.M. Zhang, H. Jiang, Q. Wang, Raman study of Kr ion irradiated sodium aluminoborosilicate glass, *Nucl. Instr. Meth. B.* 307 (2013) 566–569.
- [23] G.F. Zhang, T.S. Wang, K.J. Yang, L. Chen, L.M. Zhang, H.B. Peng, W. Yuan, F. Tian, Raman spectra and nano-indentation of Ar-irradiated borosilicate glass, *Nucl. Instr. Meth. B.* 316 (2013) 218–221.
- [24] H.B. Peng, M.L. Sun, X. Du, W. Yuan, D. Yang, L. Chen, B.H. Duan, T.S. Wang, Variation of hardness and modulus of borosilicate glass irradiated with Kr ions, *Nucl. Instr. Meth. B.* 406 (2017) 561–565.
- [25] W. Yuan, H. Peng, M. Sun, X. Du, P. Lv, Y. Zhao, F. Liu, B. Zhang, X. Zhang, L. Chen, T. Wang, Structural origin of hardness decrease in irradiated sodium borosilicate glass, *J. Chem. Phys.* 147 (2017) 234502.
- [26] M.L. Sun, H.B. Peng, B.H. Duan, F.F. Liu, X. Du, W. Yuan, B.T. Zhang, X.Y. Zhang, T.S. Wang, Comparison of hardness variation of ion irradiated borosilicate glasses with different projected ranges, *Nucl. Instrum. Methods Phys. Res. Sect. B* 419 (2018) 8–13.
- [27] M. Guan, X.Y. Zhang, K.J. Yang, T.T. Wang, F.F. Liu, M.L. Sun, X. Du, T.S. Wang, H.B. Peng, Difference in radiation effects of sodium borosilicate glass and vitreous silica with ions, *J. Non Cryst. Solids* 518 (2019) 118–122.
- [28] L.H. Kieu, D. Kilymis, J.M. Delaye, S. Peugeot, Discussion on the structural origins of the fracture toughness and hardness changes in rapidly quenched borosilicate glasses: a molecular dynamics study, *Procedia Mater. Sci.* 7 (2014) 262–271.
- [29] K. Januchta, M.M. Smedskjaer, Indentation deformation in oxide glasses: Quantification, structural changes, and relation to cracking, *J. Non-Crystalline Solids: X* 1 (2019) 100007.
- [30] B. Li, Z. Wang, K. Wei, T. Shen, C. Yao, H. Zhang, Y. Sheng, X. Lu, A. Xiong, W. Han, Evaluation of helium effect on irradiation hardening in F82H, ODS, SIMP and T91 steels by nano-indentation method, *Fusion Eng. Des.* 142 (2019) 6–12.
- [31] W.D. Nix, H. Gao, Indentation size effects in crystalline materials a law for strain gradient plasticity, *J. Mech. Phys. Solids* 46 (1998) 411–425.
- [32] J.F. Ziegler, M.D. Ziegler, J.P. Biersack, SRIM – The Stopping and Range of Ions in Matter, *Nucl. Instr. Meth. B.* 268 (2010) 1818–1823.
- [33] W.J. Weber, Y. Zhang, Predicting damage production in monoatomic and multi-elemental targets using stopping and range of ions in matter code: Challenges and recommendations, *Curr. Opin. Solid State Mater. Sci.* 23 (2019) 100757.




- [34] Y. Zhang, W.J. Weber, Ion irradiation and modification: The role of coupled electronic and nuclear energy dissipation and subsequent nonequilibrium processes in materials, *Appl. Phys. Rev.* 7 (2020) 041307.
- [35] A. Pasquarello, R. Car, Identification of Raman Defect Lines as Signatures of Ring Structures in Vitreous Silica, *Phys. Rev. Lett.* 80 (1998) 5145–5147.
- [36] D. Manara, A. Grandjean, D.R. Neuville, Advances in understanding the structure of borosilicate glasses: a Raman spectroscopy study, *Am. Mineral.* 94 (2009) 777–784.
- [37] D. Manara, A. Grandjean, D.R. Neuville, Structure of borosilicate glasses and melts: A revision of the Yun, Bray and Dell model, *J. Non Cryst. Solids* 355 (2009) 2528–2531.
- [38] S.G. Motke, S.P. Yawale, S.S. Yawale, Infrared spectra of zinc doped lead borate glasses, *Bull. Mater. Sci.* 25 (2002) 75–78.
- [39] W.A. Pisarski, J. Pisarska, W. Ryba-Romanowski, Structural role of rare earth ions in lead borate glasses evidenced by infrared spectroscopy:  $\text{BO}_3 \leftrightarrow \text{BO}_4$  conversion, *J. Mol. Struct.* 744–747 (2005) 515–520.
- [40] C. Gautam, A.K. Yadav, A.K. Singh, A Review on Infrared Spectroscopy of Borate Glasses with Effects of Different Additives. *ISRN Ceramics*. 2012 (2012) 1–17.
- [41] E.I. Kamitsos, M.A. Karakassides, G.D. Chryssikos, Vibrational Spectra of Magnesium-Sodium-Borate Glasses. 2. Raman and Mid-Infrared Investigation of the Network Structure *J. Phys. Chem.* 91 (1986) 1073–1079.
- [42] J. Serra, P. González, S. Liste, C. Serra, S. Chiussi, B. León, M. Pérez-Amor, H.O. Ylänen, M. Hupa, FTIR and XPS studies of bioactive silica based glasses, *J. Non Cryst. Solids* 332 (2003) 20–27.
- [43] W. Yuan, H.-b. Peng, X. Du, P. Lv, M.-l. Sun, L. Chen, T.-s. Wang, Origin of molecular oxygen formation in irradiated borosilicate glasses studied by molecular dynamics simulation, *Int. J. Appl. Glass Sci.* 9 (2018) 344–351.
- [44] Q. Zheng, H. Zeng, Progress in modeling of glass properties using topological constraint theory, *Int. J. Appl. Glass Sci.* 11 (2020) 432–441.
- [45] K. Januchta, R.E. Youngman, A. Goel, M. Bauchy, S.L. Logunov, S.J. Rzoska, M. Bockowski, L.R. Jensen, M.M. Smedskjaer, Discovery of Ultra-Crack-Resistant Oxide Glasses with Adaptive Networks, *Chem. Mater.* 29 (2017) 5865–5876.
- [46] S.K. Lee, P.J. Eng, H.-k. Mao, Y. Meng, M. Newville, M.Y. Hu, J. Shu, Probing of bonding changes in  $\text{B}_2\text{O}_3$  glasses at high pressure with inelastic X-ray scattering, *Nat. Mater.* 4 (2005) 851–854.



# Paper II

## Article

# Indentation Response of Calcium Aluminoborosilicate Glasses Subjected to Humid Aging and Hot Compression

Xiangting Ren <sup>1</sup>, Pengfei Liu <sup>1</sup>, Sylwester J. Rzoska <sup>2</sup>, Boleslaw Lucznik <sup>2</sup> , Michal Bockowski <sup>2</sup>   
and Morten M. Smedskjaer <sup>1,\*</sup> 

<sup>1</sup> Department of Chemistry and Bioscience, Aalborg University, 9220 Aalborg, Denmark; xiangtingr@bio.aau.dk (X.R.); pli@bio.aau.dk (P.L.)

<sup>2</sup> Institute of High-Pressure Physics, Polish Academy of Sciences, 01-142 Warsaw, Poland; sylwester.rzoska@gmail.com (S.J.R.); bolo@unipress.waw.pl (B.L.); bocian@unipress.waw.pl (M.B.)

\* Correspondence: mos@bio.aau.dk

**Abstract:** Aluminoborosilicate glasses find a wide range of applications, which require good mechanical reliability such as surface damage resistance. Calcium aluminoborosilicate (CABS) glasses have recently been found to exhibit so-called intermediate behavior in terms of their response to sharp contact loading. That is, these glasses deform with less shear than normal glass and less densification than anomalous glasses. This deformation mechanism is believed to give rise to high crack initiation resistance of certain CABS glasses. In order to further improve and understand the micromechanical properties of this glass family, we studied the indentation response of different CABS glasses subjected to two types of post-treatment, namely hot compression and humid aging. Upon hot compression, density, elastic moduli, and hardness increased. Specifically, elastic modulus increased by as much as 20% relative to the as-made sample, while the largest change in hardness was 1.8 GPa compared to the as-made sample after hot compression. The pressure-induced increase in these properties can be ascribed to the increase in network connectivity and bond density. On the other hand, the crack initiation resistance decreased, as the hot compression increased the residual stress driving the indentation cracking. Humid aging had only a minor impact on density, modulus, and hardness, but an observed decrease in crack initiation resistance. We discuss the correlations between hardness, density, crack resistance, and deformation mechanism and our study thus provides guidelines for tailoring the mechanical properties of oxide glasses.

**Keywords:** calcium aluminoborosilicate (CABS) glasses; indentation response; hot compression; humid aging



**Citation:** Ren, X.; Liu, P.; Rzoska, S.J.; Lucznik, B.; Bockowski, M.; Smedskjaer, M.M. Indentation Response of Calcium Aluminoborosilicate Glasses Subjected to Humid Aging and Hot Compression. *Materials* **2021**, *14*, 3450. <https://doi.org/10.3390/ma14133450>

Academic Editor: Halina Kaczmarek

Received: 10 May 2021

Accepted: 17 June 2021

Published: 22 June 2021

**Publisher's Note:** MDPI stays neutral with regard to jurisdictional claims in published maps and institutional affiliations.



**Copyright:** © 2021 by the authors. Licensee MDPI, Basel, Switzerland. This article is an open access article distributed under the terms and conditions of the Creative Commons Attribution (CC BY) license (<https://creativecommons.org/licenses/by/4.0/>).

## 1. Introduction

Oxide glass materials find various applications due to their high hardness, transparency, and chemical durability [1]. Their mechanical properties have in particular received widespread attention. This is because the low practical strength and fracture toughness limit the present and potential future applications. The low strength arises due to surface flaws, at which the stress concentrates and could lead to catastrophic damage [2], and the glasses also do not have a stable shearing mechanism. To enable the design of stronger and more damage-resistant oxide glasses, different intrinsic [3] and extrinsic post-treatment methods have been tried, including chemical strengthening to limit the formation and propagation of strength-limiting cracks through the creation of a surface layer with high compressive stress [4].

Indentation testing can, to some extent and for certain applications, be used to simulate real-life damage events under controlled conditions. This is because sharp contact is often the main failure mode of glasses. The sample area required for indentation testing is relatively small and the experiment time is short. In terms of their Vickers indentation behavior, oxide glasses can be classified into “normal”, “anomalous”, or “intermediate”.

The normal glasses deform by a shearing mechanism and form median/radial and lateral cracks, while anomalous glasses mainly deform through densification and often form ring/cone cracks. The intermediate glasses have some characteristics of typical normal and anomalous glasses, as they deform with less shear than normal glass and less densification than anomalous glass, but do not have ring/cone and median cracks [5]. The indentation deformation mechanism (e.g., degree of shear flow and densification) therefore depends to a large extent on the glass composition. Since densification is an effective way to dissipate the elastic energy applied to the material in the process of indentation, there has been an increasing interest in tailoring the deformation mechanism and thus cracking behavior through rational composition design.

The number of possible oxide glass compositions is extremely high [6] and outside the range of what could be tested experimentally, at least with the current methods for composition–structure–property studies. In the effort to improve the indentation response of oxide glasses, it is thus important to establish relationships between glass composition, indentation deformation mechanism, and the resulting indentation response. Knowledge of such relationships will advance the design of tailored oxide glasses, with the goal to shift the field from trial-and-error to model-based glass design. To enable this, it is important to understand at the atomic-scale the structural rearrangements that occur due to the high stress levels induced by indentation. For instance, Lee et al. [7] showed that for vitreous boric oxide at room temperature, the average coordination number of boron increases with pressure, with irreversible changes starting at a pressure of 4–7 GPa. This pressure level is usually achieved in indentation experiments.

In this study, we focused on the indentation response of a family of calcium aluminoborosilicate (CABS) glasses. They are interesting, as they have been found in recent work to exhibit intermediate indentation behavior, i.e., they deform with higher densification than typical normal glasses and also more shear deformation than anomalous glasses [8]. This gives rise to a high crack initiation resistance during indentation, which in turn has been related to high shear band density in some CABS glasses. In general, such aluminoborosilicate glasses can be applied as flat panel display substrates, photochromic components, bioactive materials, and nuclear waste encapsulation materials [9]. The network connectivity of the intermediate CABS glasses is lower than that of anomalous glasses, which leads to the greater degree of shear deformation, allowing them to be relieved from the stresses that form ring and median cracks [10]. However, in the studied CABS glass series with varying  $\text{SiO}_2/\text{B}_2\text{O}_3$  ratios [6], the relative amounts of shear and densification deformation were constant, but the load leading to indentation cracking varied depending on the chemical composition. Therefore, in this work, we aimed to further explore and understand the structure and composition dependence of the indentation response of CABS glasses. In CABS glasses,  $\text{SiO}_2$  and  $\text{B}_2\text{O}_3$  are the basic network formers, due to the low cation size and high bond strength. Boron is found in either a three- or four-fold coordinated state with oxygen in a random configuration [11]. Both four-fold coordinated boron and aluminum need to be stabilized by calcium cations, or alternatively through the formation of five- or six-fold coordinated aluminum or oxygen triclusters. The addition of alumina to borate glass thus changes the boron speciation [12].

Besides composition optimization, we explored the effects of post-processing methods on the mechanical properties of CABS glasses. These methods included hot compression and humid aging treatment. First, heating the glass at a temperature close to the glass transition temperature ( $T_g$ ) under elevated pressure (i.e., so-called hot compression) can be used to permanently change the structure and properties of oxide glasses [13]. That is, hot compression at pressures of 1–2 GPa around  $T_g$  is known to increase density, hardness, and elastic moduli, whereas crack initiation resistance decreases [14–16]. In addition to being an important method that could help to tune the properties, compression experiments can provide insights into the indentation deformation mechanism due to the high stress that can be generated in glasses under sharp contact loading [17–19]. Second, humid aging treatment has been found to influence the mechanical properties. For example, Kim et al.

studied the subsurface damage of soda–lime–silica float glass before and after hydrothermal treatment [20,21]. The glass–water reactions were accelerated at the subsurface damage layer. Interestingly, compared with the original float glass, the surface of hydrothermally treated glass exhibited lower hardness, higher crack resistance, and lower resistance to mechanochemical wear under higher humidity. Another study explored the influence of relative humidity during mechanical testing on the crack resistance of an alkaline earth aluminosilicate glass. Vickers hardness was not significantly influenced by the environmental conditions, whereas crack resistance decreased with the increase of humidity [22]. Recently, it was found that a cesium aluminoborate glass exhibits excellent crack resistance after being subjected to humid surface aging prior to indentation testing [23]. Such water entry into the glass surface may exert compressive stresses in the contact area [24,25], which could help to suppress the formation and propagation of cracks. In addition, the diffusion of water into the glass network may lead to rapid stress release [26]. However, the aging of a lithium aluminoborate glass [27] does not cause the ultra-high crack resistance values as for the cesium aluminoborate glasses. There is thus a need to understand the composition dependence of the effect of humid aging on glass mechanics. Considering their high inherent crack initiation resistance, performing humid aging treatment on CABS glasses is particularly interesting.

In this work, we used the  $15\text{CaO}-15\text{Al}_2\text{O}_3-25\text{B}_2\text{O}_3-45\text{SiO}_2$  (named CABS-ref) glass from the previous study [6] as the reference composition, since it showed the highest crack initiation resistance and it was thus interesting to investigate if it could be further improved. We then performed five systematic composition variations in 5 mol% oxide increments, as shown in Table 1: CABS-SiB (Si/B increase), CABS-CaB (Ca/B increase), CABS-BAl (B/Al increase), CABS-CaSi (Ca/Si increase), and CABS-CaAl (Ca/Al increase). We performed hot compression and/or humid aging treatment on the six glasses and characterized their mechanical properties through ultrasound echography and micro-indentation. The indentation deformation mechanism was also explored.

**Table 1.** Nominal chemical compositions of the CABS glasses as well as their measured glass transition temperature ( $T_g$ ). Coloring indicates reference content or  $T_g$  (grey), increasing content or  $T_g$  relative to reference (green), and decreasing content or  $T_g$  relative to reference (red). The error in  $T_g$  was within  $\pm 2$  °C.

Glass ID	SiO <sub>2</sub> (mol%)	Al <sub>2</sub> O <sub>3</sub> (mol%)	B <sub>2</sub> O <sub>3</sub> (mol%)	CaO (mol%)	Note	$T_g$ (°C)
CABS-ref	45	15	25	15	Reference glass	677
CABS-SiB	50	15	20	15	Si/B increase	652
CABS-CaB	45	15	20	20	Ca/B increase	683
CABS-BAl	45	10	30	15	B/Al increase	636
CABS-CaSi	40	15	25	20	Ca/Si increase	668
CABS-CaAl	45	10	25	20	Ca/Al increase	665

## 2. Materials and Methods

### 2.1. Sample Preparation

We prepared the six calcium aluminoborosilicate (CABS) glasses using traditional melt quenching technology, with the nominal chemical compositions given in Table 1. The raw materials were CaCO<sub>3</sub> (99.5%, ChemSolute, Renningen, Germany), Al<sub>2</sub>O<sub>3</sub> (99.5%, Sigma-Aldrich, Seelze, Germany), H<sub>3</sub>BO<sub>3</sub> ( $\geq 99.5\%$ , Honeywell International, Schnelldorf, Germany), and SiO<sub>2</sub> ( $\geq 99.5\%$ , 0.2–0.8 mm, Merck KGaA, Schnelldorf, Germany). First, these are weighed and thoroughly mixed based on the target composition. To remove H<sub>2</sub>O and CO<sub>2</sub>, the mixed batch was gradually added to a crucible (Pt–Rh) in an electric furnace at 800 °C. Depending on the composition, these mixtures were then melted at 1600 °C. The melt was then poured onto a steel plate for quenching and then transferred to the annealing furnace at the glass transition temperature ( $T_g$ ). The actual  $T_g$  values were later determined from differential scanning calorimetry measurements (STA 449 F3 Jupiter, Netzsch, Selb, Germany) at 10 K/min.  $T_g$  values are summarized in Table 1 and also in Table S1 along

with other property data. After these measurements, the glasses were reannealed at their measured  $T_g$  values for another 0.5 h and then cooled to room temperature with the cooling rate of about 3 K/min. After re-annealing, we cut the glasses into the required size for the subsequent characterization. Diamond grinding disks were then used to polish the samples in ethanol. Based on X-ray diffraction analyses (Empyrean XRD, PANalytical, Stanford, CA, USA) of all samples, no signs of crystallization were present (Figure S1 in the Supplementary Materials).

For the hot compression treatment, the glasses were isostatically compressed in a 1.0 GPa  $N_2$  atmosphere at their respective  $T_g$  values. The high temperature and pressure were maintained for 30 min, and subsequently the samples were cooled to room temperature at a cooling rate of 60 K/min to achieve permanent compression of the glass samples. The pressure chamber was then decompressed at a rate of 30 MPa/min. The humid aging treatment of all polished glass samples was done using an autoclave. Both as-made and compressed samples were subjected to this treatment. The conditions of the autoclave were at 120 °C and relative humidity of 100%. The treatment was carried out for a duration of 24 h, whereafter the temperature of the autoclave has dropped to room temperature and the glass sample was removed for relevant experimental tests.

## 2.2. Characterization

The density ( $\rho$ ) values of the as-prepared and post-treated glasses were determined by Archimedes' principle of buoyancy. The weight of each sample (at least 1.5 g) was measured 10 times in ethanol.

An ultrasonic thickness gauge (38DL Plus, Olympus, MA, USA), equipped with 20 MHz delay line transducers for the determination of the longitudinal  $V_1$  and transversal wave velocities  $V_2$ , was used to determine the elastic properties of the glasses. Based on these velocity and density values, we calculated Young's modulus  $E$ , bulk modulus  $B$ , and shear modulus  $G$  as well as Poisson ratio  $\nu$  using the relations for isotropic materials.

We also calculated the atomic packing density ( $C_g$ ). To do so, we assumed four-fold coordination for Si, six-fold coordination for Ca, two-fold coordination for O, while the speciation for boron and aluminum was based on previous structural data for the CABS glasses [6].  $C_g$  is defined as the ratio between the theoretical molar volume provided by the ions and the effective molar volume of the glass. The atomic packing density ( $C_g$ ) can then be calculated as,

$$C_g = \rho \frac{\sum f_i V_i}{\sum f_i M_i}, \quad (1)$$

where  $V_i = \frac{4}{3}\pi N(xr_A^3 + yr_B^3)$  represents the molar volume of an oxide  $A_xB_y$  with the molar mass  $M_i$  and the molar fraction  $f_i$ ,  $N$  is the Avogadro number, and  $r_A$  and  $r_B$  are the ionic radii [28–30].

Micro-indentation measurements were carried out with a Nanovea CB500 hardness tester to determine the Vickers hardness ( $H_V$ ) and crack resistance (CR). On each sample, 20 indentations with a maximum load of 4.9 N (1 kgf) were generated to determine  $H_V$ , with a loading duration of 15 s and a dwell time of 10 s. We then used an optical microscope to analyze the residual imprints and calculate the  $H_V$ . CR, i.e., the resistance of the glass to the initiation of cracks in the corners upon indentation, was determined using two different diamond indenters, namely, the 136° four-sided pyramid Vickers tip and the three-sided pyramid cube corner tip with mutually perpendicular faces. For the same glass, the sharper cube's corner tip leads to higher residual stress, less densification, and easier crack initiation compared to the Vickers tip. In both cases, we used increasing loads (from 4.8 to 30 N for Vickers and from 0.1 to 0.9 N for cube corner) and counted the numbers of corner cracks 2 h after unloading (see Figure S2). CR was calculated based on the method of Wada [31]. That is, the probability of crack occurrence (PCI) was defined as the ratio between the number of corner cracks and the total number of corners on all indents. CR is a load that generates 2 or 1.5 cracks (PCI = 50%) on average for Vickers and cube corner, respectively. At least 30 indents were performed on each sample using a loading duration and dwell time of 15 s

and 10 s, respectively. Measurements were performed under laboratory conditions (room temperature, relative humidity ~37% RH).

To better understand the indentation deformation mechanism (i.e., the relative propensity for densification vs. shear flow) in the different glasses, we explored the recovery of the indent side length. This analysis consists of recording images of the indent site before treatment and after a thermal treatment at  $0.9 T_g$  for 2 h [32], and then measuring how much the side length of the indent cavity shrinks after the annealing treatment. Such side length recovery is in turn related to the degree of densification upon indentation, as the densified region will recover during the  $0.9 T_g$  annealing but not the displacement due to shear flow. We explored at least 10 indents with the load of 4.9 N for each specimen, loading duration of 15 s, and dwell time of 10 s. The side length recovery ( $L_{SR}$ ) can then be calculated as,

$$L_{SR} = \frac{L_{s,i} - L_{s,f}}{L_{s,i}}, \quad (2)$$

where  $L_{s,i}$  is the indentation side length as defined from the optical microscope before the treatment and  $L_{s,f}$  is the indentation side length after annealing at  $0.9 T_g$  for 2 h.

### 3. Result and Discussion

#### 3.1. Density and Elasticity

Table 2 summarizes the density results for the CABS glasses before and after the different post-treatments. First, considering the as-prepared (annealed) glasses, we found that the density was generally higher for the glasses with 20 mol% CaO (CABS-CaB, CABS-CaSi, CABS-CaAl) than those with 15 mol% CaO (CABS-ref, CABS-SiB, CABS-BAl). This is likely because the modifying  $Ca^{2+}$  ions occupy open spaces in the network, as also seen from the variation in the atomic packing density showed in Table S2 in the Supplementary Materials. When the content of CaO was constant, the change in the proportion of  $Al_2O_3$  and  $B_2O_3$  basically had no effect on density of the glass system. Upon hot compression, we found that the density increased, consistent with the results of other oxide glass systems [15,33–36]. We quantified the extent of this increase by calculating the so-called plastic compressibility ( $\beta_{hot}$ ) as  $-(1/V)(dV/dp)$  where  $V$  is volume and  $p$  is applied pressure (see Table 2). The reference CABS glass had the highest value of  $\beta_{hot}$ . In particular, the addition of CaO and the removal of  $B_2O_3$  and  $Al_2O_3$  had a negative effect on  $\beta_{hot}$ , likely because there is less room for volume densification in these more-packed glasses with fewer B and Al that can undergo coordination number changes [2]. Generally, we found that the humid aging treatment only had a minor impact on density for both as-made and compressed samples.

**Table 2.** Density ( $\rho$ ) of the as-made, hot-compressed, humid-aged, and hot-compressed/humid-aged CABS glasses. Plastic compressibility ( $\beta_{hot}$ ), i.e., the relative increase in density upon hot compression, is also given. Coloring indicates density or plastic compressibility value of reference glass or within  $\pm 0.2\%$  (grey), increasing density or plastic compressibility relative to reference (green), and decreasing density or plastic compressibility relative to reference (red). The error in density was within  $\pm 0.002 \text{ g cm}^{-3}$ .

Glass ID	$\rho_{as-made}$ ( $\text{g cm}^{-3}$ )	$\rho_{hot}$ ( $\text{g cm}^{-3}$ )	$\rho_{aging}$ ( $\text{g cm}^{-3}$ )	$\rho_{hot-aging}$ ( $\text{g cm}^{-3}$ )	$\beta_{hot}$ ( $\text{GPa}^{-1}$ )
CABS-ref	2.411	2.556	2.430	2.563	6.01
CABS-SiB	2.424	2.552	2.403	2.541	5.28
CABS-CaB	2.539	2.634	2.541	2.637	3.74
CABS-BAl	2.395	2.515	2.388	2.515	5.01
CABS-CaSi	2.497	2.640	2.503	2.635	5.73
CABS-CaAl	2.499	2.603	2.506	2.607	4.16

Table 3 indicates the composition and the post-treatment dependence of Young's modulus ( $E$ ), which is the resistance of the glass to elastic deformation along the axis when



the opposite force is applied along the axis.  $E$  increased following hot compression for all these CABS glasses, consistent with previous findings [16].  $E$  increased up to 14 GPa, which was an increase of ~20% relative to the as-made sample. This was ascribed to the increase in atomic packing density and the increase in connectivity of the glass network. That is, in the compressed glass more bonds are stretched or broken per unit volume upon loading, which increases the resistance to deformation and results in an increase in  $E$  [12]. It can be seen from Table 3 that the changes for samples with different components in Young's modulus were similar to those for density (Table 2), and the changes in components also had an effect on the elastic modulus. Table 3 also demonstrates that the changes in  $E$  for the CABS glasses with the process of surface aging were negligible (i.e., the value was similar to those of the as-made glass).

**Table 3.** Young's moduli ( $E$ ) of the as-made, hot-compressed, humid-aged, and hot-compressed/humid-aged CABS glasses. Coloring indicates Young's moduli of reference glass (grey), increasing Young's moduli relative to reference (green), and decreasing Young's moduli relative to reference (red). The error was within  $\pm 2$  GPa.

Glass ID	$E_{as-made}$ (GPa)	$E_{hot}$ (GPa)	$E_{aging}$ (GPa)	$E_{hot-aging}$ (GPa)
CABS-ref	67	81	72	83
CABS-SiB	65	78	70	80
CABS-CaB	73	85	77	82
CABS-BAl	63	76	67	78
CABS-CaSi	72	86	72	87
CABS-CaAl	71	80	76	81

### 3.2. Glass Transition Temperature

The glass transition temperature values were determined from differential scanning calorimetry measurements (Figure S3). Among the different glasses, CABS-CaB had the highest  $T_g$  value (683 °C) and CABS-BAl had the lowest  $T_g$  value (636 °C) (Table 1). Considering the CABS-CaB glass, the ratio of CaO and  $B_2O_3$  increased relative to CABS-ref. Upon addition of more alkaline earth oxide into glass, more of the boron atoms will be converted from a three- to a four-coordinated [37–39]. As discussed above, the addition of four-coordinated boron results in a more rigid glass network, which can explain the higher  $T_g$  [40,41]. For the CABS-BAl glass, the content of  $Al_2O_3$  is lower and that of  $B_2O_3$  is higher, and the corresponding  $T_g$  value decreased accordingly. Among all the samples, the  $B_2O_3$  content in CABS-BAl was the largest (30 mol%). The high total content of  $B_2O_3$  in this glass and therefore also high amount of three-fold coordinated B makes the glass less rigid.  $^{[3]}B$  has a planar and open structure as it does not require charge compensation. This can explain the lower  $T_g$  [40,41].

### 3.3. Hardness

As shown in Table 4, there were only minor differences in the Vickers hardness ( $H_V$ ) of the as-made CABS glasses with different composition. However, it was found that the Vickers hardness ( $H_V$ ) of all samples increased after hot compression. That is,  $H_V$  increased from 5.8 to 7.0 GPa, 5.5 to 7.3 GPa, 5.6 to 7.4 GPa, 5.6 to 6.7 GPa, 5.8 to 7.1 GPa, and 6.1 to 7.3 GPa for CABS-ref, CABS-SiB, CABS-CaB, CABS-BAl, CABS-CaSi, and CABS-CaAl samples, respectively. Hardness increased by up to 1.8 GPa upon hot compression compared to the as-made sample. We also note that  $H_V$  exhibited the same pressure dependence as density, consistent with previous research [42] and indicating that the densification of the overall network is also the reason for the increase in hardness during compression. In addition, it is known that the coordination number of boron and aluminum increases after hot compression, which results in more network bonds per atom. The increase in bond density and network connectivity is the reason for the increase in hardness induced by pressure [43]. Indeed, we found an approximate positive correlation

between the atomic packing density and hardness (Figure 1). For the samples subjected to humid surface aging treatment, hardness remained almost unchanged compared with the as-made samples. This finding was also supported from the comparison between the compressed samples and the samples with combined treatment of hot compression and surface aging. The possible reason may be that there is little change or influence of surface aging on the internal structure of the glass. Since the hardness testing was performed at a load of 4.9 N, the indenter penetration depth was around 5  $\mu\text{m}$  for these samples.

**Table 4.** Vickers hardness ( $H_V$ ) of the as-made, hot-compressed, humid-aged, and hot-compressed/humid-aged CABS glasses. Coloring indicates  $H_V$  value of reference glass (grey), increasing  $H_V$  relative to reference (green), and decreasing  $H_V$  relative to reference (red). The error in hardness was within  $\pm 0.2$  GPa.

Glass ID	$H_V$ as-made (GPa)	$H_V$ hot (GPa)	$H_V$ aging (GPa)	$H_V$ hot-aging (GPa)
CABS-ref	5.82	6.96	5.70	6.88
CABS-SiB	5.54	7.31	5.97	6.96
CABS-CaB	5.62	7.39	6.11	7.66
CABS-BAl	5.58	6.72	5.50	6.69
CABS-CaSi	5.81	7.14	5.94	7.41
CABS-CaAl	6.11	7.28	6.25	7.32

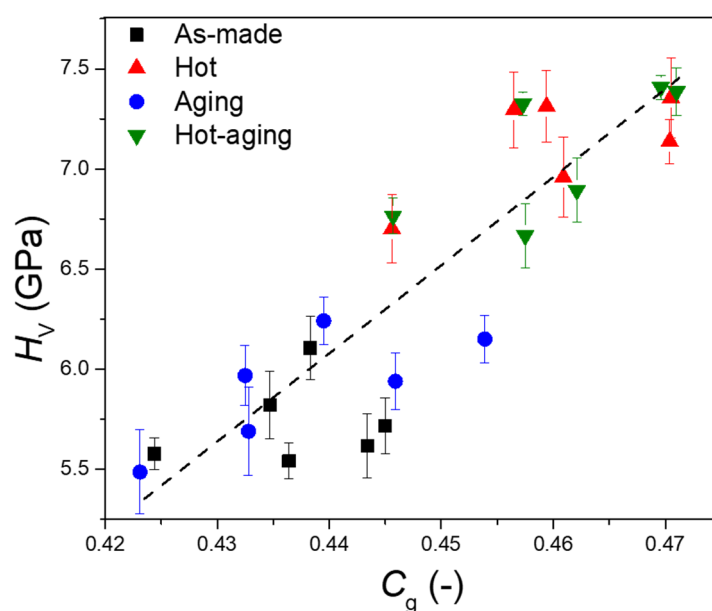


**Figure 1.** Relationship between Vickers hardness ( $H_V$ ) and atomic packing density ( $C_g$ ) of the CABS glasses subjected to different post-treatment. The dashed line is a guide to the eye.

### 3.4. Crack Resistance

Indentation-induced crack initiation occurs under a sufficiently high load due to the mismatch between the amount of plastic deformation and the surrounding elastically deformed material. We used the indentation data generated at different loads to calculate the crack resistance (CR), which is defined as the load that causes two corner cracks to form per indent for the four-sided pyramid indenter. We note that corner cracks were the main type of cracks in the investigated glass. Different experimental conditions (such as loading rate and relative humidity) and composition changes will have a significant impact on the CR value. Therefore, compared with the starting glass CABS-ref, samples with different compositions also had different values of CR.

Among the CABS glasses, CABS-BAl had the largest CR value (18.9 N) and CABS-CaB had the lowest CR value (5.6 N) for Vickers indentation (Table 5). As discussed previously,



the CABS-CaB glass has a more rigid structure that gives rise to more residual stress and thus a lower CR value. This is also seen from Figure 2 that shows the relation between CR from Vickers indentation and Vickers hardness. As the hardness increased, the crack resistance generally showed a decreasing trend. The results generally show that changing the fraction of CaO had a pronounced input on the mechanical properties, which in turn depended on the balance between the atomic bonding energies, the packing efficiency of atoms, and the ability of the network to structurally rearrange or densify. Therefore, after adding modified oxides (such as CaO), in addition to converting the three-fold coordinated B into four-fold coordinated B, the interstices are filled with modified cations. This is expected to partially hinder the indentation-induced densification and cause the glass to be more prone to deform through shear flow [44]. Alkaline earth modifier cations such as  $\text{Ca}^{2+}$  form relatively strong ionic bonds with oxygen, which also leads to higher hardness and modulus compared to alkali cations [45,46]. For the CABS-BAl glass, the ratio of  $\text{B}_2\text{O}_3$  to  $\text{Al}_2\text{O}_3$  increases and the glass thus have more three coordinated B atoms as discussed previously. As crack resistance is known to increase with increasing  $^{[3]}\text{B}$  content [47], it explains the high CR value of this glass. The positive effect of  $^{[3]}\text{B}_2\text{O}_3$  on CR is due to the relatively high single bond strength [48], with  $^{[3]}\text{BO}$  (499 kJ/mol) >  $\text{AlO}$  (293–423 kJ/mol) [49]. Moreover,  $^{[3]}\text{B}$  has an open structure as it does not require charge compensation, and  $^{[3]}\text{B}$  also has a planar structure, which makes it easier to densify and increase its coordination number during indentation.

**Table 5.** Crack resistance (CR) for Vickers indentation of the as-made, hot-compressed, humid-aged, and hot-compressed/humid-aged CABS glasses. Coloring indicates CR value of reference glass (grey), and decreasing CR relative to reference (red). The error in CR was within 15%.

Glass ID	$CR_{as-made}$ (N)	$CR_{hot}$ (N)	$CR_{aging}$ (N)	$CR_{hot-aging}$ (N)
CABS-ref	13.0	5.6	5.4	4.4
CABS-SiB	13.6	7.8	6.1	3.9
CABS-CaB	5.6	3.8	2.9	2.8
CABS-BAl	18.9	8.0	5.0	3.4
CABS-CaSi	14.5	8.4	8.1	4.6
CABS-CaAl	8.2	6.9	3.9	2.6

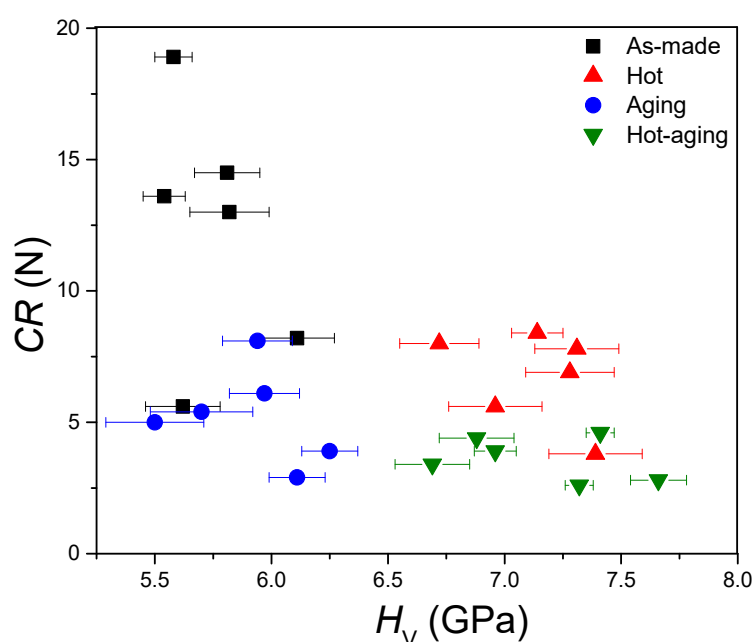


**Figure 2.** Relationship between crack resistance for Vickers indentation (CR) and hardness ( $H_V$ ) of the CABS glasses subjected to different post-treatment.

For the glasses subjected to the sharper cube corner tip (Table 6), the starting glass (CABS-ref) had the largest value of CR and CABS-BAl surprisingly had the smallest CR. This must be ascribed to different deformation mechanisms as the tip sharpness changes [5]. That is, when the tip is sharper, the glass is not able to densify as much as with the blunter Vickers tip. Therefore, the main advantage of the CABS-BAl glass (i.e., its structural densification ability) disappears.

**Table 6.** Crack resistance (CR) for cube corner indentation of the as-made, hot-compressed, humid-aged, and hot-compressed/humid-aged CABS glasses. Coloring indicates CR value of reference glass (grey), and decreasing CR relative to reference (red).

Glass ID	CR <sub>as-made</sub> (N)	CR <sub>hot</sub> (N)	CR <sub>aging</sub> (N)	CR <sub>hot-aging</sub> (N)
CABS-ref	0.58	0.46	0.15	0.12
CABS-SiB	0.96	0.54	0.28	0.11
CABS-CaB	0.82	0.33	0.27	0.14
CABS-BAl	0.43	0.38	0.16	0.07
CABS-CaSi	0.52	0.25	0.21	0.13
CABS-CaAl	0.51	0.27	0.20	0.06

Upon subsection of the glasses to compression at  $T_g$  and 1 GPa, the residual stress that drives the indentation cracking is higher than that of the as-made glass. This leads to more pronounced cracking. Therefore, the material cannot dissipate mechanical energy through densification, resulting in lower CR values under both indenter tips (Tables 5 and 6). After the humid aging treatment of the samples, the CR values of CABS glasses all decreased. On the one hand, in less chemically durable aluminoborate glasses, it has been found that CR can increase upon humid aging, for example due to a compressive stress layer [5]. On the other hand, it has been found that water can facilitate crack formation in some silicate glass [34,35]. Earlier research has also suggested that water may be causing a weakening of the glass network [50–52]. Water could also initiate cracks from a blunt crack under a subcritical stress while other liquids cannot. In the relatively durable CABS glasses, it is therefore expected that CR decreases after humid aging in the relatively low-RH atmosphere. Consequently, the combined treatment of hot compression and humid aging also decreases the CR values of these CABS glasses.

### 3.5. The Recovery of the Indentation Side Length ( $L_{SR}$ )

Table 7 shows the composition dependence of indentation side recovery ( $L_{SR}$ ) for the present as-made glasses.  $L_{SR}$  is a measure of the degree of shrinkage of a Vickers indent as caused by a thermal treatment below  $T_g$ , and previous studies have shown that  $L_{SR}$  can be used as a measure to determine the densification contribution to indentation deformation [47]. As seen in Figure 3, the indent had partially recovered its shape after annealing. CABS-BAl had the largest  $L_{SR}$  value (37.3%), while CABS-CaB had the lowest  $L_{SR}$  value (29.7%) relative to the  $L_{SR}$  value of CABS-ref (35.9%). Considering the CABS-BAl glass, it may be explained by the higher proportion of  $B_2O_3$  and thus concentration of three-fold coordinated B atoms. The open planar structure of these made it easier for the glass to densify during the indentation process and thus resulted in a higher  $L_{SR}$ . The low  $L_{SR}$  value of CABS-CaB may be because the addition of CaO converted more of the three-fold coordinated boron atoms into four-fold coordinated boron. This resulted in a more rigid structure, with less densification during the indentation process.

**Table 7.** Indentation side recovery ( $L_{SR}$ ) for the as-made calcium aluminoborosilicate glasses. The reported  $L_{SR}$  value and corresponding error are based on results from ten independent indentations.

Glass ID	CABS-Ref	CABS-SiB	CABS-CaB	CABS-BAl	CABS-CaSi	CABS-CaAl
$L_{SR}$ (%)	35.9	33.7	29.7	37.3	34.3	30.9
Error	1.8	1.9	1.8	1.2	2.0	1.8

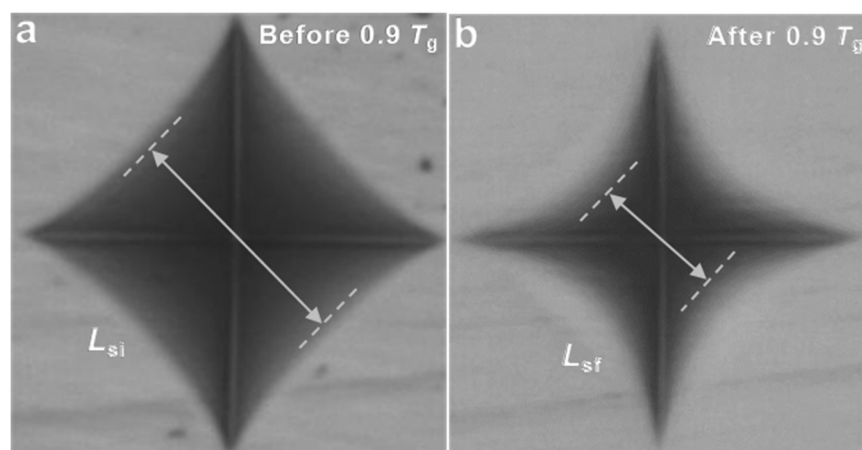


**Figure 3.** Optical micrographs of indents generated at 4.9 N on the surface of the CABS glass before and after re-annealing at  $0.9T_g$  for 2 h.

In general, CABS glasses with lower CaO content (15%) had a larger identification side recovery ( $L_{SR}$ ) value. This is also similar to the variation in CR. Figure 4 shows how CR was generally positively related to the degree of recovery and thus the extent of densification. This is in agreement with previous studies, showing that densification is favorable for increasing the crack initiation resistance as it allows the glass network to lower the residual stress, i.e., the driving force for the crack initiation.

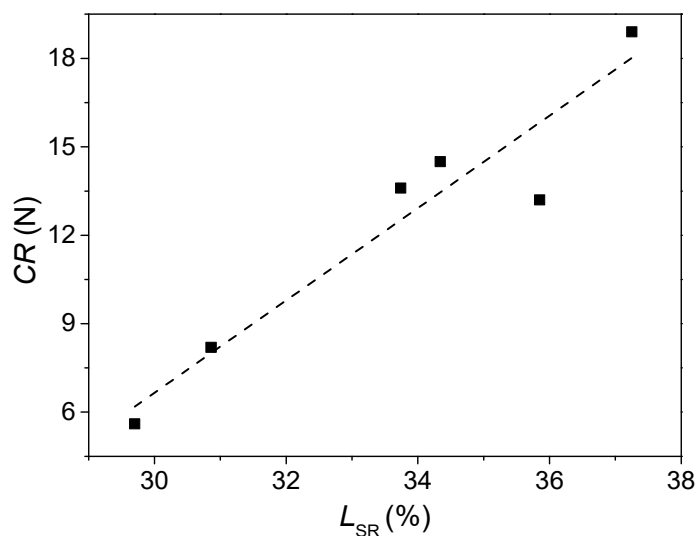


**Figure 4.** Relationship between crack resistance for Vickers indentation (CR) and indentation side recovery ( $L_{SR}$ ) of the as-made CABS glasses.

#### 4. Conclusions

We studied the mechanical properties of a series of calcium aluminoborate glasses (CABS) with different composition ratios and subjected these to two types of post-treatment, namely hot compression and humid aging. For the glasses subjected to an isostatic compression treatment at their respective  $T_g$  at the pressure of 1.0 GPa, the density, elastic moduli, and hardness increased. Young's modulus increases by up to 20% relative to the as-made sample, which was mainly due to the increase in atomic packing density. Hardness increased up to 1.8 GPa compared to the as-made sample after hot compression, which was ascribed to the increase in network connectivity and bond density. On the other hand, the crack initiation resistance decreased, as the residual stress driving the indentation cracking was higher compared in the hot compressed glass than that in the as-made glass. Upon the treatment in a humid atmosphere, only minor effects on density, modulus, and

hardness were observed, whereas the crack resistance decreased. Therefore, we can adjust the mechanical properties by changing the composition, as well as through the treatment of hot compression and humid aging. We observed positive relations between hardness and atomic packing density on one hand and crack resistance and the extent of densification on the other, while hardness and crack resistance appeared to be negatively correlated. These approaches thus provide a means to tailor the mechanical properties of glasses.

**Supplementary Materials:** The following are available online at <https://www.mdpi.com/article/10.3390/ma14133450/s1>, Figure S1: X-ray diffraction spectra of the calcium aluminoborosilicate (CABS) glasses. Figure S2: Crack probability as a function of applied indentation load for the calcium aluminoborosilicate (CABS) glasses. Figure S3: Differential scanning calorimetry heating scans of the calcium aluminoborosilicate (CABS) glasses. Table S1: Overview of the properties of the pristine glasses, including glass transition temperature ( $T_g$ ), density ( $\rho$ ), Young's modulus ( $E$ ), shear modulus ( $G$ ), bulk modulus ( $B$ ), Poisson's ratio ( $\nu$ ), Vickers hardness ( $H_v$ ), and crack resistance (CR). Table S2: Atomic packing density ( $C_g$ ) of the as-made, hot compressed, humid aged, and hot-compressed/humid-aged CABS glasses.

**Author Contributions:** Methodology: X.R., P.L., S.J.R., B.L., and M.B.; writing—original draft preparation: X.R. and M.M.S.; conceptualization and supervision: M.M.S. All authors have read and agreed to the published version of the manuscript.

**Funding:** This research was funded by the China Scholarship Council (CSC No. 201906250152).

**Institutional Review Board Statement:** Not applicable.

**Informed Consent Statement:** Not applicable.

**Data Availability Statement:** The data presented in this study are available on reasonable request from the corresponding author.

**Conflicts of Interest:** The authors declare no conflict of interest.

## References

- Rosales-Sosa, G.A.; Masuno, A.; Higo, Y.J.; Inoue, H. Crack-resistant  $\text{Al}_2\text{O}_3$ - $\text{SiO}_2$  glasses. *Sci. Rep.* **2016**, *6*, 23620. [CrossRef] [PubMed]
- Januchta, K.; Youngman, R.E.; Goel, A.; Bauchy, M.; Logunov, S.L.; Rzoska, S.J.; Bockowski, M.; Jensen, L.R.; Smedskjaer, M.M. Discovery of ultra-crack-resistant oxide glasses with adaptive networks. *Chem. Mater.* **2017**, *29*, 5865–5876. [CrossRef]
- Mauro, J.C.; Tandia, A.; Vargheese, K.D.; Mauro, Y.Z.; Smedskjaer, M.M. Accelerating the design of functional glasses through modeling. *Chem. Mater.* **2016**, *28*, 4267–4277. [CrossRef]
- Kistler, S.S. Stresses in glass produced by nonuniform exchange of monovalent ions. *J. Am. Ceram. Soc.* **1962**, *45*, 59–68. [CrossRef]
- Gross, T.M. Deformation and cracking behavior of glasses indented with diamond tips of various sharpness. *J. Non-Cryst. Solids* **2012**, *358*, 3445–3452. [CrossRef]
- Zanotto, E.D.; Coutinho, F.A.B.J. How many non-crystalline solids can be made from all the elements of the periodic table? *J. Non-Cryst. Solids* **2004**, *347*, 285. [CrossRef]
- Lee, S.K.; Eng, P.J.; Mao, H.-K.; Meng, Y.; Newville, M.; Hu, M.Y.; Shu, J. Probing of Bonding Changes in  $\text{B}_2\text{O}_3$  Glasses at High Pressure with Inelastic X-Ray Scattering. *Nat. Mater.* **2005**, *4*, 851–854. [CrossRef]
- Gross, T.M.; Wu, J.; Baker, D.E.; Price, J.J.; Yongsunthon, R. Crack-resistant glass with high shear band density. *J. Non-Cryst. Solids* **2018**, *494*, 13–20. [CrossRef]
- Morin, E.I.; Stebbins, J.F. Separating the effects of composition and fictive temperature on Al and B coordination in Ca, La, Y aluminosilicate, aluminoborosilicate and aluminoborate glasses. *J. Non-Cryst. Solids* **2016**, *432*, 384–392. [CrossRef]
- Yoffe, E.H. Elastic stress fields caused by indenting brittle materials. *Philos. Mag. A* **1982**, *46*, 617. [CrossRef]
- Motke, S.G.; Yawale, S.P.; Yawale, S.S. Infrared spectra of zinc doped lead borate glasses. *Bull. Mater. Sci.* **2002**, *25*, 75–78. [CrossRef]
- Januchta, K.; Youngman, R.E.; Goel, A.; Bauchy, M.; Rzoska, S.J.; Bockowski, M.; Smedskjaer, M.M. Structural origin of high crack resistance in sodium aluminoborate glasses. *J. Non-Cryst. Solids* **2017**, *460*, 54–65. [CrossRef]
- Tatsumisago, M.; Morimoto, H.; Yamashita, H.; Minami, T. Preparation of amorphous solid electrolytes in the system  $\text{Li}_2\text{S}$ - $\text{SiS}_2$ - $\text{Li}_4\text{SiO}_4$  by mechanical milling. *Solid State Ion.* **2000**, *136–137*, 483–488. [CrossRef]
- Guerette, M.; Ackerson, M.R.; Thomas, J.; Yuan, F.; Watson, E.B.; Walker, D.; Huang, L. Structure and properties of silica glass densified in cold compression and hot compression. *Sci. Rep.* **2015**, *5*, 15343. [CrossRef]

15. Svenson, M.N.; Bechgaard, T.K.; Fuglsang, S.D.; Pedersen, R.H.; Tjell, A.Ø.; Østergaard, M.B.; Youngman, R.E.; Mauro, J.C.; Rzoska, S.J.; Bockowski, M.; et al. Composition-Structure-Property Relations of Compressed Borosilicate Glasses. *Phys. Rev. Appl.* **2014**, *2*, 024006. [\[CrossRef\]](#)
16. Striepe, S.; Smedskjaer, M.M.; Deubener, J.; Bauer, U.; Behrens, H.; Potuzak, M.; Youngman, R.E.; Mauro, J.C.; Yue, Y. Elastic and micromechanical properties of isostatically compressed soda-lime-borate glasses. *J. Non-Cryst. Solids* **2013**, *364*, 44–52. [\[CrossRef\]](#)
17. Koch, C.C. Amorphization of single composition powders by mechanical milling. *Scr. Mater.* **1996**, *34*, 21–27. [\[CrossRef\]](#)
18. Fukunaga, T.; Kajikawa, S.; Hokari, Y.; Mizutani, U. The structure of amorphous Se-S prepared by mechanical alloying. *J. Non-Cryst. Solids* **1998**, *232–234*, 465–469. [\[CrossRef\]](#)
19. Esaka, T.; Takai, S.; Nishimura, N.; Kagaku, D. Preparation of the Bi<sub>2</sub>O<sub>3</sub>-based Fluorite-type solid solutions by mechanical alloying. *Denki Kagaku* **1996**, *64*, 1021. [\[CrossRef\]](#)
20. Luo, J.W.; Huynh, H.; Pantano, C.G.; Kim, S.H. Hydrothermal reactions of soda lime silica glass- Revealing subsurface damage and alteration of mechanical properties and chemical structure of glass surfaces. *J. Non-Cryst. Solids* **2016**, *452*, 93–101. [\[CrossRef\]](#)
21. Gross, T.M.; Guryanov, G.M. Water-Containing Glass-Based Articles with High Indentation Cracking Threshold. U.S. Patent 2019/0152838 A1, 23 May 2019.
22. Striepe, S.; Deubener, J.; Smedskjaer, M.M.; Potuzak, M. Environmental effects on fatigue of alkaline earth aluminosilicate glass with varying fictive temperature. *J. Non-Cryst. Solids* **2013**, *379*, 161–168. [\[CrossRef\]](#)
23. Januchta, K.; Stepniewska, M.; Jensen, L.R.; Zhang, Y.; Somers, M.A.J.; Bauchy, M.; Yue, Y.; Smedskjaer, M.M. Breaking the limit of micro-ductility in oxide glasses. *Adv. Sci.* **2019**, *6*, 1901281. [\[CrossRef\]](#)
24. Gross, T.M.; Sarafian, A.R.; Wu, J.S.; Zheng, Z.M. Water Vapor Strengthenable Alkali-Free Glass Compositions. U.S. Patent 2020/0156995 A1, 21 May 2020.
25. Gross, T.M.; Sarafian, A.R.; Wu, J.S.; Zheng, Z.M. Glass Compositions and Methods for Strengthening via Steam Treatment. U.S. Patent 2020/0156996 A1, 21 May 2020.
26. Tomozawa, M.; Aaldenberg, E.M. The role of water in surface stress relaxation of glass. *Phys. Chem. Glasses Eur. J. Glass Sci. Technol. Part B* **2017**, *58*, 156–164. [\[CrossRef\]](#)
27. Liu, P.F.; Youngman, R.E.; Jensen, L.R.; Bockowski, M.; Smedskjaer, M.M. Achieving ultrahigh crack resistance in glass through humid aging. *Phys. Rev. Mater.* **2020**, *4*, 063606. [\[CrossRef\]](#)
28. Shannon, R.D. Revised effective ionic radii and systematic studies of interatomic distances in halides and chalcogenides. *Acta Cryst. A* **1976**, *32*, 751–767. [\[CrossRef\]](#)
29. Whittaker, E.J.W.; Muntus, R. Ionic radii for use in geochemistry. *Geochimica Cosmochimica Acta* **1970**, *34*, 945–956. [\[CrossRef\]](#)
30. Rouxel, T. Elastic Properties and Short-to Medium-Range Order in Glasses. *J. Am. Ceram. Soc.* **2007**, *90*, 3019–3039. [\[CrossRef\]](#)
31. Wada, M.; Furukawa, H.; Fujita, K. Crack resistance of glass on Vickers indentation. *Proc. Int. Congr. Glass* **1974**, *11*, 39–46.
32. Yoshida, S.; Sanglebeuf, J.C.; Rouxel, T. Quantitative evaluation of indentation-induced densification in glass. *J. Mater. Res.* **2005**, *20*, 3404–3412. [\[CrossRef\]](#)
33. Uhlmann, D.R. Densification of alkali silicate glasses at high pressure. *J. Non-Cryst. Solids* **1973**, *13*, 89–99. [\[CrossRef\]](#)
34. Hirao, K.; Zhang, Z.; Morita, H.; Soga, N. Effect of densification treatment on the mechanical properties of borate glasses. *J. Soc. Mater. Sci. Jpn.* **1991**, *40*, 400–404. [\[CrossRef\]](#)
35. Wondraczek, L.; Sen, S.; Behrens, H.; Youngman, R.E. Structure-energy map of alkali borosilicate glasses: Effects of pressure and temperature. *Phys. Rev. B* **2007**, *76*, 014202. [\[CrossRef\]](#)
36. Smedskjaer, M.M. Indentation size effect and the plastic compressibility in glass. *Appl. Phys. Lett.* **2014**, *104*, 251906. [\[CrossRef\]](#)
37. Varshneya, A.K. *Fundamentals of Inorganic Glasses*; Society of Glass Technology: Sheffield, UK, 2006.
38. Jellison, G.E.; Panek, L.W.; Bray, P.J.; Rouse, G.B. Determinations of structure and bonding in vitreous B<sub>2</sub>O<sub>3</sub> by means of B<sup>10</sup>, B<sup>11</sup>, and O<sup>17</sup> NMR. *J. Chem. Phys.* **1977**, *66*, 802–812. [\[CrossRef\]](#)
39. Youngman, R.E.; Zwanziger, J.W. Multiple boron sites in borate glass detected with dynamic angle spinning nuclear magnetic resonance. *J. Non-Cryst. Solids* **1994**, *168*, 293–297. [\[CrossRef\]](#)
40. Micolaut, M.; Naumis, G.G. Glass transition temperature variation crosslinking and structure in network glasses: A stochastic approach. *Europhys. Lett.* **1999**, *47*, 568. [\[CrossRef\]](#)
41. Januchta, K.; Bauchy, M.; Youngman, R.E.; Rzoska, S.J.; Bockowski, M.; Smedskjaer, M.M. Modifier field strength effects on densification behavior and mechanical properties of alkali aluminoborate glasses. *Phys. Rev. Mater.* **2017**, *1*, 063603. [\[CrossRef\]](#)
42. Svenson, M.N.; Guerette, M.; Huang, L.; Lönnroth, N.; Mauro, J.C.; Rzoska, S.J.; Bockowski, M.; Smedskjaer, M.M. Universal behavior of changes in elastic moduli of hot compressed oxide glasses. *Chem. Phys. Lett.* **2016**, *651*, 88–91. [\[CrossRef\]](#)
43. Kapoor, S.; Wondraczek, L.; Smedskjaer, M.M. Pressure-induced densification of oxide glasses at the glass transition. *Front. Mater.* **2017**, *4*, 1. [\[CrossRef\]](#)
44. Arora, A.; Marshall, D.B.; Lawn, B.R.; Swain, M.V. Indentation deformation/fracture of normal and anomalous glasses. *J. Non-Cryst. Solids* **1979**, *31*, 415. [\[CrossRef\]](#)
45. Yamane, M.; Mackenzie, J. Vicker's Hardness of glass. *J. Non-Cryst. Solids* **1974**, *15*, 153. [\[CrossRef\]](#)
46. Weigel, C.; Le Losq, C.; Vialla, R.; Dupas, C.; Clément, S.; Neuville, D.R.; Rufflé, B. Elastic moduli of XAlSiO<sub>4</sub> aluminosilicate glasses: Effects of charge-balancing cations. *J. Non-Cryst. Solids* **2016**, *447*, 267. [\[CrossRef\]](#)
47. Kato, Y.; Yamazaki, H.; Kubo, Y.; Yoshida, S.; Matsuoka, J.; Akai, T. Effect of B<sub>2</sub>O<sub>3</sub> content on crack initiation under vickers indentation test. *J. Ceram. Soc. Jpn.* **2010**, *118*, 792–798. [\[CrossRef\]](#)

- 
48. Januchta, K.; Liu, P.F.; Hansen, S.R.; To, T.; Smedskjaer, M.M. Indentation cracking and deformation mechanism of sodium aluminoborosilicate glasses. *J. Am. Ceram. Soc.* **2020**, *103*, 1656–1665. [[CrossRef](#)]
  49. Sun, K.H. Fundamental condition of glass formation. *J. Am. Ceram. Soc.* **1947**, *30*, 277–281. [[CrossRef](#)]
  50. Hirao, K.; Tomozawa, M. Dynamic Fatigue of Treated High-Silica Glass: Explanation by Crack Tip Blunting. *J. Am. Ceram. Soc.* **1987**, *70*, 377–382. [[CrossRef](#)]
  51. Wakabayashi, H.; Tomorawa, M. Effect of Ammonia on Static Fatigue of Silica Glass. *J. Non-Cryst. Solids* **1988**, *102*, 95–99. [[CrossRef](#)]
  52. Hirao, K.; Tomozawa, M. Microhardness of SiO<sub>2</sub> Glass in Various Environments. *J. Am. Ceram. Soc.* **1987**, *70*, 497–502. [[CrossRef](#)]



# Indentation Response of Calcium Aluminoborosilicate Glasses Subjected to Humid Aging and Hot Compression

Xiangting Ren <sup>1</sup>, Pengfei Liu <sup>1</sup>, Sylwester J. Rzoska <sup>2</sup>, Boleslaw Lucznik <sup>2</sup>, Michal Bockowski <sup>2</sup> and Morten M. Smedskjaer <sup>1,\*</sup>

<sup>1</sup> Department of Chemistry and Bioscience, Aalborg University, 9220 Aalborg, Denmark; xiangtingr@bio.aau.dk (X.R.); pli@bio.aau.dk (P.L.)

<sup>2</sup> Institute of High-Pressure Physics, Polish Academy of Sciences, 01-142 Warsaw, Poland; sylwester.rzoska@gmail.com (S.J.R.); bolo@unipress.waw.pl (B.L.); bocian@unipress.waw.pl (M.B.)

\* Correspondence: mos@bio.aau.dk

**Citation:** Ren, X.; Liu, P.; Rzoska, S.J.; Lucznik, B.; Bockowski, M.; Smedskjaer, M.M. Indentation Response of Calcium Aluminoborosilicate Glasses Subjected to Humid Aging and Hot Compression. *Materials* **2021**, *14*, x. <https://doi.org/10.3390/xxxxx>

Academic Editor(s): Halina Kaczmarek

Received: date

Accepted: date

Published: date

**Publisher's Note:** MDPI stays neutral with regard to jurisdictional claims in published maps and institutional affiliations.



**Copyright:** © 2021 by the authors. Submitted for possible open access publication under the terms and conditions of the Creative Commons Attribution (CC BY) license (<http://creativecommons.org/licenses/by/4.0/>).

## Supporting information

**Table S1.** Overview of the properties of the pristine glasses, including glass transition temperature ( $T_g$ ), density ( $\rho$ ), Young's modulus ( $E$ ), shear modulus ( $G$ ), bulk modulus ( $B$ ), Poisson's ratio ( $\nu$ ), Vickers hardness ( $H_v$ ), and crack resistance ( $CR$ ).

Glass ID	$T_g$ [°C]	$\rho$ [g/cm <sup>3</sup> ]	$E$ [GPa]	$G$ [GPa]	$B$ [GPa]	$\nu$ [-]	$H_v^{(1)}$ [GPa]	$CR^{(2)}$ (Vickers) [N]	$CR^{(2)}$ (cube) [N]
CABS-ref	677	2.411	67	26	47	0.260	5.82	13.0	0.5
CABS-SiB	652	2.424	65	26	47	0.267	5.54	13.6	1.0
CABS-CaB	683	2.539	73	28	55	0.275	5.62	5.6	0.8
CABS-BAl	636	2.395	63	25	42	0.249	5.58	18.9	0.4
CABS-CaSi	668	2.497	72	28	51	0.261	5.81	14.5	0.5
CABS-CaAl	665	2.499	71	28	46	0.244	6.11	8.2	0.5

(1)  $H_v$  measured at ambient conditions at load of 9.8 N (1 kgf).

(2)  $CR$  measured at ambient conditions (temperature 23.5±1 °C, relative humidity ~37%).



**Table S2.** Atomic packing density ( $C_g$ ) of the as-made, hot compressed, humid aged, and hot-compressed/humid-aged CABS glasses. Coloring indicates reference density (grey), increasing density relative to reference (green), and decreasing density relative to reference (red). The error in  $C_g$  is within  $\pm 0.001$ .

Glass ID	$C_{g \text{ as-made}}$	$C_{g \text{ hot}}$	$C_{g \text{ aging}}$	$C_{g \text{ hot-aging}}$
CABS-ref	0.434	0.461	0.438	0.462
CABS-SiB	0.436	0.459	0.433	0.457
CABS-CaB	0.453	0.470	0.454	0.470
CABS-BAl	0.424	0.445	0.423	0.446
CABS-CaSi	0.444	0.470	0.446	0.469
CABS-CaAl	0.438	0.456	0.439	0.457

**Figure S1.** X-ray diffraction spectra of the calcium aluminoborosilicate (CABS) glasses.

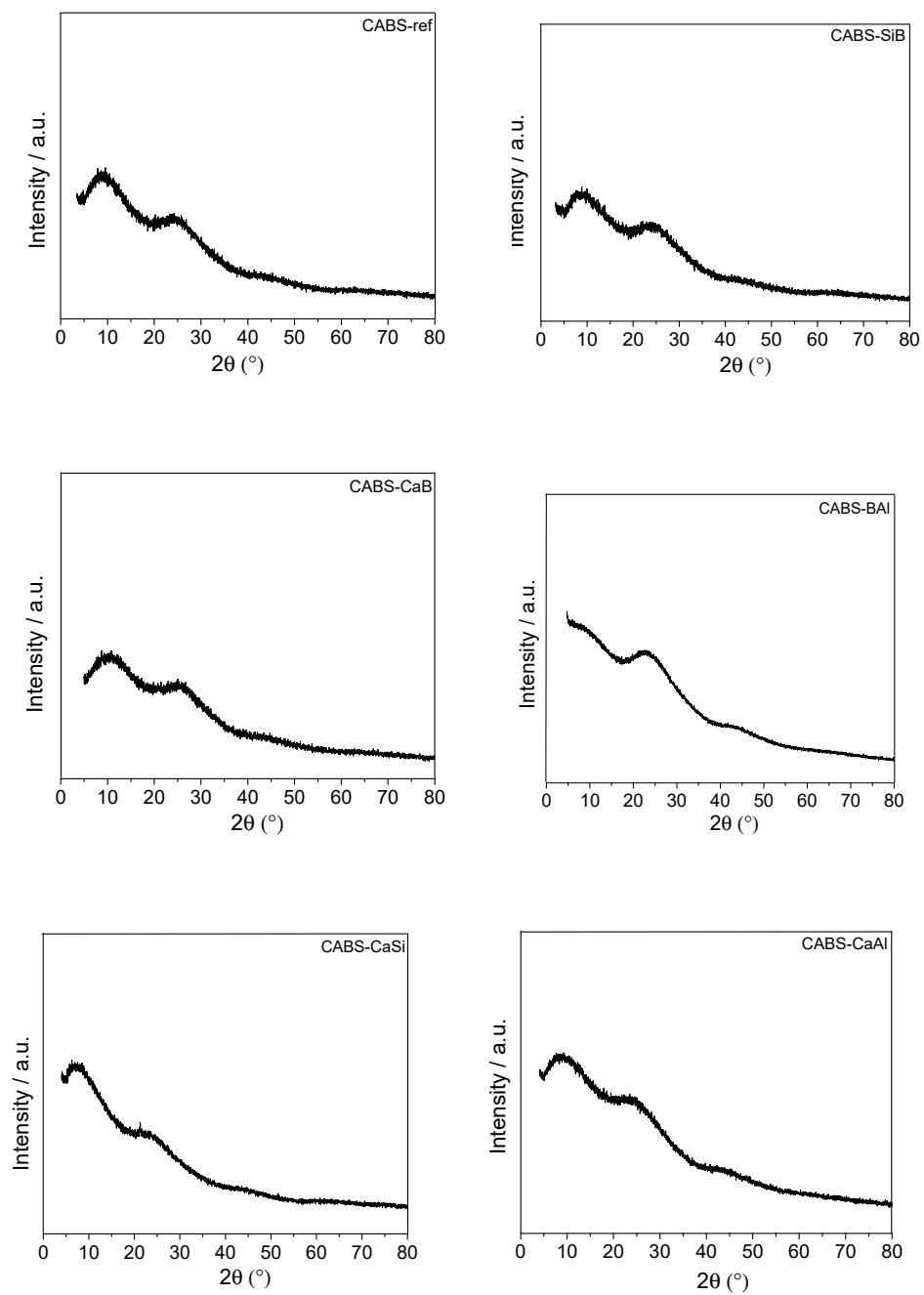
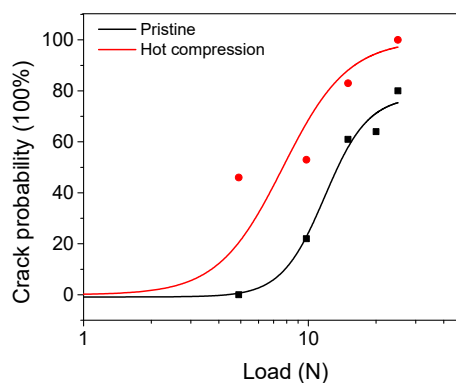
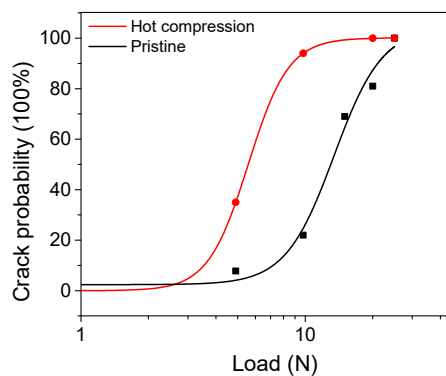


**Figure S2.** Crack probability as a function of applied indentation load for the calcium aluminoborosilicate (CABS) glasses. The experimental data was fit to a sigmoidal function of the form  $y = A_2 + (A_1 - A_2)/[1 + (x/x_0)^p]$  (solid lines).

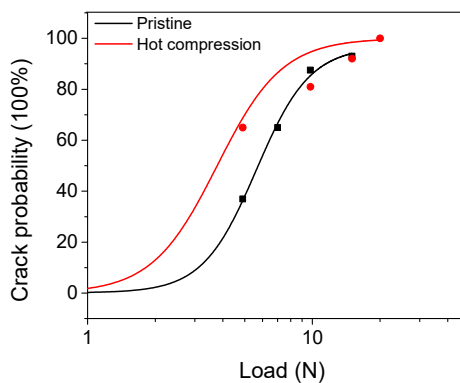
a. CABS (Hot compression) – Vickers indenter



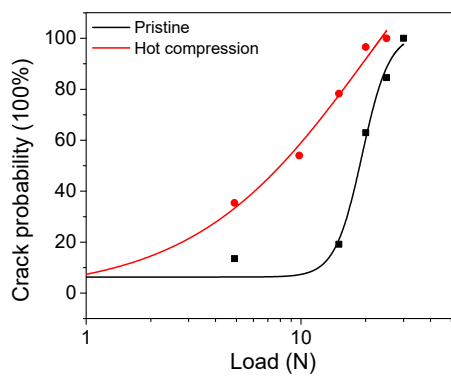
**CABS-ref**



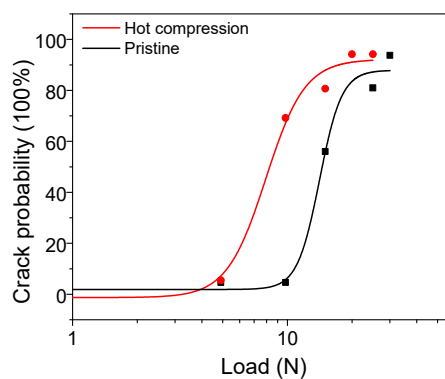
**CABS-SiB**



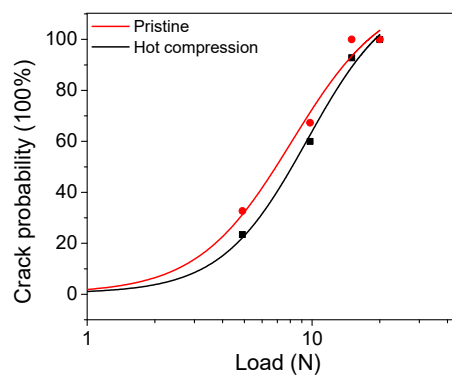
**CABS-CaB**



**CABS-BAl**

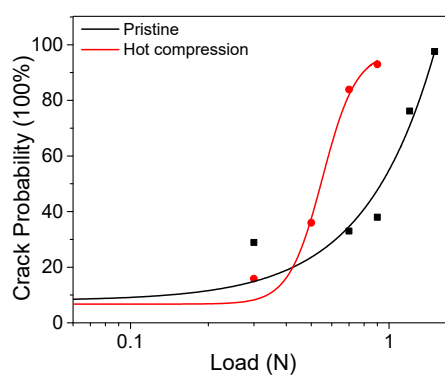


CABS-CaSi

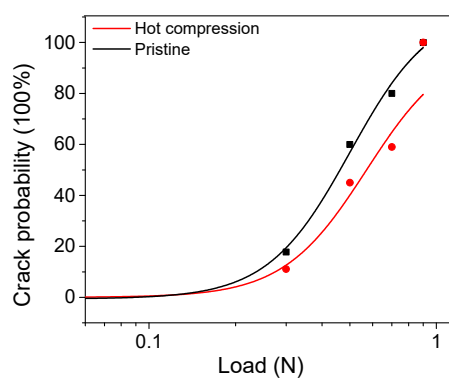


CABS-CaAl

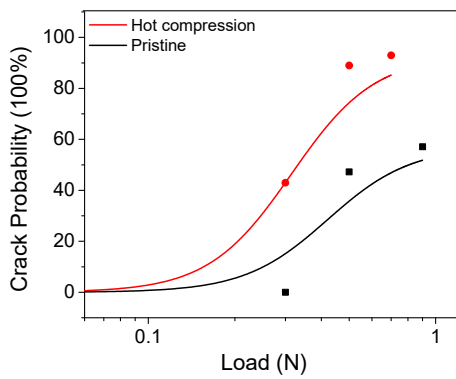
b. CABS (Hot compression) – cube corner indenter



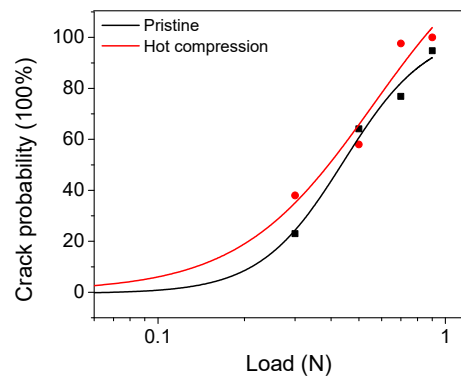
CABS-ref



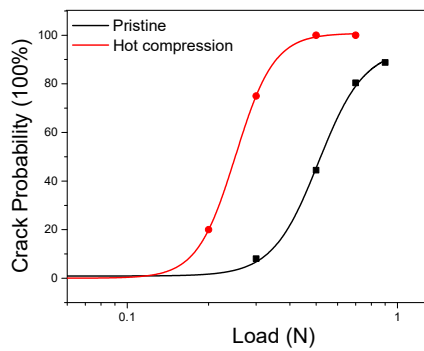
CABS-SiB



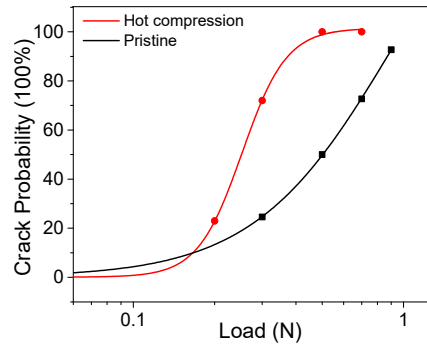
CABS-CaB



CABS-BAl

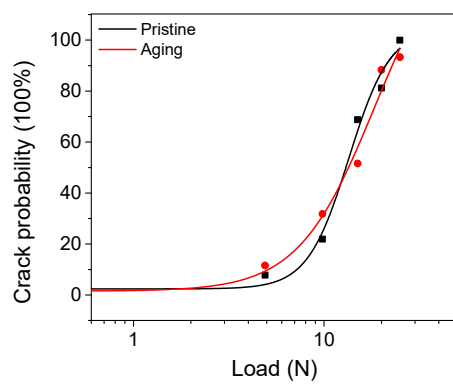
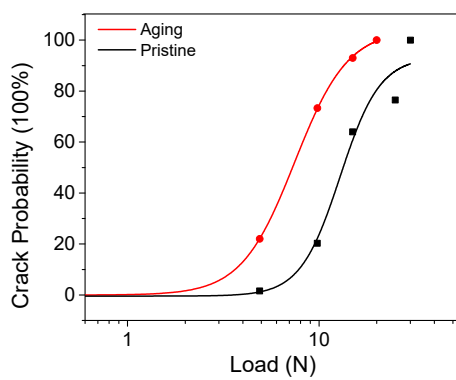


CABS-CaSi

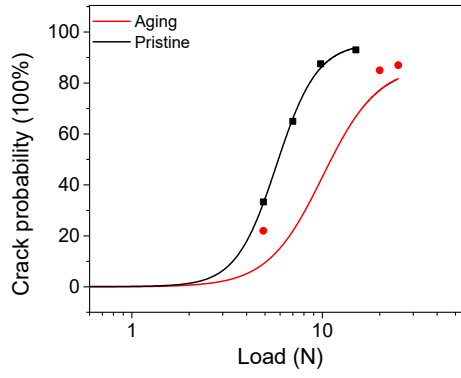


CABS-CaAl

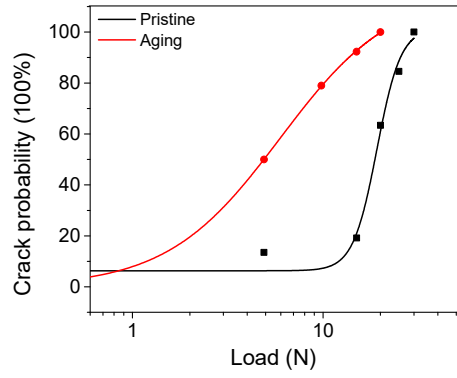
c. CABS (Humid Aging) – Vickers indenter



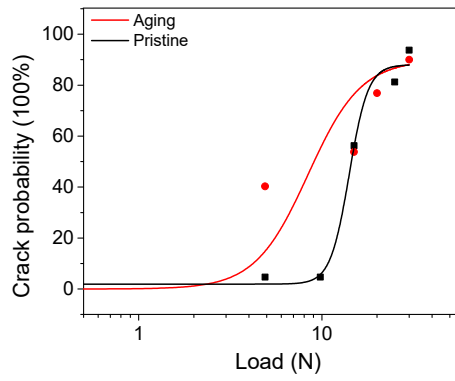
**CABS-ref**



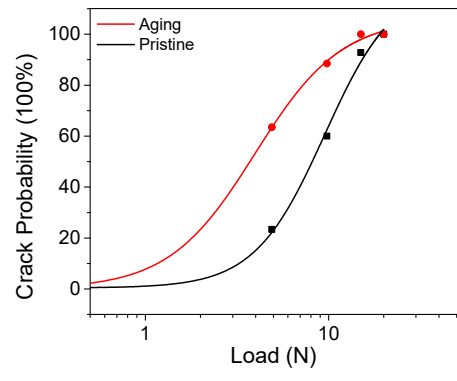
**CABS-SiB**



**CABS-CaB**



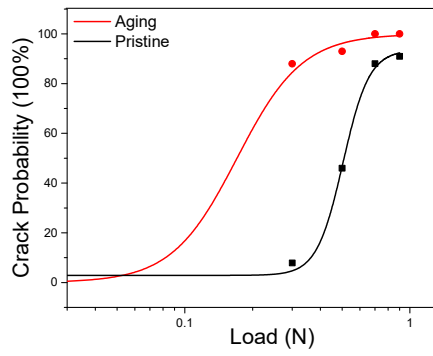
**CABS-BAI**



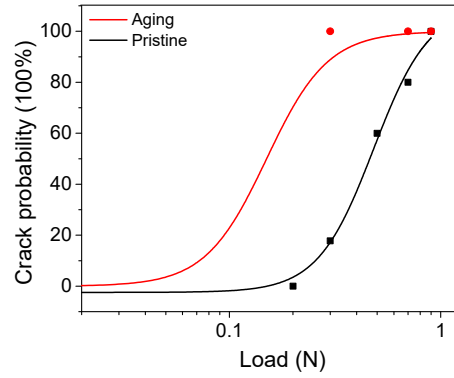
**CABS-CaSi**



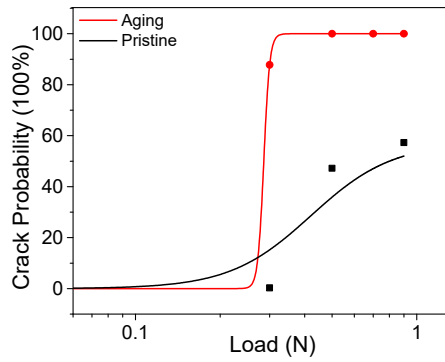
d. CABS (Humid Aging) - cube corner indenter



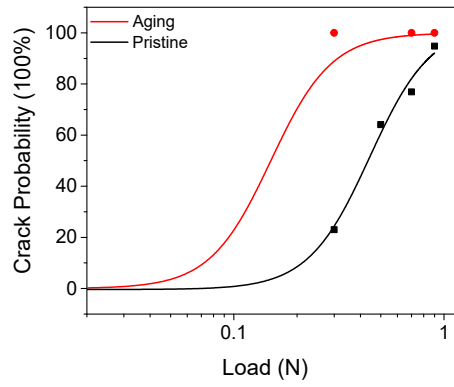
CABS-ref



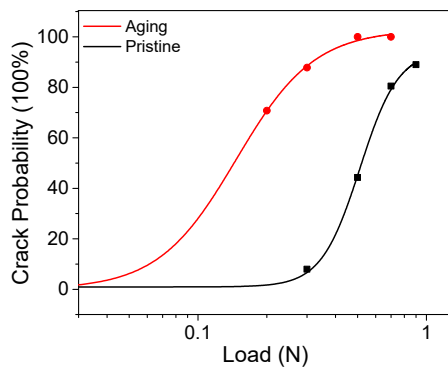
CABS-SiB



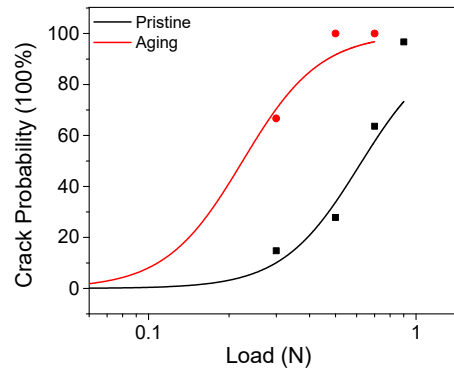
CABS-CaB



CABS-BAl

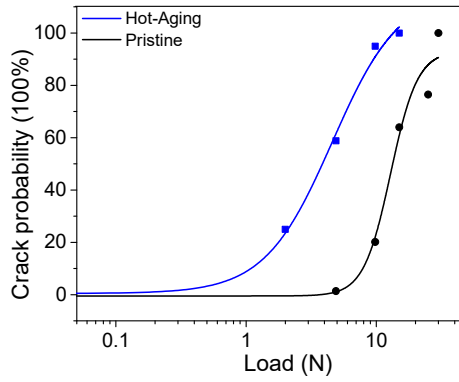


CBAS-CaSi

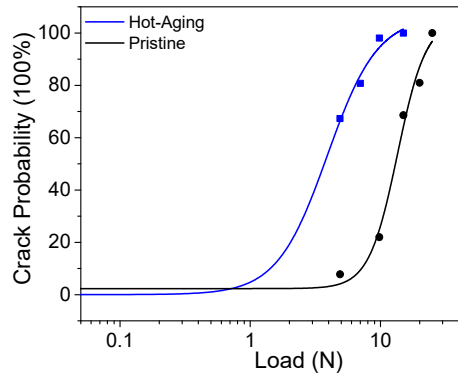


CABS-CaAl

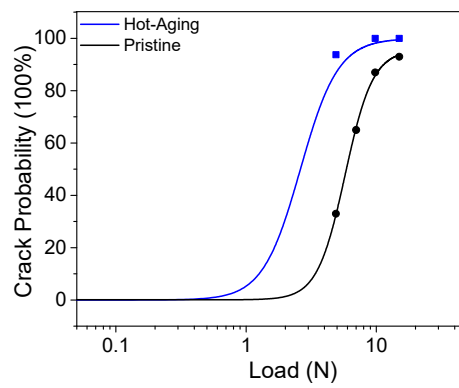
e. CABS (Hot-Aging) – Vickers indenter



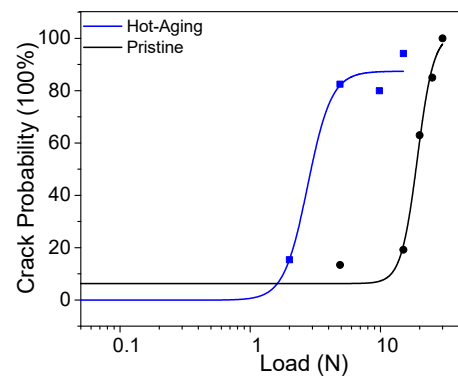
CABS-ref



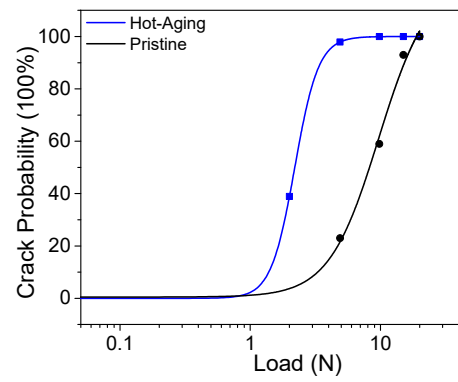
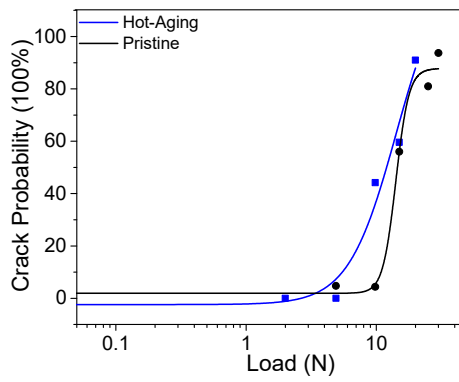
CABS-SiB



CABS-CaB



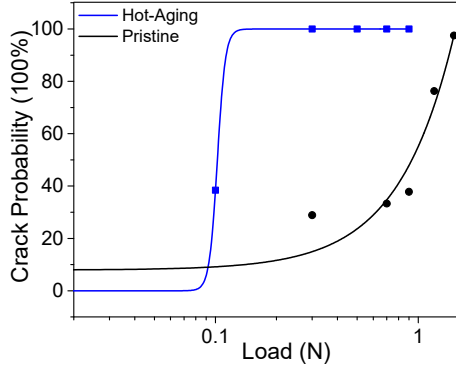
CABS-BAI



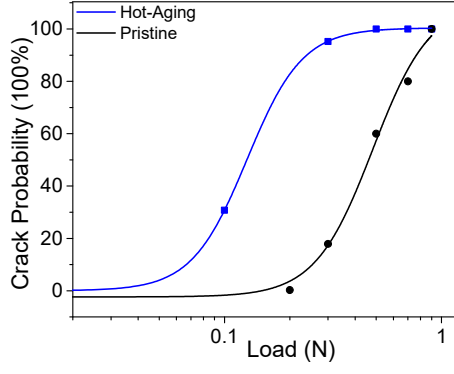


CABS-CaSi

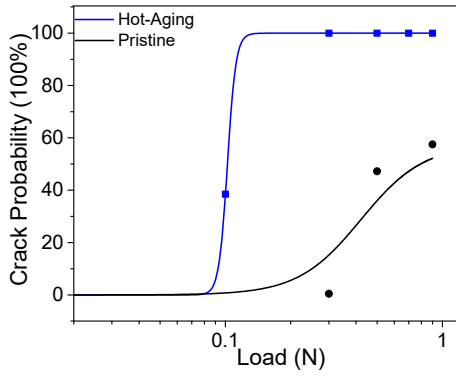
f. CABS (Hot-Aging) – cube corner indenter



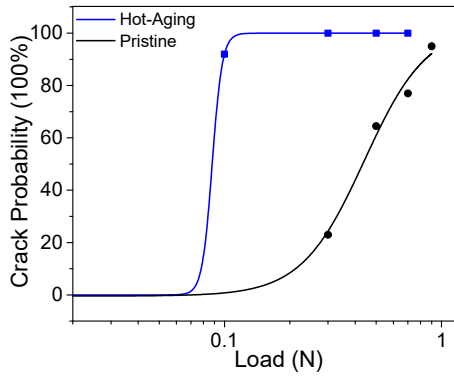
CABS-CaAl



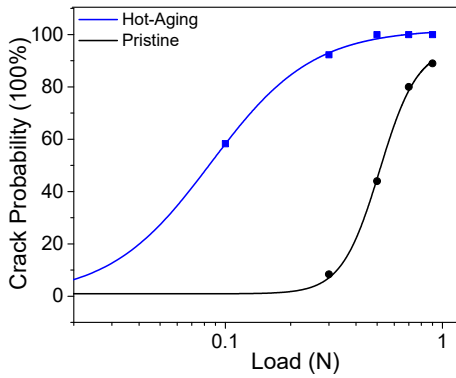
CABS-ref



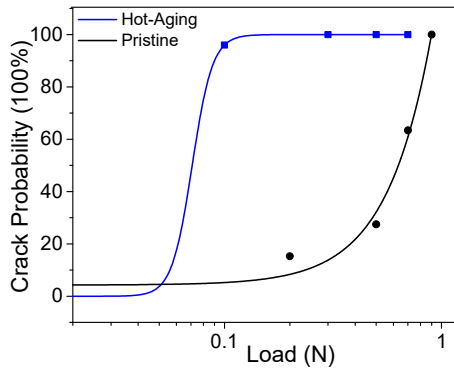
CABS-SiB



CABS-CaB



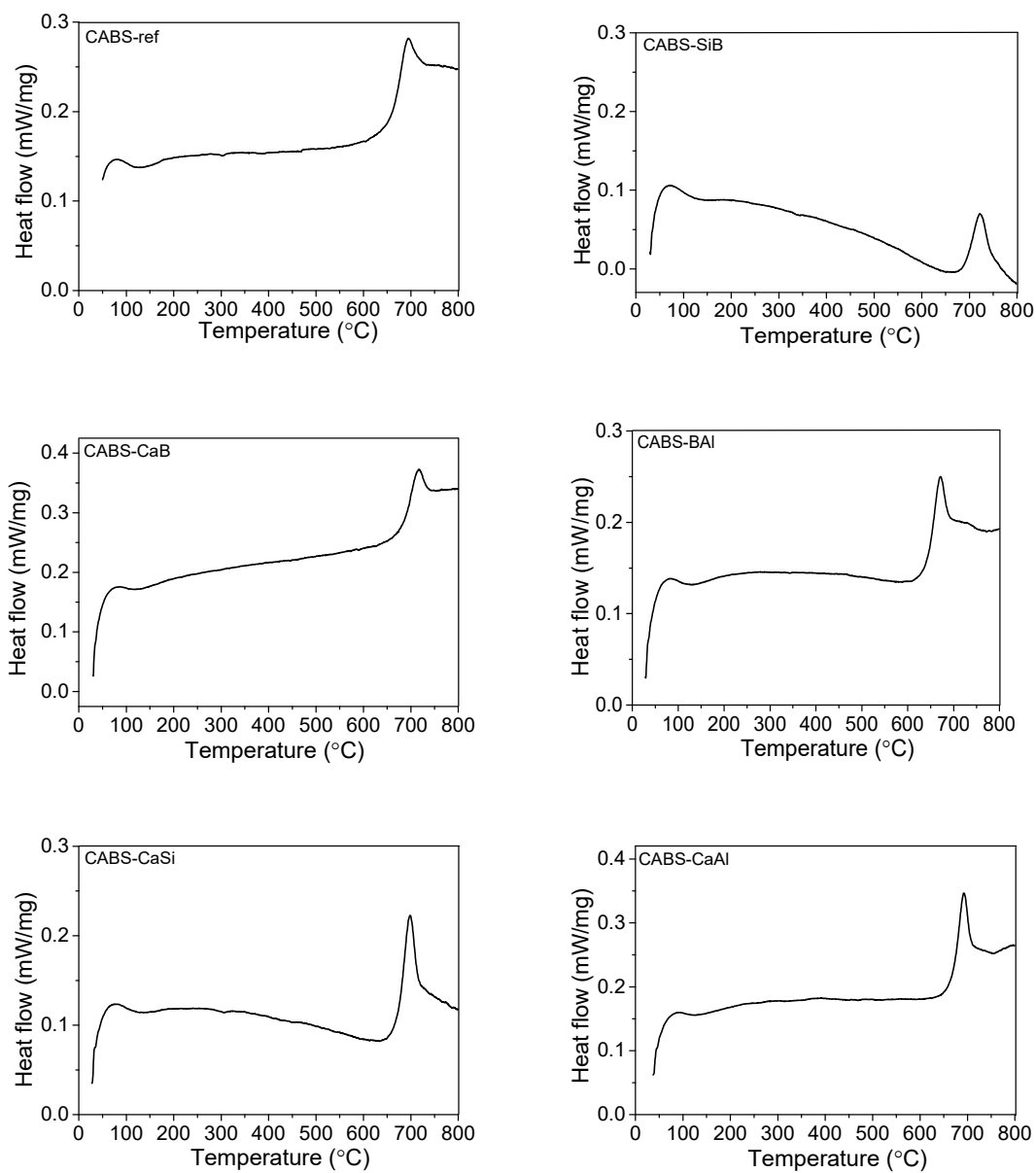
CABS-BAl



CABS-CaSi

CABS-CaAl

Figure S3. Differential scanning calorimetry heating scans of the calcium aluminoborosilicate (CABS) glasses.



# Paper III



# Irradiation-induced toughening of calcium aluminoborosilicate glasses

Xiangting Ren<sup>a,1</sup>, Tao Du<sup>a,1</sup>, Haibo Peng<sup>b</sup>, Lars R. Jensen<sup>c</sup>, Christophe A.N. Biscio<sup>d</sup>,  
Lisbeth Fajstrup<sup>d</sup>, Mathieu Bauchy<sup>e</sup>, Morten M. Smedskjaer<sup>a,\*</sup>

<sup>a</sup> Department of Chemistry and Bioscience, Aalborg University, Aalborg East 9220, Denmark

<sup>b</sup> School of Nuclear Science and Technology, Lanzhou University, Lanzhou 730000, China

<sup>c</sup> Department of Materials and Production, Aalborg University, Aalborg East 9220, Denmark

<sup>d</sup> Department of Mathematical Sciences, Aalborg University, Aalborg East 9220, Denmark

<sup>e</sup> Department of Civil and Environmental Engineering, University of California, Los Angeles, CA 90095, USA

## ARTICLE INFO

### Keywords:

Oxide glasses

Mechanical properties

Indentation

Irradiation

Molecular dynamics simulations

## ABSTRACT

Methods to improve the fracture toughness and strength of glassy materials are increasingly important for a variety of applications that remain limited by the restrictions of brittleness and surface defect propensity. Here, we report on the enhancement of glass mechanical performance through a combination of a tailored chemistry and irradiation post-treatment. Specifically, we show through both experiments and atomistic simulations that the defect (crack) initiation resistance as well as the fracture toughness of selected calcium aluminoborosilicate glasses can be significantly improved (by more than 400% in some cases) through heavy ion irradiation. The ion irradiation process reorganizes the borate subnetwork through a partial transformation of tetrahedral to trigonal boron units, which in turn also modifies the glass at longer lengths scales, such as through a coarsening in the distribution of loop structures. The improvement in both the resistance to crack formation and crack growth is ascribed to the modification of the medium-range glass structure as well as the less rigid network structure upon irradiation with coordination defects that act as local reservoirs of plasticity by allowing more bond switching activities to dissipate mechanical energy upon deformation. This work therefore highlights a new pathway to develop damage-resistant glass materials.

## 1. Introduction

Low practical strength and brittleness are the main bottlenecks for present and future applications of oxide glasses [1]. Different strengthening methods have been attempted [2], including composition optimization, ion exchange, and pressure treatment. Consistent with the lack of macroscopic brittleness, both molecular dynamics (MD) simulations and experiments suggest the existence of nanoscale ductility in some glasses [3–5]. By nanoscale ductility, we refer to the glasses' ability to deform plastically on the nanometer length scale. For example, flaw-free thin films of amorphous alumina exhibit pronounced plasticity at a high strain rate, which was attributed to bond switching events at the nanoscale, leading to mechanical relaxation and accumulating into macroscopic plastic flow [5]. Additionally, the propensity for bond switching activities of amorphous alumina is encoded in its static structure, which is correlated with the atomic environment of individual Al atoms [6]. Bulk oxide glasses typically exhibit fracture toughness

values in the range of 0.5–1 MPa m<sup>0.5</sup>, with all commercially available oxide glasses currently below a value of 1 MPa m<sup>0.5</sup> [7–9], as measured using self-consistent methods. Fracture toughness values up to 1.17 MPa m<sup>0.5</sup> have been reported in rare earth containing aluminosilicate glasses [10]. Moreover, in our recent work, we have shown that understanding of nanoscale bond switching activities can be exploited at a larger scale, as we reported a record-high fracture toughness (1.4 MPa m<sup>0.5</sup>) in a bulk oxide glass with high propensity for bond switching [11]. As such, an improved understanding of deformation and fracture mechanisms of glasses at the nanoscale is needed to improve their mechanical performance at the macroscale.

Testing the mechanical properties of glasses by indentation has been a popular method, since it can mimic some types of real-life damage events under controlled conditions [12,13]. That is, sharp contact with a high local stress is the main failure mode in many applications. According to the Vickers indentation response, glasses can be classified as normal, intermediate, or anomalous [14]. Normal glasses deform to a

\* Corresponding author.

E-mail address: [mos@bio.aau.dk](mailto:mos@bio.aau.dk) (M.M. Smedskjaer).

<sup>1</sup> These authors contributed equally.

large extent due to volume displacing shear[14–17]. For larger indentation crack systems, shear faults play the role of initial cracks, namely, middle/radial and lateral cracks under moderate loads. For anomalous glasses, the deformation is mainly due to volume-reducing densification [18]. The surface tensile stress around the contact will act on the surface defects, thereby forming a ring crack, and the tensile stress at the bottom of the elastic/plastic boundary will promote median cracking. Between normal glasses and anomalous glasses is a third subset named intermediate glasses. Compared with normal glasses, the deformation in these glasses occurs with significantly more densification, and compared with anomalous glasses, their shear deformation is much larger[14]. The intermediate glasses thus eliminate the stresses that lead to ring and median cracks[19]. Some calcium aluminoborosilicate (CABS) glasses have recently been found to belong to the group of intermediate glasses [20]. In these glasses, SiO<sub>2</sub>, B<sub>2</sub>O<sub>3</sub>, and Al<sub>2</sub>O<sub>3</sub> are the basic network formers, with the coordination numbers of Si, B, and Al being 4, 3–4, and 4–6 under ambient conditions, respectively[21]. Both 4-fold boron and aluminum need to be stabilized by calcium modifier cations, 5- or 6-fold coordinated aluminum, or oxygen triclusters[22].

The mechanical properties of nuclear waste glass under radiation damage have been studied for decades and the fracture behavior has been found to be altered depending on the irradiation dosage and temperature [23]. This includes studies on heavy ion irradiation treatment of sodium borosilicate (NBS) glasses and the effect on their structure and mechanical properties [24]. Upon irradiation, the indentation hardness of NBS glasses tends to initially decrease and then stabilize with increasing irradiation dose[25]. The difference in irradiation effect on NBS and quartz glasses indicates that the hardness reduction is not only due to the transformation of the silicate network in NBS glasses, but also the transformation of the borate network[26]. MD simulations have also been performed to study irradiated NBS glasses, also showing the decrease in hardness, in agreement with the experimental data [27–30]. Studies have also shown that the elastic modulus of NBS glasses decrease upon irradiation, but the structural changes responsible for these changes in mechanical properties are not well-understood[22].

Considering the high crack resistance of CABS glasses, it is interesting to study the effect of irradiation treatment on their mechanical properties. Recently, we found that the chemical composition of CABS glasses affects their indentation deformation and cracking behavior[22]. Therefore, we here perform irradiation treatment on three different CABS glass compositions (see Table 1). We combine the experimental characterization of hardness, crack resistance, and indentation fracture toughness with MD simulations to explain the changes in these mechanical properties. The investigated glasses have constant CaO content (20 mol%) and varying Si, Al, and B ratios to assess different structural features in the glasses. We perform irradiation treatments with different doses and characterize their structure and mechanical properties using both experiments and MD simulations. The aim is to understand the structural origins for the variation in surface mechanical properties due to irradiation treatment. We note that the experimental data for the as-made glasses (prior to irradiation) are taken from our recent study [22].

**Table 1**

Nominal chemical compositions of the CABS glasses as well as their measured glass transition temperature ( $T_g$ ). The glass ID is based on the Al<sub>2</sub>O<sub>3</sub> to B<sub>2</sub>O<sub>3</sub> ratio. The error in  $T_g$  is within  $\pm 2$  °C.

Glass ID	SiO <sub>2</sub> (mol%)	Al <sub>2</sub> O <sub>3</sub> (mol%)	B <sub>2</sub> O <sub>3</sub> (mol%)	CaO (mol%)	$T_g$ (°C)
CABS-0.4	45	10	25	20	665
CABS-0.6	40	15	25	20	668
CABS-0.75	45	15	20	20	683

## 2. Methods

### 2.1. Experimental sample preparation

The three CABS glasses (Table 1 and S1) were prepared using the melt-quenching method. CaCO<sub>3</sub> (99.5%, ChemSolute), H<sub>3</sub>BO<sub>3</sub> ( $\geq 99.5\%$ , Honeywell International), Al<sub>2</sub>O<sub>3</sub> (99.5%, Sigma-Aldrich), and SiO<sub>2</sub> ( $\geq 99.5\%$ , 0.2–0.8 mm, Merck KGaA) were used as the raw materials. First, based on the target composition, the batch of raw materials was thoroughly mixed and gradually added to a Pt-Rh crucible in a furnace at 800 °C to remove H<sub>2</sub>O and CO<sub>2</sub>. Afterwards, these mixtures were melted at 1600 °C and finally poured onto a steel plate for quenching and transferred to the annealing furnace at the glass transition temperature ( $T_g$ )[22]. After annealing, we cut the glasses into the required sizes for the subsequent irradiation and characterization. Based on X-ray diffraction analyses (Empyrean XRD, PANalytical), no signs of crystallization were present in any of the glasses (Fig. S1).

The glass samples ( $1.7 \times 1.2 \times 0.1$  cm<sup>3</sup>) were irradiated with Xe ions at room temperature at the Institute of Modern Physics (IMP), Chinese Academy of Sciences. As shown in Table S2, the penetration depth of the xenon ions (i.e., the thickness of the glass surface layer affected by irradiation) is around 1.7  $\mu$ m. The xenon ions were generated, selected, and then accelerated toward the sample with an energy of 5 MeV. A pair of grating magnets were used to generate a uniform ion beam that bombards the sample in the target chamber. The pressure in the target chamber was  $7 \times 10^{-6}$  Pa. The typical ion current was 2  $\mu$ A, and the beam spot size was  $20 \times 20$  mm<sup>2</sup>. The samples were treated with two different doses, namely "Dose 1" of  $2.0 \times 10^{13}$  ions/cm<sup>2</sup> and "Dose 2" of  $2.0 \times 10^{14}$  ions/cm<sup>2</sup>.

### 2.2. Experimental sample characterization

The density ( $\rho$ ) of the glass sample was determined using the Archimedes buoyancy principle (see Table S1). The weight of each sample (at least 1.5 g) was measured ten times in air and ethanol.

Raman spectra were collected using a micro-Raman spectrometer (inVia, Renishaw). The sample surface was excited by a 532 nm green diode pumped solid state laser for an acquisition time of 10 s. The lateral spatial resolution of the Raman measurements is estimated to be around 0.9  $\mu$ m. The range of the collected spectrum was from 250 to 1750 cm<sup>-1</sup> and the resolution was better than 2 cm<sup>-1</sup>. Spectra from five different locations on the glass surface were accumulated for each specimen to ensure homogeneity. All spectra were uniformly treated in Origin software for background correction and area normalization.

Micro-indentation measurements were carried out using a Nanovea CB500 hardness tester to determine the Vickers hardness ( $H_V$ ), crack resistance ( $CR$ ), and indentation fracture toughness ( $K_{IFT}$ ). While hardness quantifies the mean contact stress that is required to form a permanent indentation imprint, both  $CR$  and  $K_{IFT}$  are related to crack formation upon indentation. Assuming the glass cracks in a controlled and well-defined manner,  $K_{IFT}$  is a measure of the glass' resistance to crack growth based on crack length measurements [31], whereas  $CR$  is a measure of the glass' resistance to crack initiation based on the statistics of crack-counting at different loads. We therefore rely on both crack length as well as crack counting measurements to characterize the glasses' fracture properties based on indentation.

On each sample, 20 indentations with a maximum load of 4.9 N (0.5 kgf) were generated to determine  $H_V$ , with a loading duration of 15 s and dwell time of 10 s. Then we used an optical microscope to analyze the residual imprints and calculate  $H_V$ . We also calculated hardness from the force-displacement curves using the Oliver-Pharr model[32,33]. The resistance of the glass to the initiation of corner cracks upon indentation was also determined using the Vickers diamond indenter. We applied increasing loads (from 4.8 to 40 N) and counted the numbers of corner cracks after unloading.  $CR$  was calculated according to the method of Wada[34]. To this end, the probability of crack occurrence (PCI) was

determined as the ratio between the number of corners where a corner crack was formed and the total number of corners on all indents.  $CR$  is then defined as the load that generates two cracks ( $PCI = 50\%$ ) on average per indent. For each sample and each load, at least 30 indents were made with loading duration of 15 s and dwell time of 10 s. Measurements were performed under laboratory conditions (room temperature and relative humidity (RH) of  $39 \pm 5\%$ ).

We also used the indentation method to estimate the resistance against crack growth, i.e.,  $K_{IFT}$ . This approach is based on a known Young's modulus (see below) and measurements of crack lengths and impression size for a given indentation load [35–37]. We used this method instead of a standard fracture toughness ( $K_{IC}$ ) method such as the single-edge precracked beam method, since the irradiation treatment only affects the surface region. However, it is important to note that  $K_{IFT}$  from Vickers indentation is often not equal to  $K_{IC}$ , particularly due to the densification that occurs upon indentation [38]. Following the recent work of Gross et al. [14] to avoid or limit this effect, we here determine  $K_{IFT}$  using a sharper  $100^\circ$  indenter tip (with same geometry of Vickers but angle of  $100^\circ$  instead of  $136^\circ$ ) to minimize the densification component in favor of shear [14].  $K_{IFT}$  is determined using the equation from Anstis et al. [39],

$$K_{IFT} = \xi \left( \frac{E}{H} \right)^{0.5} \left( \frac{P}{C_0^{1.5}} \right) \quad (1)$$

where  $\xi$  is an empirically determined constant for a indenter that was calibrated against select materials [39].  $E$  is the Young's modulus,  $P$  is the indentation load,  $C_0$  is the average length of the radial/median cracks measured from the center of the indent impression, and  $H$  is the hardness.  $\xi$  is typically set equal to 0.016 for a Vickers indenter, whereas Gross et al. [14] found that a  $110^\circ$  tip gave a value of 0.0297. We used these values to extrapolate to a value of  $\xi = 0.035$  for the  $100^\circ$  tip used in the present study. We chose an indentation load of 3 N, since it is just high enough to produce corner cracks from the indent impressions. On each sample, six indentations were generated, with a loading duration of 15 s and dwell time of 10 s. The crack lengths and major diagonal lengths were then measured and combined with values of  $E$  and  $H$  to calculate  $K_{IFT}$ . By assuming  $K_{IFT} = K_{IC}$ , we also calculated the fracture energy ( $G_C$ ) to enable comparison with the MD simulations results following Irwin's formula (in plane strain) [40],

$$G_C = \frac{1 - \nu^2}{E} K_{IFT}^2 \quad (2)$$

where  $\nu$  is the Poisson's ratio.

The elastic properties of the glasses were measured by ultrasonic echography using an ultrasonic thickness gauge (38DL Plus, Olympus) equipped with 20 MHz delay line transducers for the determination of the longitudinal  $V_1$  and transversal wave velocities  $V_2$ . The experimental data for the as-made glasses (prior to irradiation) are taken from our recent study [22].

To probe the irradiation-induced change in surface elasticity, the Oliver-Pharr method was used to calculate the reduced elastic modulus ( $E_r$ ) of the CABS glass surfaces. These measurements were carried out using a Nanovea CB500 hardness tester with a Vickers indenter tip. The load-depth curve was obtained through the indentation test, and  $E_r$  was then calculated as,

$$S = \frac{2}{B\sqrt{\pi}} E_r \sqrt{A_{pml}} \quad (3)$$

$$\frac{1}{E_r} = \frac{1 - \nu^2}{E} + \frac{1 - \nu_i^2}{E_i} \quad (4)$$

where  $S$  is the contact stiffness,  $B$  is a geometrical factor depending on the indenter [32],  $A_{pml}$  is the projected area, and  $E$  and  $\nu$  are the elastic modulus and Poisson's ratio of the sample (from ultrasonic echography

tests), and  $E_i$  and  $\nu_i$  are the elastic modulus and Poisson's ratio of the indenter. Based on these, we could calculate the reduced elastic modulus ( $E_r$ ).

### 2.3. Simulation details

The classical MD simulations in this study were carried out using the GPU-accelerated LAMMPS software [41], and visualization of the configurations were performed with the OVITO package [42]. Periodic boundary conditions were applied in all directions during the simulations. The interaction between the constituent atoms (Ca, Al, B, O, and Si) were described with a Buckingham-Coulomb potential, following the parametrization by Du et al. [43,44]. The cutoff for Buckingham and Coulombic interactions was 10 Å. Long-range Coulombic interactions were computed using the Particle-Particle Particle-Mesh (PPPM) algorithm with an accuracy of  $10^{-5}$ . This potential has previously been used and validated in various multicomponent oxide glasses, including aluminosilicate [45], phosphate [46], borate [47], and borosilicate [48] glasses. For comparison, we also adopted another potential from Ref. [49] to simulate the pristine glasses. The structural and mechanical properties shown in Fig. S2 and Table S3 indicate that the potential by Du et al. [43] is more suitable for the glass compositions in this study. Considering the ballistic cascades during the irradiation simulations (see Section 2.5), the short-range repulsive interactions were modified by the Ziegler-Biersack-Littmark (ZBL) potential [50] coupled with high-order polynomials to ensure the smoothness of the energy, force, and their derivatives as a function of interatomic distance. The motion of atoms was described using the velocity-Verlet integration algorithm with a fixed timestep of 1 fs, except in the simulation of ballistic cascade, where we used a variable timestep to avoid the unrealistic configuration generated by the high velocity collisions.

#### 2.3.1. Simulation of melt-quenched glasses

The glass formation was simulated by the conventional melt-quenching method. The initial configurations were generated by randomly placing the atoms into a cubic box based on the experimental density, while ensuring the absence of any unrealistic proximity of atoms by using the PACKMOL package [51]. The compositions of glasses were the same as the experimental samples, and the constituents of each simulated system are given in Table 2.

The resulting configurations were then subjected to potential energy minimization to adjust the structural geometry. Afterwards, these structures were melted at 5000 K in the NVT ensemble with a Nosé–Hoover thermostat [52] for 100 ps to ensure that the memory of the initial configuration had been completely erased. After the melting process, the systems were linearly cooled down to 300 K during 1 ns in the NVT ensemble. Finally, the glasses were successively equilibrated at 300 K in the NPT ensemble at zero pressure and then in the NVT ensemble for 60 ps to remove the internal stress and obtain the density information. The simulation box was further equilibrated in the NVT ensemble for 100 ps to generate 100 frames of trajectory to compute structural and thermodynamic properties.

#### 2.3.2. Simulation of irradiation process

To match the size of samples for the following fracture simulations, the melt-quenched glass structures were duplicated by  $2 \times 2 \times 1$  along the three directions, thus now consisting of more than 14,000 atoms (dimensions of  $70 \times 70 \times 35 \text{ Å}^3$ ). These glasses were subjected to

**Table 2**

Chemical constitutions (number of atoms) of the glass models simulated herein.

Glass ID	CaO	Al <sub>2</sub> O <sub>3</sub>	B <sub>2</sub> O <sub>3</sub>	SiO <sub>2</sub>	Total atoms
CABS-0.4	200	100	250	450	3500
CABS-0.6	200	150	250	400	3600
CABS-0.75	200	150	200	450	3500



simulated irradiation using a well-established methodology by initiating a series of displacement cascades[53–56]. In each cascade, we randomly selected an atom and accelerated it with a kinetic energy of 500 eV along a random direction. The selected atom, also known as the primary knock-on atom (PKA), was alternating as projectiles and collided with the nearby atoms in the glass, thereby resulting in a ballistic cascade. Subsequently, a spherical region was created around the PKA with a radius of 10 Å, which was defined as the impacted zone. The dynamics of the atoms inside the impact zone were then equilibrated in the *NVE* ensemble, outside of which atoms were kept at a constant temperature of 300 K using a Berendsen thermostat. Note that, during this ballistic cascade, a variable timestep was used to avoid the unrealistic configuration generated by the high velocity collisions. The simulation of the cascade had a length of 20 ps, which was found to be long enough for the system to relax and converge its thermodynamic quantities (i.e., energy, temperature, and pressure), thereby confirming the PKA had come to rest in the glass. After each collision, the system was further relaxed in the *NPT* ensemble at 300 K and zero pressure for 5 ps to adjust its configuration and volume upon irradiation. The above process was iteratively repeated with different PKAs until the system reached saturation in terms of enthalpy and density.

### 2.3.3. Structure analysis of simulated glasses

The melt-quenched glass structures before and after irradiation were analyzed in terms of the bond angle distribution (BAD), ring size distribution, neutron structure factor (*S*(*Q*)), and persistence diagrams. The ring distribution was calculated using the RINGS package[57], wherein a ring structure is defined as the shortest closed path within the network formers connected by O atoms[58] and the ring size is defined in terms of the number of Al, B, and Si atoms in a ring. *S*(*Q*) was computed using the Faber–Ziman formula[59] through the Fourier transformation of the pair distribution function (*g*(*r*)) as described in Ref.[60].

To better characterize the irradiation-induced medium-range order structural changes, we used persistent homology. Persistent homology is a tool within topological data analysis that has been used to analyze the qualitative features of high-dimensional data such as point cloud data set across multiple scales. By regarding the atomic configuration as a point cloud data set, the hierarchical structural features of materials can be extracted at different scales. Based on these features, persistent homology has shown great promise in analyzing the medium-range structure of different glass systems such as oxide[61–63] and metallic glasses [62,64], as well as glass structure under pressure[63] or chemical replacement[65].

In this study, persistent homology analysis to determine persistence diagrams was carried out using the Diode[66] and Dionysus 2[67] packages. As mentioned in Refs. [68,69], the procedure for obtaining the persistence diagram is as follows: 1) Each atom is replaced by a ball with its atomic radius, and then the radius of each ball is gradually increased with the same increment. 2) Consisting at first of points (the center of the atoms), line segments  $p_i p_j$  connecting pairs  $p_i, p_j$  of points are added when the growing ball with center  $p_i$  and the one with center  $p_j$  intersect. Triangles  $p_i p_j p_k$  are added when the balls with center  $p_i, p_j$  and  $p_k$  all have a common intersection, whereas a tetrahedron  $p_i p_j p_k p_l$  is added when the four balls have a common intersection. If, during this process, all the edges in a closed sequence  $p_{i1} p_{i2}, p_{i2} p_{i3}, \dots, p_{ik} p_{i1}$  have been added, a loop is *born* at the time when the last edge is added. The loop *dies* when enough triangles have been added to fill it in or connect it to another loop, indicating that it does not surround a unique “hole” in the structure anymore. Note that an edge  $p_i p_j$  does not necessarily represent a chemical bond, as it is purely geometry. The persistence diagram is the scatter plot of the points ( $b_i, d_i$ ), where  $b_i$  denotes the birth time and  $d_i$  denotes death time of each loop. The atomic radii of each element was defined by following the approach in Ref. [68], specifically  $r_{Al} = 0.483$  Å,  $r_B = 0.158$  Å,  $r_{Ca} = 1.083$ ,  $r_O = 1.280$  Å, and  $r_{Si} = 0.333$  Å.

### 2.3.4. Fracture simulations

The as-made and irradiated glasses were subjected to fracture simulations for qualitative comparison with the experiments. We simulated the mode I fracture, i.e., with loading in perpendicular direction to the crack plane. The fracture energy was calculated using the method of Brochard et al.[70], which is based on the energetic theory of fracture mechanics and does not involve any assumptions of the material behavior. Therefore, this method can be used in calculating the fracture energy of both brittle and ductile systems[71–73]. In order to minimize the size effect, the samples were further duplicated by  $2 \times 2 \times 1$  (thus  $4 \times 4 \times 1$  supercells of the melt-quenched glasses), yielding a system size of about  $140 \times 140 \times 35$  Å<sup>3</sup> (~56,000 atoms). A precrack was introduced by removing the atoms in an ellipsoidal cylinder with a length of 1/3 and a height of 1/15 of the box dimension in the loading direction. The crack size was selected based on the crack size dependence of the fracture energy as shown in Fig. S3. Before applying stress, the system was equilibrated in the *NPT* ensemble at 300 K and zero pressure for 100 ps relaxation, which was found to be long enough for the potential energy of the new system to converge. Afterwards, the sample was subjected to uniaxial tensile loading by deforming the structure along the *x*-direction at a constant strain rate of  $5 \times 10^8$  s<sup>−1</sup>, while the dimensions in the *y*- and *z*-directions were free to deform so as to exhibit zero stress along these directions. During the fracture simulations, the system was maintained in the *NPT* ensemble, and the temperature and pressure were controlled by the Nosé–Hoover thermostat and barostat, respectively[52,74]. Strain and the corresponding stress in the loading direction were recorded until a total strain of 50%. Young’s modulus was determined as the slope of the stress-strain curve in the low strain region ( $\epsilon < 0.05$ ) using linear regression. The fracture energy was calculated by integrating the stress-strain curve up to the failure strain,

$$G_C = \frac{L_y L_z}{\Delta A} L_x \int_0^{\epsilon_{xx}^f} \sigma_{xx} d\epsilon_{xx} \quad (5)$$

where  $G_C$  is the fracture energy,  $L_x, L_y$ , and  $L_z$  are the dimensions of the simulation box,  $\Delta A$  is the newly created surface area upon fracture,  $\epsilon_{xx}^f$  is the strain in the *x*-direction when the stress dropped to zero, and  $\sigma_{xx}$  and  $\epsilon_{xx}$  are the recorded stress and strain, respectively, in the *x*-direction. The surface areas were calculated based on a surface mesh construction algorithm implemented in the OVITO package[42,75]. Specifically, the surface mesh was constructed through a spherical probe with a radius of 3.6 Å combined with a smoothing level of 10 to ensure a sufficient accuracy and no artificial voids.

### 2.3.5. Bond switching analysis

The bond breaking and re-formation events during the fracture process was characterized by the bond switching activities as a function of the applied tensile strain. The bond switching analysis was done on the Al, B, and Si atoms. That is, the fraction of atoms with a decreased, increased, or unchanged coordination number (CN) was calculated by comparing the CN of each individual atom with its initial CN at non-strained state. The swapped CN is defined as an unchanged CN for which at least one oxygen neighbor is exchanged with another one.

## 3. Results and Discussion

### 3.1. Structure of experimental glasses

Fig. 1a shows the micro-Raman spectrum of the as-made and irradiated CABS-0.6 glass (Dose 1), while the corresponding spectra for the two other glass compositions are shown in Fig. S4. We divide the spectra into four main bands from I to IV and outline the expected assignments in the following. Band region I (~250–625 cm<sup>−1</sup>) is expected to contain contributions originating from B–O–B, Al–O–Al, and B–O–Al stretching bands. Besides, vibrations due to superstructural units such as pentaborates may occur in this region. Furthermore, Si–O–Si network units

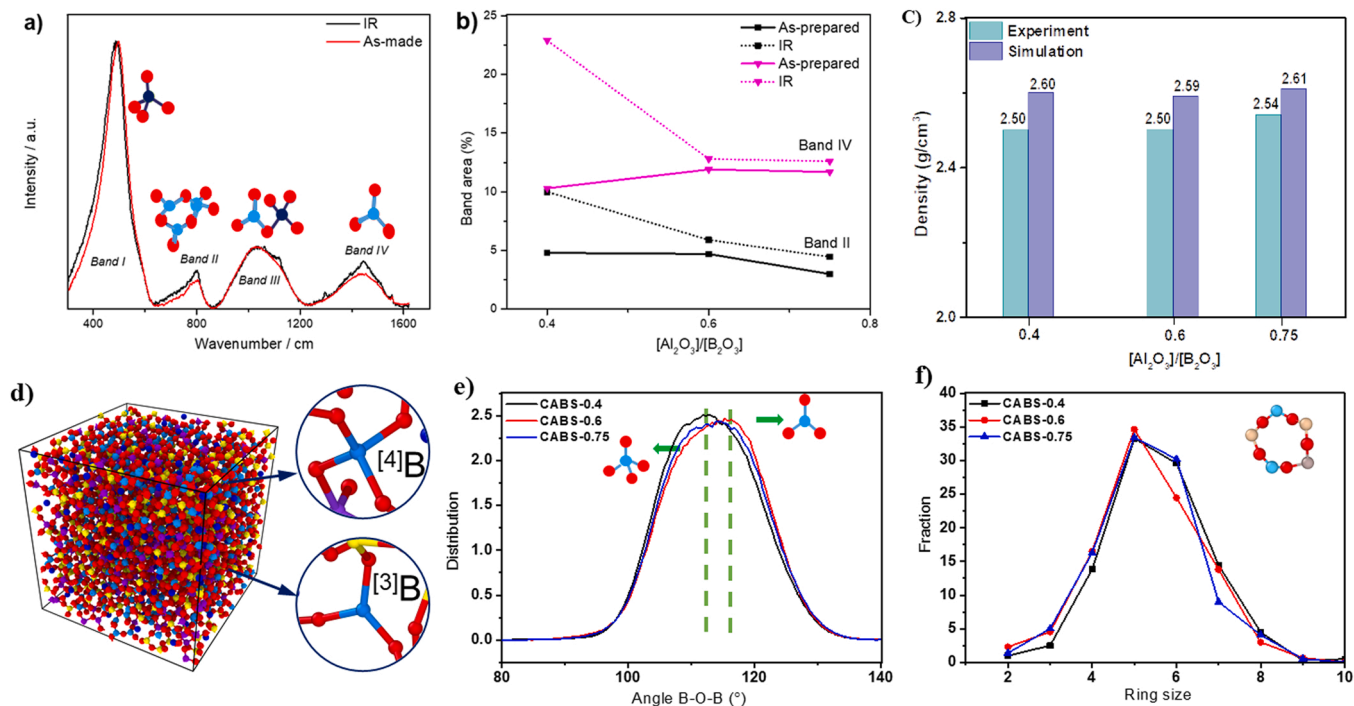


**Fig. 1.** (a) Micro-Raman spectra of the as-made and irradiated (IR) CABS-0.6 glass. The assignment of the four band regions are discussed in the text. (b) Relative area fractions of the two main Raman bands (bands II and IV) for as-made and irradiated CABS glasses. (c) Comparison of the experimental and simulated density of the as-made glasses. (d) Atomic snapshot of the simulated as-made CABS-0.6 glass, consisting of 3600 atoms. Al, B, Ca, O, Si atoms are represented by purple, cyan, blue, red, and yellow spheres, respectively. (e) Simulated O-B-O bond angle distribution and (f) ring size distribution in the CABS glasses.

may also occur in this region[76]. Band region II ( $\sim 625\text{--}860\text{ cm}^{-1}$ ) is characteristic for  $\text{B}_2\text{O}_3$ -rich glasses[76], since peaks in this frequency range are typically assigned to borate superstructures such as chain and ring metaborates[77,78], di-triborates[79], and penta-, tetra-, or triborates[77,80], as well as boroxol rings[77,81]. In addition, B-O-Al stretching and aluminate network may occur in this region. The presence of triborates ( $\sim 770\text{ cm}^{-1}$ ) and ditriborates ( $\sim 755\text{ cm}^{-1}$ ) may also be found in this region, considering the high intensity in this range of wavenumbers and the fact that they consist of both  $^{[3]}\text{B}$  and  $^{[4]}\text{B}$  units. The Si-O stretching vibration also contributes ( $800\text{ cm}^{-1}$ ). Band region III ( $\sim 860\text{--}1200\text{ cm}^{-1}$ ) is expected to contain contributions originating from the  $Q^n$  species ( $\text{SiO}_4$  units with  $n$  bridging oxygens)[76], with bands at  $1000\text{ cm}^{-1}$  attributed to the stretching Si-O vibration in  $Q^2$  species[82]. Finally, band region IV ( $\sim 1200\text{--}1600\text{ cm}^{-1}$ ) is typically assigned to signal contributions from vibrations of  $^{[3]}\text{B}$  units[83].

Fig. 1a-b also show that compared to the as-made CABS glasses, the areas of bands II and IV increase upon irradiation with two different doses (Fig. S4). This suggests that the irradiation treatment (at two different doses) mainly influences the structure around the B units in the CABS glass structure, which is also consistent with previous studies[25, 84]. Moreover, we have collected micro-Raman spectra on indented glasses (Fig. S5), for which the stress increases toward the center of the indent[85]. For the irradiated glasses, the structural changes induced by indentation are more obvious compared to those for the as-made glasses. Specifically, the indentation most influences bands II and IV, similarly to the results in Fig. 1a for irradiation-induced changes.

### 3.2. Structure of simulated glasses

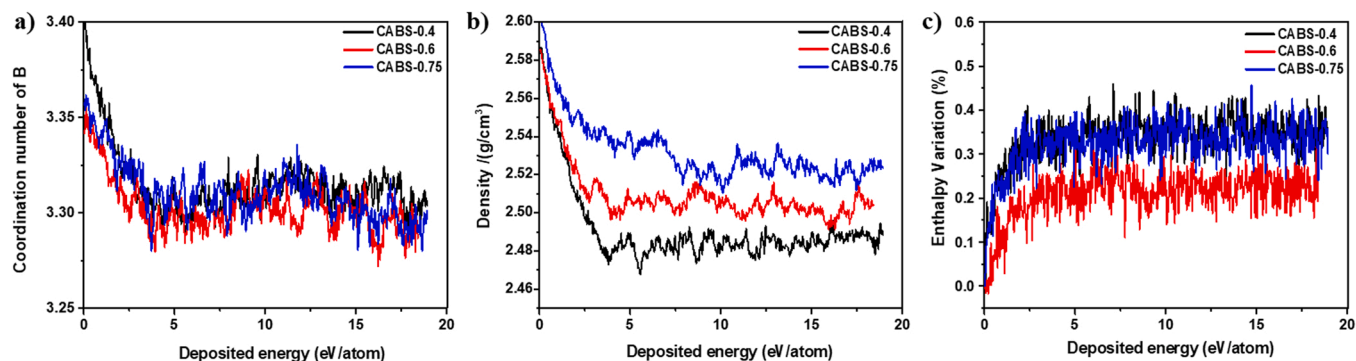
To examine the ability of the utilized MD potential to reproduce the properties of the CABS glasses, we first analyze the structure of the different glass compositions. Fig. 1c shows the composition dependence of density of the as-made glasses. Although the simulated densities are slightly overestimated (by about 3.8%), the compositional scaling of density is well-reproduced, i.e., the CABS-0.75 and CABS-0.6 glasses

exhibit the largest and lowest density, respectively. An atomic snapshot of the as-made CABS-0.6 glass is shown in Fig. 1d, illustrating the coexistence of  $^{[3]}\text{B}$  and  $^{[4]}\text{B}$  units in the glass structure.

We then analyze the short- and medium-range structures of the as-made glasses by calculating the pair distribution, bond angle distribution, and ring size distribution. As shown in Fig. S6, all the compositions exhibit three peaks in the pair distribution function, which are assigned to the B-O ( $1.45\text{ \AA}$ ), Si-O ( $1.60\text{ \AA}$ ), and Al-O ( $1.76\text{ \AA}$ ) bonds, respectively. The distribution of O-B-O bond angle is shown in Fig. 1e, providing evidence for the existence of both  $^{[3]}\text{B}$  and  $^{[4]}\text{B}$  units. Specifically, the tetrahedral  $^{[4]}\text{B}$  unit with O-B-O angle of about  $109^\circ$  and the planar  $^{[3]}\text{B}$  unit with O-B-O angle of  $120^\circ$ . We find that the fraction of  $^{[4]}\text{B}$  units decreases in the order  $\text{CABS-0.4} > \text{CABS-0.75} > \text{CABS-0.6}$ . The ring structures containing Al, B, Si, and O atoms are used to characterize the medium-range structure in the as-made glasses. As shown in Fig. 1f, most of the rings in all three glasses are five-membered rings, in good agreement with simulation results for related borosilicate glasses [86].

Fig. 2a shows how the average CN of B decreases monotonically and eventually reaches a constant value in all the glasses with an increase in the deposited energy. That is, the irradiation induces the partial conversion of  $^{[4]}\text{B}$  to  $^{[3]}\text{B}$ . These findings echo the experimental Raman results, showing irradiation-induced  $^{[4]}\text{B}$  to  $^{[3]}\text{B}$  conversion (Fig. 1a). Interestingly, despite the differences in the initial CN of B in the three glasses, the final CN of B reaches a value of around 3.3 when the irradiation energy saturates. On the other hand, there is no obvious changes of CN of Al and Si atoms upon irradiation (see Figs. S7a and S7b). In addition, Fig. 2b shows that the densities of the CABS glasses also decrease and then reach a plateau value upon irradiation, consistent with the literature[86–88]. As shown in Fig. 2c, the enthalpy becomes less negative and eventually saturates upon irradiation. Since the enthalpy is mostly influenced by the short-range structure[53], the increase of enthalpy is mainly attributed to the formation of  $^{[3]}\text{B}$  species, which is favored at higher temperatures caused by irradiation events [86]. We have confirmed this by calculating the distribution of enthalpy





**Fig. 2.** Evolution of (a) average coordination number of B, (b) density, and (c) normalized enthalpy changes of CABS glasses as a function of the deposited energy during the simulated irradiation process.

per atom of  $^{10}\text{B}$  and  $^{11}\text{B}$  as shown in Fig. S8. This phenomenon is similar to an increase in fictive temperature of the glass—it becomes less stable, and more similar to a hyperquenched glass. Additionally, through the cluster analysis of  $^{10}\text{B}$  atoms, the irradiated glass remains in a homogeneous state despite the increased number of  $^{10}\text{B}$  after irradiation (see Fig. S9).

As shown in Fig. 3a for the CABS-0.4 glass, the O-B-O bond angle distribution shifts towards a higher angle upon irradiation, which manifests itself through the increase of intensity of the  $120^\circ$  angle at the expense of the  $109^\circ$  angle (results of the other compositions are shown in Fig. S10). Among the three compositions, the CABS-0.4 glass exhibits the most pronounced structural changes upon irradiation, potentially because it has the highest fraction of  $^{10}\text{B}$  units in the as-made glass (see Fig. 1e). Next, we focus on the effect of irradiation on the ring structures. As shown in Fig. 3b for the CABS-0.4 glass, the ring size distribution exhibits some coarsening upon irradiation, wherein the fractions of some small rings (i.e., three- and four-membered) and large rings (i.e., seven-membered and larger) increase at the expense of intermediate-

sized rings (i.e., five-membered), in agreement with the behavior for other irradiated silicate glasses [53,86]. The results for the other compositions can be found in Figs. S10c and S10d. As shown in Fig. 3c, we generally find that the simulated neutron structure factors for different irradiated states are similar, with minor differences observed for the first sharp diffraction peak (FSDP) (see results of the other compositions in Fig. S11). Specifically, the FSDP slightly shifts towards a lower  $Q$  value while its intensity decreases with an increase in the deposited energy, indicating an increased disorder in the medium-range structure and swelling of CABS glasses upon irradiation.

To characterize the irradiation-induced structural changes at different length scales, we rely on persistent homology analysis of the simulated glass structures. As shown in Fig. 3d-f, we observe that the distribution of the characteristic regions in the persistence diagrams starts to diffuse to the high-death regions upon irradiation, especially in the low-birth region (i.e., loops are chemically bonded like ring structures), indicating that the sizes of the loops increase upon irradiation. This result is in agreement with the results of Figs. 3b and 3c,

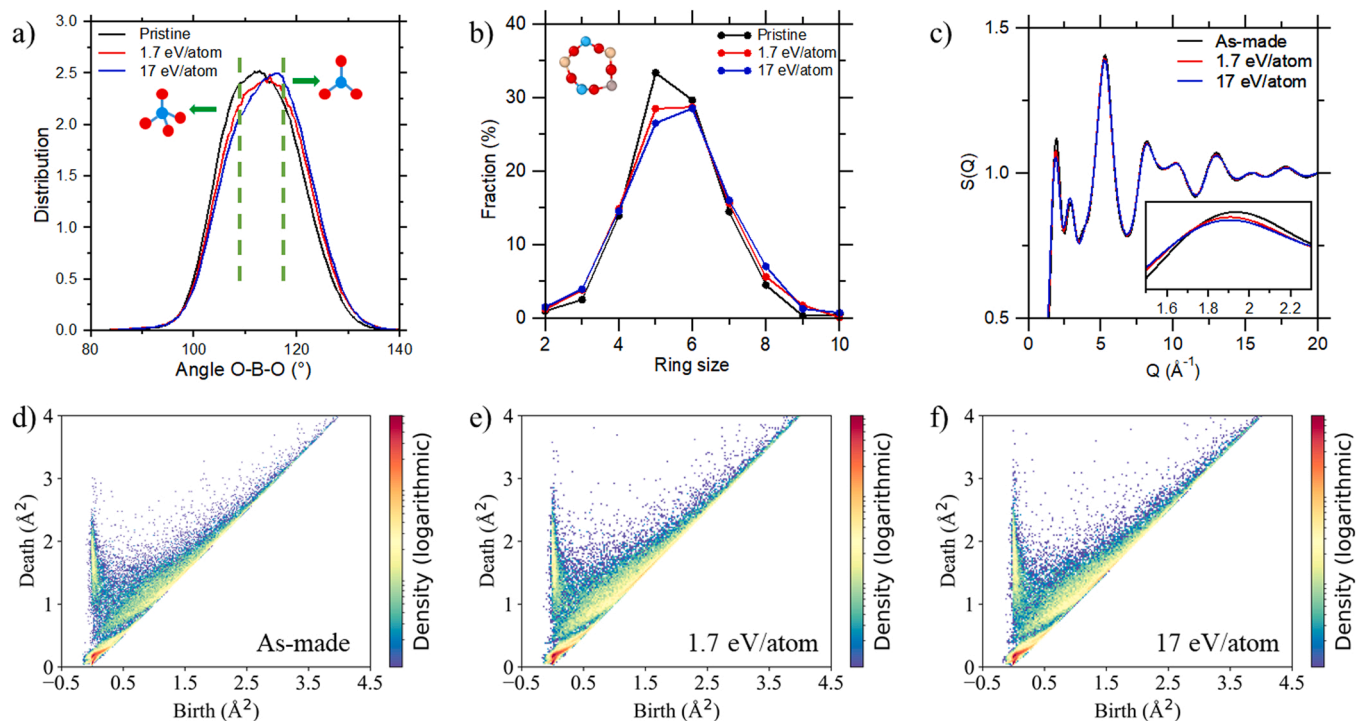


**Fig. 3.** (a) Simulated O-B-O bond angle distribution, (b) ring size distribution and (c) simulated neutron structure factor of the CABS-0.4 glasses subjected to different amounts of irradiation energies, namely, 0, 1.7, and 17 eV/atom. (d-f) Persistence diagrams for CABS-0.4 glass structure for (d) as-made state and subjected to irradiation with dose of (e) 1.7 eV/atom, and (f) 17 eV/atom.

demonstrating that irradiation changes the medium-range order structure of CABS glasses (results of the other compositions are in Fig. S12).

We further calculated the quantities of persistence diagrams at different regions to compare the structural changes upon irradiation. As shown in Fig. 4a, the high-density region in the red dashed box with low birth and death values correspond to the short-range order structure, e.g., chemically bonded three-membered loops. The structural features of network formers (i.e., Al, B and Si atoms) are analyzed through the persistence diagram of configuration with only Si, B, and Al elements. As shown in Fig. 4b, there is a dispersed curve at a low-birth region, which corresponds to the loop structure consisting of network formers. Since the birth values are around  $2 \text{ \AA}^2$ , the edge of the loop structure is estimated to be around  $3 \text{ \AA}$ , close to the distance of two Si atoms bonded by a bridging oxygen atom.

We then calculate the total loop numbers per atom for pristine and irradiated glasses (Fig. 4c), showing that the loop numbers in all three glasses are reduced upon irradiation, i.e., a less connected structure appears after irradiation. When grouping the 3-membered loops based on their types, we find that most of the 3-membered loops are in the form of O-Al-O, O-B-O, and O-Si-O. Fig. 4d-f show the changes in the different loop numbers, revealing that most of the 3-membered loops are O-Si-O type. After irradiation, the number of O-Si-O and O-B-O loops decrease.

For O-B-O, the number decreases as the CN decreases. However, since the CN of Si remains constant upon irradiation, the reduction of loop numbers indicates the distortion of  $\text{SiO}_4$  tetrahedra. The histograms of death values in the red dashed box region of Fig. 4b are shown in Fig. 4g-i. We observe that all the distributions become more dispersed upon irradiation. Given that the death values are correlated with the loop sizes, these results suggest a broader distribution of various loop structures, which agrees well with the results shown in Fig. 1f and Figs. S10(c, d).

We further calculated the accumulated persistence function (APF) for loops in the glass structures based on these persistence diagrams (see Fig. S13). APF is a cumulative sum of all points in the persistence diagram weighted by their “lifetime” ( $d_i - b_i$ ), which quantifies how close neighboring atoms are in a loop and weighs it against the separation of the most distant atoms. Here, we observe that the shapes of the APF curves are qualitatively similar for all the glasses before and after irradiation. However, the maximum value decreases with increasing value of the deposited energy. Since the value of APF represents the number of loops [69], these results further confirm the irradiation-induced swelling and decreased connectivity in the CABS glass structure. Overall, we conclude that irradiation not only influences the short-range structure (e.g.,  $^{41}\text{B}$  to  $^{10}\text{B}$  conversion), but also the medium-range order (e.g.,

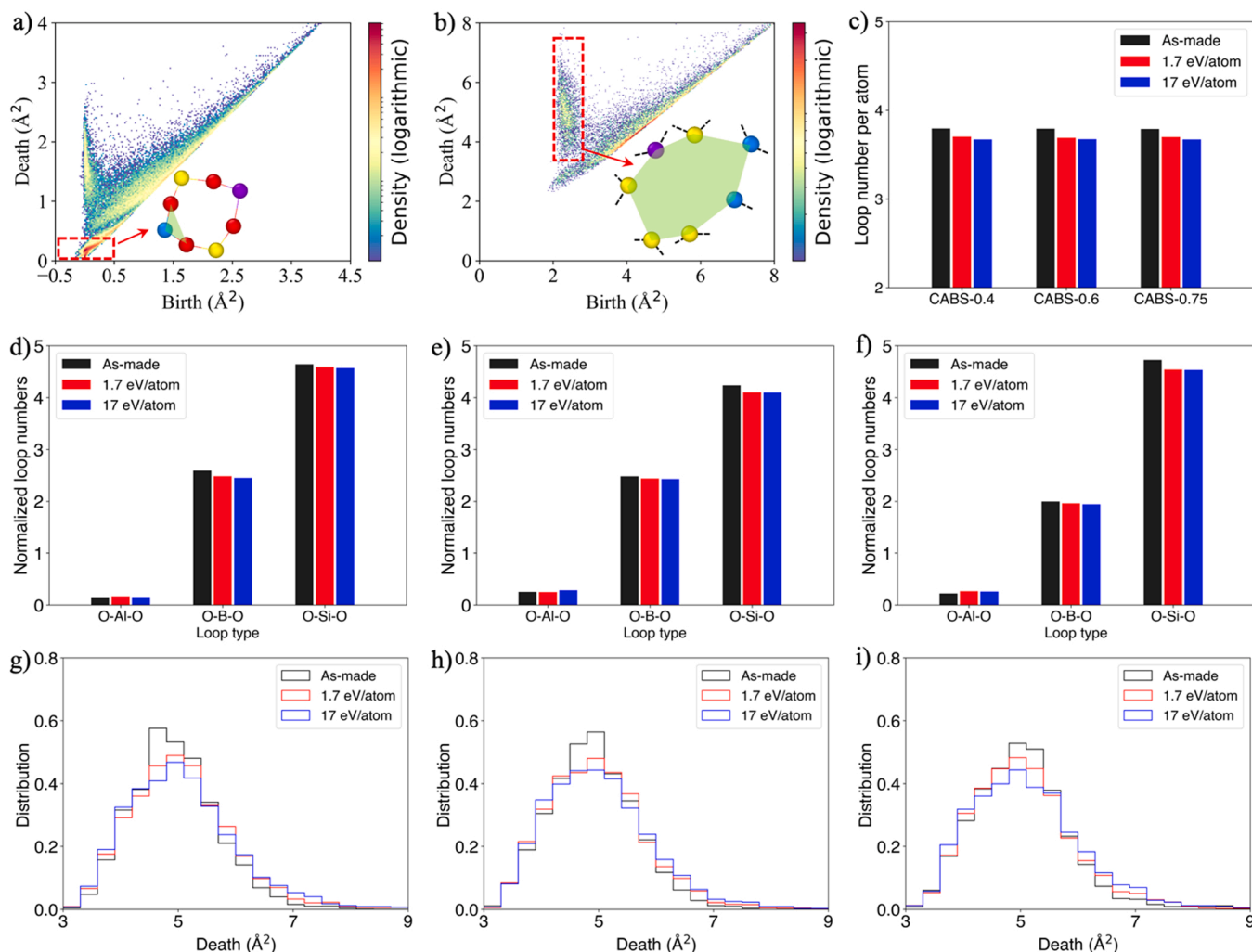


**Fig. 4.** Schematic of (a) short-range structure (i.e., 3-membered loop) in the persistence diagram of CABS-0.4 glass before irradiation and (b) medium-range structure in the persistence diagram of configuration with only Si, B, and Al elements in CABS-0.4 glass before irradiation. (c) Loop number per atom in simulated CABS glasses of different irradiated states. Note that the loop numbers are normalized by the number of each cation type. (d-f) Numbers of different 3-membered loops in the as-made and irradiated states of (d) CABS-0.4, (e) CABS-0.6, and (f) CABS-0.75 glasses. (g-i) Distributions of death scales in the red dashed box region of (b) in the pristine and irradiated states of (g) CABS-0.4, (h) CABS-0.6, and (i) CABS-0.75 glasses.

loop sizes increasing with reduced loop numbers).

### 3.3. Experimental mechanical properties

The experimental determination of micro-mechanical properties using the micro-indentation is schematically illustrated in Fig. 5a. Based on the experimental indentation test, the related micro-mechanical properties of CABS glasses before and after irradiation were explored, including the hardness ( $H_v$ ), crack resistance (CR), and indentation fracture toughness ( $K_{IFT}$ ). Here, CR reflects the resistance for crack initiation while  $K_{IFT}$  represents the resistance of crack propagation.

Fig. 6a shows Young's modulus data for the as-made and irradiated CABS glasses. For the as-made glasses, the modulus was measured by ultrasonic echography, but the values were also determined from the load-depth curves (see Fig. S14) based on the indentation test, since the irradiation process only affects the surface region ( $\sim 1.7 \mu\text{m}$ , see Table S2). The absolute values differ between the two tests, as also reported previously for other glasses[89], but the compositional trend is the same. The modulus values of the irradiated CABS glasses derived from indentation decrease compared to the as-made glasses, with a larger decrease for a larger irradiation dose. The decrease of modulus may be explained by the density and structural changes. That is, the less rigid and open structure of  $^{13}\text{B}$  can likely explain the decrease in modulus upon irradiation[90], since modulus is mainly controlled by the bond strengths and the number of bonds per volume[91]. In addition, Kieu et al. found that the decrease in modulus is proportional to the increase in the fraction of  $^{13}\text{B}$  atoms in the glass network[92]. The transition from  $^{14}\text{B}$  to  $^{13}\text{B}$  also allows the formation of more non-bridging oxygens. That is, the  $\text{Ca}^{2+}$  ions that originally charge-compensated the  $[\text{BO}_4]$  groups can be converted into a network modifier that is connected to the  $\text{SiO}_4$  unit. In addition, based on the medium range structural changes (see Fig. 3c-f), the formation of larger loops will decrease the bond density, also contributing to the reduced modulus after irradiation.

Fig. 6b shows the hardness data for the as-made and irradiated CABS glasses. Hardness decreases upon irradiation, consistent with previous findings for hardness of some borosilicate glasses irradiated with different ions[84,91,93,94]. The changes in hardness of the samples under different doses is more pronounced when performing the

indentation using a smaller load (0.1 N), with the irradiation-induced decrease of hardness being positively correlated with the dose (Fig. S15). Structural analysis from both Raman and MD simulations indicates that some of the four-coordinated B atoms transform into the three-coordinated B atoms after irradiation.  $^{13}\text{B}$  has a more open structure as it does not require charge compensation, and  $^{13}\text{B}$  also has a planar structure, which makes it easier to undergo densification and increase its coordination number during indentation[90]. Studies indicate that the larger the fraction of three-coordinated B, the larger the decrease in hardness[95]. Therefore, due to the free volume accumulation and reduction of boron coordination in parallel with the formation of non-bridging oxygen, plastic deformation will be promoted, which will also result in the decrease in hardness[96]. Fig. 6c shows the load dependence of hardness for the CABS-0.4 glass, with an initial decrease in hardness with the increase of applied load for the as-made sample before it reaches an approximately constant value. For the irradiated sample, as the applied load increases, the hardness of the sample first decreases first, then slightly increases, and finally it also reaches a constant value. The smallest hardness is at about  $1.7 \mu\text{m}$  for the irradiated glass (Fig. S16), then slowly increases and then stabilizes, which may also be related to the reduced hardness of the irradiated layer. In the process of indentation, as the applied load increases, the corresponding depth also increases, and the proportion of the irradiation layer will be relatively reduced.

Based on optical images of indents (Fig. 5b), we find that the crack resistance of the irradiated glasses increases compared to the as-made glasses. That is, the optical images for indentation under 15 N for the three irradiated CABS glasses show no cracks compared to the as-made glasses, which exhibits a higher damage-resistant behavior after irradiation. Fig. 6d shows the crack resistance for the as-made and irradiated CABS glasses, with the individual crack probability vs. load curves shown in Fig. S17. CR increases upon irradiation, specifically, crack resistance increased by more than 400% (from 5.6 N to 28 N) for the irradiated CABS-0.75 glass compared to the as-made one. Based on the MD simulation results (Fig. 2a), it can be found that the initial CN of B in CABS-0.4 and CABS-0.75 is relatively higher than that in CABS-0.6 before irradiation, and eventually reaches a constant value in all the glasses with an increase in the deposited energy. This indicates that for CABS-0.4 and CABS-0.75 glasses, the transition from  $^{14}\text{B}$  to  $^{13}\text{B}$  is more pronounced, which is consistent with the trend of CR change in the experiment.

It has been shown that the residual stress is the driving force for the radial crack[97–99]. Based on the expanding cavity model, densification serves as an alternative to the plastic zone expansion under the indenter[99]. Therefore, the densification deformation tends to produce less residual stress and less subsurface damage, as a result, the threshold load required to initiate cracks increases. In other words, crack resistance usually increases with the increasing contribution of densification under the indenter. Studies have shown that the high shear deformation tendency of boron atoms and the easiness of boron coordination transformation under load improve the crack resistance[100]. For these mechanisms to be effective, it is not just the boron content that is important, but the initial threefold boron content in the glass. Therefore, as the four-coordinated B is transformed into the three-coordinated B after irradiation, the "reversible" coordination change of CABS under indentation helps to improve its crack resistance as it dissipates energy and reduces stress accumulation[100].

Fracture toughness is an important property used in glass fracture mechanics to predict the combination of stress and defect size required for fracture. In this study, an indentation test was performed on CABS glass to calculate the indentation fracture toughness ( $K_{IFT}$ ) (Table S4). As shown in Fig. 6e, irradiation treatment causes  $K_{IFT}$  to increase, with a larger increase for a larger irradiation dose. We have also calculated the fracture energy ( $G_c$ ) from the  $K_{IFT}$  data (Table S5). Fig. 6f shows that the  $G_c$  of CABS glass increases after irradiation. Interestingly, we also observe that the most toughening occurs for the CABS-0.4 glass, which

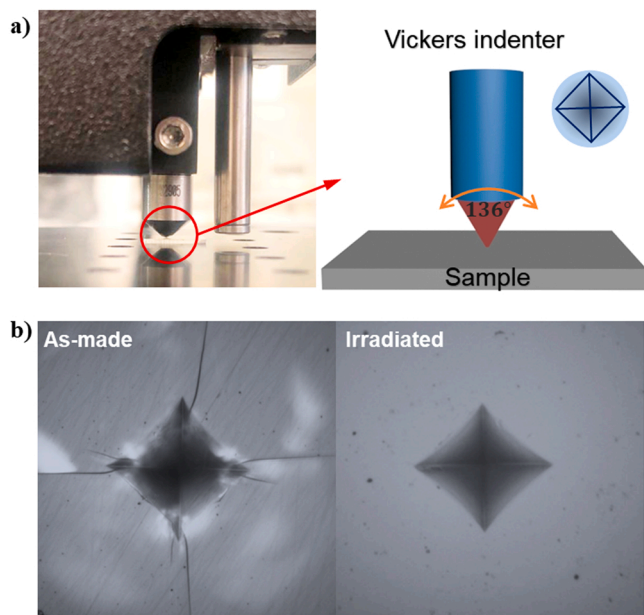
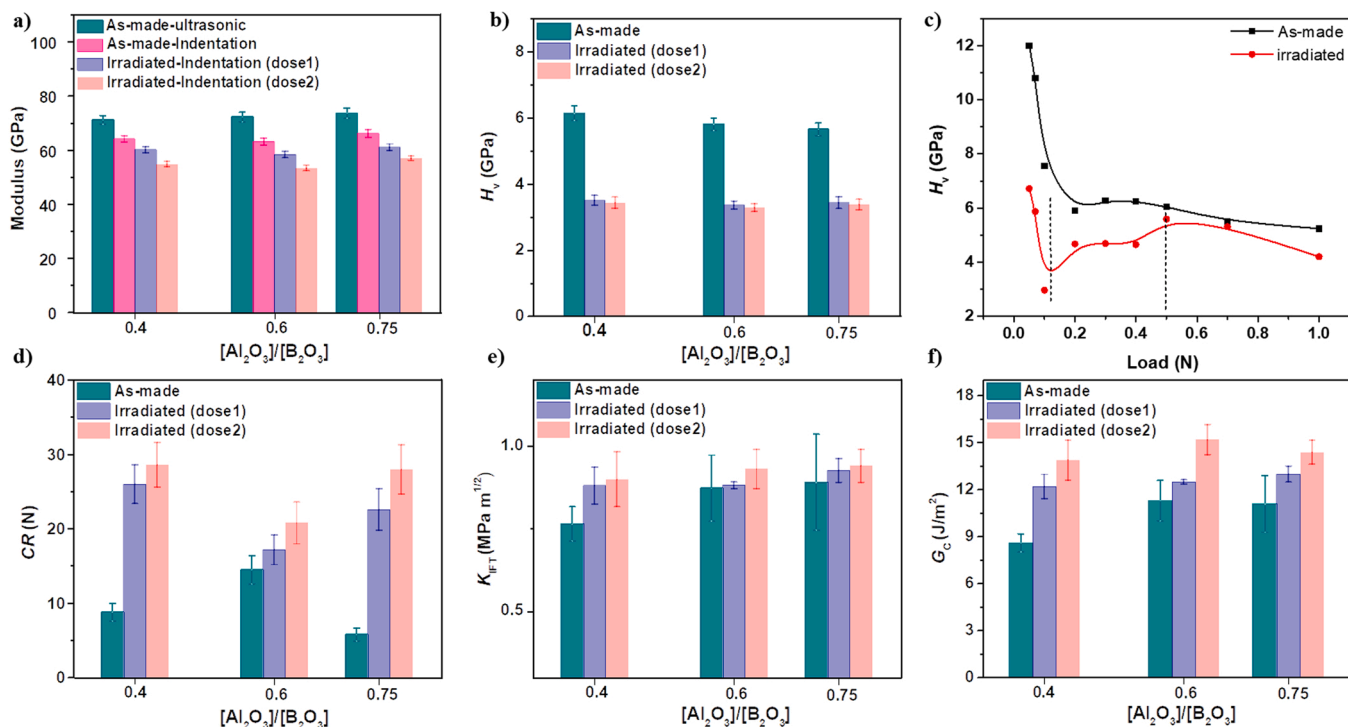


Fig. 5. (a) Example of Vickers indentation of the CABS-0.4 glass. (b) Optical images of indents produced at 15 N on the surface of the as-made (left) and the irradiated (right) CABS-0.4 glasses, respectively.





**Fig. 6.** (a) Young's modulus ( $E$ ) of the as-made and irradiated CABS glasses as determined from ultrasonic echography or the load-depth indentation curve. Dose 1 and Dose 2 refer to irradiation doses of  $2.0 \cdot 10^{13}$  ions/cm<sup>2</sup> and  $2.0 \cdot 10^{14}$  ions/cm<sup>2</sup>, respectively. (b) Vickers hardness ( $H_V$ ) of the irradiated glass and as-made glasses. (c) Load dependence of hardness for the CABS-0.4 glass. (d) Crack resistance ( $CR$ ) from Vickers indentation of the as-made and irradiated CABS glasses. (e) Indentation fracture toughness ( $K_{IF}$ ) determined using a sharp  $100^\circ$  tip of the as-made and irradiated CABS glasses. (f) Calculated fracture energy ( $G_c$ ) based on  $K_{IF}$  data for the as-made and irradiated CABS glasses.

also experienced the most obvious  $^{[4]}\text{B}$  to  $^{[3]}\text{B}$  conversion after irradiation. Since fracture is closely related to the reorganization of atomic structure under deformation, which is challenging to characterize experimentally, we here use MD simulation to reveal the mechanism of irradiation-induced toughening in the following section.

### 3.4. Fracture simulations

To gain a deeper understanding of the structure-properties relationship of the irradiated CABS glasses, the fracture behavior of the as-made and irradiated glasses is simulated with MD. We simulated the mode I fracture of the glass samples with a precrack (see Section 2.3.4). As shown in Fig. 7a, the crack grows from the edges of the precrack and then propagates perpendicular to the loading direction upon tension. Comparing the fracture behaviors at a strain of 0.2, we clearly observe that while the as-made glass is almost fractured, the irradiated glass structures are still relatively intact with a more ductile fracture response. The fracture process of the two other compositions exhibit a similar behavior (see Fig. S18). Fig. 7b-d show the stress-strain curves of the three CABS glasses upon uniaxial fracture. The as-made glasses exhibit a fairly brittle response, which manifests itself by a sudden drop in the stress-strain curve after the crack starts to propagate. However, the irradiated samples feature an improved nanoductility by exhibiting a slower decay of stress after the crack initiation. This irradiation-induced nanoductility has also previously been observed in silica systems[56, 101]. Additionally, we also note that the slope of the stress-strain curves in the elastic region (strain  $\varepsilon < 0.05$ ) decreases upon irradiation, indicating a reduced stiffness induced by irradiation. Interestingly, we find that the irradiated CABS-0.4 glasses exhibit a more ductile fracture without a lower yield stress, indicating a higher fracture energy after irradiation for this glass composition.

Based on the stress-strain curves, we determine the Young's modulus  $E$  and fracture energy  $G_c$ . As shown in Table 3, both the values and the

trend of Young's modulus are in good agreement with the experimental values (see Fig. 6a). Although the fracture energies are slightly underestimated relative to the experimental values from indentation techniques (Fig. 6f), the irradiation dependence on the fracture energy is fully captured by MD simulations. Specifically, the  $G_c$  values of all the CABS glasses increases after irradiation, with the CABS-0.4 sample increasing the most from the initially lowest  $G_c$ . We also note that the  $^{[4]}\text{B}$  to  $^{[3]}\text{B}$  conversion upon irradiation in the CABS-0.4 sample is the most pronounced, indicating that the  $^{[4]}\text{B}$  to  $^{[3]}\text{B}$  conversion is responsible for the irradiation induced nanoductility.

The origin of irradiation-induced nanoductility is further investigated by analyzing the bond switching activities of the network formers in the CABS glasses (i.e., Al, B, and Si atoms). Here, the fraction of bond switching atoms are categorized by comparing the CN of each atom with its initial CN at nonstrained state, i.e., whether atom will increase, decrease, or swap its neighbor atoms under tensile deformation. As shown in Fig. S19, all the bond switching activities increase with an increase in strain, indicating that the structural reorganization is closely related to bond switching to dissipate the strain energy[5]. Under deformation, most of the bond switching events are related to Al and B atoms. When the glass is subjected to irradiation, the fraction of swapped CN Al atoms increases significantly, while all the bond switching of B atoms also rise at varying degrees. Interestingly, although the CN of Al atoms do not exhibit large changes upon irradiation, the propensity for Al atoms to swap its CN significantly increase with increasing deposited energy. This can be attributed to the fact that the  $^{[4]}\text{B}$  to  $^{[3]}\text{B}$  conversion decreases the number of Ca atoms used for charge compensating  $^{[4]}\text{B}$  atoms, which in turn facilitates the increase in the number of non-bridging oxygens. As shown in Fig. S20, the  $Q_n$  units of Al atoms with less connectivity ( $n < 4$ ,  $Q_n$  denotes Al atom connects with  $n$  bridging oxygens) increase upon irradiation, promoting the bond switching of Al atoms.

Meanwhile, the medium-range structure also changes upon

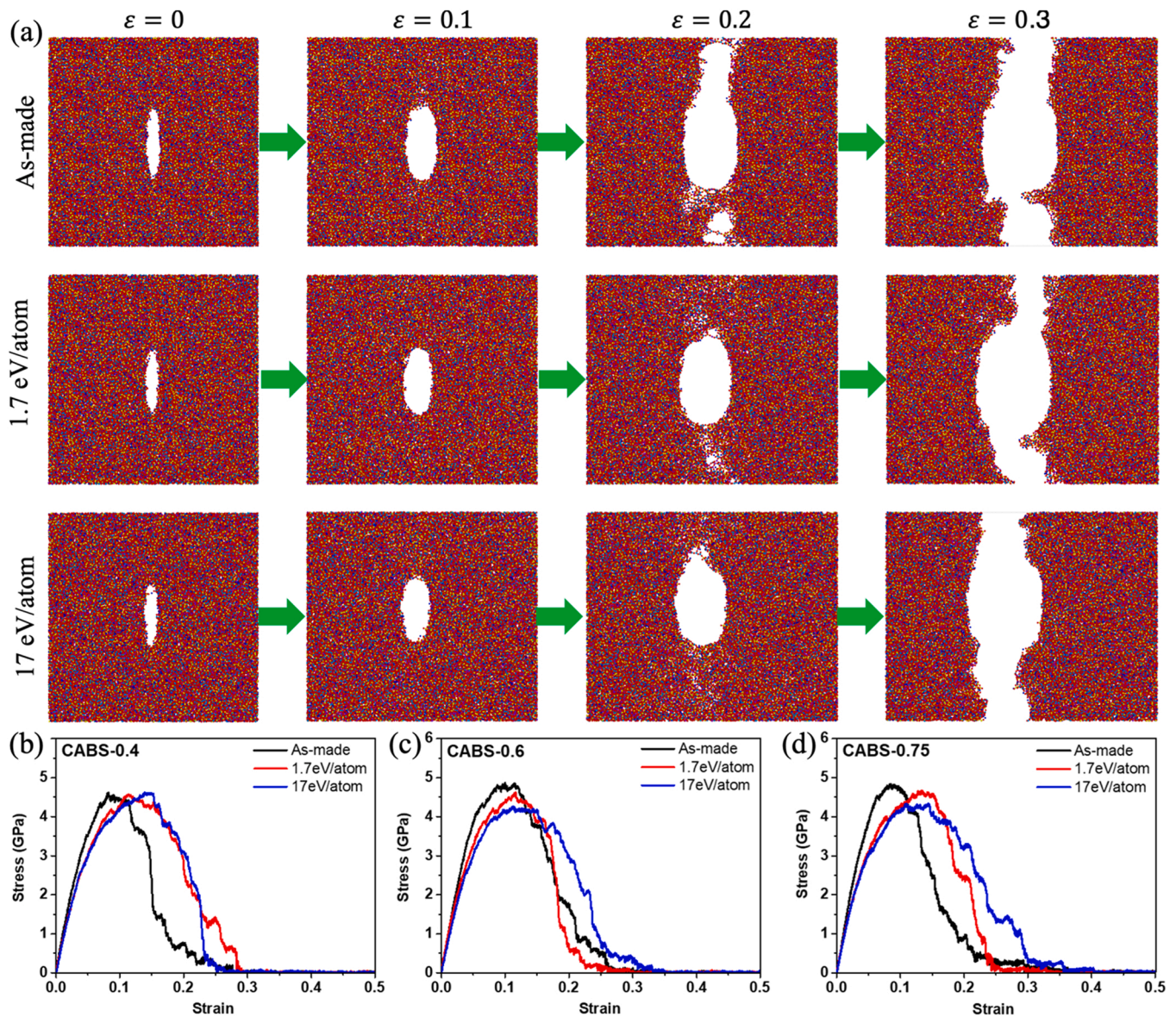


**Fig. 7.** (a) Evolution of fracture in the pre-cracked CABS-0.4 glass at tensile strains of 0, 0.1, 0.2, and 0.3. (b-d) Stress-strain curves of (b) CABS-0.4, (c) CABS-0.6, and (d) CABS-0.75 glasses subjected to different amounts of irradiation energies (0, 1.7, and 17 eV/atom).

**Table 3**

Young's modulus and fracture energy calculated based on MD simulations.

	Young's modulus $E$ (GPa)			Fracture energy $G_c$ (J/m <sup>2</sup> )		
	As-made	1.7 eV/atom	17 eV/atom	As-made	1.7 eV/atom	17 eV/atom
CABS-0.4	71.2	60.4	61.4	4.1	4.4	5.9
CABS-0.6	78.3	63.5	60.6	4.9	4.7	5.0
CABS-0.75	78.8	61.5	60.9	4.3	4.7	5.0

irradiation to facilitate bond switching and leads to an improved nanoductility, e.g., the formation of small rings (less than four atoms), which are over-constrained and tend to reorganize upon deformation. This indicates that the irradiation-induced nanoductility can be attributed to the structural changes originating from the <sup>[4]B</sup> to <sup>[3]B</sup> conversion, which in turn promotes the propensity for bond switching of both Al and B atoms. In metallic glasses, the irradiation-induced ductility is

found to be correlated with formation of liquid-like structures, which causes the deformation pattern to transition from localized shear banding to homogeneous shear flow [102,103]. The atoms with higher potential energy induced by irradiation are more likely to participate in shear transformations [104]. As such, the toughening mechanism induced by irradiation in oxide and metallic glasses can be both explained through the formation of atoms with high propensity for plastic rearrangement.

#### 4. Conclusion

In this work, we have investigated the relation between structure and mechanical properties in CABS glasses subjected to irradiation through both experimental measurements and MD simulations. We find that the irradiation-induced structure changes in CABS glasses are mainly attributed to the boron speciation changes from <sup>[4]B</sup> to <sup>[3]B</sup>, which leads to a more open structure with an increased disorder at the medium-range length scale. The structure of CABS glasses with higher initial fraction of tetrahedral boron units are therefore found to be more susceptible to change upon irradiation. Upon irradiation of the glass surface



layers, the modulus and hardness decrease, while the crack resistance increases significantly. Specifically, crack resistance increased by more than 400% for the irradiated CABS-0.75 glass compared to the as-made one. In the case of hardness, the experiments performed at different loads showed that hardness first decreased with load, then increased slightly, and finally reached a constant value. This can be related to the decrease in the hardness of the  $\mu\text{m}$ -sized irradiated layer. Furthermore, both the experimental and simulation data show that the fracture energy also increases upon irradiation, with an improved nanoductility in the irradiated structures. This irradiation-induced nanoductility is attributed to the changes in medium-range structure, which facilitates bond switching of Al and B atoms. Interestingly, the CABS glass composition with the largest increase in CR and  $K_{\text{IFT}}$  is the one with the most  $^{14}\text{B}$ -rich structure, which is more susceptible to structural reorganization upon irradiation.

### CRedit authorship contribution statement

**Xiangting Ren:** Methodology, Investigation, Writing – original draft. **Tao Du:** Formal analysis, Investigation, Writing – original draft. **Haibo Peng:** Investigation, Writing – review & editing. **Lars R. Jensen:** Investigation, Writing – review & editing. **Christophe A. N. Biscio:** Formal analysis, Writing – review & editing. **Lisbeth Fajstrup:** Formal analysis, Writing – Review & Editing. **Mathieu Bauchy:** Conceptualization, Writing – review & editing. **Morten M. Smedskjaer:** Conceptualization, Supervision, Writing – original draft.

### Declaration of Competing Interest

The authors declare that they have no known competing financial interests or personal relationships that could have appeared to influence the work reported in this paper.

### Data Availability

The raw and processed data required to reproduce these findings are available from the corresponding author upon request.

### Acknowledgements

This work was supported by grants from the China Scholarship Council (No. 201906250152) to X.R., the Marie Skłodowska-Curie Individual Fellowship (No. 101018156) to T.D., the Independent Research Fund Denmark (No. 1026-00037B) to M.M.S., C.A.N.B. and L.F., the Fundamental Research Funds for the Central Universities of China (No. lzujbky-2021-kb11) to H.P., and the National Science Foundation (No. CMMI-1762292 and DMR-1944510) to M.B. We also thank Aalborg University for providing the computational resources through CLAAUDIA.

### Appendix A. Supporting information

Supplementary data associated with this article can be found in the online version at [doi:10.1016/j.mtcomm.2022.103649](https://doi.org/10.1016/j.mtcomm.2022.103649).

### References

- [1] L. Wondraczek, J.C. Mauro, J. Eckert, U. Kühn, J. Horbach, J. Deubener, T. Rouxel, *Adv. Mater.* 23 (2011) 4578–4586.
- [2] J.C. Mauro, A. Tandia, K.D. Vargheese, Y.Z. Mauro, M.M. Smedskjaer, *Chem. Mater.* 28 (2016) 4267–4277.
- [3] J. Luo, J. Wang, E. Bitzek, J.Y. Huang, H. Zheng, L. Tong, Q. Yang, J. Li, S.X. Mao, *Nano Lett.* 16 (2016) 105–113.
- [4] K. Zheng, C. Wang, Y.-Q. Cheng, Y. Yue, X. Han, Z. Zhang, Z. Shan, S.X. Mao, M. Ye, Y. Yin, E. Ma, *Nat. Commun.* 1 (2010) 24.
- [5] E.J. Frankberg, J. Kalikka, F.G. Ferré, L. Joly-Pottuz, T. Salminen, J. Hintikka, M. Hokka, S. Konet, T. Douillard, M. Vanazzi, L. Roiban, J. Akola, F.D. Fonzo, E. Levänen, K. Masenelli-Varlot, *Science* (2019) 7.
- [6] T. Du, H. Liu, L. Tang, S.S. Sørensen, M. Bauchy, M.M. Smedskjaer, *ACS Nano* 15 (2021) 17705–17716.
- [7] G.D. Quinn, J.J. Swab, *J. Eur. Ceram. Soc.* 37 (2017) 4243–4257.
- [8] T. To, *Fracture Toughness and Fracture Surface Energy of Inorganic and Non-Metallic Glasses*, These de doctorat, Rennes 1, 2019.
- [9] M.B. Østergaard, S.R. Hansen, K. Januchta, T. To, S.J. Rzoska, M. Bockowski, M. Bauchy, M.M. Smedskjaer, *Materials* 12 (2019) 2439.
- [10] J. Luo, J.C. Mauro, *Transparent Silicate Glasses with High Fracture Toughness*, WO2018017638A1, 2018.
- [11] T. To, S.S. Sørensen, J.F.S. Christensen, R. Christensen, L.R. Jensen, M. Bockowski, M. Bauchy, M.M. Smedskjaer, *ACS Appl. Mater. Interfaces* 13 (2021) 17753–17765.
- [12] T.M. Gross, J.J. Price, *Front. Mater.* 4 (2017).
- [13] J.J. Price, G.S. Glaesemann, D.A. Clark, T.M. Gross, K.L. Barefoot, *SID Symp. Dig. Tech. Pap.*, 40, 2009, pp. 1049–1051.
- [14] T.M. Gross, *J. Non-Cryst. Solids* 358 (2012) 3445–3452.
- [15] K.W. Peter, *J. Non-Cryst. Solids* 5 (1970) 103–115.
- [16] A. Arora, D.B. Marshall, B.R. Lawn, M.V. Swain, *J. Non-Cryst. Solids* 31 (1979) 415–428.
- [17] J.T. Hagan, *J. Mater. Sci.* 15 (1980) 1417–1424.
- [18] J.D. Mackenzie, *J. Am. Chem. Soc.* 46 (1963) 461–470.
- [19] E.H. Yoffe, *Philos. Mag.* 46, 1982, pp. 617–628.
- [20] T.M. Gross, J. Wu, D.E. Baker, J.J. Price, R. Yongsunthorn, *J. Non-Cryst. Solids* 494 (2018) 13–20.
- [21] S.G. Motke, S.P. Yawale, S.S. Yawale, *Bull. Mater. Sci.* 25 (2002) 75–78.
- [22] X. Ren, P. Liu, S.J. Rzoska, B. Lucznik, M. Bockowski, M.M. Smedskjaer, *Materials* 14 (2021) 3450.
- [23] G. Hj. Matzke, J.C. Della Mea, G. Dran, B. Linker, Tiveron, *Nucl. Instrum. Methods Phys. Res. Sect. B Beam Interact. Mater.* 46 (1990) 253–260.
- [24] C.M. Jantzen, D.I. Kaplan, N.E. Bibler, D.K. Peeler, M. John Plodinec, *J. Nucl. Mater.* 378 (2008) 244–256.
- [25] W. Yuan, H. Peng, M. Sun, X. Du, P. Lv, Y. Zhao, F. Liu, B. Zhang, X. Zhang, L. Chen, T. Wang, *J. Chem. Phys.* 147 (2017), 234502.
- [26] M. Guan, X.Y. Zhang, K.J. Yang, T.T. Wang, F.F. Liu, M.L. Sun, X. Du, T.S. Wang, H.B. Peng, *J. Non-Cryst. Solids* 518 (2019) 118–122.
- [27] D.A. Kilymis, J.M. Delaye, *J. Non-Cryst. Solids* 382 (2013) 87–94.
- [28] D.A. Kilymis, J.-M. Delaye, *J. Chem. Phys.* 141 (2014), 014504.
- [29] D.A. Kilymis, J.-M. Delaye, *J. Non-Cryst. Solids* 401 (2014) 147–153.
- [30] D.A. Kilymis, J.-M. Delaye, S. Ispas, *J. Chem. Phys.* 145 (2016), 044505.
- [31] M. Sebastiani, K.E. Johannis, E.G. Herbert, G.M. Pharr, *Curr. Opin. Solid State Mater. Sci.* 19 (2015) 324–333.
- [32] G.M. Pharr, W.C. Oliver, F.R. Brotzen, *J. Mater. Res.* 7 (1992) 613–617.
- [33] E. Broitman, *Tribol. Lett.* 65 (2016) 23.
- [34] M. Wada, H. Furukawa, K. Fujita, *Proc. 10th Int. Congr. Glass* 11 (1974).
- [35] K. Niihara, R. Morena, D.P.H. Hasselman, *J. Mater. Sci. Lett.* 1 (1982) 13–16.
- [36] B.R. Lawn, M.V. Swain, *J. Mater. Sci.* 10 (1975) 113–122.
- [37] A. Makishima, J.D. Mackenzie, *J. Non-Cryst. Solids* 12 (1973) 35–45.
- [38] D.B. Marshall, R.F. Cook, N.P. Padture, M.L. Oyen, A. Pajares, J.E. Bradby, I. E. Reimanis, R. Tandon, T.F. Page, G.M. Pharr, B.R. Lawn, *J. Am. Ceram. Soc.* 98 (2015) 2671–2680.
- [39] G.R. Anstis, P. Chantikul, B.R. Lawn, D.B. Marshall, *J. Am. Ceram. Soc.* 64 (1981) 533–538.
- [40] G.R. Irwin, *Fract. Hanbuck Phys. VI Elast. Plast.*, 1958, pp. 551–590.
- [41] S. Plimpton, *J. Comput. Phys.* 117 (1995) 1–19.
- [42] A. Stukowski, *Model. Simul. Mater. Sci. Eng.* 18 (2009), 015012.
- [43] L. Deng, J. Du, *J. Am. Ceram. Soc.* 102 (2019) 2482–2505.
- [44] J. Du, *Mol. Dyn. Simul. Disord. Mater. Netw. Glas. Phase-Change Mem. Alloys*, Springer International Publishing C. Massobrio J. Du M. Bernasconi P.S. Salmon Cham 2015 157 180.
- [45] F. Lodesani, M.C. Menziani, H. Hijiya, Y. Takato, S. Urata, A. Pedone, *Sci. Rep.* 10 (2020) 2906.
- [46] P.H. Kuo, J. Du, *J. Phys. Chem. C* 123 (2019) 27385–27398.
- [47] S.S. Sørensen, H. Johra, J.C. Mauro, M. Bauchy, M.M. Smedskjaer, *Phys. Rev. Mater.* 3 (2019), 075601.
- [48] X. Lu, L. Deng, S. Gin, J. Du, *J. Phys. Chem. B* 123 (2019) 1412–1422.
- [49] M. Wang, N.M. Anoop Krishnan, B. Wang, M.M. Smedskjaer, J.C. Mauro, M. Bauchy, *J. Non-Cryst. Solids* 498 (2018) 294–304.
- [50] J.F. Ziegler, J.P. Biersack, in: D.A. Bromley (Ed.), *Treatise Heavy-Ion Sci. Vol. 6 Astrophys. Chem. Condens. Matter*, Springer US, Boston, MA, 1985, pp. 93–129.
- [51] L. Martínez, R. Andrade, E.G. Birgin, J.M. Martínez, *J. Comput. Chem.* 30 (2009) 2157–2164.
- [52] S. Nosé, *Mol Phys* 52 (1984) 255–268.
- [53] N.M.A. Krishnan, B. Wang, Y. Yu, Y. Le Pape, G. Sant, M. Bauchy, *Phys. Rev. X* 7 (2017), 031019.
- [54] N.M.A. Krishnan, B. Wang, G. Sant, J.C. Phillips, M. Bauchy, *ACS Appl. Mater. Interfaces* 9 (2017) 32377–32385.
- [55] N.M.A. Krishnan, R. Ravinder, R. Kumar, Y. Le Pape, G. Sant, M. Bauchy, *Acta Mater.* 166 (2019) 611–617.
- [56] R. Ravinder, A. Kumar, R. Kumar, P. Vangla, N.M.A. Krishnan, *J. Am. Ceram. Soc.* 103 (2020) 3962–3970.
- [57] S. Le Roux, P. Jund, *Comput. Mater. Sci.* 49 (2010) 70–83.
- [58] L. Guttman, *J. Non-Cryst. Solids* 116 (1990) 145–147.
- [59] T.E. Faber, J.M. Ziman, *Philos. Mag. J. Theor. Exp. Appl. Phys.* 11 (1965) 153–173.
- [60] Q. Zhou, Y. Shi, B. Deng, T. Du, L. Guo, M.M. Smedskjaer, M. Bauchy, *J. Non-Cryst. Solids* 573 (2021), 121138.

- [61] Y. Onodera, S. Kohara, S. Tahara, A. Masuno, H. Inoue, M. Shiga, A. Hirata, K. Tsuchiya, Y. Hiraoka, I. Obayashi, K. Ohara, A. Mizuno, O. Sakata, *J. Ceram. Soc. Jpn.* 127 (2019) 853–863.
- [62] Y. Hiraoka, T. Nakamura, A. Hirata, E.G. Escolar, K. Matsue, Y. Nishiura, *Proc. Natl. Acad. Sci.* 113 (2016) 7035–7040.
- [63] Y. Onodera, S. Kohara, P.S. Salmon, A. Hirata, N. Nishiyama, S. Kitani, A. Zeidler, M. Shiga, A. Masuno, H. Inoue, S. Tahara, A. Polidori, H.E. Fischer, T. Mori, S. Kojima, H. Kawaji, A.I. Kolesnikov, M.B. Stone, M.G. Tucker, M.T. McDonnell, A.C. Hannon, Y. Hiraoka, I. Obayashi, T. Nakamura, J. Akola, Y. Fujii, K. Ohara, T. Taniguchi, O. Sakata, *NPG Asia Mater.* 12 (2020) 85.
- [64] S. Hosokawa, J.-F. Bérar, N. Boudet, W.-C. Pilgrim, L. Pusztai, S. Hiroi, K. Maruyama, S. Kohara, H. Kato, H.E. Fischer, A. Zeidler, *Phys. Rev. B* 100 (2019), 054204.
- [65] Y. Onodera, Y. Takimoto, H. Hijiya, T. Taniguchi, S. Urata, S. Inaba, S. Fujita, I. Obayashi, Y. Hiraoka, S. Kohara, N.P.G. Asia, *NPG Asia Mater.* 11 (2019) 1–11.
- [66] Diode—Persistent Dmitry, *Homol. Softw.* (2021).
- [67] Dionysus2—Persistent Dmitry, *Homol. Softw.* (2021).
- [68] Y. Hiraoka, T. Nakamura, A. Hirata, E.G. Escolar, K. Matsue, Y. Nishiura, *Proc. Natl. Acad. Sci.* 113 (2016) 7035–7040.
- [69] S.S. Sørensen, C.A.N. Biscio, M. Bauchy, L. Fajstrup, M.M. Smedskjaer, *Sci Adv.* 6 (2020), eabc2320.
- [70] L. Brochard, G. Hantal, H. Laubie, F.J. Ulm, R.J.-M. Pellenq, (2013) 2471–2480.
- [71] M. Bauchy, H. Laubie, M.J. Abdolhosseini Qomi, C.G. Hoover, F.-J. Ulm, R.J.-M. Pellenq, *J. Non-Cryst. Solids* 419 (2015) 58–64.
- [72] B. Wang, Y. Yu, Y.J. Lee, M. Bauchy, *Front. Mater.* 2 (2015).
- [73] T. Du, M. Blum, C. Chen, M.G. Muraleedharan, A.C.T. van Duin, P. Newell, *Eng. Fract. Mech.* 250 (2021), 107749.
- [74] W.G. Hoover, *A. Phys. Rev.* 31 1985 1695 1697.
- [75] A. Stukowski, *JOM* 66 (2014) 399–407.
- [76] H. Li, Y. Su, L. Li, D.M. Strachan, *J. Non-Cryst. Solids* 292 (2001) 167–176.
- [77] W.L. Konijnendijk, J.M. Stevels, *J. Non-Cryst. Solids* 20 (1976) 193–224.
- [78] E.I. Kamitsos, G.D. Chrysikos, *J. Mol. Struct.* 247 (1991) 1–16.
- [79] B.N. Meera, J. Ramakrishna, *J. Non-Cryst. Solids* 159 (1993) 1–21.
- [80] K. Vignarooban, P. Boolchand, M. Micoulaut, M. Malki, W.J. Bresser, *Europhys. Lett.* 108 (2014) 56001.
- [81] J. Krogh-Moe, *J. Non-Cryst. Solids* 1 (1969) 269–284.
- [82] N. Ollier, T. Charpentier, B. Boizot, G. Wallez, D. Ghaleb, *J. Non-Cryst. Solids* 341 (2004) 26–34.
- [83] T. Yano, N. Kunimine, S. Shibata, M. Yamane, *J. Non-Cryst. Solids* 321 (2003) 137–146.
- [84] L.T. Chen, X.T. Ren, Y.N. Mao, J.J. Mao, X.Y. Zhang, T.T. Wang, M.L. Sun, T. S. Wang, M.M. Smedskjaer, H.B. Peng, *J. Nucl. Mater.* 552 (2021), 153025.
- [85] K. Januchta, R.E. Youngman, A. Goel, M. Bauchy, S.L. Logunov, S.J. Rzoska, M. Bockowski, L.R. Jensen, M.M. Smedskjaer, *Chem. Mater.* 29 (2017) 5865–5876.
- [86] R. Kumar, A. Jan, M. Bauchy, N.M.A. Krishnan, *J. Am. Ceram. Soc.* n/a (n.d.).
- [87] J.-M. Delaye, S. Peugnet, G. Bureau, G. Calas, *J. Non-Cryst. Solids* 357 (2011) 2763–2768.
- [88] A. Jan, J.-M. Delaye, S. Gin, S. Kerisit, *J. Non-Cryst. Solids* 505 (2019) 188–201.
- [89] S.M. Garner, *Flexible Glass: Enabling Thin, Lightweight, and Flexible Electronics*, John Wiley & Sons, 2017.
- [90] K. Januchta, M. Bauchy, R.E. Youngman, S.J. Rzoska, M. Bockowski, M. M. Smedskjaer, *Phys. Rev. Mater.* 1 (2017), 063603.
- [91] L. Chen, W. Yuan, S. Nan, X. Du, D.F. Zhang, P. Lv, H.B. Peng, T.S. Wang, *Nucl. Instrum. Methods Phys. Res. Sect. B Beam Interact. Mater.* 370 (2016) 42–48.
- [92] L.-H. Kieu, J.-M. Delaye, C. Stolz, *J. Non-Cryst. Solids* 358 (2012) 3268–3279.
- [93] H.B. Peng, M.L. Sun, K.J. Yang, H. Chen, D. Yang, W. Yuan, L. Chen, B.H. Duan, T. S. Wang, *J. Non-Cryst. Solids* 443 (2016) 143–147.
- [94] S. Peugnet, P.-Y. Noël, J.-L. Loubet, S. Pavan, P. Nivet, A. Chenet, *Nucl. Instrum. Methods Phys. Res. Sect. B Beam Interact. Mater.* 246 (2006) 379–386.
- [95] J. de Bonfils, S. Peugnet, G. Panczer, D. de Ligny, S. Henry, P.-Y. Noël, A. Chenet, B. Champagnon, *J. Non-Cryst. Solids* 356 (2010) 388–393.
- [96] L.-H. Kieu, D. Kilymis, J.-M. Delaye, S. Peugnet, *Procedia Mater. Sci.* 7 (2014) 262–271.
- [97] B. Lawn, *Fracture of Brittle Solids*, second ed., Cambridge University Press, Cambridge, 1993.
- [98] R.F. Cook, G.M. Pharr, *J. Am. Ceram. Soc.* 73 (1990) 787–817.
- [99] S.S. Chiang, D.B. Marshall, A.G. Evans, *J. Appl. Phys.* 53 (1982) 298–311.
- [100] H. Liu, B. Deng, S. Sundararaman, Y. Shi, L. Huang, *J. Appl. Phys.* 128 (2020), 035106.
- [101] L. Tang, H. Liu, G. Ma, T. Du, N. Mousseau, W. Zhou, M. Bauchy, *Mater. Horiz.* 8 (2021) 1242–1252.
- [102] D.J. Magagnosc, R. Ehrbar, G. Kumar, M.R. He, J. Schroers, D.S. Gianola, *Sci. Rep.* 3 (2013) 1096.
- [103] Q. Xiao, L. Huang, Y. Shi, *J. Appl. Phys.* 113 (2013), 083514.
- [104] D.Z. Chen, D. Jang, K.M. Guan, Q. An, W.A. Goddard, J.R. Greer, *Nano Lett.* 13 (2013) 4462–4468.

## Supporting information

### **Irradiation-Induced Toughening of Calcium Aluminoborosilicate Glasses**

Xiangting Ren<sup>1,†</sup>, Tao Du<sup>1,†</sup>, Haibo Peng<sup>2</sup>, Lars R. Jensen<sup>3</sup>, Christophe A. N. Biscio<sup>4</sup>, Lisbeth Fajstrup<sup>4</sup>, Mathieu Bauchy<sup>5</sup>, Morten M. Smedskjaer<sup>1,\*</sup>

<sup>1</sup>*Department of Chemistry and Bioscience, Aalborg University, Aalborg East 9220, Denmark*

<sup>2</sup>*School of Nuclear Science and Technology, Lanzhou University, Lanzhou 730000, China*

<sup>3</sup>*Department of Materials and Production, Aalborg University, Aalborg East 9220, Denmark*

<sup>4</sup>*Department of Mathematical Sciences, Aalborg University, Aalborg East 9220, Denmark*

<sup>5</sup>*Department of Civil and Environmental Engineering, University of California, Los Angeles, California 90095, USA*

† These authors contributed equally.

\* Corresponding author. e-mail: mos@bio.aau.dk



**Table S1.** Overview of the properties of the pristine experimental glasses, including glass transition temperature ( $T_g$ ), density ( $\rho$ ), Young's modulus ( $E$ ), Vickers hardness ( $H_v$ ), and crack resistance ( $CR$ ). The error in density is within  $\pm 0.002 \text{ g cm}^{-3}$ .

Glass (As-made)	$T_g$ [°C]	$\rho$ [g/cm <sup>3</sup> ]	$E$ [GPa]	$H_v^{(1)}$ [GPa]	$CR^{(2)}$ (Vickers) [N]
CABS-0.4	665	2.499	71	6.11	8.2
CABS-0.6	668	2.497	72	5.81	14.5
CABS-0.75	683	2.539	73	5.62	5.6

(1)  $H_v$  measured at ambient conditions at load of 4.9 N.

(2)  $CR$  measured at ambient conditions (temperature  $23 \pm 1$  °C, relative humidity  $\sim 39 \pm 5\%$ ).

**Table S2.** Irradiation treatments of the three experimental CABS glasses.

Glass	Ion Energy (MeV)	dE/dX Nuclear (MeV/(mg/cm <sup>2</sup> ))	Projected Range ( $\mu\text{m}$ )	Longitudinal Straggling ( $\text{\AA}$ )	Lateral Straggling ( $\text{\AA}$ )
CABS-0.4	5.00	9.151	1.73	1772	1839
CABS-0.6	5.00	9.132	1.73	1773	1842
CABS-0.75	5.00	9.080	1.71	1770	1835

**Table S3.** Elastic constants of the pristine glasses simulated using two different classical potentials.

		Potential (Deng)	Potential (Wang)
CABS-0.4	E(GPa)	113.34	96.9
	K(GPa)	87.03	71.31
	G(GPa)	44.18	38.04
CABS-0.6	E(GPa)	112.85	120.55
	K(GPa)	82.57	93.34
	G(GPa)	44.35	46.92
CABS-0.75	E(GPa)	113.88	111.4
	K(GPa)	81.94	84.57
	G(GPa)	44.89	43.5

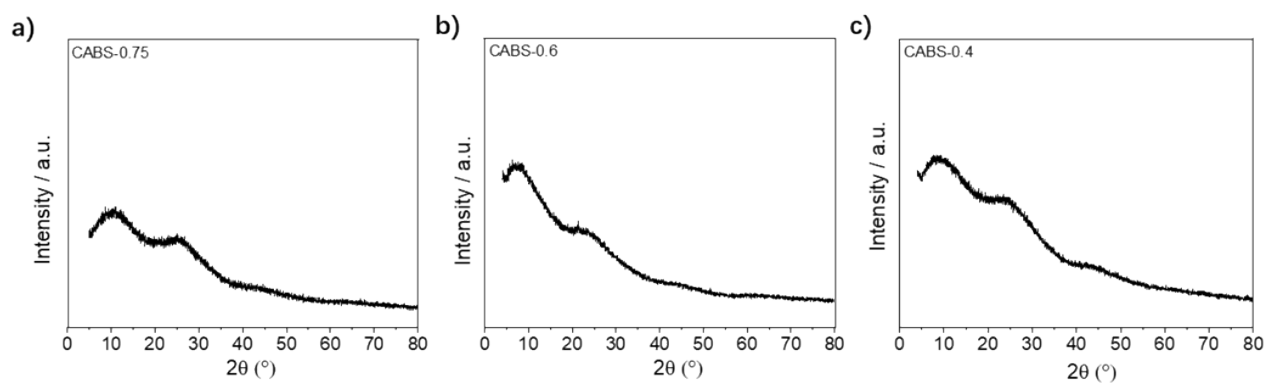
**Table S4.** Indentation fracture toughness ( $K_{\text{IFT}}$ ) (MPa m<sup>0.5</sup>) of the as-made and irradiated CABS glasses.

	<b>CABS-0.75</b>	<b>CABS-0.6</b>	<b>CABS-0.4</b>
As-made	0.891	0.873	0.766
Dose 1	0.927	0.882	0.881
Dose 2	0.941	0.931	0.900

**Table S5.** Experimental fracture energy ( $G_c$ ) (J/m<sup>2</sup>) for the as-made and irradiated CABS glasses.

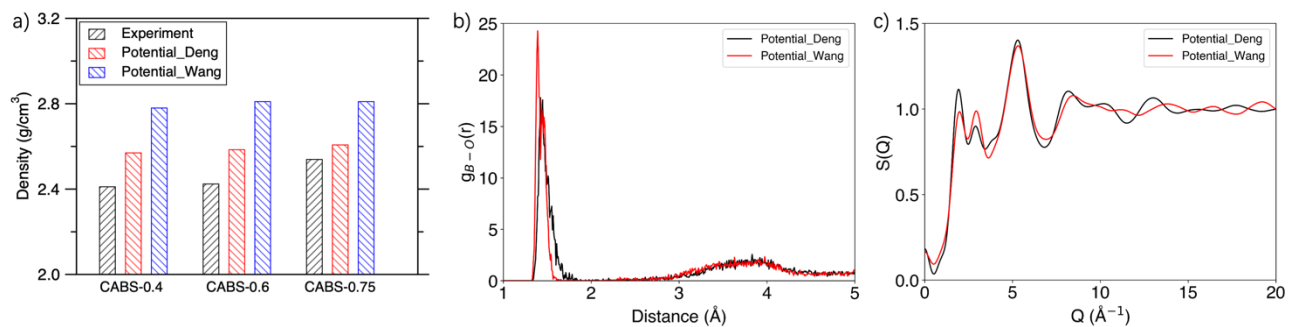
	<b>CABS-0.75</b>	<b>CABS-0.6</b>	<b>CABS-0.4</b>
As-made	11.1	11.3	8.6
Dose 1	13.0	12.5	12.2
Dose 2	14.4	15.2	13.9

**Figure S1**



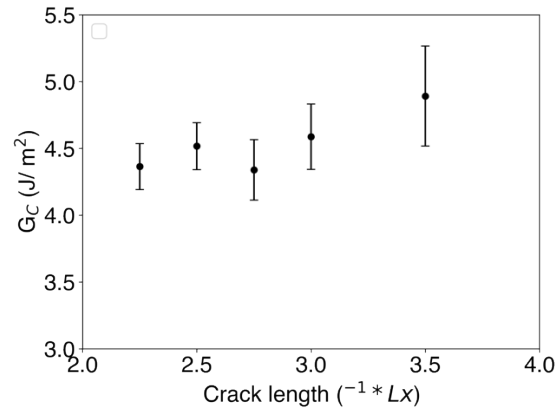
**Figure S1.** XRD spectra of the as-made a) CABS-0.75, b) CABS-0.6, c) CABS-0.4 glasses, showing no signs of crystallization.

**Figure S2**



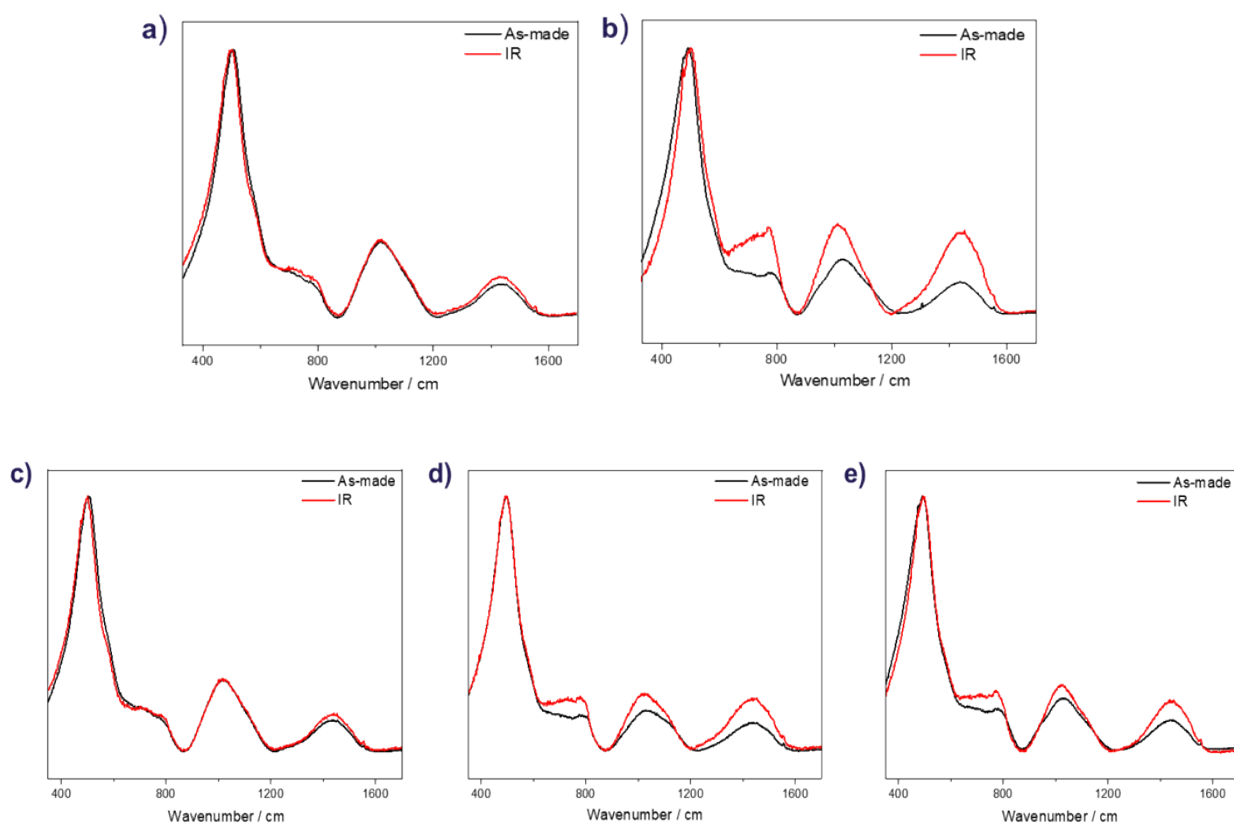
**Figure S2.** (a) Experimental and simulated density of glasses by two different classical potentials. (b) B-O partial pair distribution function and (c) neutron structure factors simulated by two different classical potentials.

**Figure S3**



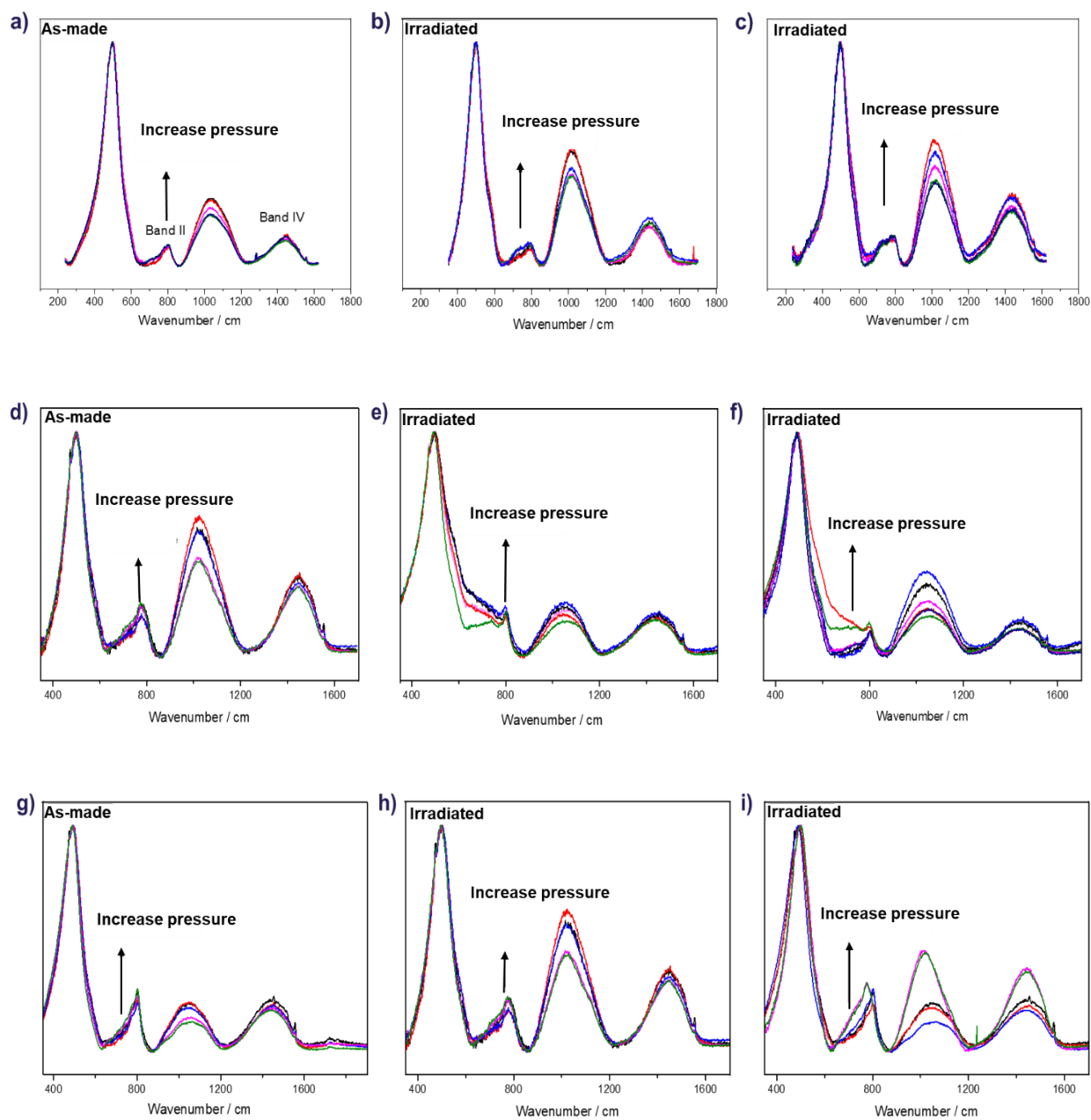
**Figure S3.** Crack size dependence of the simulated fracture energy ( $G_C$ ) in CABS-0.75 glass.  $x$  value of 3 represents the crack length of  $Lx/3$ . By estimating  $G_C$  of the same glass structure with four different crack lengths, we found that the size dependence is small when crack length is less than  $Lx/3$ . Therefore, the crack size of  $Lx/3$  is used in all the simulations.

**Figure S4**



**Figure S4.** Micro-Raman spectra of the as-made and irradiated (IR) glasses: **a)** CABS-0.75 glass (dose 1), **b)** CABS-0.4 glasses (dose 1), **c)** CABS-0.75 glass (dose2), **d)** CABS-0.6 glass (dose2), and **e)** CABS-0.4 glass (dose2).

**Figure S5**



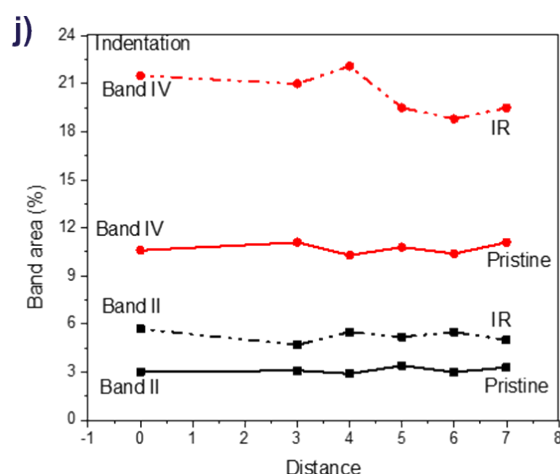


**Figure S5.** Micro-Raman spectra of the as-made **a)** CABS-0.6, **d)** CABS-0.75, **g)** CABS-0.4 glasses recorded at increasing distances from the center of a Vickers indent produced at 4.9 N. Micro-Raman spectra for irradiated (Dose 1) glasses **b)** CABS-0.6, **e)** CABS-0.75, **h)** CABS-0.4 recorded at increasing distances from the center of a Vickers indent produced at 4.9 N. Micro-Raman spectra for irradiated (Dose 2) glasses **c)** CABS-0.6, **f)** CABS-0.75, **i)** CABS-0.4 recorded at increasing distances from the center of a Vickers indent produced at 4.9 N. **j)** Relative area fractions of the two main Raman bands for as-made and irradiated glass at increasing distances from the center of a Vickers indent produced at 4.9 N for CABS-0.6 (Dose2).



**Figure S6**

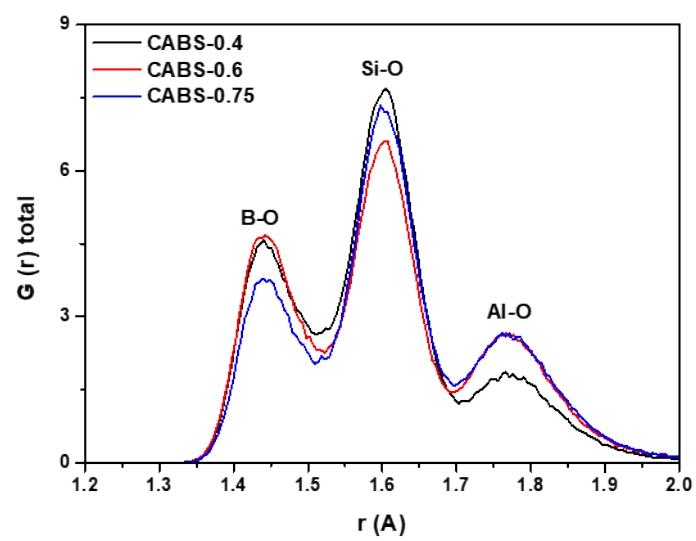


**Figure S6.** Simulated total pair distributions of the as-made CABS glasses.

**Figure S7**

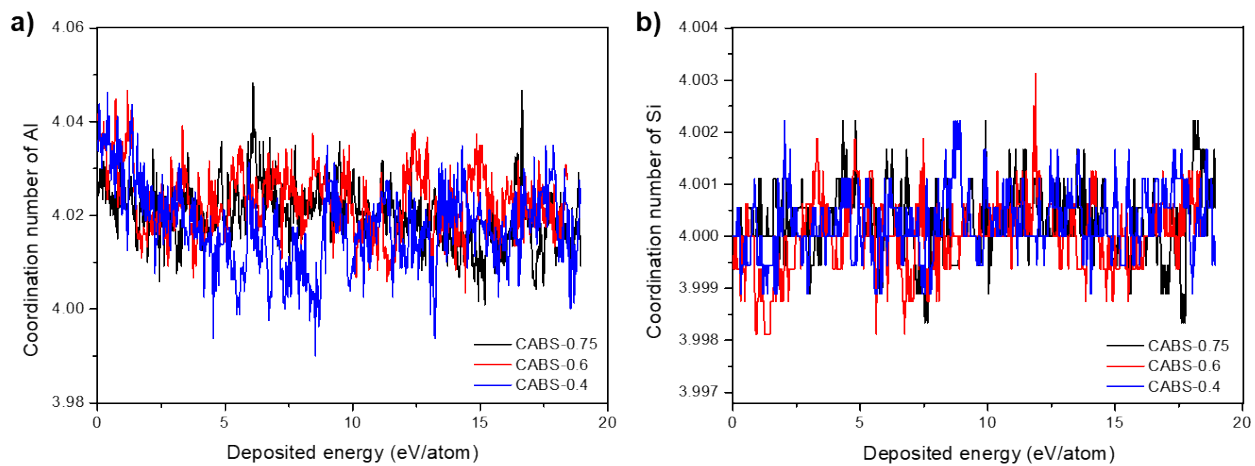


**Figure S7.** a) Simulated average coordination number of Al and b) Si of CABS glasses as function of the deposited energy during the irradiation process.

**Figure S8**

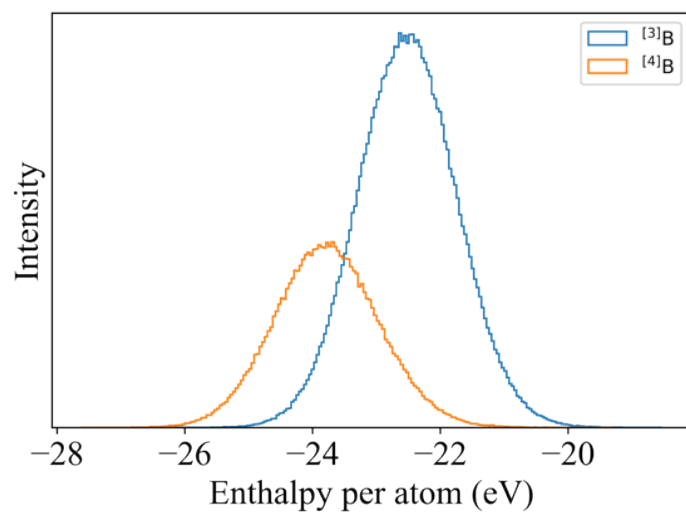


**Figure S8.** Distribution of enthalpy per atom of  $[^3]\text{B}$  and  $[^4]\text{B}$  in the simulated CABS-0.4 sample.

**Figure S9**

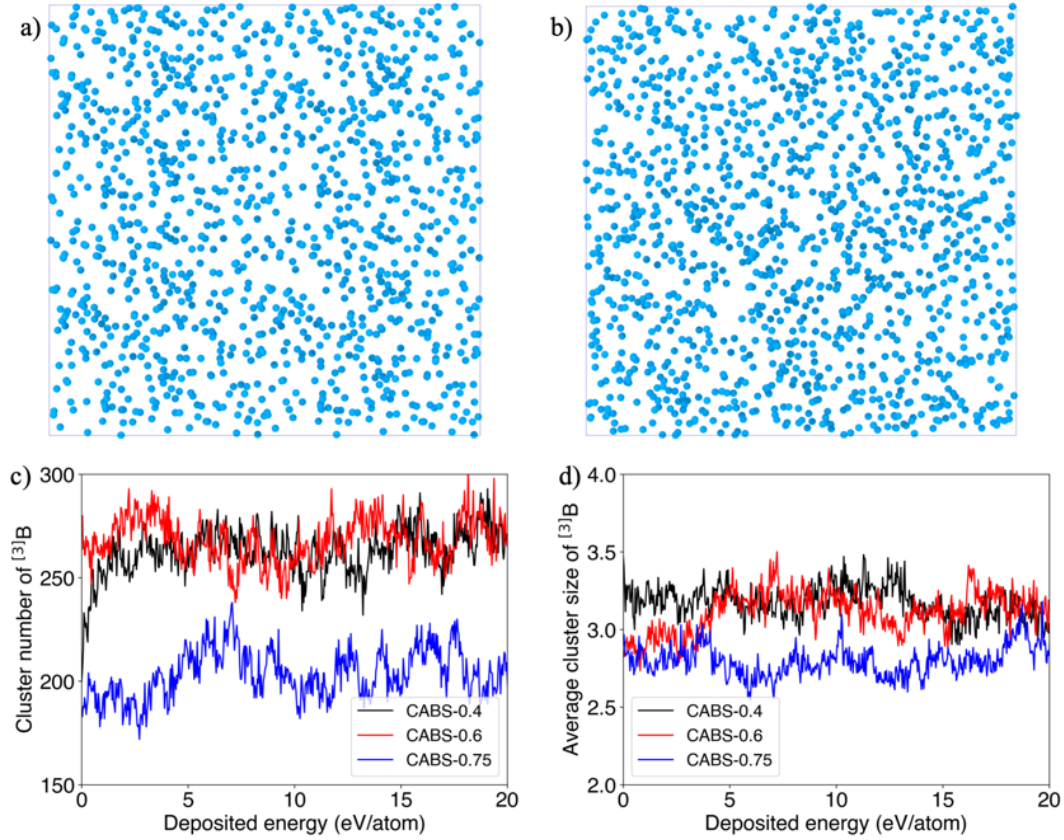


**Figure S9.** Atomic snapshot of  $^{10}\text{B}$  atoms in the simulated CABS-0.4 glass (a) before and (b) after irradiation with dose of 17 eV/atom. Evolution of (c) cluster number and (d) average cluster size of  $^{10}\text{B}$  atoms as a function of the deposited energy during the irradiation process. A cluster is defined as a group of  $^{10}\text{B}$  atoms with a minimum number of two within a cutoff of 3.2 Å. The cutoff is selected as the minimum after the first peak in the B–B partial pair distribution function.

**Figure S10**

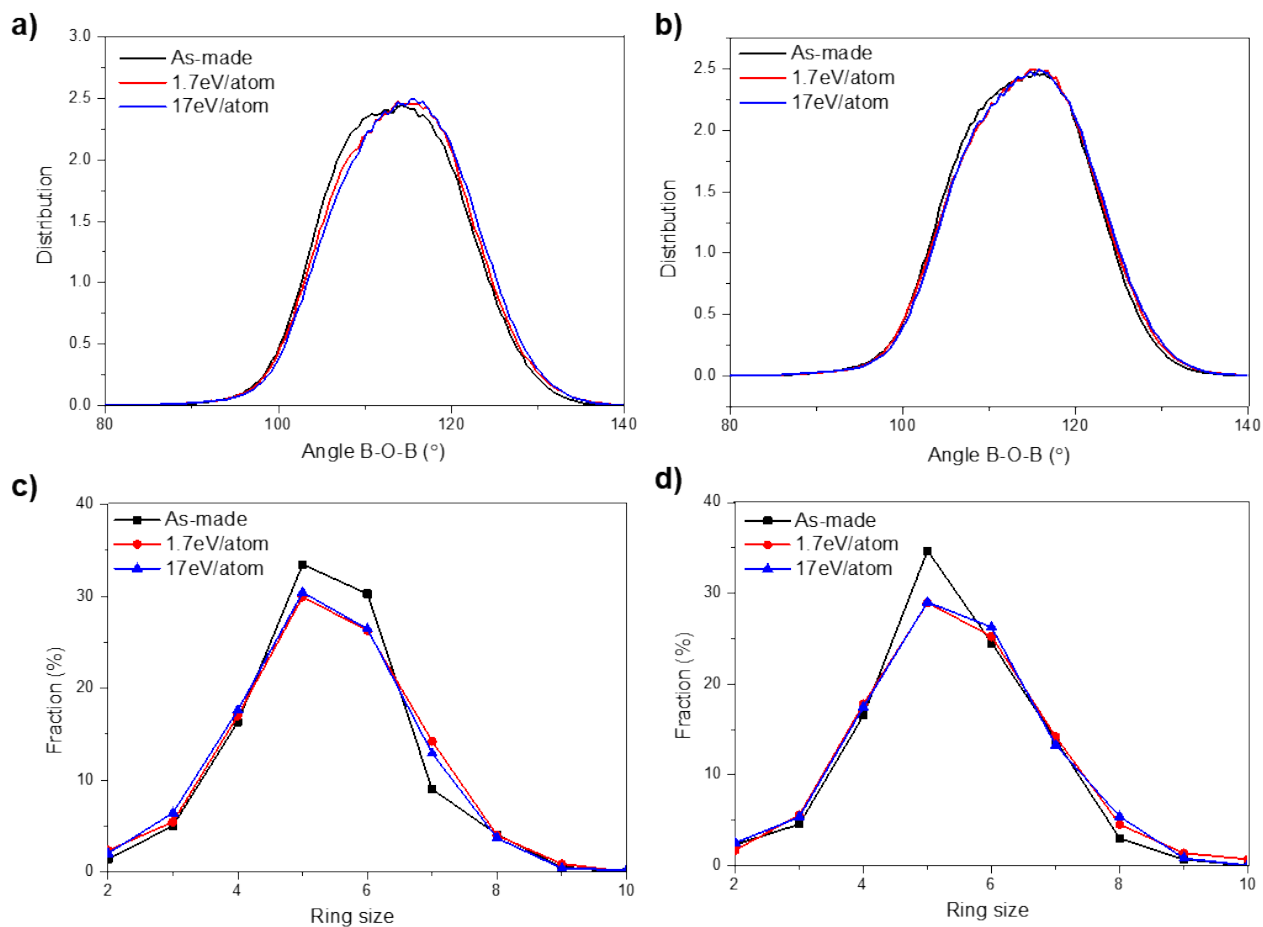


**Figure S10.** Simulated O-B-O bond angle distributions in the **a)** CABS-0.75 and **b)** CABS-0.6 glasses. Ring size distributions of glasses subjected to different amounts of irradiation energies, namely, 0 eV/atom, 1.7 eV/atom, and 17 eV/atom in the samples of **c)** CABS-0.75, **d)** CABS-0.6 glasses.

**Figure S11**

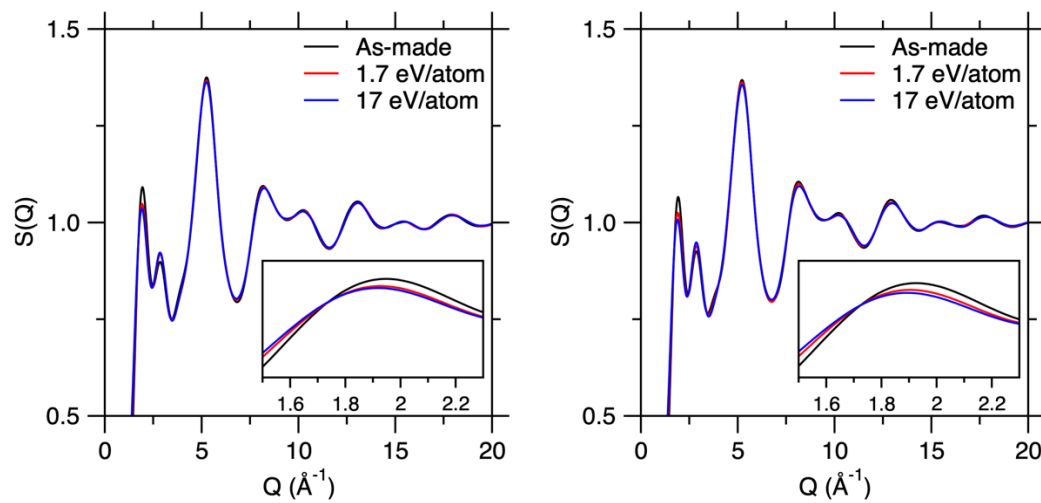


**Figure S11.** Simulated neutron structure factor of the **a)** CABS-0.6 and **b)** CABS-0.75 glasses subjected to different amounts of irradiation energies, namely, 0, 1.7, and 17 eV/atom.

**Figure S12**

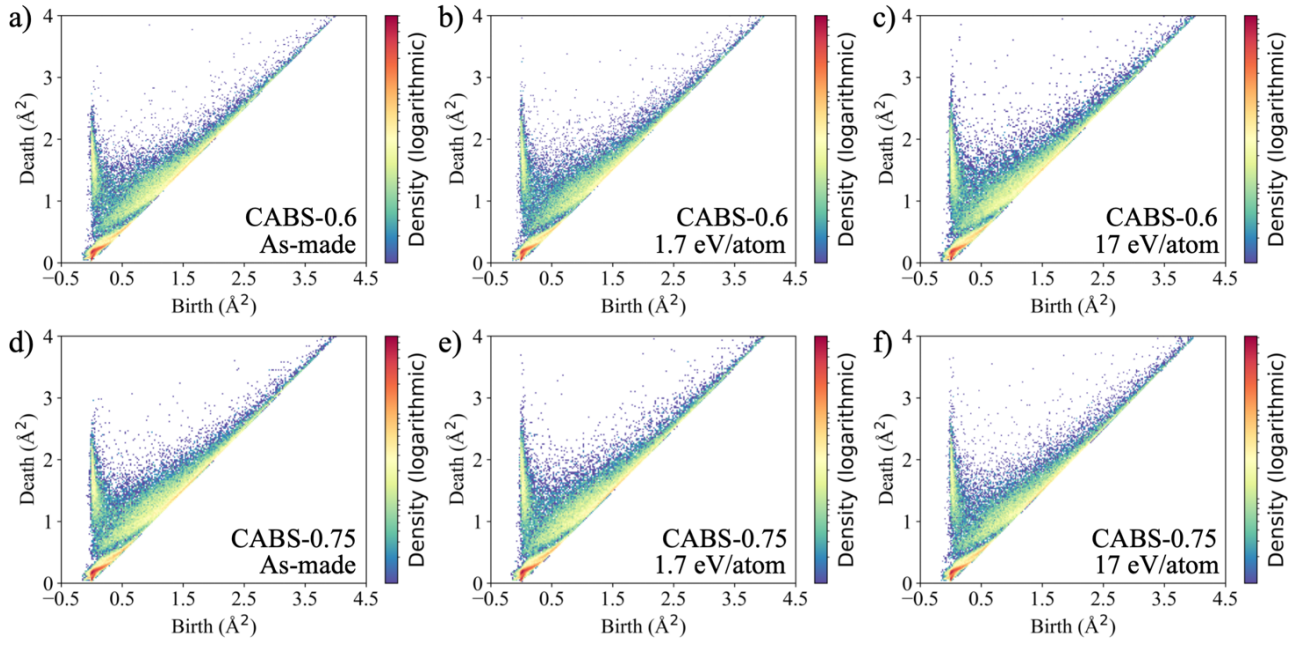


**Figure S12.** Persistence diagrams for CABS-0.6 glass structure at **a)** as-made state, subjected to **b)** 1.7 eV/atom, and **c)** 17 eV/atom. For CABS-0.75 glass structure at **d)** as-made state, subjected to **e)** 1.7 eV/atom, and **f)** 17 eV/atom.

**Figure S13**

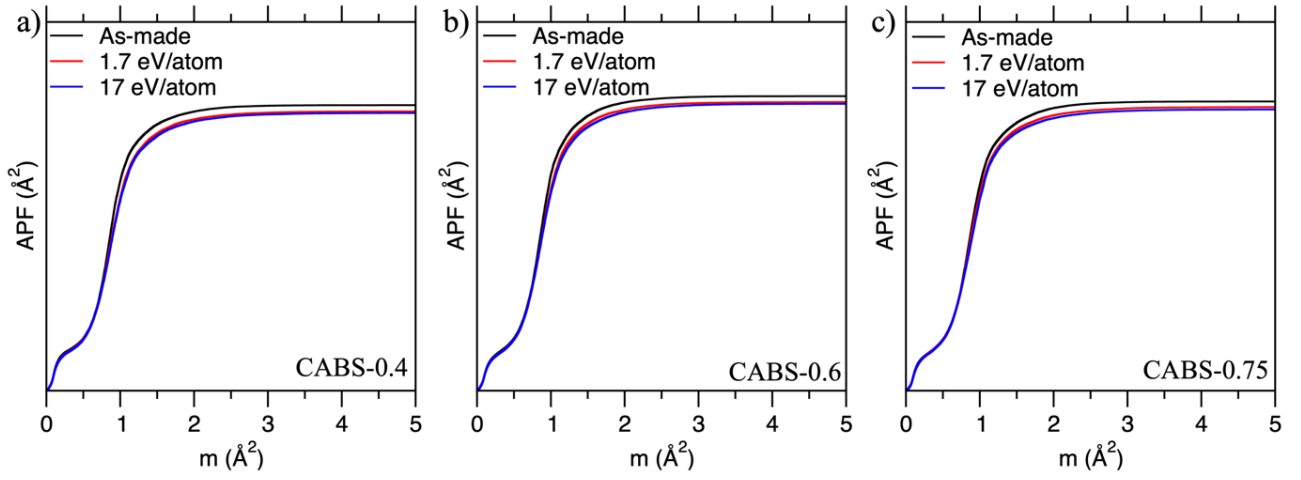


**Figure S13.** Quantitative analysis of persistence diagrams using the APF function of **a)** CABS-0.4, **b)** CABS-0.6, and **c)** CABS-0.75 glasses subjected to different amounts of irradiation energies. The APF functions are calculated by summing up all the points  $(d_i, b_i)$  in the persistence diagram as:  $APF(t) = \sum_{i: (b_i + d_i)/2 \leq t} (d_i - b_i)$ .



**Figure S14**

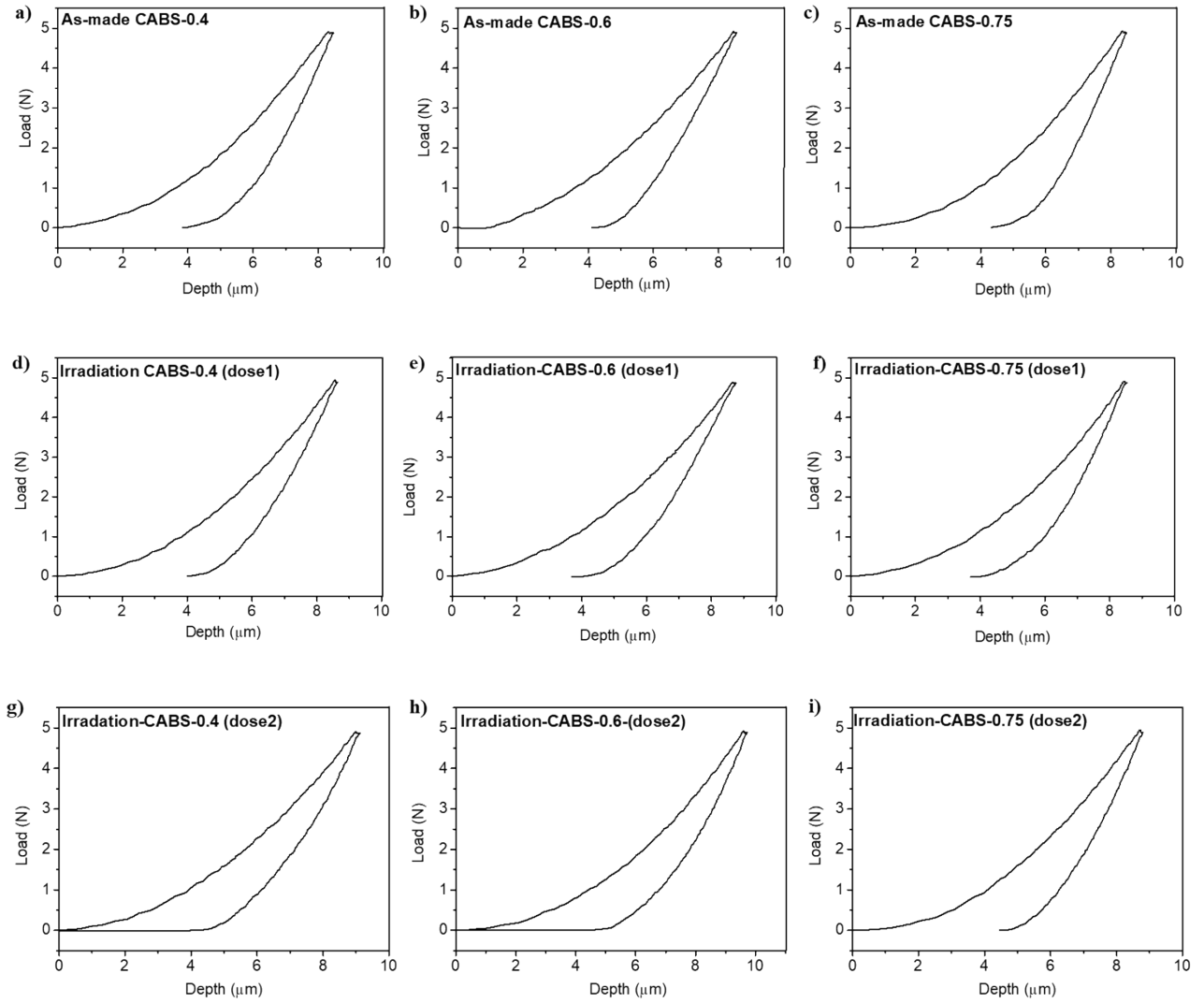


**Figure S14.** Experimental load-depth curves for as-made **a)** CABS-0.4, **b)** CABS-0.6, **c)** CABS-0.75, for irradiated **d)** CABS-0.4, **e)** CABS-0.6, **f)** CABS-0.75, for irradiated **g)** CABS-0.4, **h)** CABS-0.6, **i)** CABS-0.75.

**Figure S15**

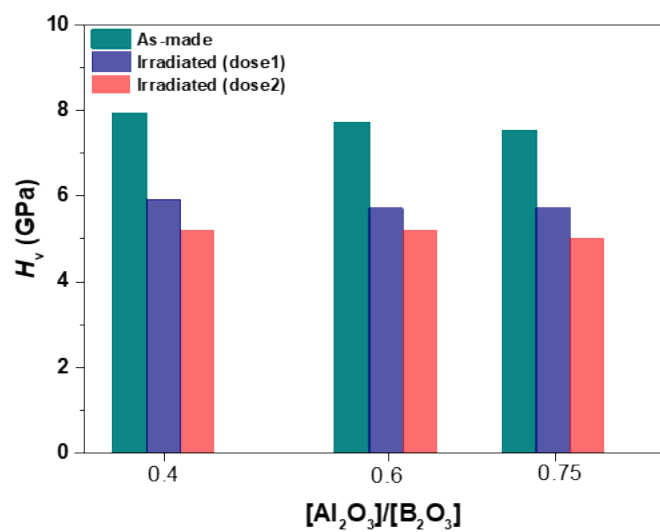


**Figure S15.** Vickers hardness ( $H_V$ ) of the as-made and irradiated glasses measured at an indentation load of 0.1N.

**Figure S16**

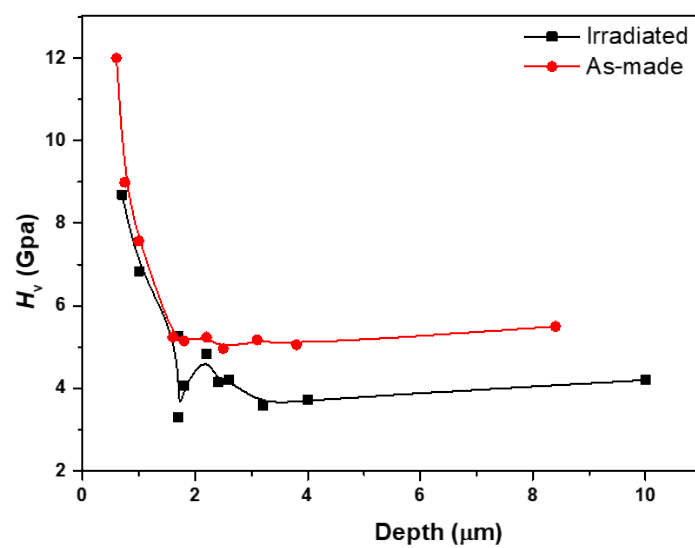


**Figure S16.** Depth dependence of hardness for the CABS-0.4 glass.

**Figure S17**

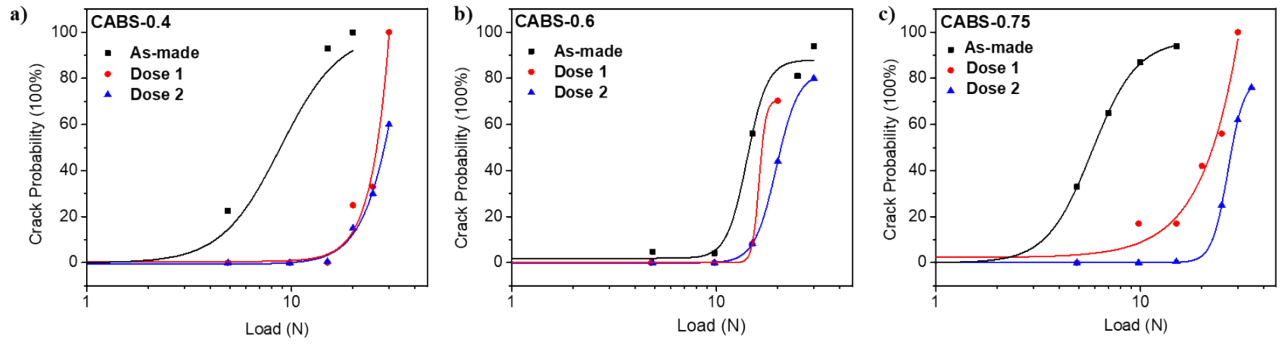


**Figure S17.** Crack probability as a function of applied indentation load for the as-made and irradiated CABS-0.4 glass **a)**, CABS-0.6 glass **b)**, CABS-0.75 glass **c)**. The experimental data was fit to a sigmoidal function of the form  $y = A_2 + (A_1 - A_2) / \left[ 1 + \left( x/x_0 \right)^p \right]$  (solid lines).

**Figure S18**

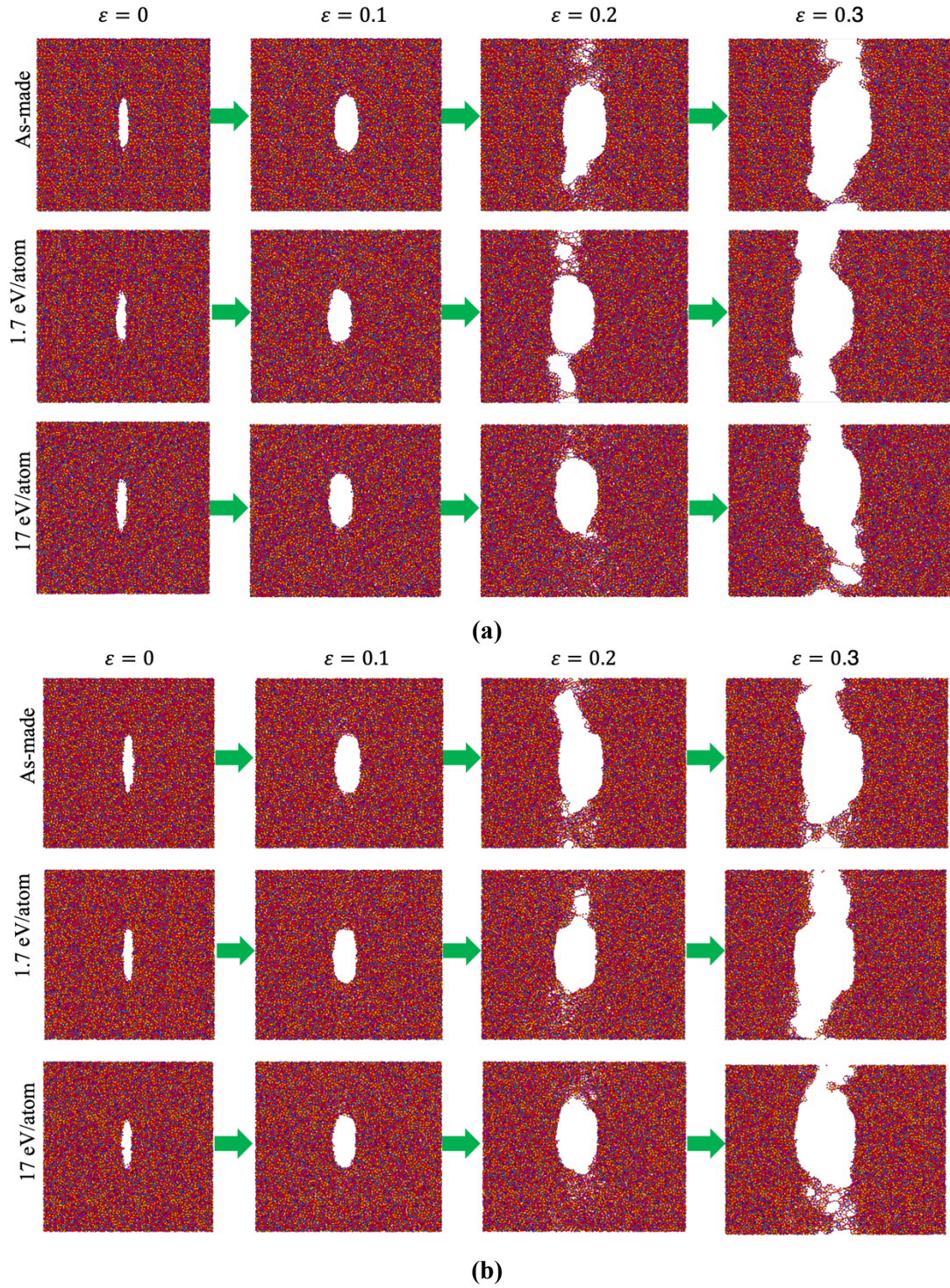


**Figure S18.** Evolution of fracture in the pre-cracked (a) CABS-0.6 and (b) CABS-0.75 glasses of different irradiation states at tensile strains of 0, 0.1, 0.2, and 0.3.

**Figure S19**

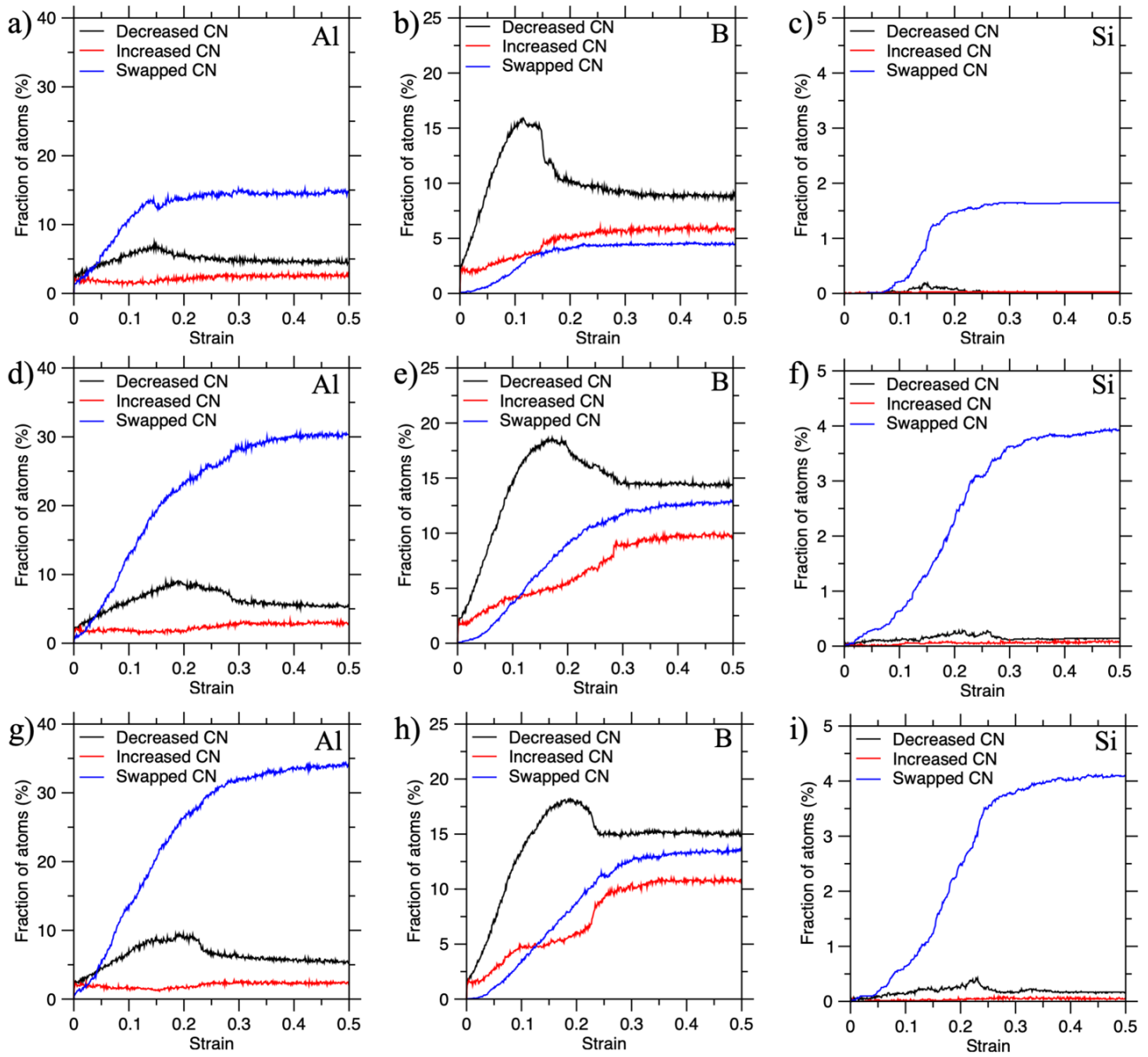


**Figure S19.** Fraction of network formers in the CABS glasses that have changed their coordination numbers (CN) during the tensile loading process. **a-c)** Al, B, and Si atoms in the as-made CABS glasses. **d-f)** Al, B, and Si atoms in the CABS glasses subjected to 1.7 eV/atom. **g-i)** Al, B, and Si atoms in the CABS glasses subjected to 17 eV/atom.



**Figure S20**

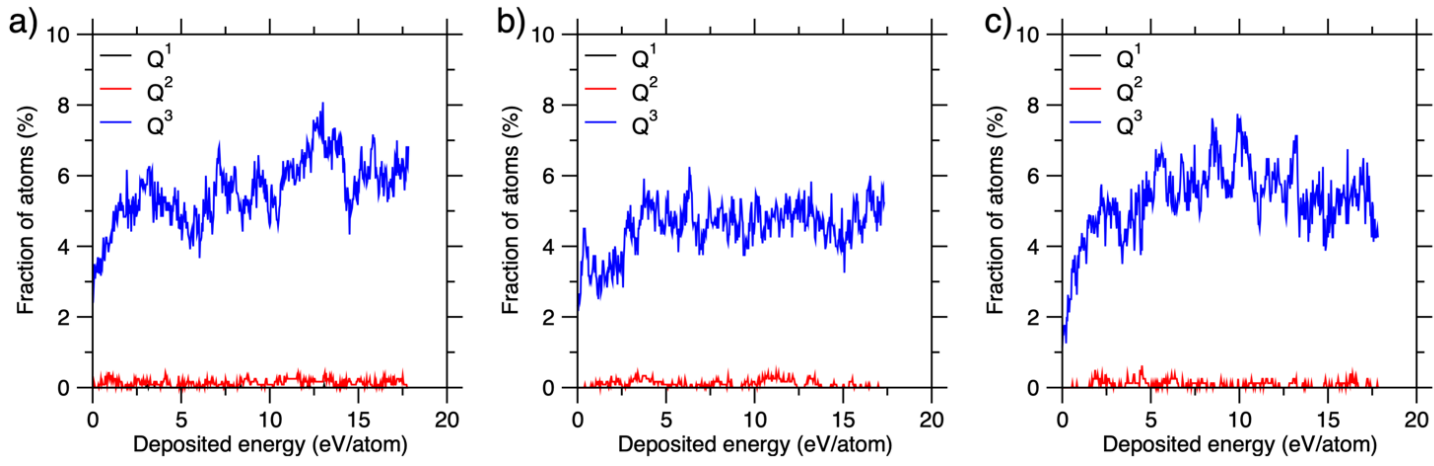


**Figure S20.** Simulated distribution of the  $Q^n$  units of Al atoms for **a)** CABS-0.4, **b)** CABS-0.6, and **c)** CABS-0.75 glasses as function of the deposited energy during the irradiation process.

# Paper IV



# Water as a modifier in a hybrid coordination network glass

Søren S. Sørensen<sup>1,†</sup>, Xiangting Ren<sup>1,†</sup>, Tao Du<sup>1,†</sup>, Shibo Xi<sup>2</sup>, Lars R. Jensen<sup>3</sup>, John Wang<sup>4</sup>, Morten M.

Smedskjaer<sup>1,\*</sup>

<sup>1</sup> *Department of Chemistry and Bioscience, Aalborg University, Aalborg, Denmark*

<sup>2</sup> *Institute of Chemical & Engineering Sciences, Agency for Science, Technology and Research (A\*STAR),  
Singapore, 627833, Singapore*

<sup>3</sup> *Department of Materials and Production, Aalborg University, Aalborg, Denmark*

<sup>4</sup> *Department of Materials Science and Engineering, National University of Singapore, 117574,  
Singapore*

\*Corresponding author email: [mos@bio.aau.dk](mailto:mos@bio.aau.dk)

**Keywords:** Hybrid glasses, glass modifier, water, melting, coordination network

## Abstract

Chemical diversification of hybrid organic-inorganic glasses remains limited, especially compared to traditional oxide glasses, for which continuous composition variation and thus property tuning is possible through addition of weakly bonded modifier cations. In this work, we show that water addition can depolymerize polyhedra with labile metal-ligand bonds in a cobalt-based coordination network, yielding a series of non-stoichiometric glasses. Based on calorimetric, spectroscopical, X-ray absorption, and *ab initio* simulation studies, we demonstrate that the added water promotes breakage of cobalt-oxygen bonds, which leads to lower melting and glass transition temperatures. These structural changes also modify both the physical and chemical properties of the melt-quenched glass, with strong parallels to the modifier concept in oxide glasses. This approach will enable diversification of hybrid glass chemistry, including non-stoichiometric glass compositions, continuous tuning of physical and chemical properties, and a significant increase in the number of glass-forming hybrid systems by allowing them to melt before they thermally decompose.

## Introduction

Hybrid organic-inorganic networks, including three-dimensional metal-organic frameworks (MOFs) and one- or two-dimensional coordination polymers (CPs), have opened new and applications avenues within solid state chemistry throughout the last few decades.<sup>1,2</sup> The materials typically consist of metal-nodes connected by organic linkers, and in some cases including additional interplaying metallic-node centers, e.g., in perovskite structures.<sup>3,4</sup> The majority of these discovered structures are crystalline and typically synthesized by hydrothermal processes,<sup>5</sup> but recently it was discovered that some members of this chemical family can form a stable liquid phase upon heating (prior to thermal decomposition), allowing subsequent supercooling into a glassy state.<sup>6,7</sup> This work has opened a new glass family, notably distinct from the existing metallic, organic, and inorganic glasses, and with possible applications within, e.g., radioactive waste storage,<sup>8</sup> thermoelectrics,<sup>4</sup> gas separation,<sup>9</sup> and energy storage,<sup>10</sup> as well as the possibility to produce bulk-sized hybrid organic-inorganic samples (>1 cm) without grain boundaries.<sup>11</sup>

Although these hybrid glasses are chemically distinct from the traditional glass families, they share a number of structural similarities to network glasses (e.g., oxides), as the metallic nodes (for oxides typically Si, Ge, P; for hybrids typically transition metals) bridge through single oxygens (for oxide glasses) and large organic linkers (for hybrid glasses).<sup>12</sup> Similarly, the metal nodes in the two glass families share the same range of coordination numbers (typically 4-6).<sup>12-14</sup> However, there is a major difference in the discovery and design of new glasses. Hybrid glasses are typically made by melt-quenching or ball-milling a specific crystal and thus restricted to stoichiometric compositions. On the other hand, the compositions of oxide glasses can be continuously adjusted through the addition of so-called modifiers or “fluxes” (e.g., alkali oxides), which results in the breakage of the continuous network structure of the pure network-forming oxide, creating non-bridging oxygens, i.e., oxygens which will only covalently bond to one metal node.<sup>12</sup> This leads to changes in the physical properties, for example lowering of the melting and glass transition temperatures, enabling melting at significantly lower

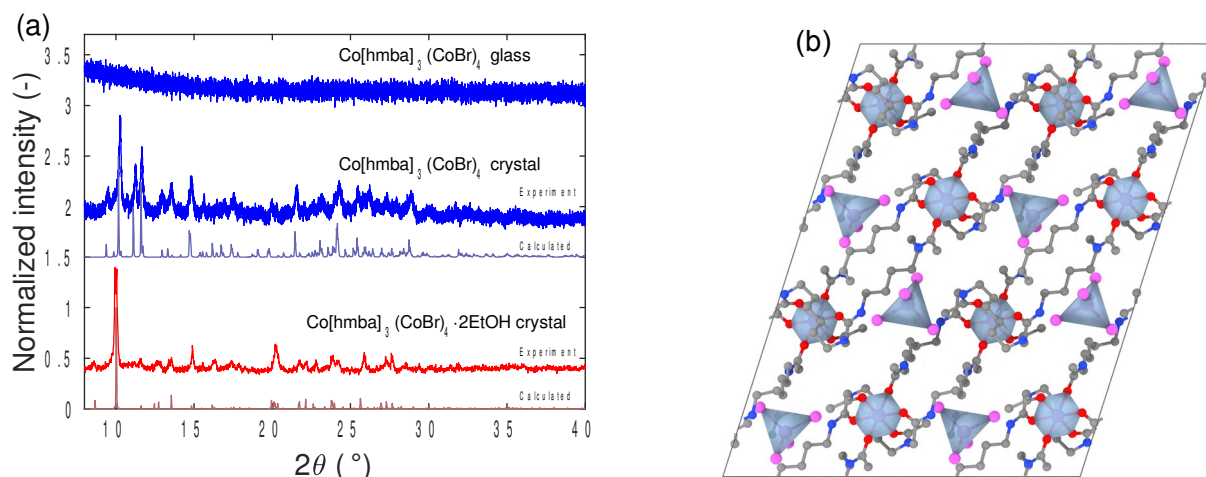
temperatures.<sup>12</sup> The modified addition in oxide glasses thus enables a chemical diversity that has led to a broad range of applications, from window glasses and touchscreen displays to optical fibers and pharmaceutical vials. The possibility to tune the structure and properties of hybrid glasses through modifier addition has not yet been realized, although we note that the term flux melting has been used to describe the co-melting of two MOFs from the zeolitic imidazolate framework family.<sup>15</sup>

In this work, we present experimental and computational evidence for water acting as a modifier in a cobalt-based bis-acetamide hybrid coordination network glass (HCNG) of composition  $\text{Co}(\text{hmba})_3[\text{CoBr}_4]$ , where hmba: *N,N'*-1,6-hexamethylenebis(acetamide). Structurally, in the crystalline state, this system consists of octahedral  $\text{Co}^{2+}$  nodes connected through weak coordination bonds to uncharged hmba structures in a 2D layer-like structure, with non-interconnected charge compensating  $[\text{CoBr}_4]^{2-}$  units situated in between network layers.<sup>14,16</sup> While this glass is fully water soluble, we show that careful water addition results in significant alteration of physical properties including the melting and glass transition temperatures. Experiments and *ab initio* simulations show that water facilitates breaking of the network-forming Co-O bonds, ultimately allowing for the tuning of glass properties within this glass family. We believe these findings opens a new avenue for tuning the melting temperatures of other hybrid crystals to allow them to melt before thermal decomposition, and hence the formation of more melt-quenched hybrid glasses.

## Results and Discussion

The studied hybrid coordination network crystal was synthesized following the procedure of Ref.<sup>14</sup>, creating single crystals with ethanol of composition  $\text{Co}(\text{hmba})_3[\text{CoBr}_4] \cdot 2\text{EtOH}$ . The ethanol molecules were subsequently removed by prolonged storage under vacuum (<10 mbar) and moderate heating (~30-40 °C), resulting in a polycrystalline powder that is isostructural to a Mn-analogue of composition  $\text{Mn}(\text{hmba})_3[\text{MnBr}_4]$  (as reported in Ref.<sup>16</sup> and deposited in the Cambridge Crystallographic Data Centre

(CCDC)<sup>17</sup> with deposition number 120454). Figure 1a shows the measured X-ray diffraction (XRD) patterns of the crystal before and after drying together with a simulated spectrum of both  $\text{Co}(\text{hmba})_3[\text{CoBr}_4] \cdot 2\text{EtOH}$  and  $\text{Co}(\text{hmba})_3[\text{CoBr}_4]$  structures as based on the unit cell structures of their Mn-analogues. Images of the two crystalline products are presented in Figure S1a. For both  $\text{Co}(\text{hmba})_3[\text{CoBr}_4] \cdot 2\text{EtOH}$  and  $\text{Co}(\text{hmba})_3[\text{CoBr}_4]$ , we observe an excellent reproduction of the XRD peaks (Figure 1a), confirming the expected structural change upon storage and subsequent desolvation<sup>14,16</sup> and the generation of the  $\text{Co}(\text{hmba})_3[\text{CoBr}_4]$  crystal structure that can subsequently be melt-quenched. The unit cell structure of  $\text{Co}(\text{hmba})_3[\text{CoBr}_4]$  is presented in Figure 1b, while that in Figure 1c highlights the (i) layer-like percolating network of Co and hmba-linkers and (ii) interpenetrating  $[\text{CoBr}_4]^{2-}$ -tetrahedra positioned in the vacancies of the layered network.



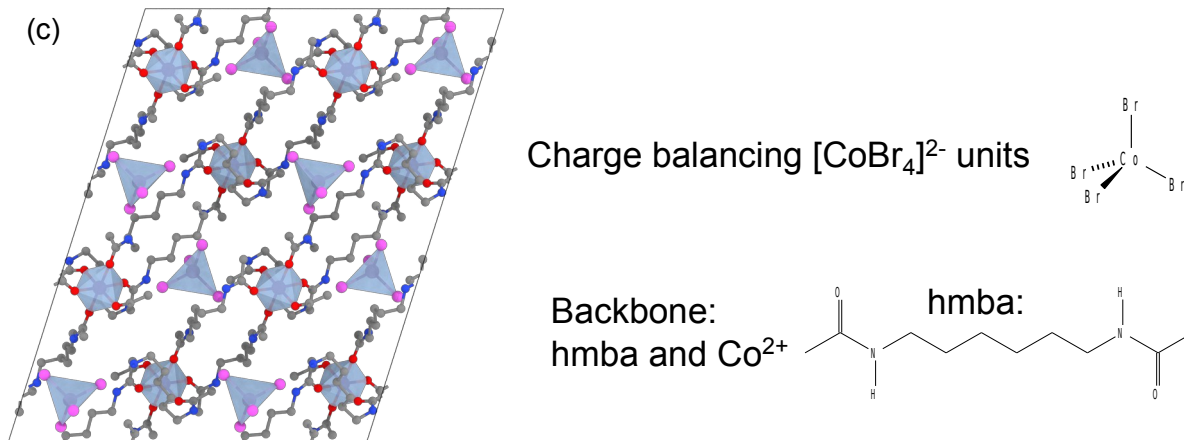


**Figure 1.** (a) X-ray diffraction patterns of synthesized ethanol-containing crystals ( $\text{Co(hmba)}_3[\text{CoBr}_4] \cdot 2\text{EtOH}$ ) and subsequently dried crystals ( $\text{Co(hmba)}_3[\text{CoBr}_4]$ ) as well as the corresponding melt-quenched  $\text{Co(hmba)}_3[\text{CoBr}_4]$  glass. The calculated reference spectra are based on the CIF files of Ref.<sup>16</sup> which have also been deposited in the CCDC<sup>17</sup> with deposition numbers 120454 and 120455, respectively, where Mn is exchanged for Co. (b) Unit cell of crystalline  $\text{Co(hmba)}_3[\text{CoBr}_4]$  with highlights of Co tetrahedra and octahedra (shaded in grey), with the colored spheres representing carbon (grey), nitrogen (blue), oxygen (red), and bromine (pink) atoms. Hydrogens are omitted for clarity. (c)  $\text{Co(hmba)}_3[\text{CoBr}_4]$  structure overlaid with highlighting showing how  $\text{Co}^{2+}$  and hmba serve as the network part of the structure (blue), while  $[\text{CoBr}_4]^{2-}$ -tetrahedra are placed between the layers within the network (red).

The melting and subsequent glass formation has been described previously for both  $\text{Co(hmba)}_3[\text{CoBr}_4]$  (see example picture of molten  $\text{Co(hmba)}_3[\text{CoBr}_4]$  in Figure S1b) as well as other bis-acetamide-containing HCNGs.<sup>14</sup> Here, we demonstrate that the properties of this system are highly sensitive to the water content. Figure 2a shows differential scanning calorimetry heating scans for the pristine  $\text{Co(hmba)}_3[\text{CoBr}_4]$  crystal and glass with no or 7 wt% added water, respectively. Upon water addition, the

melting transition clearly becomes broader and ends at a significantly lower temperature (right part of Figure 2a), while the glass transition temperature decreases significantly (left part of Figure 2a). The dependence of the melting temperature ( $T_m$ ) and glass transition temperatures ( $T_g$ ) on water content is shown in Figure 2b. The increasing water concentration significantly lowers the melting temperature from  $\sim 110$  °C to a constant value of  $\sim 70$  °C at a water concentration of  $\sim 15$  wt%, with no changes upon further water addition.

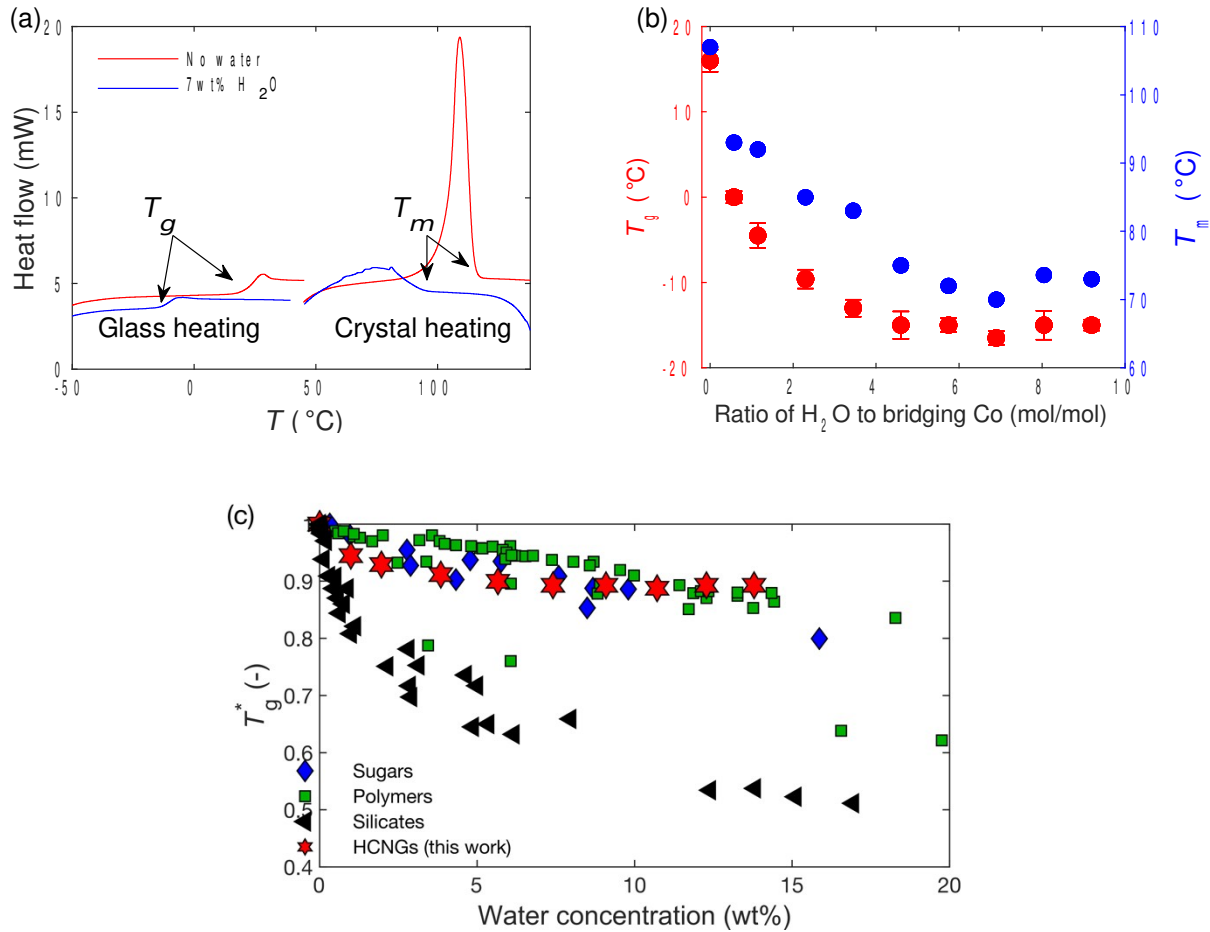


**Figure 2.** (a) Differential scanning calorimetry heating scans of crystalline (right) and glassy (left)  $\text{Co(hmba)}_3[\text{CoBr}_4]$ . Results of shown for both dry samples (red lines) and those with 7 wt% added water (blue lines). (b) Melting and glass transition temperatures ( $T_m$  and  $T_g$ , respectively) of the  $\text{Co(hmba)}_3[\text{CoBr}_4]$  as a function of the ratio of  $\text{H}_2\text{O}$  to bridging-Co (i.e., Co atoms bonded to hmba linkers). (c) Reduced glass transition temperature ( $T_g^* = T_g/T_g^{\text{WF}}$ , scaled in Kelvin and where  $T_g^{\text{WF}}$  is the

glass transition temperature of the water-free glass) of the  $\text{Co(hmba)}_3[\text{CoBr}_4] \cdot \text{water}$  glasses at different water concentrations as well as for several different sugars, organic polymers, and silicate glasses as obtained from Refs.<sup>18–20</sup>.

We find a decrease in the glass transition temperature from a pristine value of 16 °C to -15 °C for the highest water content, which corresponds to nine water molecules per bridging Co atom, where bridging-Co refers to Co atoms bonded to hmba linkers. Notably, a significant initial decrease followed by stabilization is observed for both  $T_m$  and  $T_g$ . Specifically,  $T_m$  and  $T_g$  reach a constant value when around three to four water molecules per bridging-Co have been added. Interestingly, this is equivalent to the ratio of bridging-Co to hmba in the system, suggesting that at the point of convergence one water molecule per hmba linker is present. Considering the chemical environment of the percolating network, i.e., Co-nodes connected by bidentate hmba-linkers through Co-O coordination bonds, the monodentate water species thus appear to replace the bridging carbonyl oxygens around the Co-centers. This leads to a fully depolymerized network of Co atoms surrounded by a distribution of hmba-linkers and water molecules, while the  $[\text{CoBr}_4]^{2-}$ -tetrahedra would remain intact. As such, this behavior is equivalent to water-based modifier addition in the HCNG system, which has not previously been reported for hybrid glasses to our knowledge.

The water-induced depolymerization and decrease in  $T_g$  has been observed in other glassy systems, including silicates, organic polymers and sugars. To compare the extent of the decrease, we plot the reduced glass transition temperature ( $T_g^* = T_g T_g^{\text{WF}}$ , where  $T_g^{\text{WF}}$  is the glass transition temperature of the water-free glass) as a function of water content in Figure 2c. Results are shown for the present  $\text{Co(hmba)}_3[\text{CoBr}_4]$  glass well as various systems from literature.<sup>18–20</sup> Water addition has a pronounced effect on the  $T_g$  of the inorganic silicates and some polymers, with a decrease in their  $T_g$  by ~50% when adding 10-15 wt% water. This contrasts the behavior of the majority of the sugars and polymers as well as the present HCNG, which exhibit only a minor (~10-15%) reduction in  $T_g$  in the same water concentration range. However, interestingly our HCNGs also seem to feature a more converging  $T_g$  compared to other



systems upon water addition – likely due to how water significantly outnumbers bridging Co atoms at rather low water concentrations (~5-10 wt%), ultimately yielding a glassy system which is rather controlled by weak cohesive forces of longer range rather than by the Co-hmba network.

To further clarify the glass transition behavior of the  $\text{Co(hmba)}_3[\text{CoBr}_4]$  glasses, we performed annealing experiments at  $0.9T_g$  of both pristine and hydrated samples. Based on the DSC measurements of these samples, we find that  $T_g$  decreases and the endothermic overshoot of the glass transition increases with annealing duration (Figure S2). This is consistent previous findings for other glass families<sup>21,22</sup> and is a consequence of the decreasing in the overall enthalpy of the system through the hopping between metastable states and, upon such heating, into local minima of the potential energy surface.<sup>23</sup> Additionally, we determined the liquid fragility ( $m$ ), which quantifies the extent of non-Arrhenius temperature dependence of viscosity at  $T_g$ . This was done on both pristine and hydrated glasses using a DSC-based method.<sup>24</sup> Specifically, glasses were heated from below to above  $T_g$  using a range of heating rates (5, 10, 15, 20, 25, and 30 K min<sup>-1</sup>) and the shift in fictive temperature was recorded. This gave  $m$  values of ~42 and ~47 for the pristine and hydrated glass, respectively. This is in the same as many modified oxide and metallic glass-forming systems ( $m \approx 30$ -70),<sup>25,26</sup> but considerably lower than most organic systems<sup>24</sup> and higher than the hybrid ZIF-62 ( $m=23$ )<sup>27</sup> as well as pure  $\text{SiO}_2$  ( $m=20$ )<sup>28</sup>.

To understand these changes in melting and glass transition behavior upon water addition, we subjected the HCNGs to a variety of spectroscopic analysis methods, including *in situ* Raman spectroscopy measurements during melting of the crystal and a subsequent cooling/heating cycle (Figure S3), and *ex situ* FT-IR spectroscopy measurements (Figure S4). However, both techniques could not detect any significant changes of the spectra upon water addition, and only a slight broadening when the system transitioned to the molten/glassy state. This is in somewhat good agreement with the *in situ* FTIR data of Ref.<sup>14</sup>. Then, to probe any structural changes around the Co atoms, we measured the visible absorption spectra of the pristine and hydrated glasses (Figure 3a). We were unable to quantify the used film thickness and hence the absorption coefficient, but note that higher water content lead to smaller

absorption, in agreement with the expectation of that glass fraction of the sample is “diluted” by the added water. The large band around 6-700 nm present in all samples can be assigned to the crystal field splitting in  $[\text{CoBr}_4]^{2-}$ , where Br<sup>-</sup> ligands are tetrahedrally coordinated to Co-centers, as<sup>29</sup> (i) Br<sup>-</sup> is in the lowest splitting part of the spectrochemical series and (ii) lower coordination is known to induce lower splitting. As such, the octahedral Co atoms surrounded by carbonyls should absorb at smaller wavelengths (higher energies) due to its expected larger splitting (based on the spectrochemical series) and higher coordination state. This interpretation implies that only the Co-hmba network is reorganized during the melt-quenching procedure, while the charge compensating  $[\text{CoBr}_4]^{2-}$  units remain stable both in the pristine and hydrated glasses.

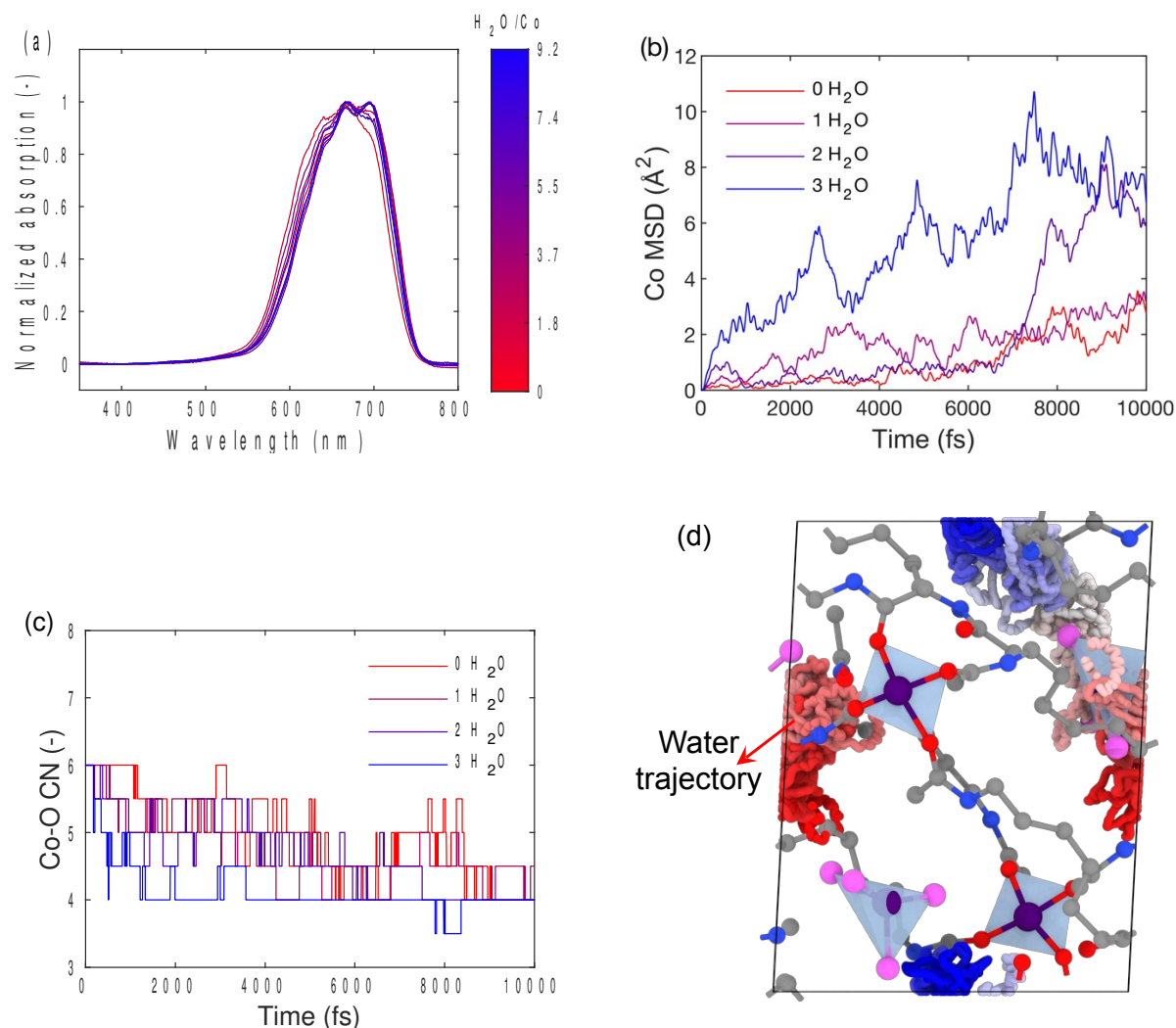


**Figure 3.** (a) Normalized visible absorption spectra of HCNGs with varying water content (see colorbar). (b) Simulated mean square displacement (MSD) of Co atoms in the the  $\text{Co(hmba)}_3[\text{CoBr}_4]$  system at 1000 K with 0, 1, 2, or 3 water molecules in the unit cell structure. (c) Simulated average coordination number (CN) of the Co-O correlation in structures containing 0, 1, 2, or 3 water molecules. (d) Trace of one water molecule's trajectory over 10 ps of simulation time at 1000 K, where blue refers to the initial position and red to the final position. The remaining part of the structure is shown as the final frame. Note the movement across the periodic boundaries.

The melting mechanism of the  $\text{Co(hmba)}_3[\text{CoBr}_4]$  system as well as that with 0, 1, 2, or 3 water molecules added was further studied by *ab initio* molecular dynamics simulations. We are restricted to studying the crystal/molten state as the quenching to a glassy state is computationally infeasible. First, we considered dynamics of the pristine, water-free crystal structure (as obtained from its CIF file) at temperatures of 500, 1000, and 1500 K to calculate the mean square displacement (MSD). The results are shown in Figure 3b for Co MSD at 1000 K for different water content and in Figure S5 for both Co and Br MSD at the different temperatures. The simulations at 500 K present solid-like behavior (i.e., constant value of MSD), while the simulations at 1500 K present a liquid/gas-like behavior (i.e., increasing MSD with time). The simulations at 1000 K exhibit behavior in-between these extrema, thus representing an initiation of melting. We confirm through calculation of the Lindemann ratio ( $\Delta$ ), i.e., the ratio of the estimated amplitude of the atomic vibrations divided by the bond length<sup>30,31</sup> of the Co-O bonds. As shown in the inset of Figure S5a,  $\Delta$  increases from  $\sim 0.10$  to  $\sim 0.18$  when increasing the temperature from 500 to 1500 K. Generally, melting is considered to occur when  $\Delta$  reaches a value of around 0.10-0.15,<sup>30,31</sup> matching the values from the simulation data at 1000 K. By adding water to the system at 1000 K, the Co MSD increases more rapidly with time (Figure 3b), suggesting that water promotes the melting process. The

same trend that the MSD increases with both temperature and water content is also found for Br (Figures S5b-c).

The melting process of the  $\text{Co(hmba)}_3[\text{CoBr}_4]$  system can be also be investigated through analysis of the simulated coordination numbers (CNs) of the two different Co-centers (i.e., the Co-O and Co-Br CNs). interestingly, we find that the CN of the Co-O and Co-Br correlations differ significantly (see Figure 3c for Co-O and Figure S6 for Co-Br). We note that the stepwise nature of the data in these figures is due to the small number of Co atoms in each simulated box. Upon initializing dynamics at 1000 K of the crystalline system with 0, 1, 2, or 3 water molecules, we observe a major decrease in the Co-O CN (i.e., the network percolating species) from 6 to  $\sim 4$  within the first 10 ps. This decrease in CN is found to be promoted by the presence of water, as seen from the more rapid decrease of CN in the first picosecond of the simulation with the largest amount of water. Simultaneously, the Co-Br centers exhibit only minor deviations from the the initial four-fold coordinated state as caused by the high temperature, yet deviations quickly surge upon further increases in time to subsequently re-establish the tetrahedral state, independently of the water content (Figure S6). Figure 3d illustrates the movement of a water molecule inside the structure at 1000 K, highlighting how water appears to explore multiple parts of the structural space, including both the Co-O octahedra as well as the Co-Br tetrahedra. However, the water molecule does not fully approach neither the Co-centers nor replace the oxygens in hmba or the bromide ions. This is supported by calculations of the time-resolved bond distance between the oxygens from water and the Co atoms in the structure, with separation distances surpassing 3 Å (Figure S7) in contrast to the network-forming Co-O and interconnected Co-Br bonds, exhibiting bond distances in the range of 1.8-2.5 Å (Figures S8-11).

To complement the *ab initio* simulations and provide real space temperature-resolved structural information of the hybrid coordination network system in both the crystalline, molten, and glassy states, we have performed *in situ* extended X-ray absorption fine structure (EXAFS) measurements (see raw data in Figure S12). The Fourier transformed extended X-ray absorption fine structure (FT-EXAFS) spectra

are shown in Figure 4 for both the pristine (Figure 4a) and hydrated (Figure 4b) systems in the crystalline (red), molten (green), and glassy states (blue). In the water-free system, the cobalt environment features a bimodal distribution of bond lengths, with the shortest one corresponding to Co-O (just below 2 Å) and the longer one to the Co-Br distance (above 2 Å). Upon heating to 140 °C, we find a decrease in the overall peak area of both the Co-O and Co-Br correlations, suggesting a decrease in the CNs for both Co environments in the structure. We note that the simulations mainly showed breakage of the Co-O bonds, but this may reflect the general limits in terms of simulation time. Furthermore, we find that the Co-Br bonds appear to be reestablished when cooling into the glassy state, while the Co-O bonds appear to be permanently shortened and with a smaller CN (see Figure 4a, blue curve). This is consistent with the persistent blue color from the  $[\text{CoBr}_4]^{2-}$  centers observed in the optical absorption spectra (Figure 3a).

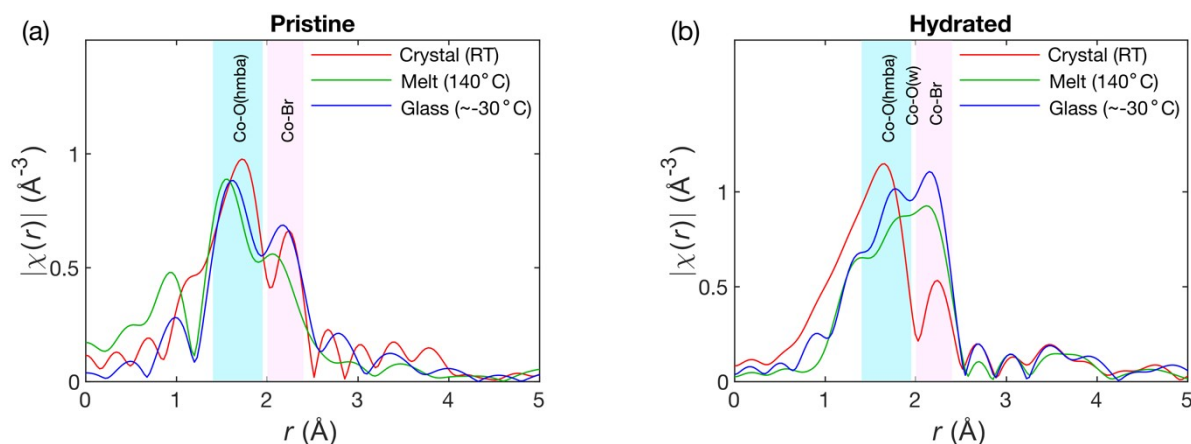


**Figure 4.** *In situ* Fourier transformed extended X-ray absorption fine structure (FT-EXAFS) spectra of (a) pristine and (b) hydrated  $\text{Co}(\text{hmba})_3[\text{CoBr}_4]$  systems in the crystalline state (red), molten phase at 140 °C (green), and glassy state at approximately -30 °C (blue). Areas for the approximate radial distances corresponding to cobalt coordinating to oxygens from hmba as well as Br are shaded in blue and pink, respectively.

Significant changes in the FT-EXAFS spectra are observed upon water addition (Figure 4b). First, considering the crystalline state with added water, the overall peak intensities are similar to those of the pristine system (see direct comparison in Figure S13a). However, upon heating to 140 °C (green curve in

Fig. 4b), the local geometry of Co is altered, with significant changes in both the bond lengths and coordination environments. An apparent trimodal distribution is observed, which can likely be ascribed to Co-O(hmba), Co-O(water), and Co-Br bonds, respectively. That is, the initial Co-O peak (bond length of  $\sim 1.8$  Å) seems to split into two peaks with shorter and longer bond distances, respectively, than in the crystalline state, respectively. It is not possible to ambiguously ascribe this to a certain chemical species, but since the absorption results suggest that the  $[\text{CoBr}_4]^{2-}$  centers remain largely intact (Figure 3a), we infer that oxygens from water (O(w) in Figure 4b) coordinate and partially replace hmba-oxygens, producing a signal that is partially overlapping with that of the Co-Br correlation. Notably, this is consistent with the fact that aquo-cobalt complexes typically exhibit Co-O bond distances of around 2.1-2.2 Å,<sup>32</sup> that is, between those of Co-O(hmba) ( $\sim 1.8$  Å) and Co-Br ( $\sim 2.5$  Å). Furthermore, correlations in the initial Co-O(hmba) range of  $\sim 1.8$  Å are found to be present in the hydrated glass structure, thus suggesting that Co atoms still coordinate to hmba in the hydrated sample (although at a lower CN). This ultimately suggests that the Co centers percolating the network partially exchange oxygen coordination from hmba to water.

Finally, based on the performed simulations and experiments, we propose a melting mechanism of the  $\text{Co(hmba)}_3[\text{CoBr}_4]$  system (Figure 5). First, upon heating of the anhydrous system, the labile bonds between Co and O in hmba (i.e., the red spheres in Figure 5) tend to break, leading to a decrease in the overall network connectivity and ultimately the formation of a molten state. This is accompanied by a minor degree of breakage of the tetrahedral Co-Br units. Upon cooling this liquid into the solid glass state, the  $[\text{CoBr}_4]^{2-}$  units reform, while the Co-O network undergoes only partial reformation. Addition of water to the crystal enhances the temperature-induced de-coordination process dramatically. That is, while the  $[\text{CoBr}_4]^{2-}$  centers generally behave similarly as in the water-free state, the Co-O(hmba) bonds break much more easily in the hydrated system and are ultimately replaced by water molecules in the glassy state. In addition, when water replaces the oxygens of hmba, dangling organic motifs are created as

shown by the significant reduction in the  $T_g$  from 16 °C to -15 °C for the fully polymerized and fully depolymerized glass structures, respectively.

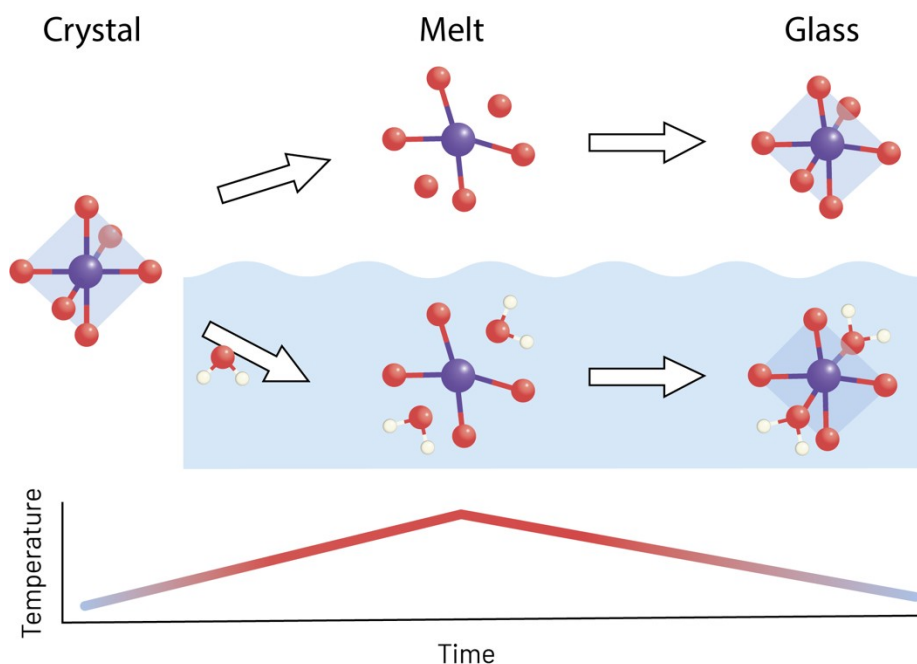


**Figure 5.** Proposed melting and glass-forming mechanism of the Co-O octahedra of the studied cobalt-based hybrid coordination network system. Cobalt, oxygen, bromine, and hydrogen are represented as violet, red, pink, and white spheres, respectively. The process is shown from the crystalline (left) to the molten (middle) and ultimately glassy (right) state in both the case without (top) and with (bottom) water.

## Conclusions

We have shown that a cobalt-based hybrid coordination network crystal is an excellent glass former and, by adding water, may have its melting point and glass transition temperature significantly suppressed. Through calorimetric, spectroscopic, diffraction, X-ray absorption, and simulation methods, we have a

proposed a mechanism for the water-promoted breakdown of the internal network of  $\text{Co}^{2+}$  ions and bis-acetamide organic linkers, while the  $[\text{CoBr}_4]^{2-}$  centers remain relatively intact. The former is obtained by replacing labile Co-O bonds from the organic ligand with coordination to water molecules. This mechanism resembles that of water and other network “modifiers” in traditional oxide glass-forming systems, where such structural modification is used to design and tune glass properties for industrial applications. As such, the present results may pave the way for a significant expansion of the meltable and glass-forming hybrid systems as well as substantial non-stoichiometric chemical diversification of these systems.

## Methods

### *Crystal and glass synthesis*

Synthesis of  $\text{Co}(\text{hmba})_3[\text{CoBr}_4] \cdot 2\text{EtOH}$  crystals were performed according to the procedure in Refs.<sup>14,16</sup>. Before starting the synthesis, ethanol (EtOH) and ethyl acetate (EtOAc) were dried using molecular sieves for at least 24 h. Then, *N,N'*-1,6-hexamethylenebis(acetamide) (hmba, ~133 mg) was heated in 1.5 mL of EtOH and 13.5 mL of EtOAc under reflux. We observed that hmba would only partially dissolve upon reflux and magnetic stirring of this solution. Separately, ~75 mg of  $\text{CoBr}_2$  was added to 10 mL of EtOH, which was heated on a hot plate to form a clear blue solution. This solution was then slowly added to the heated solution of hmba using a syringe to finally form a clear blue solution. The latter was left under  $\text{N}_2$  flow overnight to allow for evaporation and clear blue-purple crystals to form in the solution. These crystals were filtered, washed using anhydrous diethyl ether, and finally dried on the filter by allowing further suction of  $\text{N}_2$  (see Figure S1a).

We confirmed these crystals to be isostructural to the  $\text{Co}(\text{hmba})_3[\text{CoBr}_4] \cdot 2\text{EtOH}$  crystals formed in previous studies.<sup>14,16</sup> Similarly to these previous reports, upon storage at slightly above room temperature and high vacuum, the  $\text{Co}(\text{hmba})_3[\text{CoBr}_4] \cdot 2\text{EtOH}$  structure was found to spontaneously release the bound



EtOH molecules and form the  $\text{Co(hmba)}_3[\text{CoBr}_4]$  structure upon storage (see Figure S1b). Both crystalline structures were confirmed by X-ray diffraction analysis (Figure 1a). All crystals were stored in a desiccator or under vacuum ( $<10$  mbar) and slightly elevated temperatures ( $40^\circ\text{C}$ ). Glasses, which were produced by melt-quenching and found to be X-ray amorphous (Figure 1a), were always produced immediately prior to or during analysis to avoid effects of storage (e.g., possible crystallization or unwanted hydration effects). We tested the stability of the melt by melting the crystal for 2, 5, 10, 20, and 40 mins, finding no decomposition to the organic linker, as seen from  $^1\text{HNMR}$  results in Figure S14 and an example of an interpreted spectrum in Figure S15.

### *Experimental characterization*

X-ray diffraction (XRD) analysis was performed using a Panalytical Empyrean instrument equipped with a Cu-source ( $\lambda_{\text{K}\alpha 1}=1.50498\text{ \AA}$ ). Scan ranges were  $2\theta=5\text{-}70^\circ$ .

Thermal analysis was performed using a TA Q2000 differential scanning calorimeter (DSC) using hermetically sealed Al pans. Approximately 5 mg of  $\text{Co(hmba)}_3[\text{CoBr}_4]$  was used per scan with varying amounts of water (in the range of  $0\text{-}0.8\text{ }\mu\text{L}$  of deionized water).

Visible absorption measurements were performed by melting the  $\text{Co(hmba)}_3[\text{CoBr}_4]$  crystal on a fused quartz glass slide. After melting, the melt was made into a film by pressing with another fused quartz slide. Following measurements, the visible spectrum showed strong absorption, but it was not possible to quantify the absorption coefficient due to uncertainties in estimating the film thickness.

$^1\text{HNMR}$  spectra were recorded in solutions of  $\sim 10$  mg glass in  $\sim 0.5$  mL of DMSO- $d_6$  on a Bruker Avance III 600 MHz NMR spectrometer. The data analysis was performed in TOPSPIN.

To investigate the structural changes during glass formation after hydration, Fourier transform infrared (FT-IR) spectroscopy measurements were performed on pristine glass and hydrated glass samples. FT-IR

spectra were acquired using an attenuated total reflection setup (incorporating crystalline Ge) under ambient conditions using a Spectrum One spectrometer (PerkinElmer STA 6000) followed by background subtraction. Absorption spectra were collected in the wavenumber region from 500 to 4000  $\text{cm}^{-1}$ . Glass samples were prepared in advance in a closed crucible before testing at ambient temperature.

Raman measurements were carried out using a micro-Raman spectrometer (inVia, Renishaw). The sample surface was excited by a 532 nm green diode pumped solid state laser for an acquisition time of 10 s. First, we prepared pristine samples before the measurement in a closed crucible followed by Raman measurements. Next, we performed the measurement during the entire glass formation process of two samples (pristine and hydrated glass) by adding crystal ( $\sim 5$  mg) and water (0 and 0.8  $\mu\text{L}$  for the pristine and hydrated glass, respectively) to an *in situ* cell. The samples were then measured at different temperatures, from room temperature up to 140°C (melting process) before cooling to -60°C. Raman spectra were acquired every 20°C. All heating and cooling processes were performed using rates of 10 K  $\text{min}^{-1}$ .

To more accurately and deeply explore the effect of hydration on the structure of the glass formation process, extended X-ray absorption fine structure analysis (EXAFS) was conducted.

Similar to the Raman measurements, the EXAFS measurements covered the glass formation process of the pristine and hydrated samples. The temperature during the measurement process started at room temperature before increasing the temperature to 430 K (melting process), and then cooling to 240 K (cooling process). Measurements were carried out every 20 K during the whole process. Subsequent data analysis were performed using the Demeter software suite.

### *First principles simulations*

The  $\text{Co(hmba)}_3[\text{CoBr}_4]$  structure was simulated by employing a unit cell structure from Ref.<sup>16</sup> (CCDC Deposition number: 120455). The melting process of  $\text{Co(hmba)}_3[\text{CoBr}_4]$  structure with different water

contents were simulated using density functional theory (DFT) based molecular dynamics simulations. All the simulations were carried out on the Vega HPC cluster using the Quickstep module<sup>33</sup> embedded in the CP2K package<sup>34</sup> with the hybrid Gaussian and plane wave method (GPW). The systems were melted in the isothermal isobaric ensemble (*NPT*) at elevated temperatures (i.e., 500 K, 1000 K, and 1500 K) with a timestep of 0.5 fs. The total duration of melting process was 10.5 ps. The temperature was controlled using a canonical sampling thermostat (CSVR) by a velocity rescaling algorithm.

The parameters of the simulations were based on those used for a similar system in Ref.<sup>35</sup> In particular, the exchange correlation energy was calculated using the PBE approximation,<sup>36</sup> while dispersion interactions were handled at the DFT-D3 level.<sup>37</sup> In all the simulations, periodic boundary conditions were applied with a cutoff value of 600 Ry and relative cutoff of 40 Ry, as used in Refs.<sup>38,39</sup>. The pseudo potential GTH-PBE combined with the corresponding basis sets DZVP-GTH-PBE for H, C, and N; DZVP-MOLOPT-SR-GTH for O and Br; and DZV-GTH-PADE in the case of Co were employed.

The initial configuration of the crystalline  $\text{Co(hmba)}_3[\text{CoBr}_4]$  structure was adjusted from Ref.<sup>16</sup>, containing 216 atoms in a triclinic cell with cell parameters  $a = 11.597 \text{ \AA}$ ,  $b = 12.652 \text{ \AA}$ ,  $c = 16.040 \text{ \AA}$ , and  $\alpha = 72.018^\circ$ ,  $\beta = 85.26^\circ$ , and  $\gamma = 83.69^\circ$  (CCDC Deposition number: 120455). For the water containing systems, 1, 2 or 3 water molecules were inserted in the unit cell of  $\text{Co(hmba)}_3[\text{CoBr}_4]$  structure while ensuring the absence of any unrealistic overlap between the atoms.

Trajectory analysis. Co-O (O in the ligands), Co-Br, Co-O(w) (O in water) partial pair distribution functions (PDFs), and total PDF of the system excluding water as a function of time were calculated during the melting process. To quantify the liquid nature of the  $\text{Co(hmba)}_3[\text{CoBr}_4]$  structure influenced by water content and temperature, the Lindemann ratio  $\Delta$  for Co-O interatomic distances was calculated by measuring the width of the first peak in the partial PDF following,

$$\Delta = \text{FWHM}/d_0 \quad (1)$$

Where FWHM is the full width at half maximum of the first peak in the partial PDF obtained from a Gaussian fit and  $d_0$  is the location of the first peak. Here,  $d_0$  was determined as 2 Å for Co-O. The coordination number of Co for O and Br were calculated by taking the cut-off of the first coordination shell. The cut-offs for Co-O and Co-Br were both 3 Å, i.e., the position of the minimum after the first peak in the partial PDF of Co-O and Co-Br.

## Acknowledgments

This work was supported by the Independent Research Fund Denmark (0136-00011), the China Scholarship Council (201906250152), and the European Union's Horizon 2020 research and innovation programme (Marie Skłodowska-Curie grant agreement No. 101018156). The authors also acknowledge EuroHPC for computing resources on the Vega HPC (EU2010PA6249) as well as the Singapore Synchrotron Light Source (SSLS) for providing the facilities necessary for conducting the experimental X-ray absorption spectroscopy measurements. The SSLS is a National Research Infrastructure under the National Research Foundation, Singapore.

## Notes

The authors declare no competing interests.

## REFERENCES

- (1) Kuppler, R. J.; Timmons, D. J.; Fang, Q. R.; Li, J. R.; Makal, T. A.; Young, M. D.; Yuan, D.; Zhao, D.; Zhuang, W.; Zhou, H. C. Potential Applications of Metal-Organic Frameworks. *Coord. Chem. Rev.* **2009**, 253 (23–24), 3042–3066. <https://doi.org/10.1016/j.ccr.2009.05.019>.
- (2) Furukawa, H.; Cordova, K. E.; O'Keeffe, M.; Yaghi, O. M. The Chemistry and Applications of

- Metal-Organic Frameworks. *Science* (80-. ). **2013**, *341* (6149), 1230444.  
<https://doi.org/10.1126/science.1230444>.
- (3) Singh, A.; Jana, M. K.; Mitzi, D. B. Reversible Crystal–Glass Transition in a Metal Halide Perovskite. *Adv. Mater.* **2021**, *33* (3), 1–7. <https://doi.org/10.1002/adma.202005868>.
  - (4) Shaw, B. K.; Hughes, A. R.; Ducamp, M.; Moss, S.; Debnath, A.; Sapnik, A. F.; Thorne, M. F.; McHugh, L. N.; Pugliese, A.; Keeble, D. S.; et al. Melting of Hybrid Organic–Inorganic Perovskites. *Nat. Chem.* **2021**, *13* (8), 778–785. <https://doi.org/10.1038/s41557-021-00681-7>.
  - (5) Park, K. S.; Ni, Z.; Cote, A. P.; Choi, J. Y.; Huang, R.; Uribe-Romo, F. J.; Chae, H. K.; O’Keeffe, M.; Yaghi, O. M. Exceptional Chemical and Thermal Stability of Zeolitic Imidazolate Frameworks. *Proc. Natl. Acad. Sci. U. S. A.* **2006**, *103* (27), 10186–10191.  
<https://doi.org/10.1073/pnas.0602439103>.
  - (6) Bennett, T. D.; Tan, J. C.; Yue, Y.; Baxter, E.; Ducati, C.; Terrill, N. J.; Yeung, H. H. M.; Zhou, Z.; Chen, W.; Henke, S.; et al. Hybrid Glasses from Strong and Fragile Metal-Organic Framework Liquids. *Nat. Commun.* **2015**, *6*, 8079. <https://doi.org/10.1038/ncomms9079>.
  - (7) Bennett, T. D.; Yue, Y.; Li, P.; Qiao, A.; Tao, H.; Greaves, N. G.; Richards, T.; Lampronti, G. I.; Redfern, S. A. T.; Blanc, F.; et al. Melt-Quenched Glasses of Metal-Organic Frameworks. *J. Am. Chem. Soc.* **2016**, *138* (10), 3484–3492. <https://doi.org/10.1021/jacs.5b13220>.
  - (8) Bennett, T. D.; Saines, P. J.; Keen, D. A.; Tan, J. C.; Cheetham, A. K. Ball-Milling-Induced Amorphization of Zeolitic Imidazolate Frameworks (ZIFs) for the Irreversible Trapping of Iodine. *Chem. - A Eur. J.* **2013**, *19* (22), 7049–7055. <https://doi.org/10.1002/chem.201300216>.
  - (9) Wang, Y.; Jin, H.; Ma, Q.; Mo, K.; Mao, H.; Feldhoff, A.; Cao, X.; Li, Y.; Pan, F.; Jiang, Z. A MOF Glass Membrane for Gas Separation. *Angew. Chemie - Int. Ed.* **2020**, *59* (11), 4365–4369.

<https://doi.org/10.1002/anie.201915807>.

- (10) Jiang, G.; Qu, C.; Xu, F.; Zhang, E.; Lu, Q.; Cai, X.; Hausdorf, S.; Wang, H.; Kaskel, S. Glassy Metal–Organic-Framework-Based Quasi-Solid-State Electrolyte for High-Performance Lithium-Metal Batteries. *Adv. Funct. Mater.* **2021**, *31* (43). <https://doi.org/10.1002/adfm.202104300>.
- (11) To, T.; Sørensen, S. S.; Stepniewska, M.; Qiao, A.; Jensen, L. R.; Bauchy, M.; Yue, Y.; Smedskjaer, M. M. Fracture Toughness of a Metal-Organic Framework Glass. *Nat. Commun.* **2020**, *11*, 2593. <https://doi.org/10.1038/s41467-020-16382-7>.
- (12) Varshneya, A. K. *Fundamentals of Inorganic Glasses*; **2013**.
- (13) Madsen, R. S. K.; Qiao, A.; Sen, J.; Hung, I.; Chen, K.; Gan, Z.; Sen, S.; Yue, Y. Ultrahigh-Field  $^{67}\text{Zn}$  NMR Reveals Short-Range Disorder in Zeolitic Imidazolate Framework Glasses. *Science* (80-. ). **2020**, *367* (6485), 1473–1476. <https://doi.org/10.1126/science.aaz0251>.
- (14) Liu, M.; McGillicuddy, R. D.; Vuong, H.; Tao, S.; Slavney, A. H.; Gonzalez, M. I.; Billinge, S. J. L.; Mason, J. A. Network-Forming Liquids from Metal-Bis(Acetamide) Frameworks with Low Melting Temperatures. *J. Am. Chem. Soc.* **2021**. <https://doi.org/10.1021/jacs.0c11718>.
- (15) Longley, L.; Collins, S. M.; Li, S.; Smales, G. J.; Erucar, I.; Qiao, A.; Hou, J.; Doherty, C. M.; Thornton, A. W.; Hill, A. J.; et al. Flux Melting of Metal-Organic Frameworks. *Chem. Sci.* **2019**, *10* (12), 3592–3601. <https://doi.org/10.1039/c8sc04044c>.
- (16) Goodgame, D. M. L.; Grachvogel, D. A.; Hussain, I.; White, A. J. P.; Williams, D. J. Formation of Polymeric Network Arrays by Complexes of Manganese(II) or Cobalt(II) with Alkane Chain Linked Bis(Amide) Ligands of Biological Relevance. *Inorg. Chem.* **1999**, *38* (9), 2057–2063. <https://doi.org/10.1021/ic9812609>.
- (17) Groom, C. R.; Bruno, I. J.; Lightfoot, M. P.; Ward, S. C. The Cambridge Structural Database. *Acta*

- Crystallogr. Sect. B* **2016**, 72 (2), 171–179. <https://doi.org/10.1107/S2052520616003954>.
- (18) Hancock, B. C.; Zografi, G. The Relationship Between the Glass Transition Temperature and the Water Content of Amorphous Pharmaceutical Solids. *Pharmaceutical Research: An Official Journal of the American Association of Pharmaceutical Scientists*. **1994**, pp 471–477. <https://doi.org/10.1023/A:1018941810744>.
- (19) Cummins, H. Z.; Zhang, H.; Oh, J.; Seo, J. A.; Kim, H. K.; Hwang, Y. H.; Yang, Y. S.; Yu, Y. S.; Inn, Y. The Liquid-Glass Transition in Sugars: Relaxation Dynamics in Trehalose. *J. Non. Cryst. Solids* **2006**, 352 (42-49 SPEC. ISS.), 4464–4474. <https://doi.org/10.1016/j.jnoncrysol.2006.02.182>.
- (20) Deubener, J.; Müller, R.; Behrens, H.; Heide, G. Water and the Glass Transition Temperature of Silicate Melts. *J. Non. Cryst. Solids* **2003**, 330 (1–3), 268–273. [https://doi.org/10.1016/S0022-3093\(03\)00472-1](https://doi.org/10.1016/S0022-3093(03)00472-1).
- (21) Zhou, C.; Stepniewska, M.; Longley, L.; Ashling, C. W.; Chater, P. A.; Keen, D. A.; Bennett, T. D.; Yue, Y. Thermodynamic Features and Enthalpy Relaxation in a Metal-Organic Framework Glass. *Phys. Chem. Chem. Phys.* **2018**, 20 (27), 18291–18296. <https://doi.org/10.1039/c8cp02340a>.
- (22) Smedskjaer, M. M.; Youngman, R. E.; Striepe, S.; Potuzak, M.; Bauer, U.; Deubener, J.; Behrens, H.; Mauro, J. C.; Yue, Y. Irreversibility of Pressure Induced Boron Speciation Change in Glass. *Sci. Rep.* **2014**, 4, 3770. <https://doi.org/10.1038/srep03770>.
- (23) Debenedetti, P. G.; Stillinger, F. H. Review Article Supercooled Liquids and the Glass Transition. *Nature* **2001**, 410 (March), 259.
- (24) Wang, L. M.; Velikov, V.; Angell, C. A. Direct Determination of Kinetic Fragility Indices of

- Glassforming Liquids by Differential Scanning Calorimetry: Kinetic versus Thermodynamic Fragilities. *J. Chem. Phys.* **2002**, *117* (22), 10184–10192. <https://doi.org/10.1063/1.1517607>.
- (25) Sidebottom, D. L. Connecting Glass-Forming Fragility to Network Topology. *Front. Mater.* **2019**, *6* (June), 1–14. <https://doi.org/10.3389/fmats.2019.00144>.
- (26) Gallino, I. On the Fragility of Bulk Metallic Glass Forming Liquids. *Entropy* **2017**, *19* (9). <https://doi.org/10.3390/e19090483>.
- (27) Qiao, A.; Bennett, T. D.; Tao, H.; Krajnc, A.; Mali, G.; Doherty, C. M.; Thornton, A. W.; Mauro, J. C.; Greaves, G. N.; Yue, Y. A Metal-Organic Framework with Ultrahigh Glass-Forming Ability. *Sci. Adv.* **2018**, *4* (3), eaao6827. <https://doi.org/10.1126/sciadv.aao6827>.
- (28) Böhmer, R.; Ngai, K. L.; Angell, C. A.; Plazek, D. J. Nonexponential Relaxations in Strong and Fragile Glass Formers. *J. Chem. Phys.* **1993**, *99* (5), 4201–4209. <https://doi.org/10.1063/1.466117>.
- (29) Rayner-Canham, G.; Overton, T. *Descriptive Inorganic Chemistry*, 6th ed.; W. H. Freeman and Company, 2013.
- (30) Gaillac, R.; Pullumbi, P.; Beyer, K. A.; Chapman, K. W.; Keen, D. A.; Bennett, T. D.; Coudert, F. X. Liquid Metal–Organic Frameworks. *Nat. Mater.* **2017**, *16*, 1149–1155. <https://doi.org/10.1038/NMAT4998>.
- (31) Gersten, J. I.; Smith, F. W. *The Physics and Chemistry of Materials*; Wiley, 2001.
- (32) Lincoln, S. F.; Richens, D. T.; Sykes, A. G. Metal Aqua Ions. In *Comprehensive Coordination Chemistry II*; Elsevier, 2003; pp 515–555.
- (33) Vandevondele, J.; Krack, M.; Mohamed, F.; Parrinello, M.; Chassaing, T.; Hutter, J. Quickstep: Fast and Accurate Density Functional Calculations Using a Mixed Gaussian and Plane Waves



- Approach. *Comput. Phys. Commun.* **2005**, *167* (2), 103–128.  
<https://doi.org/10.1016/j.cpc.2004.12.014>.
- (34) Kühne, T. D.; Iannuzzi, M.; Del Ben, M.; Rybkin, V. V.; Seewald, P.; Stein, F.; Laino, T.; Khaliullin, R. Z.; Schütt, O.; Schiffmann, F.; et al. CP2K: An Electronic Structure and Molecular Dynamics Software Package -Quickstep: Efficient and Accurate Electronic Structure Calculations. *J. Chem. Phys.* **2020**, *152* (19). <https://doi.org/10.1063/5.0007045>.
- (35) Shaw, B. K.; Hughes, A. R.; Ducamp, M.; Moss, S.; Debnath, A.; Sapnik, A. F.; Thorne, M. F.; McHugh, L. N.; Pugliese, A.; Keeble, D. S.; et al. Melting of Hybrid Organic–Inorganic Perovskites. *Nat. Chem.* **2021**, *13* (8), 778–785. <https://doi.org/10.1038/s41557-021-00681-7>.
- (36) Perdew, J. P.; Burke, K.; Ernzerhof, M. Generalized Gradient Approximation Made Simple. *Phys. Rev. Lett.* **1996**, *77* (18), 3865–3868. <https://doi.org/10.1103/PhysRevLett.77.3865>.
- (37) Grimme, S.; Antony, J.; Ehrlich, S.; Krieg, H. A Consistent and Accurate Ab Initio Parametrization of Density Functional Dispersion Correction (DFT-D) for the 94 Elements H–Pu. *J. Chem. Phys.* **2010**, *132* (15). <https://doi.org/10.1063/1.3382344>.
- (38) Haigis, V.; Coudert, F. X.; Vuilleumier, R.; Boutin, A. Investigation of Structure and Dynamics of the Hydrated Metal–Organic Framework MIL-53(Cr) Using First-Principles Molecular Dynamics. *Phys. Chem. Chem. Phys.* **2013**, *15* (43), 19049–19056. <https://doi.org/10.1039/c3cp53126k>.
- (39) Gaillac, R.; Pullumbi, P.; Coudert, F. X. Melting of Zeolitic Imidazolate Frameworks with Different Topologies: Insight from First-Principles Molecular Dynamics. *J. Phys. Chem. C* **2018**, *122* (12), 6730–6736. <https://doi.org/10.1021/acs.jpcc.8b00385>.

# Supporting Information

*for*

## **Water as a modifier in a hybrid coordination network glass**

Søren S. Sørensen<sup>1,†</sup>, Xiangting Ren<sup>1,†</sup>, Tao Du<sup>1,†</sup>, Shibo Xi<sup>2</sup>, Lars R. Jensen<sup>3</sup>, John Wang<sup>4</sup>, Morten M.

Smedskjaer<sup>1,\*</sup>

<sup>1</sup> *Department of Chemistry and Bioscience, Aalborg University, Aalborg, Denmark*

<sup>2</sup> *Institute of Chemical & Engineering Sciences, Agency for Science, Technology and Research (A\*STAR),  
Singapore, 627833, Singapore*

<sup>3</sup> *Department of Materials and Production, Aalborg University, Aalborg, Denmark*

<sup>4</sup> *Department of Materials Science and Engineering, National University of Singapore, 117574,  
Singapore*

\*Corresponding author email: mos@bio.aau.dk

**Figure S1**

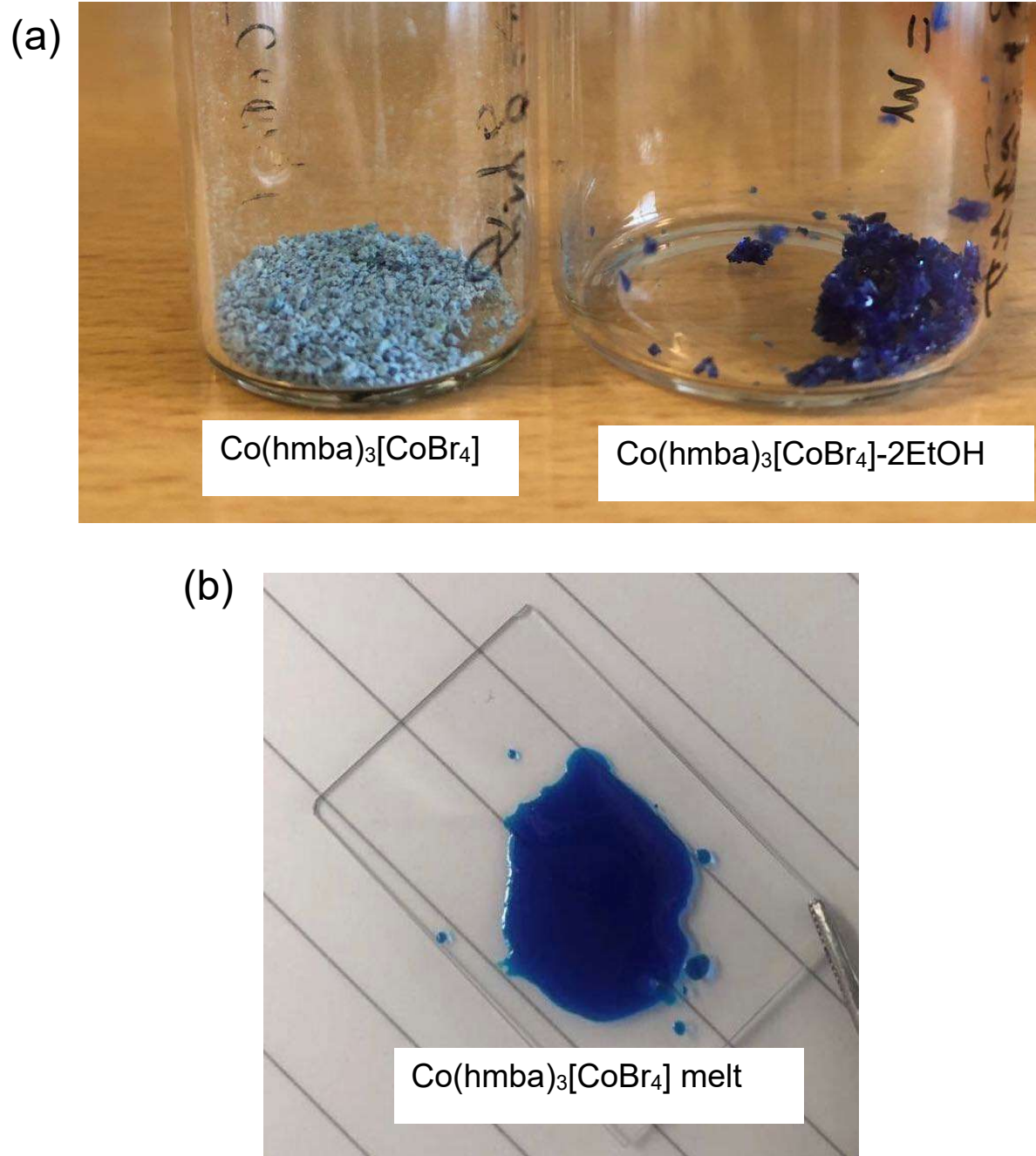


**Figure S1.** (a) Images of as-synthesized Co(hmba)<sub>3</sub>[CoBr<sub>4</sub>]-2EtOH crystal (dark blue, right), same sample after drying for 1-2 weeks, forming Co(hmba)<sub>3</sub>[CoBr<sub>4</sub>] (light blue, left). (b) Image of molten Co(hmba)<sub>3</sub>[CoBr<sub>4</sub>] on a transparent microscope glass slide. Distance between lines is ~9 mm.

**Figure S2**

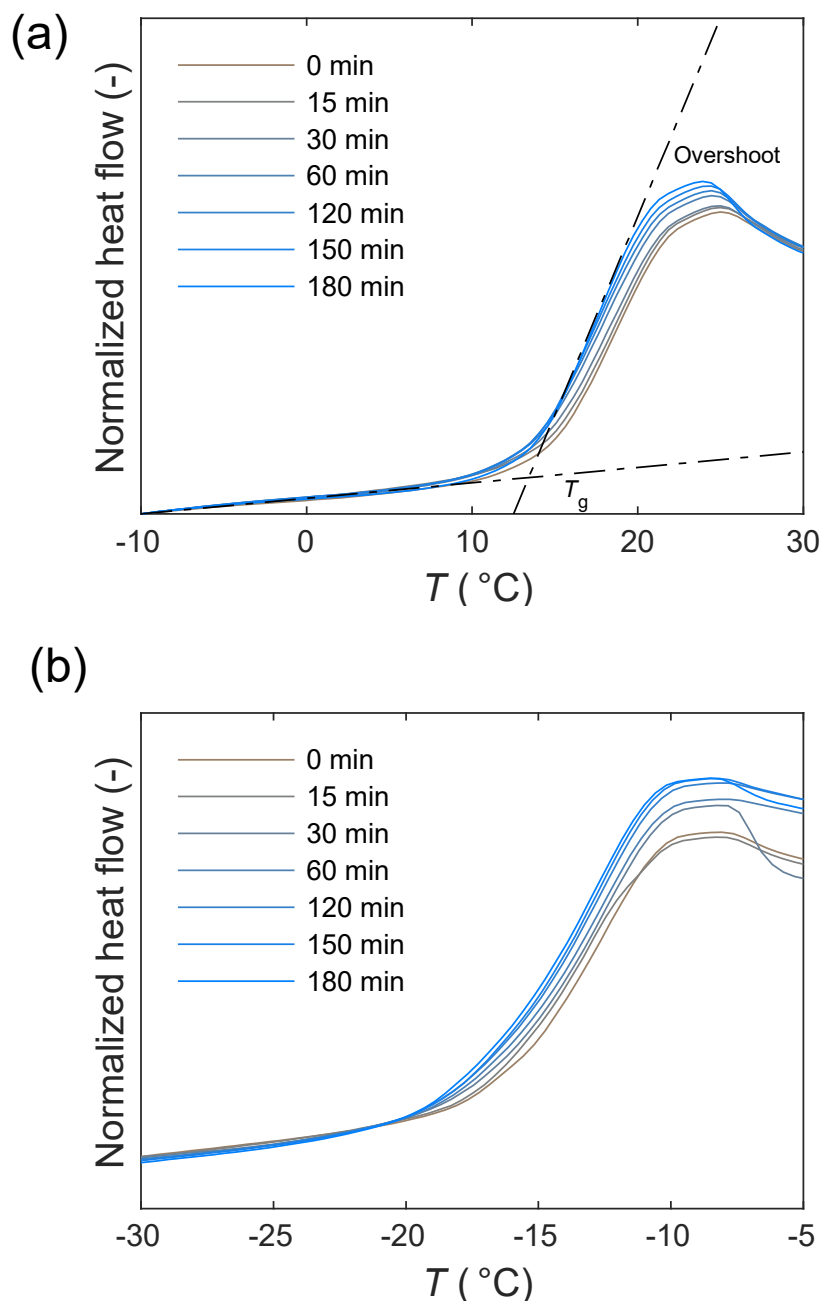


**Figure S2.** Differential scanning calorimetry heating scans after annealing at  $0.9T_g$  for 0, 15, 30, 60, 120, 150, and 180 min for (a) an anhydrous glass and (b) a hydrated glass. The glass transition temperature ( $T_g$ ) is determined as the onset temperature, as shown for the 180 min annealed sample in (a).

**Figure S3**

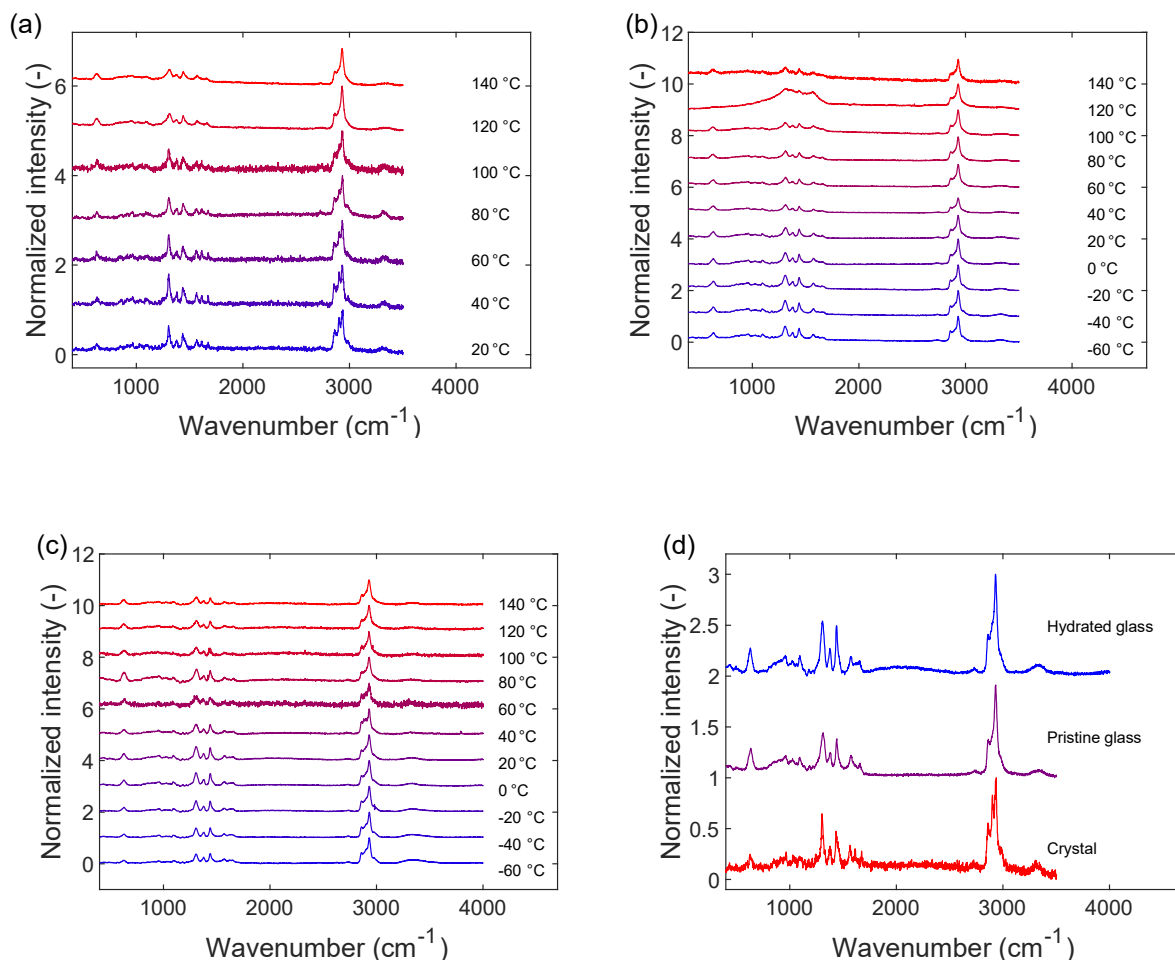


**Figure S3.** *In situ* Raman spectroscopy data as collected during heating of (a) anhydrous crystal into the molten phase from room temperature to 140 °C, and (b) anhydrous glass and (c) hydrated glass from -60 to 140 °C, as well as (d) direct comparisons of the Raman spectra of crystalline and glassy  $\text{Co}(\text{hmba})_3[\text{CoBr}_4]$  as well as a hydrated glass. All spectra are shifted vertically for clarity.

**Figure S4**

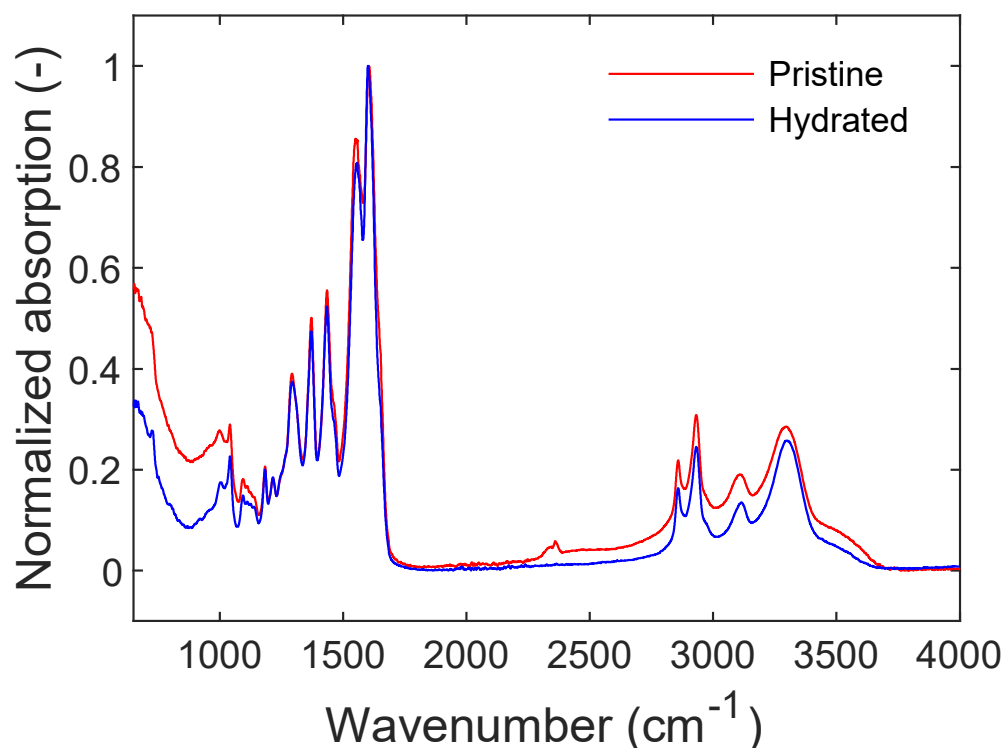


**Figure S4.** Fourier-transform infrared (FT-IR) spectra of anhydrous and hydrated  $\text{Co(hmba)}_3[\text{CoBr}_4]$  glasses measured at room temperature.

**Figure S5**

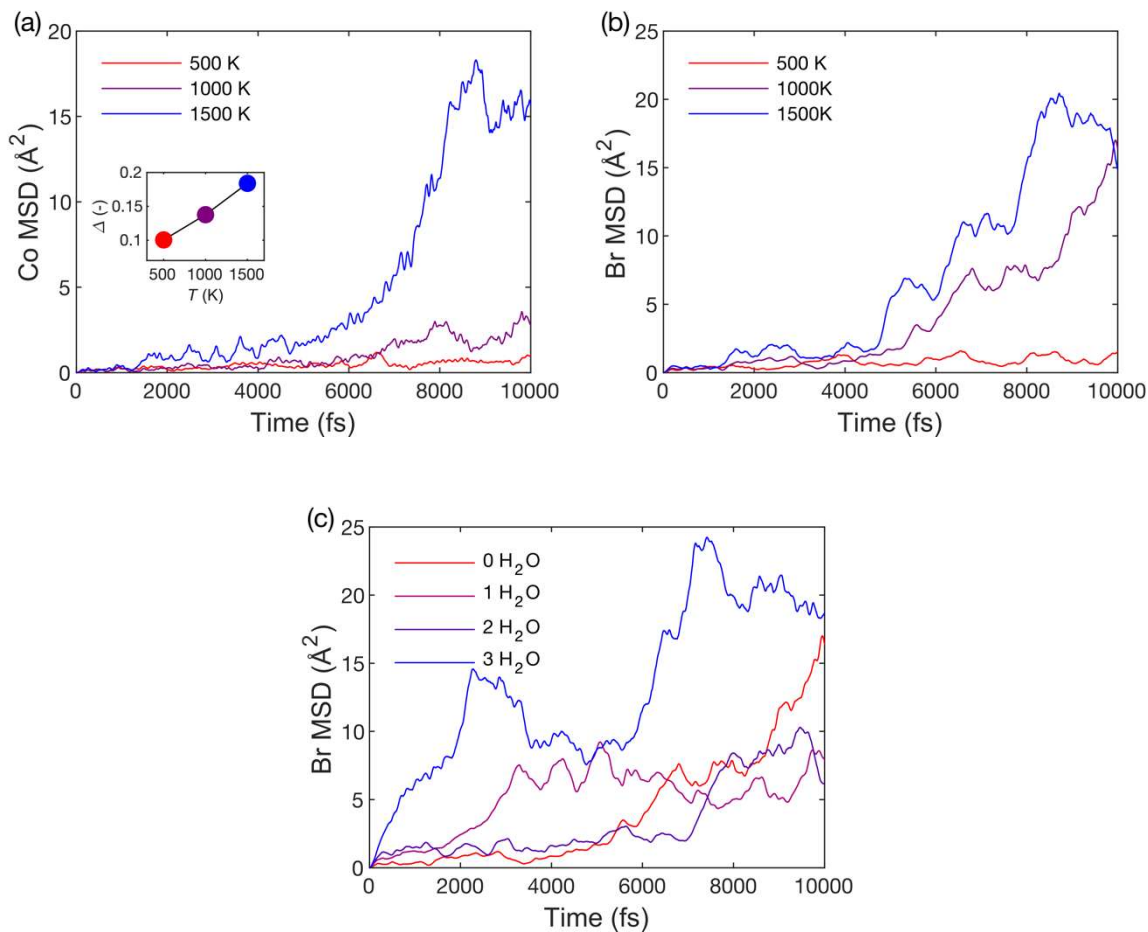


**Figure S5.** Simulated mean-square displacement (MSD) of (a) Co and (b) Br as a function of temperature (500, 1000, and 1500 K). The inset in (a) shows the Lindemann ratio of the Co-O bonds ( $\Delta$ ) at the three studied temperatures. (c) MSD of Br atoms as a function of the number of water molecules in the unit cell structure at 1000 K, showing an increase in MSD with increasing amount of water.

**Figure S6**

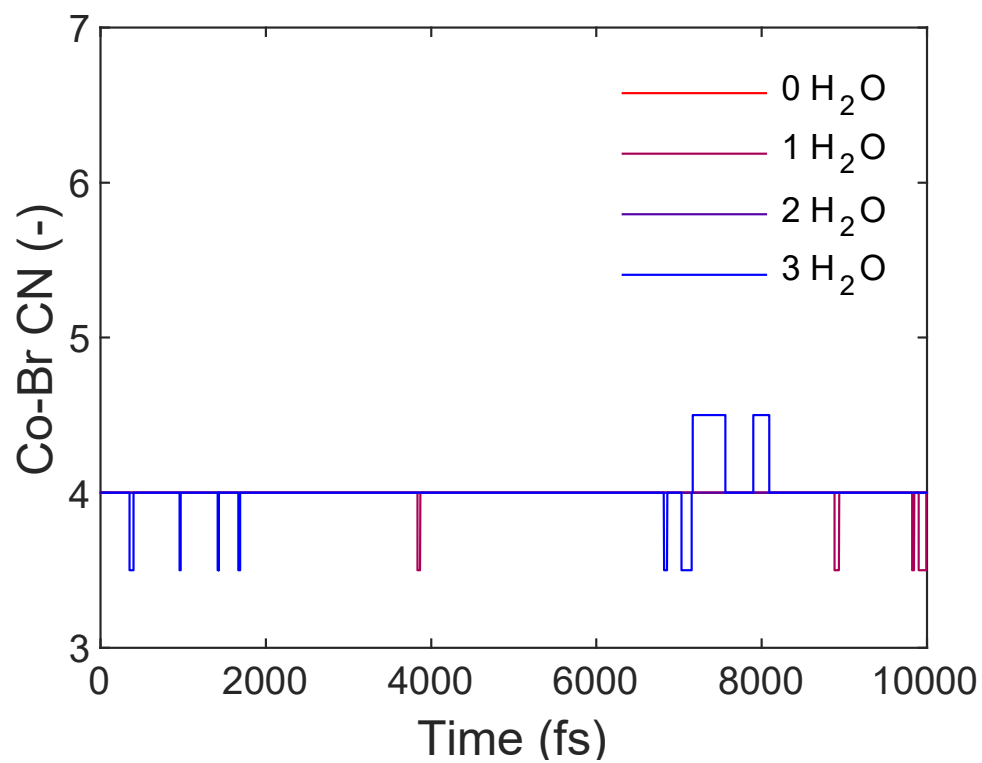


**Figure S6.** Simulated Co-Br coordination numbers of Co atoms initially surrounded by Br atoms over the simulated time range. Results are shown for simulations boxes with 0, 1, 2, and 3 water molecules at 1000 K.



**Figure S7**

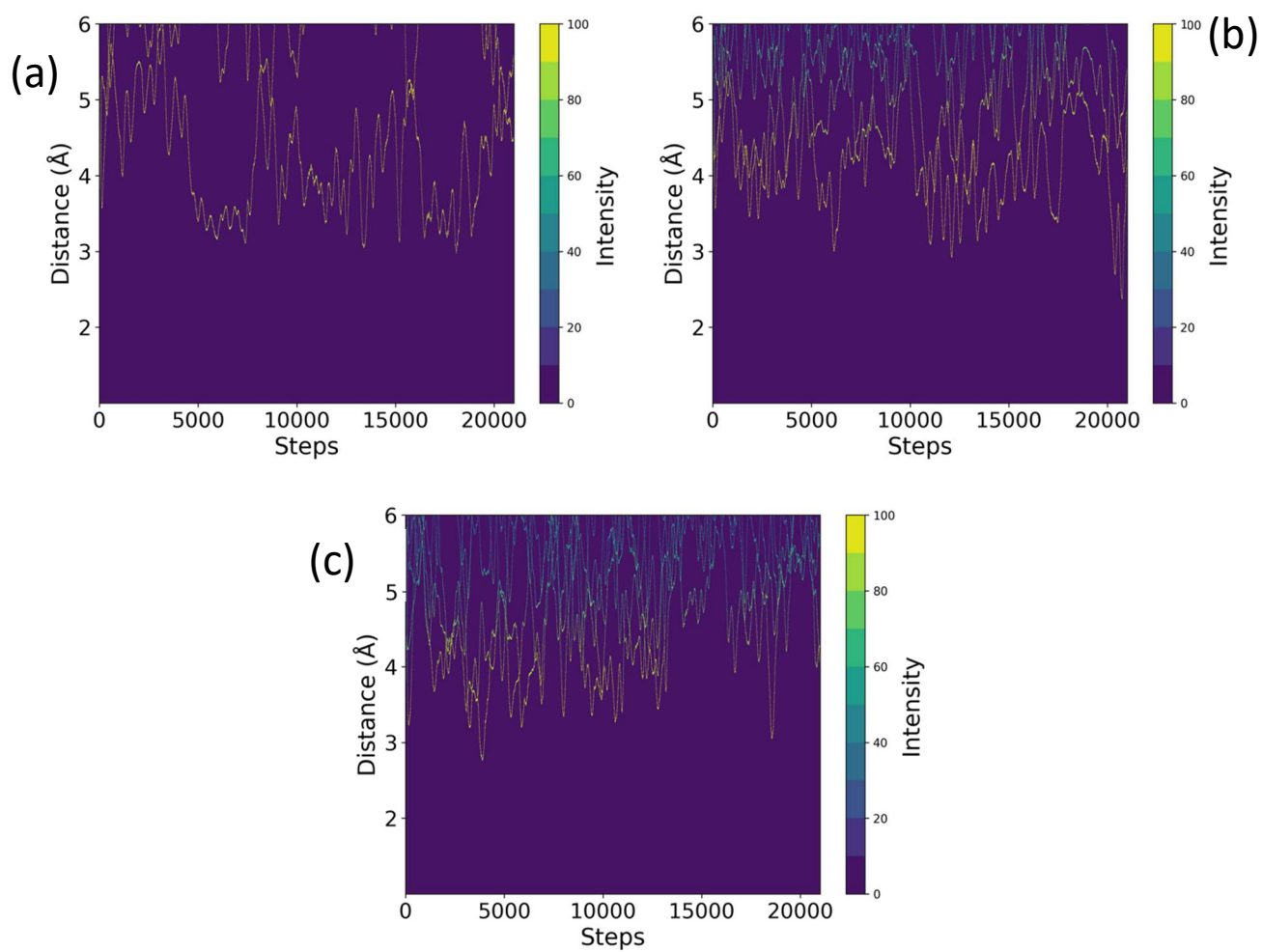


**Figure S7.** Simulated distances between cobalt atoms and oxygen in water molecules at 1000 K for (a) 1; (b) 2; and (c) 3 water molecules in the unit cell structure.

**Figure S8**

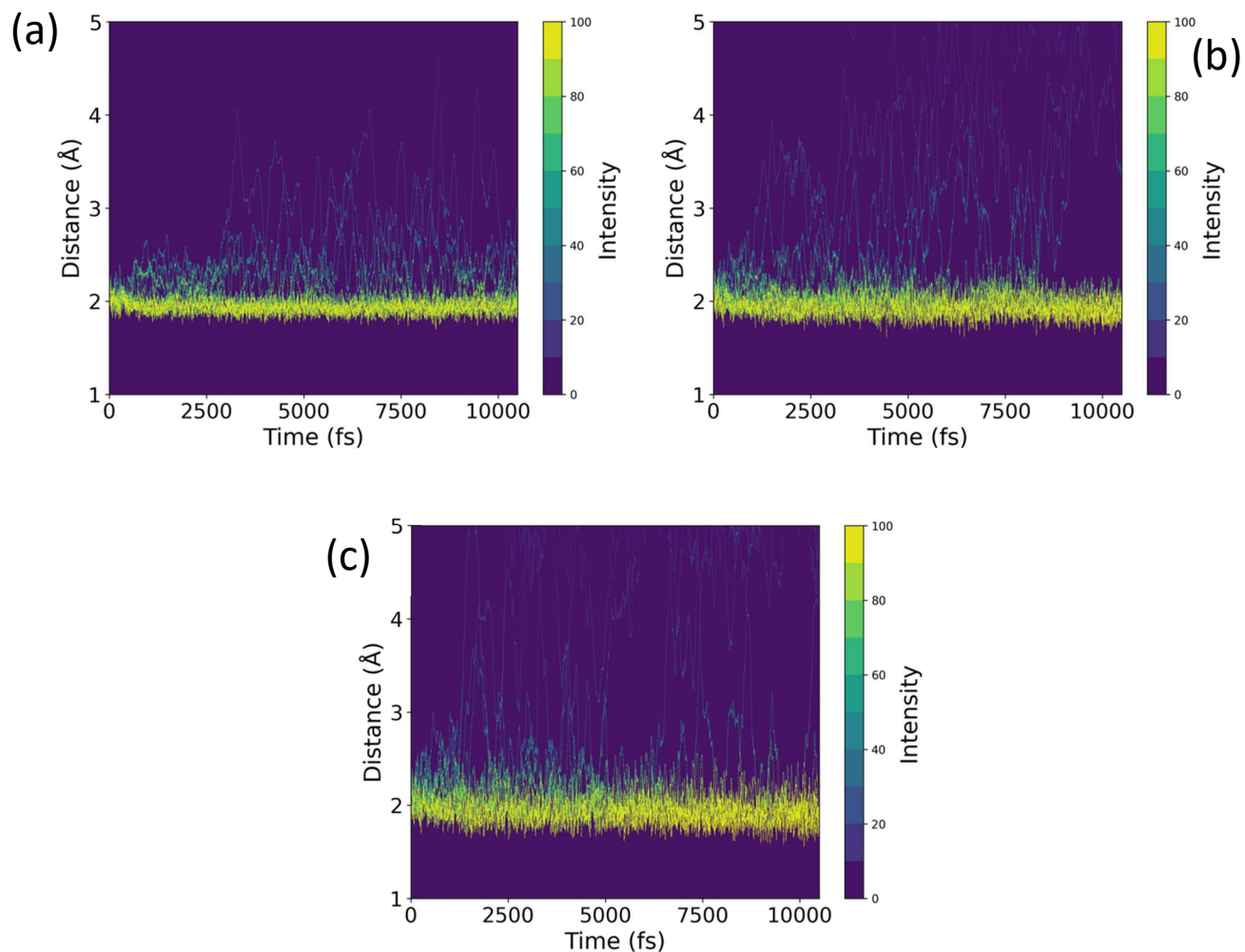


**Figure S8.** Simulated distances between cobalt atoms and oxygen in hmba molecules at (a) 500 K; (b) 1000 K; and (c) 1500 K as a function of simulation time.

**Figure S9**

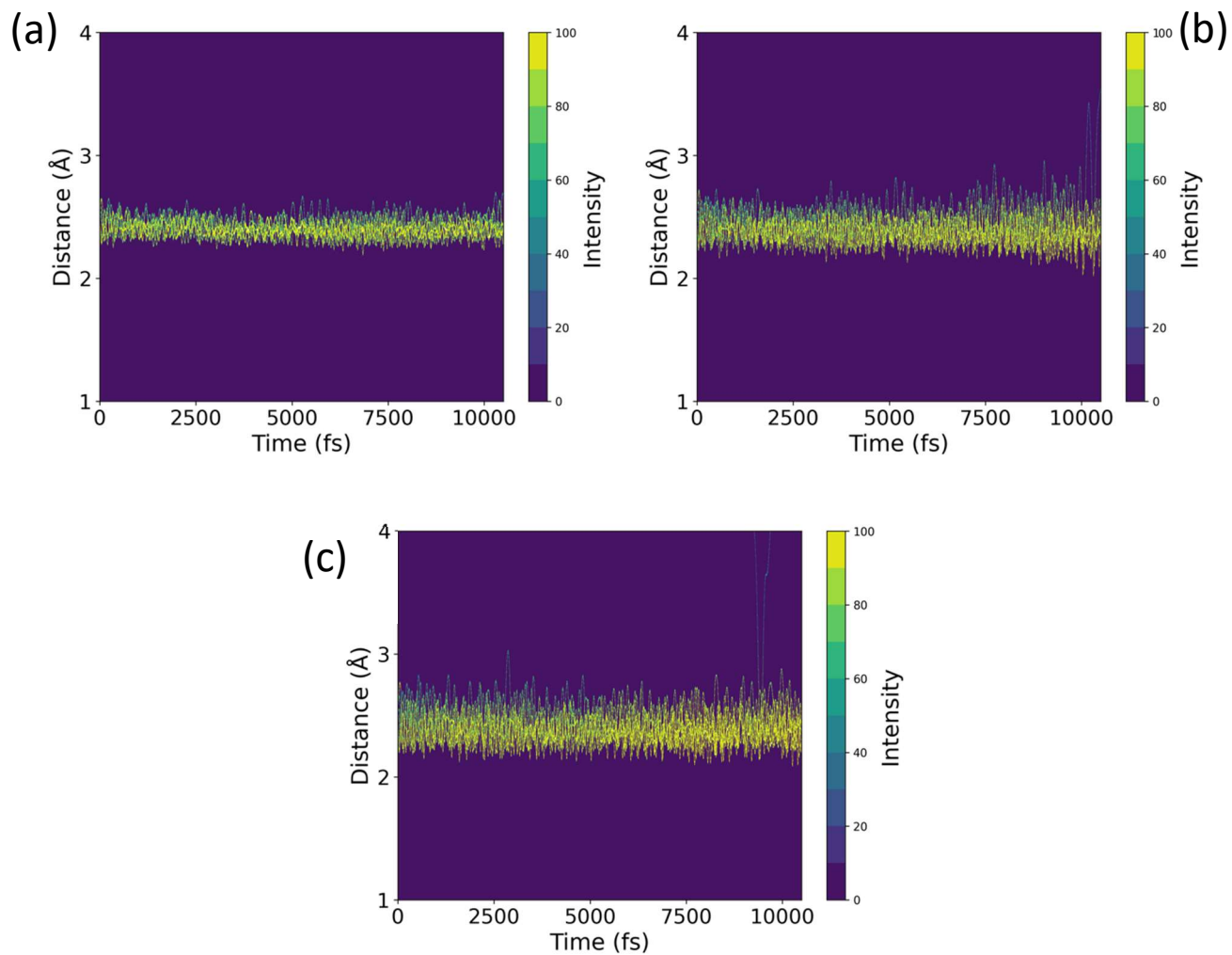


**Figure S9.** Simulated distances between cobalt and bromine atoms at (a) 500 K; (b) 1000 K; and (c) 1500 K as a function of simulation time.

**Figure S10**

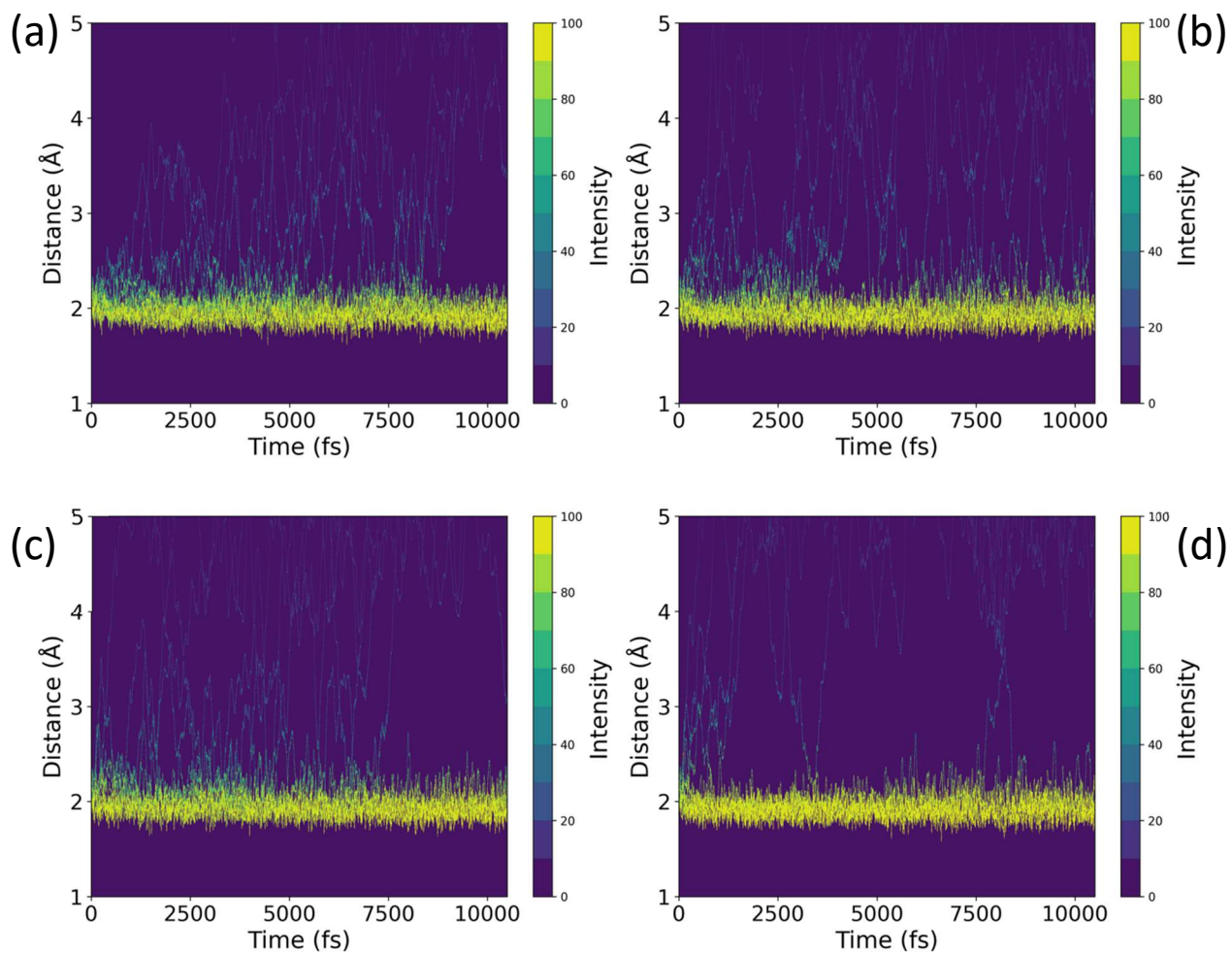


**Figure S10.** Simulated distances between cobalt atoms and oxygen in hmba molecules at 1000 K for (a) 0; (b) 1; (c) 2; and (d) 3 water molecules in the unit cell structure.

**Figure S11**

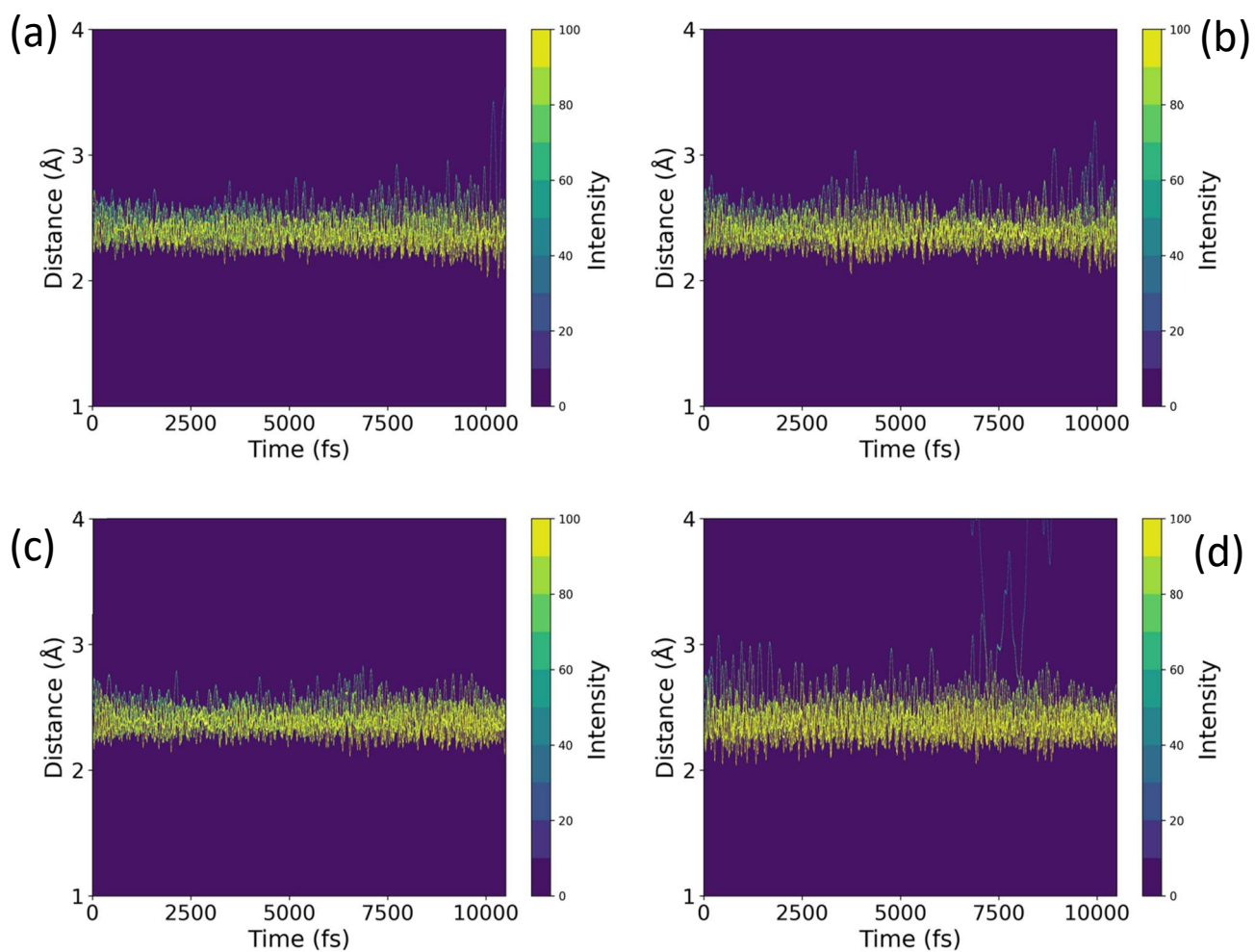


**Figure S11.** Simulated distances between cobalt and bromine atoms at 1000 K for (a) 0; (b) 1; (c) 2; and (d) 3 water molecules in the unit cell structure.

**Figure S12**

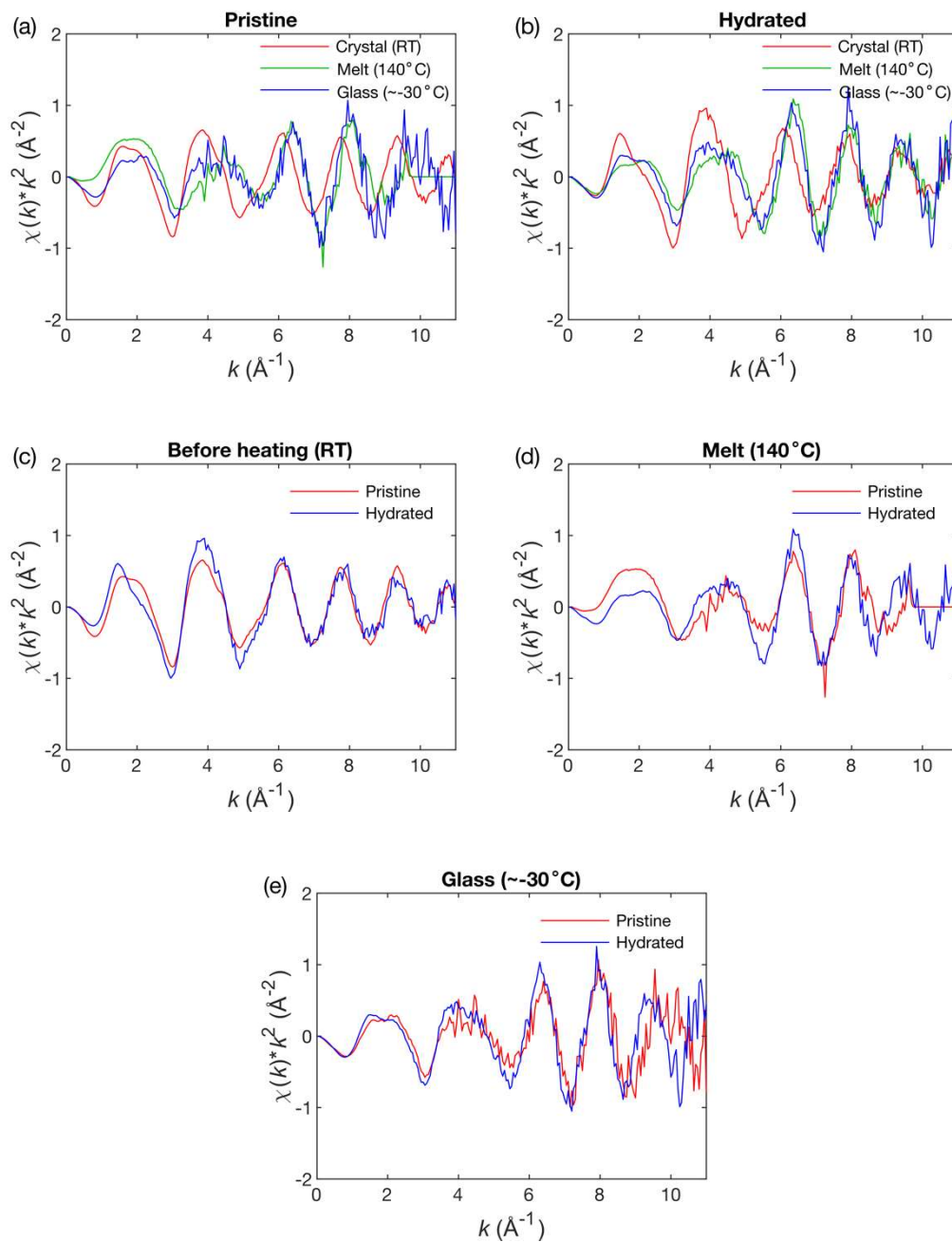


**Figure S12.** Extended X-ray absorption fine structure (EXAFS) data comparisons at different steps in the melting process for (a) pristine and (b) hydrated systems, and (c-e) comparisons at each temperature for pristine and hydrated systems.

**Figure S13**

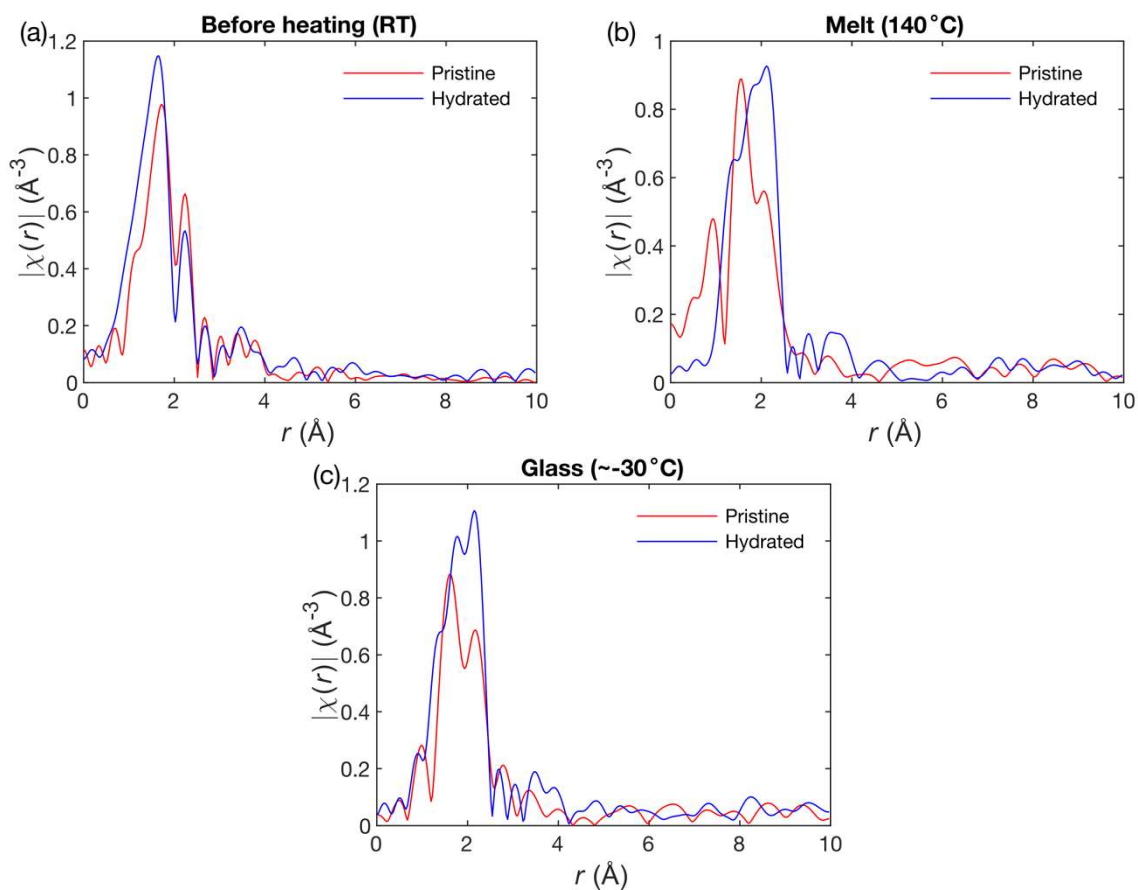


**Figure S13.** Direct comparison of the magnitude of Fourier transform of the EXAFS data for the pristine and hydrated  $\text{Co(hmba)}_3[\text{CoBr}_4]$  systems (a) before heating, (b) in the melt, and (c) in the glassy state.

**Figure S14**

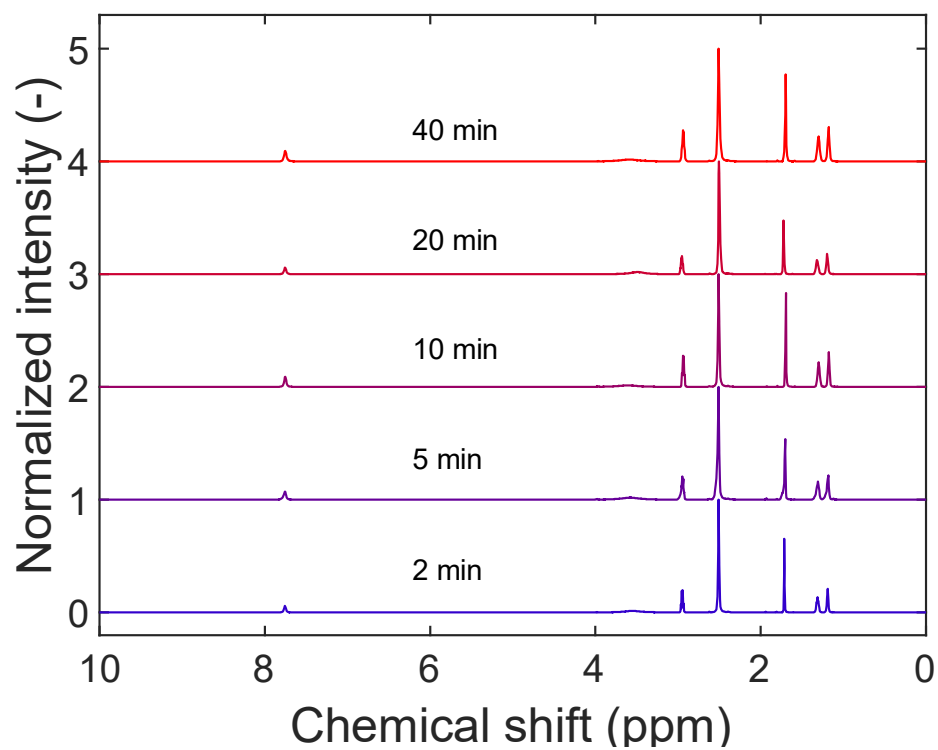


**Figure S14.** Liquid state  $^1\text{H}$  NMR spectra of digested anhydrous  $\text{Co}(\text{hmba})_3[\text{CoBr}_4]$  glasses melted for 2, 5, 10, 20, and 40 min, showing remarkable chemical stability of the hmba linker. Spectra were recorded in  $\text{DMSO-d}_6$ . An example of chemical assignment for the glass melted for 2 min is presented in Fig. S15.



**Figure S15**

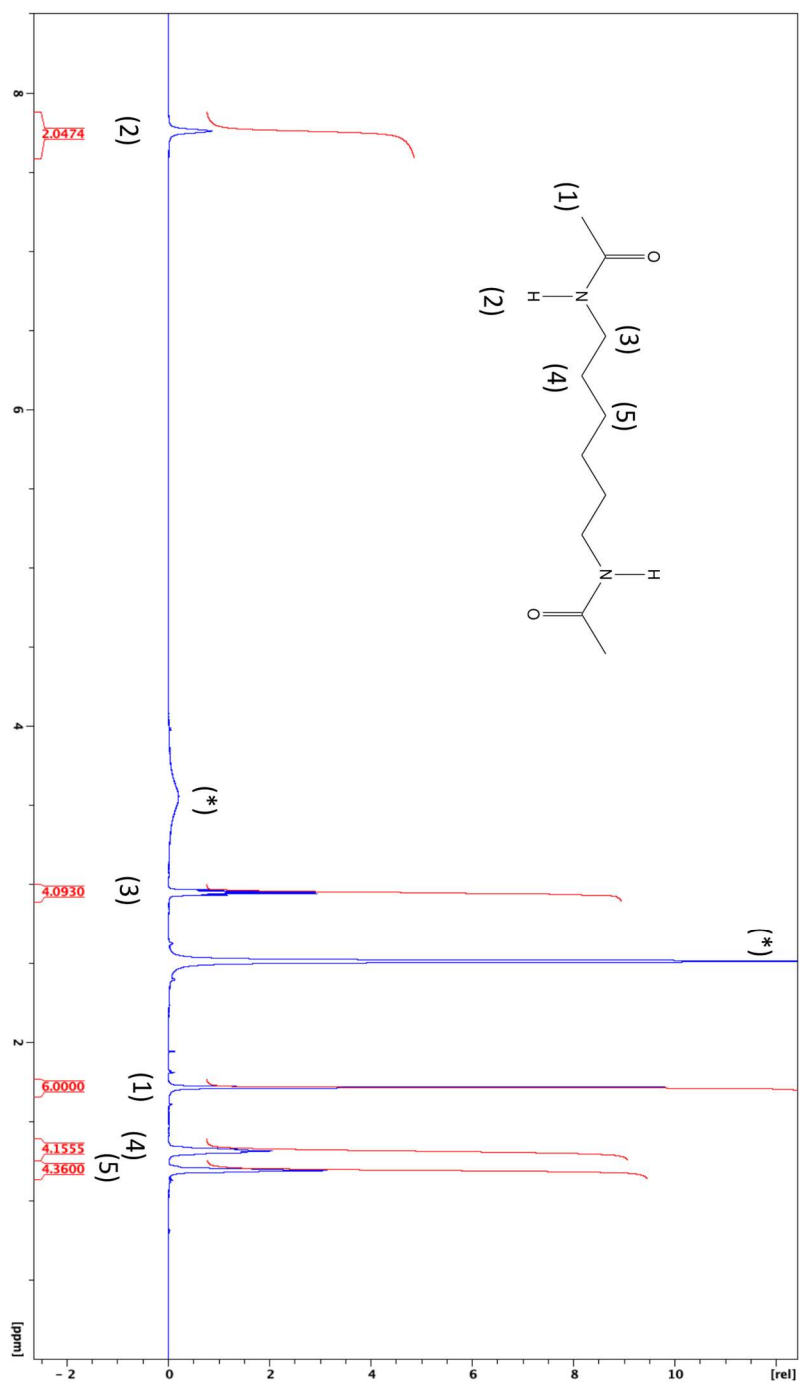


**Figure S15.** Liquid state  $^1\text{H}$  NMR spectra of digested anhydrous  $\text{Co}(\text{hmba})_3[\text{CoBr}_4]$  glass melted for 2 min with chemical assignments to parts of the hmba linker structure. (\*) refers to solvent or solvent impurity.

## SUPPORTING REFERENCES

- (1) Kuppler, R. J.; Timmons, D. J.; Fang, Q. R.; Li, J. R.; Makal, T. A.; Young, M. D.; Yuan, D.; Zhao, D.; Zhuang, W.; Zhou, H. C. Potential Applications of Metal-Organic Frameworks. *Coord. Chem. Rev.* **2009**, 253 (23–24), 3042–3066. <https://doi.org/10.1016/j.ccr.2009.05.019>.
- (2) Furukawa, H.; Cordova, K. E.; O’Keeffe, M.; Yaghi, O. M. The Chemistry and Applications of Metal-Organic Frameworks. *Science (80-. )*. **2013**, 341 (6149), 1230444. <https://doi.org/10.1126/science.1230444>.
- (3) Park, K. S.; Ni, Z.; Cote, A. P.; Choi, J. Y.; Huang, R.; Uribe-Romo, F. J.; Chae, H. K.; O’Keeffe, M.; Yaghi, O. M. Exceptional Chemical and Thermal Stability of Zeolitic Imidazolate Frameworks. *Proc. Natl. Acad. Sci. U. S. A.* **2006**, 103 (27), 10186–10191. <https://doi.org/10.1073/pnas.0602439103>.
- (4) Bennett, T. D.; Tan, J. C.; Yue, Y.; Baxter, E.; Ducati, C.; Terrill, N. J.; Yeung, H. H. M.; Zhou, Z.; Chen, W.; Henke, S.; et al. Hybrid Glasses from Strong and Fragile Metal-Organic Framework Liquids. *Nat. Commun.* **2015**, 6, 8079. <https://doi.org/10.1038/ncomms9079>.
- (5) Bennett, T. D.; Yue, Y.; Li, P.; Qiao, A.; Tao, H.; Greaves, N. G.; Richards, T.; Lampronti, G. I.; Redfern, S. A. T.; Blanc, F.; et al. Melt-Quenched Glasses of Metal-Organic Frameworks. *J. Am. Chem. Soc.* **2016**, 138 (10), 3484–3492. <https://doi.org/10.1021/jacs.5b13220>.
- (6) Bennett, T. D.; Saines, P. J.; Keen, D. A.; Tan, J. C.; Cheetham, A. K. Ball-Milling-Induced Amorphization of Zeolitic Imidazolate Frameworks (ZIFs) for the Irreversible Trapping of Iodine. *Chem. - A Eur. J.* **2013**, 19 (22), 7049–7055. <https://doi.org/10.1002/chem.201300216>.

- (7) Shaw, B. K.; Hughes, A. R.; Ducamp, M.; Moss, S.; Debnath, A.; Sapnik, A. F.; Thorne, M. F.; McHugh, L. N.; Pugliese, A.; Keeble, D. S.; et al. Melting of Hybrid Organic–Inorganic Perovskites. *Nat. Chem.* **2021**, *13* (8), 778–785. <https://doi.org/10.1038/s41557-021-00681-7>.
- (8) Wang, Y.; Jin, H.; Ma, Q.; Mo, K.; Mao, H.; Feldhoff, A.; Cao, X.; Li, Y.; Pan, F.; Jiang, Z. A MOF Glass Membrane for Gas Separation. *Angew. Chemie - Int. Ed.* **2020**, *59* (11), 4365–4369. <https://doi.org/10.1002/anie.201915807>.
- (9) Jiang, G.; Qu, C.; Xu, F.; Zhang, E.; Lu, Q.; Cai, X.; Hausdorf, S.; Wang, H.; Kaskel, S. Glassy Metal–Organic-Framework-Based Quasi-Solid-State Electrolyte for High-Performance Lithium-Metal Batteries. *Adv. Funct. Mater.* **2021**, *31* (43). <https://doi.org/10.1002/adfm.202104300>.
- (10) To, T.; Sørensen, S. S.; Stepniewska, M.; Qiao, A.; Jensen, L. R.; Bauchy, M.; Yue, Y.; Smedskjaer, M. M. Fracture Toughness of a Metal-Organic Framework Glass. *Nat. Commun.* **2020**, *11*, 2593. <https://doi.org/10.1038/s41467-020-16382-7>.
- (11) Varshneya, A. K. *Fundamentals of Inorganic Glasses*; 2013.
- (12) Madsen, R. S. K.; Qiao, A.; Sen, J.; Hung, I.; Chen, K.; Gan, Z.; Sen, S.; Yue, Y. Ultrahigh-Field  $^{67}\text{Zn}$  NMR Reveals Short-Range Disorder in Zeolitic Imidazolate Framework Glasses. *Science* (80-. ). **2020**, *367* (6485), 1473–1476. <https://doi.org/10.1126/science.aaz0251>.
- (13) Liu, M.; McGillicuddy, R. D.; Vuong, H.; Tao, S.; Slavney, A. H.; Gonzalez, M. I.; Billinge, S. J. L.; Mason, J. A. Network-Forming Liquids from Metal-Bis(Acetamide) Frameworks with Low Melting Temperatures. *J. Am. Chem. Soc.* **2021**. <https://doi.org/10.1021/jacs.0c11718>.
- (14) Longley, L.; Collins, S. M.; Li, S.; Smales, G. J.; Erucar, I.; Qiao, A.; Hou, J.; Doherty, C. M.; Thornton, A. W.; Hill, A. J.; et al. Flux Melting of Metal-Organic Frameworks. *Chem. Sci.* **2019**, *10* (12), 3592–3601. <https://doi.org/10.1039/c8sc04044c>.

- (15) Goodgame, D. M. L.; Grachvogel, D. A.; Hussain, I.; White, A. J. P.; Williams, D. J. Formation of Polymeric Network Arrays by Complexes of Manganese(II) or Cobalt(II) with Alkane Chain Linked Bis(Amide) Ligands of Biological Relevance. *Inorg. Chem.* **1999**, 38 (9), 2057–2063. <https://doi.org/10.1021/ic9812609>.
- (16) Groom, C. R.; Bruno, I. J.; Lightfoot, M. P.; Ward, S. C. The Cambridge Structural Database. *Acta Crystallogr. Sect. B* **2016**, 72 (2), 171–179. <https://doi.org/10.1107/S2052520616003954>.



ISSN (online): 2446-1636  
ISBN (online): 978-87-7573-874-8

AALBORG UNIVERSITY PRESS